18 February 2005

Science

Vol. 307 No. 5712
Pages 997–1152 $10

125 YEARS OF GLOBAL Science

AAAS

Science

Volume 307
18 February 2005
Number 5712

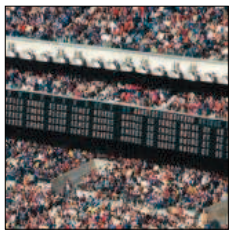

COVER Variation among humans is evident in the cover image and in a new map of key genetic signposts in three human populations, as described by Hinds *et al.* (page 1072). This resource will speed efforts to pinpoint disease-related genes and will advance population and evolutionary genetics. Also see the Policy Forum on page 1050 and the Perspective on page 1052. [Image: Joshua Moglia]

DEPARTMENTS

NEWS OF THE WEEK

NEWS FOCUS

1032

1049

1055 & 1068

LETTERS

BOOKS *ET AL.*

POLICY FORUM

PERSPECTIVES

Contents continued

Science

Review

Science Express www.sciencexpress.org

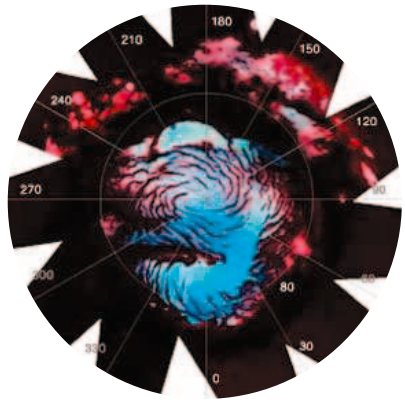

Mars Express, which has been in a polar orbit around Mars since late December 2003, has detected large water-ice crystals in the north polar cap, mapped abundant sulfate deposits, particularly around the north pole, detected absorbed water in old but not young rocks; and found large variations in the distribution of primary silicate minerals in martian rocks of different ages. The observations imply that water was only abundant in Mars' early history and that most volatiles have been lost, except for water and carbon dioxide in the polar caps. *related News story page 1025*

Brevia

Maximizing entropy in a cell or other confined space stabilizes polymers in helical structures.

Research Articles

Trace elements in Olmec pottery found throughout Mesoamerica show that the San Lorenzo region on the Gulf Coast was the only major export center. *related Perspective page 1055*

Identification of more than 1.5 million single-nucleotide polymorphisms in three diverse human populations begins to reveal the structure of human genetic variation. *related Policy Forum page 1050; Perspective page 1052*

Reports

An iridium complex breaks an ammonia N-H bond, potentially establishing a way to add ammonia catalytically and directly to unsaturated organic compounds.

Three different bipedal walking machines equipped with simple powered actuators and controllers efficiently mimic human gait and suggest improvements to humanoid robots.

A satellite has detected abundant energetic gamma-ray flashes in Earth's upper atmosphere, apparently triggered by lightning and other electrical discharges. *related Perspective page 1054*

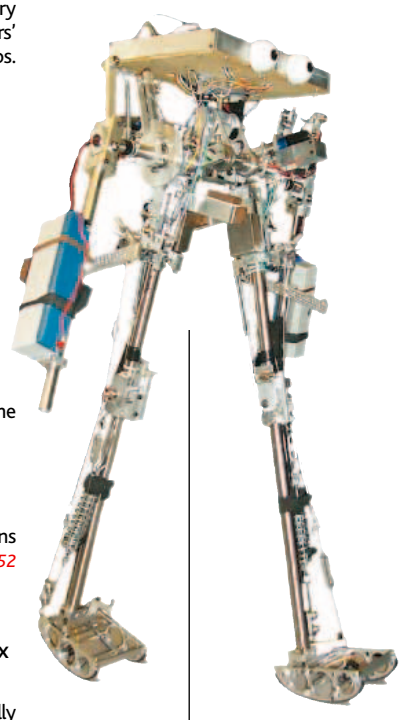

1082

Contents continued

Visit us at PITTCON Booth #972

Discover biomarkers.

Identify and quantitate protein biomarkers with confidence.

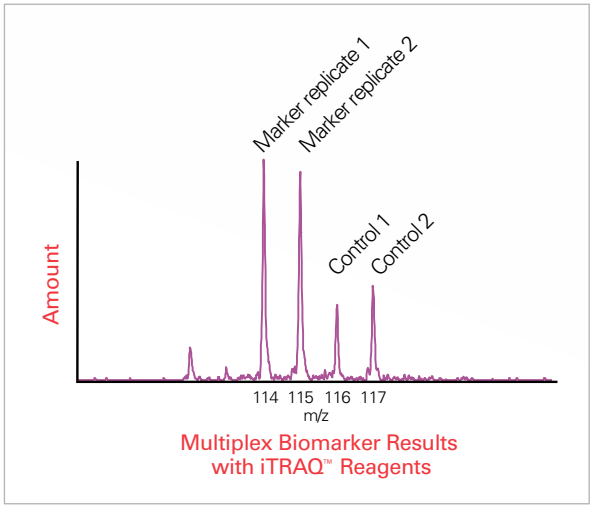

Multiplex Biomarker Results with iTRAQ™ Reagents

From discovery to validation, total system solutions from Applied Biosystems/MDS SCIEX make your protein biomarker research faster, easier, and more productive. Our innovative technologies for protein identification and relative and absolute quantitation provide rapid, accurate results from your most complex samples. In fact, using powerful new workflows and innovative BIOiTRAQ™ systems, you can confidently identify putative biomarkers and accurately quantitate them, all within a single experiment. To learn more, visit http://info.appliedbiosystems.com/**biomarkers**


BIOiTRAQ™ TT System


BIOiTRAQ™ QT System


BIOiTRAQ™ QS System

iScience. Applied Biosystems provides the innovative products, services, and knowledge resources that are enabling new, integrated approaches to scientific discovery.

Applied Biosystems | MDS SCIEX

REPORTS CONTINUED

1029 & 1104

1056 & 1114

AAAS
ADVANCING SCIENCE, SERVING SOCIETY

SCIENCE (ISSN 0036-8075) is published weekly on Friday, except the last week in December, by the American Association for the Advancement of Science, 1200 New York Avenue, NW, Washington, DC 20005. Periodicals Mail postage (publication No. 484460) paid at Washington, DC, and additional mailing offices. Domestic individual membership and subscription (51 issues): $135 ($74 allocated to subscription). Domestic institutional subscription (51 issues): $550; Foreign postage extra: Mexico, Caribbean (surface mail) $55; other countries (air assist delivery) $85. First class, airmail, student, and emeritus rates on request. Canadian rates with GST available upon request, GST #1254 88122. Publications Mail Agreement Number 1069624. **Printed in the U.S.A.**

Change of address: allow 4 weeks, giving old and new addresses and 8-digit account number. **Postmaster:** Send change of address to *Science*, P.O. Box 1811, Danbury, CT 06813–1811. **Single copy sales:** $10.00 per issue prepaid includes surface postage; bulk rates on request. **Authorization to photocopy** material for internal or personal use under circumstances not falling within the fair use provisions of the Copyright Act is granted by AAAS to libraries and other users registered with the Copyright Clearance Center (CCC) Transactional Reporting Service, provided that $15.00 per article is paid directly to CCC, 222 Rosewood Drive, Danvers, MA 01923. The identification code for *Science* is 0036-8075/83 $15.00. *Science* is indexed in the *Reader's Guide to Periodical Literature* and in several specialized indexes.

Contents continued

Science
www.scienceonline.org

sciencenow www.sciencenow.org Daily News Coverage

Yale Wins Suit Against Nobel Laureate
Former professor ordered to pay more than $1 million for fraud and larceny.

The Runaway Star
Star racing through our galaxy is destined to become an intergalactic loner.

Good Mood Food
The right diet may help relieve depression.

Networking—don't toss it away.

science's next wave www.nextwave.org Career Resources for Young Scientists

US: Tooling Up—More Than Just a Job-Seeking Tool *D. Jensen*
Networking builds useful relationships throughout your career.

Canada: Bridging the Worlds of Science and Public Policy *A. Fazekas*
A science advisor for the Canadian government discusses the challenges and rewards of her position.

Europe: Wandering Off the Beaten Track *E. Pain*
Portuguese scientist Ricardo Azevedo talks about getting a professorship in the United States.

Europe: European Science Bytes *Next Wave Staff*
Read the latest funding, training, and job market news from Europe.

MiSciNet: Houston Colleges Boost Minority Participation in STEM Fields *E. Francisco*
A new program seeks to increase minority representation in science, technology, engineering, and math.

MiSciNet: Successfully Navigating the First Year of Graduate School *T. Felder*
An assistant professor of chemistry talks about her transition into graduate school.

science's sage ke www.sageke.org Science of Aging Knowledge Environment

Review: More Is Less—Neurogenesis and Age-Related Cognitive Decline in Long-Evans Rats
J. L. Bizon and M. Gallagher
Does neurogenesis help or hinder brain function?

News Focus: Now Hear This *M. Leslie*
Gene therapy alleviates deafness in rodents.

News Focus: Short Circuit, Long Life *R. J. Davenport*
Sloppy wiring in mitochondria extends fly longevity.

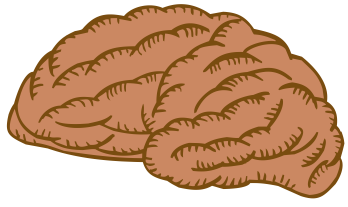

New neurons and age-related memory loss.

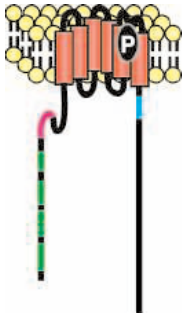

TRPC channel topology.

science's stke www.stke.org Signal Transduction Knowledge Environment

Perspective: TRAF2—A Double-Edged Sword? *Z.-P. Xia and Z. J. Chen*
TRAFs can have positive and negative roles in regulating NF-κB activity.

Review: The TRP Superfamily of Cation Channels *C. Montell*
The structure, function, and interactions of this large family of channels are reviewed.

Teaching Resource: Growth Factor and Receptor Tyrosine Kinases *S. Aaronson*
These lecture materials cover ligand-regulated signaling by receptor tyrosine kinases and Wnt signaling.

Teaching Resource: Protein Kinases *A. Caplan*
These lecture materials describe the structure and function of protein kinases.

Separate individual or institutional subscriptions to these products may be required for full-text access.

edited by Stella Hurtley and Phil Szuromi

Origins of Olmec Pottery

Olmec ceramics are associated with the origination of culture and language in Mesoamerica. Their widespread distribution has raised the questions of whether cultural development was concentrated along the Gulf Coast or arose from the interactions of several societies. **Blomster *et al.*** (p. 1068; see the Perspective by **Diehl**) tested these ideas by using trace-element chemistry of numerous Olmec ceramics to determine their provenance. The data show that all Olmec ceramics originated from the San Lorenzo region of the Gulf Coast, and other wares were not imported into this region.

Slicing Through Ammonia

During the last 40 years, late transition-metal catalysts have been developed to insert small molecules into H_2 and into Si–H, B–H, and C–H bonds. However, a homogeneous catalyst to break the N–H bond in ammonia remains elusive. **Zhao *et al.*** (p. 1080) have prepared an iridium compound with an electron-rich alkyl ligand that reacts with ammonia in room-temperature solution. Kinetic and isotopic labeling studies to show that the N–H insertion process occurs from a 14-electron Ir(I) intermediate. The studies could point the way toward a catalyst for ammonia transfer to olefins and other organic substrates.

Rabbits and Rodents Arose Relatively Recently

Rodents and their close relatives, including rabbits, make up much of the diversity of mammals, but their fossil record is sparse, and the time of divergence from other placental mammals has been controversial, with estimates spanning from near the Cretaceous-Tertiary (K-T) boundary to much earlier times. **Asher *et al.*** (p. 1091) now describe several specimens of a fossil rabbit dating to about 50 million years ago that collectively provide a more complete view of early glires (rabbits and rodents). Its primitive features imply that this group had diverged from placental mammals near the K-T boundary.

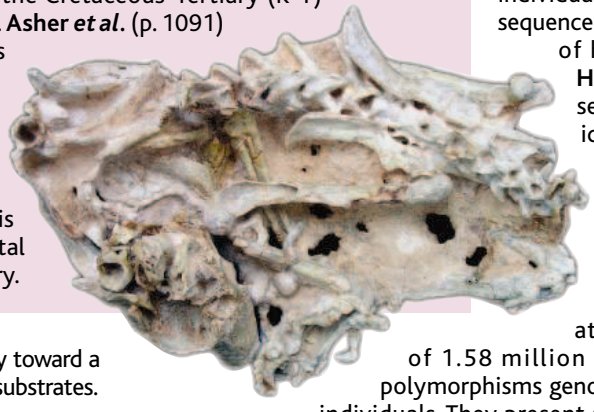

CREDIT: ASHER *ET AL.*

Walking the Walk

Conventional walking robots require large amounts of energy and complex control mechanisms. In the 1990s, researchers developed gravitationally propelled bipedal passive-dynamic walking machines that mimic human walking without active control. **Collins *et al.*** (p. 1082) have extended these passive-dynamic designs by including simple powered actuators and controllers. The bipedal robot walkers exhibit improved energy efficiency and offer insights into the mechanics of human walking.

Oceanic Iron and Atmospheric Oxygen

The oxygenation of Earth's atmosphere began 2.3 billion years ago, and some evidence, such as the presence of banded iron formations (BIFs), suggests the oceans remained largely anoxic until 1.8 billion years ago. **Rouxel *et al.*** (p. 1088; see the Perspective by **Kump**) present evidence from sedimentary sulfides which shows that the rise of atmospheric O_2 had a direct affect on iron cycling in the ocean and the ocean's redox state. Based on changes they see in the Fe isotopic composition of these rocks, they conclude that most of the Paleoproterozoic ocean became strongly stratified after 2.3 billion years ago, and that BIFs continued to form until 1.8 billion years ago by upwelling of ferrous Fe-rich plumes and rapid oxidation in the oxygenated upper layer of the ocean.

High-Energy Flashers

In 1994, researchers operating NASA's Compton Gamma-Ray Observatory detected gamma rays emitted toward space from Earth's atmosphere. These unusual emissions appeared to be correlated with lightning and other electrical discharges such as sprites and blue jets. **Smith *et al.*** (p. 1085; see the Perspective by **Inan**) have observed a series of gamma-ray events at energies up to 20 million electron volts in their data from the Reuven Ramaty High Energy Solar Spectroscopic Imager (RHESSI) satellite launched in 2002 to study solar flares. The data lend support to the explanation that a powerful electron-accelerating mechanism in the atmosphere propels particles to relativistic velocities.

A Rainbow of Human Variation

Individual differences in DNA sequence are the genetic basis of human variability. **Hinds *et al.*** (p. 1072; see the cover, the Policy Forum by **Duster**, and the Perspective by **Altshuler and Clark**) describe a large, publicly available collection of human genetic variation data consisting of 1.58 million single-nucleotide polymorphisms genotyped in each of 71 individuals. They present an initial characterization of the structure of variation within and among three human populations, and explore the application of these data for uncovering the genetic basis of complex traits. These results represent the first draft of what will eventually be a detailed haplotype map describing human variation.

Modeling Conflict, Error, and Decision-Making

We constantly have to make decisions based on integrating many types of information (see the Perspective by **Ridderinkhof and van den Wildenberg**). The anterior cingulate cortex (ACC) and neighboring areas play a role in monitoring and controlling goal-directed behavior, but how it knows that an error has occurred, or that a given set of response processes are in conflict with each other, is unclear. **Brown and Braver** (p. 1118) developed a computational model that shows how the ACC might represent a prediction of error-likelihood, such that its response to a given task condition is proportional to the perceived likelihood of an error in that condition. **Machens *et al.*** (p. 1121) studied a two-stimulus interval decision task in which subjects first perceived an initial stimulus, then held it in working memory, and finally made a decision by comparing it with a second stimulus. A simple mecha-

CONTINUED ON PAGE 1011

nistic model for how primates may solve two-interval discrimination tasks suggests a testable mechanistic architecture that bridges the gaps from neural mechanism to neural phenomenology to behavior.

Prions at Sites of Inflammation

So-called prion diseases, like bovine spongiform encephalopathy ("mad cow" disease), are thought to be caused by infectious proteins (prions) that accumulate in the brain. Neuronal and lymphoid organs have thus been excluded from the food chain with the aim of protecting public health. Under inflammatory conditions, however, immune cells are not confined to lymphoid organs, which suggests that inflammation could shift the tissue tropism of prions. **Heikenwalder *et al.*** (p. 1107, published online 20 January 2005) report that in mouse models of prion diseases, conditions that lead to inflammation of the liver, pancreas, or kidney can indeed lead to the accumulation of high levels of prion infectivity within the affected organs through the infiltration of prion-infected immune cells. The findings have far-reaching implications for prion biosafety, for example, if prion-infected farm animals have ongoing inflammation.

The Attractive Cockroach

The cockroach is despised for good reason, as it is a vector for pathogens and a major cause of allergic disease. **Nojima *et al.*** (p. 1104; see the news story by **Pennisi**) have characterized a sex pheromone from the German cockroach *Blatella germanica* that may provide a new tool in pest control. The pheromone (blattelaquinone) was purified from adult female cockroaches and characterized as gentisyl quinone isovalerate. In field tests on a cockroach-infested pig farm, adult males, but not nymphs or adult females, were attracted to traps baited with synthetic pheromone.

The Roots of Patterning

Root hairs develop on the emerging roots of *Arabidopsis* plants in a regular pattern of tidy files of neatly spaced hairs. A suite of transcription factors manages the fates of root cells in response to lateral inhibition. **Kwak *et al.*** (p. 1111, published online 23 December 2004) have now identified a gene termed *SCRAMBLED*, which encodes a putative receptor-like kinase protein that seems to function as a regulator of the overall transcriptional response. Scrambled enables the developing epidermal cells to interpret their position and establish the appropriate cell type pattern.

Keeping Hair Cells Cycling

In the mammalian ear, the hair cells critical for hearing and for maintaining balance cease proliferating and differentiate early in life. Thus, hearing loss caused by damaged hair cells is irreversible. **Sage *et al.*** (p. 1114, published online 13 January 2005; see the Perspective by **Taylor and Forge**) have now analyzed the relation between proliferation and differentiation in the mouse by manipulating the expression of one of the retinoblastoma protein family members, which can regulate cell cycle exit. In the absence of the relevant retinoblastoma protein, hair cells of the inner ear can differentiate and yet continue to proliferate. Further research is required to determine whether this effect can be extended to later in life.

Trading Bases

The action of cytidine deaminase enzymes on nucleic acids and subsequent repair of the resulting lesion can lead to base-pair modification, or "editing" of coding sequences. This process can have beneficial results, as in the case of class switching and somatic mutation of immunoglobulin loci. For a retroviral genome, however, related intracellular editing enzymes can be detrimental to viral replication, and such viruses have evolved mechanisms to counteract the activity of these host proteins. **Turelli and Trono** (p. 1061) review the evolution and relation of the diverse activity of cytidine deaminases in these different contexts of host defense.

CREDIT: KWAK *ET AL.*

Nurturing the Next Einsteins

All revolutions begin with a seminal moment. This year, we will celebrate one of the greatest in the history of science: the 100th anniversary of Albert Einstein's 1905 landmark papers that introduced the special theory of relativity and the equivalence of mass and energy. As we explore their impact, we must ask ourselves if we as a nation are doing what it takes to spark new scientific revolutions. Are we nurturing the next Einsteins? Regrettably, the answer is no. The lack of federal investment in basic research and restrictive immigration policies are eroding America's leadership in the sciences. The ripple effects of these two troublesome trends are enormous: Our future economic competitiveness and quality of life depend on our ability to stay ahead of the scientific and technological curve.

The splitting of the atom ushered in an unprecedented era of public investment in basic scientific research after World War II. The National Academy of Sciences (citing the work of Nobel Laureate Robert Solow) estimates that nearly half of our nation's economic growth since that time can be attributed to advances in science and technology.

However, in recent years investment has shifted away from research in the physical sciences and engineering to the life sciences. The irony is that advances in the life and medical sciences will be impossible without their physical and engineering counterparts. I agree with the recommendation of the President's Council of Advisors on Science and Technology that the funding levels for the physical sciences and engineering be brought to parity with that for the life sciences, which has more than doubled over the past decade. Adequate funding alone, however, will not guarantee that science in the United States maintains its strength.

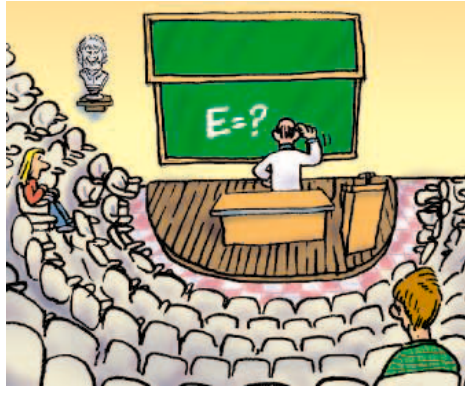

We must continue to serve as a magnet for foreign scholars while also creating an environment to attract more U.S. students to the physical sciences and engineering. History's lesson on this topic is worth heeding. Fleeing Nazi Germany, Einstein immigrated to the United States in 1933 and became a citizen in 1940. Fellow immigrants Richard Courant, Edward Teller, Eugene Wigner, Hans Bethe, and Enrico Fermi fathered stunning scientific achievements, earned Nobel Prizes, and helped build the science and mathematics departments of America's greatest universities.

Unfortunately, after September 11, 2001, delays in processing student visas have discouraged thousands of foreign students from continuing this vital tradition. The very scholars we need to be attracting—those pursuing advanced math, physics, and chemistry—are particularly hard hit, because the technical nature of their study sets off a rigorous and time-consuming screening process that is designed to prevent the transfer of sensitive technologies to other countries. Consequently, applications to U.S. graduate schools declined by 28% last year, with those from China falling by 45% and those from India by 28%. Other nations, including Australia, Great Britain, and Germany, are taking advantage of this window of opportunity by aggressively recruiting more foreign talent and retaining more of their own scholars.

For the physical sciences and engineering, this is a particularly ominous trend, because fewer Americans are pursuing advanced degrees in these areas. Close to one-third of U.S. doctoral degrees in science and engineering are awarded to foreign nationals. Nearly 40% of the current engineering faculty members at U.S. universities are foreign born. Replenishing our intellectual capital will depend on our capacity to create a timely, more transparent, and less burdensome visa process.

The stakes here are high for U.S. industry and for the other nations with whom we trade. The booming decade of the 1990s gave rise to over five million new firms, most of them science-intensive companies that were responsible for over three and a half million jobs. The generation of new patents continued at a strong pace, indicating the potential for strong job growth in the future; after all, these innovations are the rough drafts of new businesses. But continuing the pace of innovation will require a renewed commitment to investment in research and development. The centennial of Einstein's remarkable achievements presents us, his adopted compatriots, with the opportunity to reinvigorate our own passion for discovery. The quest for new frontiers is a hallmark of the American spirit. It is a national imperative we cannot afford to ignore.

Lamar Alexander

Lamar Alexander is a Republican U.S. Senator from Tennessee. He is chair of the Senate Subcommittees on Energy and on Education and Early Childhood Development.

10.1126/science.1110137

CREDIT: JOE SUTLIFF/*SCIENCE*

EDITORS' CHOICE

edited by Gilbert Chin

CLIMATE SCIENCE

Rete Mirabile

The atmospheric concentration of CO_2 and the climate are connected by an intricate web of positive and negative feedbacks. The CO_2 content of the atmosphere is increased by volcanic and metamorphic degassing and decreased by the chemical weathering of silicate rocks; yet another important influence is the vascular land plants. A fundamental difficulty in understanding the role of plants, however, is that long-term changes in CO_2 and climate affect terrestrial plant development and evolution, which in turn has consequences for the burial of organic matter in sediments and chemical weathering.

Beerling and Berner present a systems analysis of the physiological and geochemical processes linking plants and CO_2 on geological time scales and pay special attention to how this wondrous network prevents runaway changes in CO_2 and catastrophic planetary warming. By incorporating processes that affect CO_2 on million-year time scales, such as evolution and weathering, and ones occurring on much shorter time scales, such as how terrestrial ecosystems regulate the land/atmosphere exchange of water vapor and recycling of precipitation, they uncover important feedback loops not previously identified. They also find that the biota exerted a destabilizing influence on climate regulation in the Paleozoic, and this quickened the rates of terrestrial plant and animal evolution, which accelerated the diversification of terrestrial tetrapods and insects, and caused a large rise in the concentration of atmospheric oxygen. — HJS

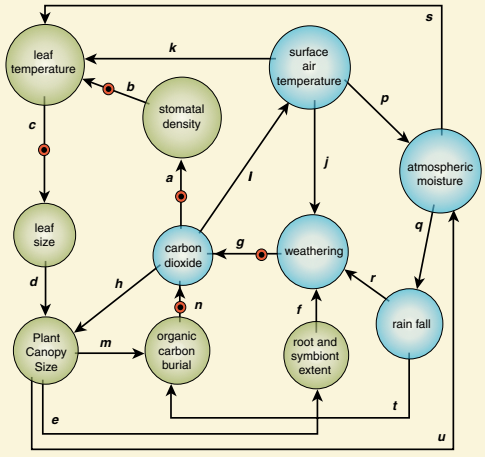

Diagram of the direct and indirect links between plants and CO_2.

Proc. Natl. Acad. Sci. U.S.A. **102**, 1302 (2005).

devices such as prosthetic heart valves. Its more aggressive relative *S. aureus* sports an arsenal of virulence factors, but how a ubiquitous skin commensal causes pathology is less clear. One useful defensive component appears to be poly-γ-DL-glutamic acid (PGA), which Kocianova *et al.* found is synthesized by all 74 strains of *S. epidermidis* they tested. In support of its commensal lifestyle, *S. epidermidis* relies on PGA to resist the wild swings in salt concentration that occur on human skin. PGA is known to protect other Gram-positive bacteria (such as *Bacillus anthracis*, which takes shelter in a capsule of PGA), from phagocytosis by host cells. PGA-nonproducing mutants of *S. epidermidis*, in which the *cap* gene locus was replaced, were wiped out by antibacterial peptides known as defensins and by neutrophil attack, whereas *cap*-intact bacteria survived. — CA

J. Clin. Invest. 10.1172/JCI200523523 (2005).

APPLIED PHYSICS

How Wet Does It Get?

The ability to manipulate small volumes of liquids has opened up the possibility of designing a lab on a chip with micrometer-scale channels. The architectures for these microfluidic chambers can either be closed—with the typical channels, pumps, valves, and reservoirs—or open, where the flow is controlled by local changes in either the wettability of the substrate or its topography.

Seemann *et al.* patterned a set of rectangular grooves into chemically modified silicon to give a system that could be described by two parameters: the aspect ratio of the grooves, defined as the depth/width, and the contact angle formed between the fluid and the substrate. At contact angles greater than 45°, the fluid formed droplets that would spill over the walls of shallow channels and that transformed into filaments in deeper trenches. At lower contact angles, the wetting was complicated by pinned wedges that formed along the corners of the channels, and the filaments could take on either a positive or negative Laplace pressure. This suggests that dynamic changes in the properties of the substrate can be used to drive a fluid through a chip, keeping in mind that the chemistry performed on a chip will affect the wettability and hence the dynamics and shape of the moving fluid. — MSL

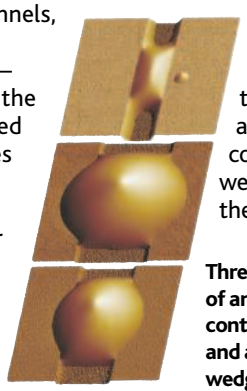

Three images (bottom to top) of an overspilling droplet (high contact angle) and a droplet and a filament overlying pinned wedges (low contact angles).

Proc. Natl. Acad. Sci. U.S.A. **102**, 1848 (2005).

MICROBIOLOGY

Hiding with Ease

Catching an intractable disease while in the hospital is a worrying prospect and has become of greater concern mostly owing to persistent *Staphylococcus epidermidis* attaching to indwelling

MICROBIOLOGY

Unequal Fission

Despite the apparent symmetry of cell division, the rod-shaped bacterium *Escherichia coli* does not produce progeny that are identical. Upon division, each daughter cell acquires a pre-existing end (old pole) from its ancestor as well as a newly created end (new pole) where the septum forms. In a present-day reenactment of the heroic lineage mapping of the nematode, Stewart *et al.* followed individual bacteria for nine generations of growth and reproduction; computerized analysis of about 35,000 cells revealed that the cell that inherited

CONTINUED ON PAGE 1017

CREDITS: (TOP) BEERLING AND BERNER, *PROC. NATL. ACAD. SCI. U.S.A.* **102**, 1302 (2005); (BOTTOM) SEEMANN *ET AL.*, *PROC. NATL. ACAD. SCI. U.S.A.* **102**, 1848 (2005)

the parent's older pole grew more slowly than the cell bequeathed the younger pole. Cells with older poles produced less biomass (summed across their offspring) and had an increased probability of death. Because these asymmetric characteristics are hallmarks of cellular aging in multicellular organisms and in yeast, the study suggests that asymmetric cell division and fundamental mechanisms of aging may be evolutionarily conserved in bacteria. — LDC

PLoS Biol. **3**, e45 (2005).

GEOCHEMISTRY

Gaining Quadruple Points

The most important binary mixture on Earth, as well as a significant one in industrial applications, is that of H_2O and CO_2. Their binary chemistry affects the atmosphere and ocean; determines volatiles in Earth's mantle and crust, including volcanoes; and plays a role in numerous industrial reactions. Although there have been many studies of the relation between CO_2 and H_2O at temperatures above the freezing point of water—involving gases, liquids, or supercritical fluids—the phase relations at lower temperatures, those at or below the freezing point of water, are less well documented. At low temperatures, the mixture is important in the upper atmosphere; in ice cores (where CO_2 is trapped as a gas); in clathrates in the deep ocean; and on other planets, notably Mars with its polar caps of water and dry ice.

Longhi explores this parameter space using thermodynamic data on the various pure phases and the H_2O + CO_2 clathrate and shows that the phase diagram is richer than previously thought. The analysis suggests that CO_2 clathrate will be stable in only some regions of the deep ocean, a critical issue with respect to carbon sequestration, and that conditions may be appropriate in some polar ice sheets for the accumulation of liquid CO_2. — BH

Geochim. Cosmochim. Acta **69**, 529 (2005).

CELL BIOLOGY

Death by Any Other Name

An enormous amount of molecular detail about the mechanisms of programmed cell death (apoptosis) has been amassed, and it is now recognized as an integral cellular pathway involved in development and in disease. During apoptosis, an orchestrated series of events leads to the inhibition of protein synthesis. Another cell death pathway, much less well understood, is known as necrosis. It occurs both when cells are subjected to physical damage and during certain pathologies, including cardiac ischemia and stroke. Saelens *et al.* show that in necrosis, cellular protein synthesis continues unabated right up until the point at which the cell membrane ruptures. This means that a necrotic cell remains an attractive abode for incoming viruses, which will be able to exploit the cellular protein synthesis machinery to generate progeny. It also means that after necrotic cell death, many more intact cellular proteins are released locally and may thereby trigger an inflammatory response. — SMH

J. Cell Biol. 10.1083/jcb.200407162 (2005).

BIOPHYSICS

A Folding Ruler

The development of a suite of fluorescent probes that can be introduced into cells has made it feasible to estimate intracellular distances (static and dynamic) via the technique of Förster resonance energy transfer (FRET). To a first approximation, the efficiency of energy transfer from a donor to an acceptor fluorophore depends on the inverse sixth power of the distance separating them. Converting efficiency into units of distance requires a calibrating ruler with a donor fixed at one end and an acceptor at the other. Schuler *et al.* use contemporary single-molecule technology to reexamine the classical ruler, a rigid rod of 12 proline residues, introduced originally by Stryer and Haugland almost four decades ago. A number of factors conspire to make the observed efficiencies deviate from the values predicted by Förster theory, especially for much longer rulers that, surprisingly, turn out to be much less rigid than the canonical polyproline helix. — GJC

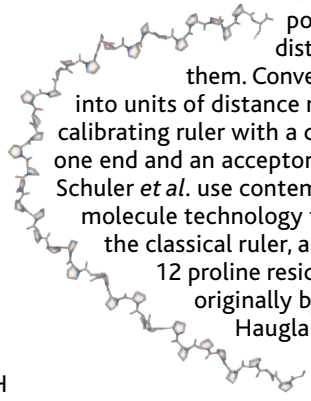

Closely apposed ends of a 40-mer strand in a molecular dynamics simulation.

CREDITS: SCHULER *ET AL.*, *PROC. NATL. ACAD. SCI. U.S.A.* **102**, 2754 (2005)

Proc. Natl. Acad. Sci. U.S.A. **102**, 2754 (2005).

www.sciencemag.org

Science

1200 New York Avenue, NW
Washington, DC 20005
Editorial: 202-326-6550, FAX 202-289-7562
News: 202-326-6500, FAX 202-371-9227

Bateman House, 82-88 Hills Road
Cambridge, UK CB2 1LQ
+44 (0) 1223 326500, FAX +44 (0) 1223 326501

Subscription Services For change of address, missing issues, new orders and renewals, and payment questions: 800-731-4939 or 202-326-6417, FAX 202-842-1065. Mailing addresses: AAAS, P.O. Box 1811, Danbury, CT 06813 or AAAS Member Services, 1200 New York Avenue, NW, Washington, DC 20005

Institutional Site Licences please call 202-326-6755 for any questions or information

Reprints Ordering/Billing/Status 800-635-7171; Corrections 202-326-6501

Permissions 202-326-7074, FAX 202-682-0816

Member Benefits Bookstore: AAAS/BarnesandNoble.com bookstore www.aaas.org/bn; Car purchase discount: Subaru VIP Program 202-326-6417; Credit Card: MBNA 800-847-7378; Car Rentals: Hertz 800-654-2200 CDP#343457, Dollar 800-800-4000 #AA1115; AAAS Travels: Betchart Expeditions 800-252-4910; Life Insurance: Seabury & Smith 800-424-9883; Other Benefits: AAAS Member Services 202-326-6417 or www.aaasmember.org.

science_editors@aaas.org (for general editorial queries)
science_letters@aaas.org (for queries about letters)
science_reviews@aaas.org (for returning manuscript reviews)
science_bookrevs@aas.org (for book review queries)

Published by the American Association for the Advancement of Science (AAAS), *Science* serves its readers as a forum for the presentation and discussion of important issues related to the advancement of science, including the presentation of minority or conflicting points of view, rather than by publishing only material on which a consensus has been reached. Accordingly, all articles published in *Science*—including editorials, news and comment, and book reviews—are signed and reflect the individual views of the authors and not official points of view adopted by the AAAS or the institutions with which the authors are affiliated.

AAAS was founded in 1848 and incorporated in 1874. Its mission is to advance science and innovation throughout the world for the benefit of all people. The goals of the association are to: foster communication among scientists, engineers and the public; enhance international cooperation in science and its applications; promote the responsible conduct and use of science and technology; foster education in science and technology for everyone; enhance the science and technology workforce and infrastructure; increase public understanding and appreciation of science and technology; and strengthen support for the science and technology enterprise.

Information for Contributors

See pages 135 and 136 of the 7 January 2005 issue or access www.sciencemag.org/feature/contribinfo/home.shtml

NetWatch

edited by Mitch Leslie

NET NEWS

Calling All Taxonomists

It's such a daunting job that nobody has pulled it off in more than 200 years: compiling a list of the world's known species. But the organizers of a new project called Wikispecies hope that everyone from biologists to birders will lend their know-how to a comprehensive online catalog of the world's roughly 1.8 million kinds of living things, such as the raft spider (*Dolomedes fimbriatus*; below).

Wikispecies hails from the same organization that launched the user-written encyclopedia Wikipedia (NetWatch, 5 September 2003, p. 1299). Like Wikipedia, the entries will evolve as contributors edit, correct, and augment one another's writing. But Wikispecies is aimed at scientists rather than the general public. "You won't have to fax your degrees" before you can add to the site, says Wikipedia founder Jimmy Wales, but submissions will have to pass muster with a technical audience. The site includes preliminary classifications for some groups, and the first species pages should post later this year, Wales says. Researchers can join the conversations about the site's structure or flesh out the classification for various groups.

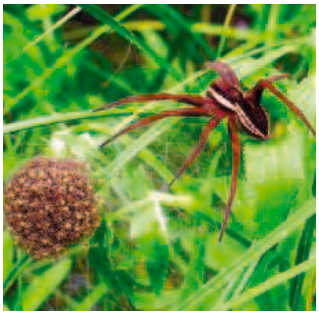

species.wikipedia.org

DATABASE

Counting Cancer's Bad Breaks

Mutations can foil the intricate mechanism that controls cell division, triggering cancer. COSMIC, a year-old database from the Sanger Institute near Cambridge, U.K., tallies the faults within genes that can promote uncontrolled growth. Curators plucked information on more than 18,000 noninherited mutations from published studies, focusing on 21 genes that don't already have their own databases. You can search the collection by gene or by tissue to find out the location and frequency of different glitches. For instance, 47% of eye tumors sport mutations in the gene *RB1*, whose protein normally keeps growth-stimulating molecules in check. The database also records instances in which a particular gene isn't mutated in a certain sample, information that can help pin down how often the change occurs in different cancers.

www.sanger.ac.uk/genetics/CGP/cosmic

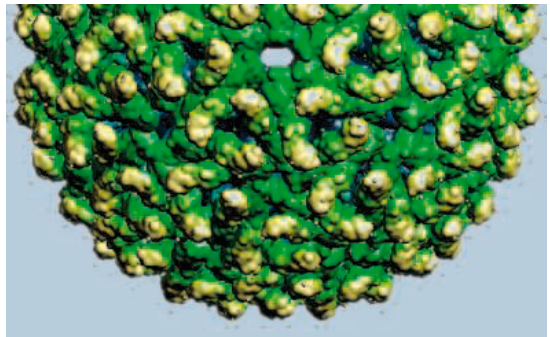

RESOURCES

Viral Visions

The surface of a virus reveals how the infectious particle breaks into cells and possibly how to thwart it. Researchers can view and analyze the exteriors of 200 viral varieties at the freshly revamped VIPERdb,* from the Scripps Research Institute in La Jolla, California. The site draws on structural coordinates stashed in the Protein Data Bank, allowing users to study different aspects of each virus's architecture. Choosing the mosquito-borne Sindbis virus (above), for instance, calls up images that illustrate its overall structure, show how its proteins fit together, and more. Other features identify the strongest and weakest interactions between sections of the virus, which can help researchers pinpoint its vulnerable spots. The recent upgrade tripled the number of viruses in the database and added tools for comparing viral characteristics.

The intricacies of viral surface structure are also on display at this colorful gallery† from the University of Wisconsin, Madison. Images and animations afford a close look at the Flock House virus, the Semliki Forest virus, and more than 30 other types.

* viperdb.scripps.edu

† rhino.bocklabs.wisc.edu/cgi-bin/virusworld/virustable.pl

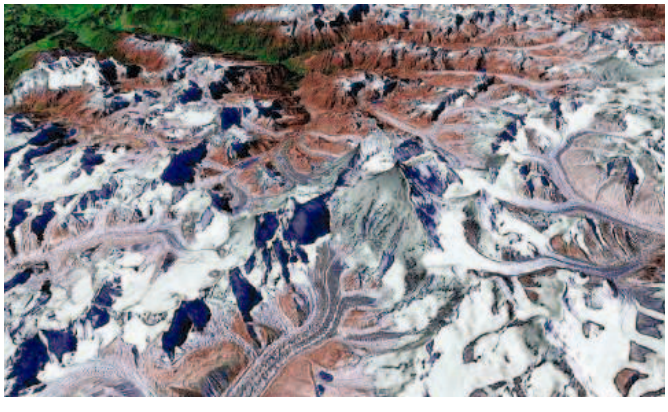

IMAGES

Above and Beyond

Even on the best relief maps, Mount Everest and other spectacular geographical features are, well, flat. But the mountain stands tall (left) at this new atlas of panoramic images aimed at geography students and curious visitors. Crafted by William Bowen, a retired professor of geography from California State University in Northridge, the collection boasts some 500 computer-generated aerial views of the world's landscapes, from the Florida Keys to the Pyrenees Mountains to the Bay of Bengal. "My plan will be a small attempt to make far-off places literally visible to anyone who wishes to see them," Bowen says.

geogdata.csun.edu/world_atlas/index.html

Send site suggestions to netwatch@aaas.org. Archive: www.sciencemag.org/netwatch

CREDITS (TOP TO BOTTOM): VIPERDB; WIKIMEDIA FOUNDATION; WILLIAM BOWEN

This Week

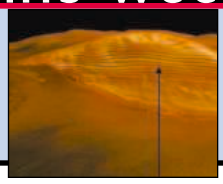

PAGE 1025
Views from Mars Express

1029
A better roach trap

HIGH-ENERGY PHYSICS

NSF Stunned by Higher Costs of Proposed DOE Facility

The National Science Foundation (NSF) has apparently lost a bet that it could do high-energy physics on the cheap. The bet involves the Rare Symmetry Violating Processes (RSVP) project, which turns out to be far more costly than envisioned a year ago. The fallout has cast doubt on the future of the long-delayed experiment and triggered a reshuffling at its host lab, the Department of Energy's (DOE's) Brookhaven National Laboratory in Upton, New York.

RSVP is designed to give scientists new ways to measure the properties of the "weak force" that is responsible for nuclear decay. It may also produce evidence for an as-yet-undetected class of particles that could account for most of the matter in the universe. Although DOE rejected the proposal in the mid-1990s as part of a decision to concentrate on nuclear physics at Brookhaven, NSF officials viewed RSVP as an exciting piece of frontier research. They also liked the fact that it would use an existing accelerator, the Alternating Gradient Synchrotron (AGS), as the source of its proton beams, an arrangement that promised to hold down costs. So NSF decided to pick up the tab.

One of the experiments, MECO, hopes to spot the decay of a muon into an electron, an event that, if it happens, would point to a flaw in the Standard Model of matter. The second experiment, dubbed KOPIO, looks at the decay of the K-long meson. Its results would measure one of the fundamental parameters of the weak force.

Last fall, after a long wait in NSF's queue of proposed facilities, RSVP received $15 million to start building what was projected to be a $158 million facility. "It was finally put in the [construction] budget," and things looked great, recalls Joseph Dehmer, head of NSF's physics division.

Anticipating a green light for construction, NSF last spring appointed physicist William Willis of Columbia University as project manager. Willis promptly commissioned a top-to-bottom review of RSVP, including updated cost estimates for construction and operations. That's when things got ugly.

In November, project scientists revealed that preparing AGS to handle the high-intensity, long-duration demands of RSVP would cost a good deal more than anticipated and bump up the price of the experiment. "Right before our eyes, huge numbers started to emerge," says one knowledgeable lab official. "It ballooned up to $300 million or above."

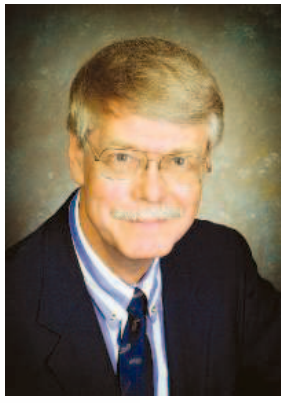

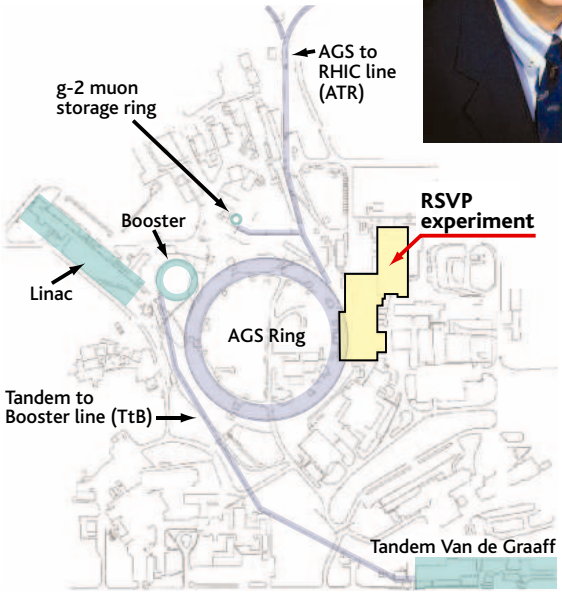

Cursed ring? The Alternating Gradient Synchrotron, which feeds the RHIC accelerator, isn't currently able to support RSVP. The fiscal implications of that problem have apparently cost Brookhaven's Thomas Kirk (*inset*) his position.

Willis says that figure, which includes a much larger contingency fund than originally planned, is the outer limit of what RSVP will cost. "The feeling now is that the [final] number will be considerably lower than the upper bound," he says.

Nevertheless, the news turned heads at NSF, which promptly informed the National Science Board, its oversight body, as well as the legislators who set NSF's budget. "We thought it was a clever idea for doing science at a small, incremental cost," says Michael Turner, head of mathematics and physical sciences at NSF. "But the assumption of parasitic operations just didn't work out because circumstances have changed. … I've had a number of unpleasant weeks going around Washington, explaining that we've had a significant increase in costs."

To understand why RSVP's price tag soared, Turner says, think of AGS as an expensive racing car that is used only to commute to work. The commuter is Brookhaven's Relativistic Heavy Ion Collider (RHIC), the centerpiece of the lab's nuclear physics program. AGS was the premier U.S. proton accelerator of its day during the 1960s and was intended to feed ISABELLE before that proposed accelerator was canceled in 1983. "The stewards of the AGS used to be high-energy physics," Turner explains. "The stewards are now nuclear physics. This means that the mentality of running that complex has changed."

Instead of running AGS as an independent, high-energy physics machine and maintaining it accordingly, Turner says, Brookhaven used it as a mere injector—which was all that was needed for RHIC operations. The problem, notes Turner, is that NSF hadn't anticipated the need to get AGS back into shape to do high-energy physics.

Those changing circumstances appear to have toppled Thomas Kirk, Brookhaven's associate laboratory director for high-energy and nuclear physics. "I didn't jump; I was pushed," says Kirk, who in early February was given the new position as special assistant to Praveen Chaudhari, Brookhaven's director. His successor is Sam Aronson, who has been chair of the physics department at Brookhaven. Chaudhari declined comment on the reshuffling.

This week Turner asked DOE's High Energy Physics Advisory Panel to examine the significance of the science RSVP will perform under different funding scenarios. That information will be combined with RSVP's internal review of costs, due to be completed this spring, into a report that could determine RSVP's fate. "We will reevaluate [RSVP's] scientific value, its cost, and then make a decision," says Turner.

–CHARLES SEIFE

CREDITS: (INSET) COURTESY OF BROOKHAVEN NATIONAL LABORATORY (BNL); GRAPHIC ADAPTED FROM BNL

NIH FUNDING

Success Rates Squeezed as Budget Growth Slows

The president's 2006 budget request last week contained dismal news for biomedical researchers—a mere 0.7% raise, to $28.8 billion, for the National Institutes of Health (NIH). And the fine print was just as bad: Success rates for grant applications are projected to be 22% this year, down from 30% in 2003. That slump, along with an 8% drop in the number of new grants (see table, right), confirms predictions of tough times following the recent 5-year doubling of NIH's budget if NIH received annual increases of less than 6% (*Science*, 24 May 2002, p. 1401).

In the last years of the doubling, NIH held the success rate (the portion of applications funded) at around 30% to avoid creating an unsustainable number of new grants. Instead, administrators increased average grant size and put more money into infrastructure. A year ago, NIH hoped it could pull off a "soft landing" after the doubling ended in 2003: It predicted only a slight dip in new and competing grants in 2004 and recovery in 2005, with a still-healthy 27% success rate. ("New and competing" refers to newly funded projects and grants coming up for renewal, which make up about one-fourth of all grants in the NIH portfolio. The rest are continuations of multiyear grants.)

But NIH received less money in 2005 for research grants than even the 2.7% increase it had expected, explains NIH Associate Director for Budget Richard Turman. NIH has also received far more applications than predicted since 2003, as some investigators increased the number of proposals they submitted. On the bright side, says NIH Deputy Director for Extramural Research Norka Ruiz Bravo, the number of new investigators supported each year continues to rise.

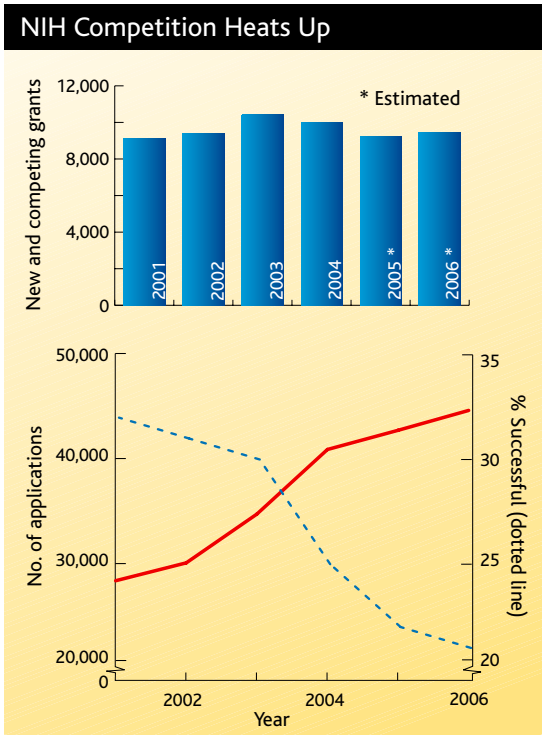

At NIH council meetings last month, some institutes announced a lowered pay line in 2005, the peer-review ranking that is the cutoff for funding. That news is raising the specter of a return to the early 1990s, when tight budgets forced reviewers to make "dysfunctional" decisions about equally good applications, says Howard Garrison, public affairs director for the Federation of American Societies for Experimental Biology.

He and others are worried that some investigators may be forced to trim staff or even leave research. "It's very hard, after downsizing your lab, to build back up again," says Susan Gerbi, who until recently was chair of molecular biology at Brown University. She hopes Congress will heed that message as it considers NIH's 2006 budget. "We are holding our breath" in current competitions, says Gerbi.

—JOCELYN KAISER

U.S. IMMIGRATION POLICY

New Rules Ease Scientific Exchanges

The United States last week changed its visa rules to make it easier for foreign students and scientists working on sensitive technologies to reenter the country after overseas trips. The new policy, announced last week by the State Department, extends the validity of security clearances, now 1 year, to 4 years for international students and 2 years for foreign scientists.

Until now, foreign scholars working in certain fields had to undergo an extensive interagency security review—known as a Visas Mantis check—every time they wanted to reenter the United States. Only those who had received a clearance within the preceding 12 months were exempt. In the tightened security environment after the 2001 terrorists attacks, that procedure resulted in major delays for thousands of international graduate students and researchers returning to the United States after visiting their home countries or attending conferences overseas. After complaints from scientific and educational associations, federal officials promised to extend the validity of Mantis clearances (*Science*, 27 August 2004, p. 1222).

"We now have better information sharing between federal agencies and systems to track whether students and researchers have changed their fields of study," says C. Stewart Verdery, outgoing assistant secretary for Border/Transportation Security Policy at the Department of Homeland Security and one of the officials who worked on the extension. "Given those factors, it seems like a redundancy to do repeat security checks for the same individual."

The new policy "eliminates a lot of uncertainty for foreign students in the United States," says Nils Hasselmo, president of the Association of American Universities. More broadly, he says, "it sends a message that international students and scholars are welcome here."

Scientists in other countries who visit the United States often will also benefit from another change that extends the validity of a Mantis clearance for such visits from the duration of a single visit to a year. Verdery says the change ensures that "security constraints don't make the United States less attractive as a venue for scientific conferences."

—YUDHIJIT BHATTACHARJEE

CREDIT: NIH

PLANETARY SCIENCE

And Now, the Younger, Dry Side of Mars Is Coming Out

The news from Mars lately has been all wet: a shallow, salty sea where the rover Opportunity landed, and rock-rotting groundwater, at least, where Spirit is roaming in Gusev Crater's Columbia Hills (*Science*, 17 December 2004, p. 2010). Although the planet was indeed drenched in potentially life-giving water, it didn't stay that way long, according to papers published online this week by *Science* (www.scienceexpress.org). In the papers, 39 researchers led by Jean-Pierre Bibring of the University of Paris, Orsay, report their first results from the mineralogical mapper OMEGA (Observatoire pour la Minéralogie, l'Eau, la Glace, et l'Activité) orbiting Mars on board the European Mars Express spacecraft.

Among other things, notes planetary scientist James Head of Brown University, OMEGA has spotted water-altered minerals well beyond the two rover landing sites—but none that appear to have formed during the past several billion years. The researchers conclude that for most of its history, Mars resembled the Dry Valleys of Antarctica at their driest rather than a landscape of shallow seas. OMEGA's global perspective "is ushering in an entirely new era of geoscience analysis on Mars," Head says.

Scientists say the new, dry-eyed view of martian history came about largely because OMEGA's spectrometer, unlike those on earlier missions, sees well in near-infrared light. In that range, the mineral products of water alteration absorb solar radiation at distinctive wavelengths. Thanks to its spectral edge, OMEGA is handily identifying sulfate salts of the sort the Opportunity rover found at two sites in Meridiani Planum. Sulfuric acid from volcanic eruptions apparently combined with water to corrode martian rock and produce sulfates around the planet. The several hundred meters of light-toned, sulfate-rich sediments beneath Opportunity also appear hundreds of kilometers to the north and east of the rover's landing site, OMEGA found. The intermittently puddled salt flats and salt dunes making up the layered deposit seen by Opportunity were no fluke.

In fact, OMEGA's partial coverage of the planet has also found light-toned, sulfate-rich layered formations in parts of the great canyon system of Valles Marineris and in the chaotic terrain of Margaritifer Terra. It also found a 60-by-200-kilometer patch of terrain rich in gypsum, a calcium sulfate salt, hard against the northern ice cap. Even the Spirit rover kicked in its own sulfate find this week with the discovery in Gusev Crater's Columbia Hills of finely layered, sulfate-rich sandstone bedrock, says rover science team leader Steven Squyres of Cornell University.

All the sulfate finds are, as Squyres says of the Spirit discovery, "profound evidence for [rock] interaction with liquid water." It's just that Mars seems to have been wet so long ago. The rover sulfates almost certainly date from 3 billion or 4 billion years ago, says Squyres, in the planet's first billion years. The canyon and chaos formations appear to be equally ancient, says Bibring, and need not have been formed by surface waters; he and his teammates emphasize instead the possible role of groundwaters and acidic snow and frost. And the gypsum deposit could well be the evaporative residue of a one-time outburst of groundwater at least a couple of billion years ago, says Head.

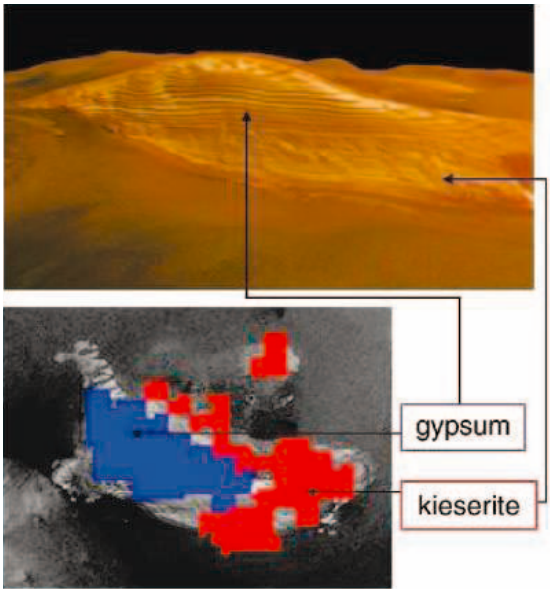

Whole lot of weathering. In Juventae Chasma, a 2.5-kilometer-high pile of sulfate-rich layered sediments (top, in 3D; bottom, from overhead) attests to sulfuric acid alteration.

Beyond ancient sulfate salts, OMEGA isn't finding much water alteration. "We don't see hydrated minerals like clays" to any great extent, says Bibring. Researchers have debated whether the northern lowland plains, which account for a third of the planet, are covered by silica-rich lavas or water-altered weathering products. OMEGA sees no clear signs of either. Instead, the plains may be ▶

SOURCE: J.-P. BIBRING *ET AL.*, *SCIENCE*. FROM HRSC/MEX (TOP) AND NASA/JPL/MSSS (BOTTOM); CREDIT (LOWER RIGHT): NASA

ScienceScope

White House Nominates New FDA Chief

The longtime acting head of the Food and Drug Administration (FDA) has been nominated for the agency's top post. Lester Crawford, a 66-year-old pharmacologist and veterinary medicine specialist, served as FDA's deputy commissioner during the brief tenure of Mark McClellan and has been acting commissioner since then. But some agency watchdogs have criticized his leadership. "We strongly oppose" his nomination, says Sidney Wolfe, director of the health research group Public Citizen in Washington, D.C., who cites Crawford's delays in removing the diet drug ephedra from the market and slapping warnings on the painkiller Vioxx.

–JENNIFER COUZIN

Boost for African Science Academies

The science academies of Nigeria, Uganda, and South Africa have been selected to team up with the U.S. National Academies in a new $20 million project to help African scientists provide their governments with advice on science and public policy. The 10-year program, funded by the Bill & Melinda Gates Foundation, will tackle some of the continent's most serious health issues, such as the HIV/AIDS epidemic, chronic malnutrition, and malaria. The hope is that these academies can eventually fill the same role for their governments that the National Academies perform for U.S. policymakers. "We are hoping all of sub-Saharan Africa will benefit," says Patrick Kelley, director of the academies' Board on African Science Academy Development.

–AMITABH AVASTHI

Astronaut to Keep NASA Aloft

Former astronaut Frederick Gregory was named interim chief of NASA last week. He will fill in for NASA Administrator Sean O'Keefe, who left the agency on 11 February. The White House is expected to nominate O'Keefe's successor shortly, but it may take some time for Congress to confirm that candidate. Gregory, a former Air Force colonel, has served as NASA's deputy administrator since 2002. In 1985, he was the first black commander of a space shuttle mission. O'Keefe will become chancellor of Louisiana State University in Baton Rouge.

–ANDREW LAWLER

masked by the same spectrally enigmatic coating Spirit found on rocks on the floor of Gusev. That gunk may have required no more than a molecular layer of water to form. Hydrated minerals, including clays, do show up in a few scattered spots, most notably in and around craters of Syrtis Major Planitia. But once again, the alteration seems to have been ancient, perhaps due to groundwater altering crustal rock.

All in all, Mars since ancient times is looking awfully cold and dry. "There should be clays everywhere if Mars truly was warm and wet," says planetary scientist Philip Christensen of Arizona State University in Tempe. "In isolated places and times, lots of water made evaporites," he says, but for billions of years, Mars seems to have been "incredibly dry and unweathered." Perhaps the most dynamic force shaping the martian surface during those eons, Bibring and his colleagues suggest, has been the snow, ice, and glaciers that move between polar and lower latitudes as the planet tilts back and forth on its axis (*Science*, 11 April 2003, p. 234).

Next up in martian spectroscopy is the Compact Reconnaissance Imaging Spectrometer for Mars (CRISM) that will be launched on board the Mars Reconnaissance Orbiter this August. Even more capable in the near-infrared than OMEGA, CRISM will be checking out likely places for the Mars Science Laboratory rover to look in 2010 for signs of water and life.

–RICHARD A. KERR

INFLUENZA

Study Questions the Benefits of Vaccinating the Elderly

Because elderly people are most likely to be hospitalized or die from influenza, U.S. policy puts them at the front of the line for flu shots. But a provocative new analysis of influenza-related mortality in the United States over the past 3 decades suggests that the vaccine has had far less success than presumed at preventing death in those over 65.

The study, led by epidemiologist Lone Simonsen of the National Institute of Allergy and Infectious Diseases in Bethesda, Maryland, focuses on the riddling fact that U.S. influenza mortality rates in the over-65 population have *increased* despite a concurrent jump in vaccination rates in that group, from 15% to 20% in 1980 to 65% in 2001. "There's a huge disconnect here," says Simonsen, whose group published its findings in the 14 February *Archives of Internal Medicine*.

Researchers have previously explained this disconnect by pointing to two main factors. One is the aging of the elderly population: Death from influenza increases in the so-called elder elderly. The second is that several particularly nasty flu strains circulated in the 1990s, causing higher mortality rates among those infected. Simonsen and colleagues, whose "ecological" study relied on a mathematical model that crunched data from various databases, attempted to control for these two confounding variables. They concluded that "the mortality benefits of influenza vaccination may be substantially less than previously thought," that the shortage of vaccine for the elderly this year "will have little impact" on flu-related mortality, and that the mortality benefit found in several "observational" studies—which compare cohorts of vaccinated and unvaccinated people—reflects "systematic bias."

Simonsen says the vaccine may benefit some elderly, and she acknowledges that it may reduce hospitalizations, a parameter her study does not analyze. But several studies show that the vaccine is not as effective in the elderly, she stresses, because their immune systems "senesce." Simonsen and colleagues also say their findings "strongly suggest" that the cohort studies may have wrongly credited the vaccine with preventing deaths because the unvaccinated groups had a disproportionate number of very ill people. People in fragile health right before flu season, they reason, are more likely to die and less likely to receive the vaccine.

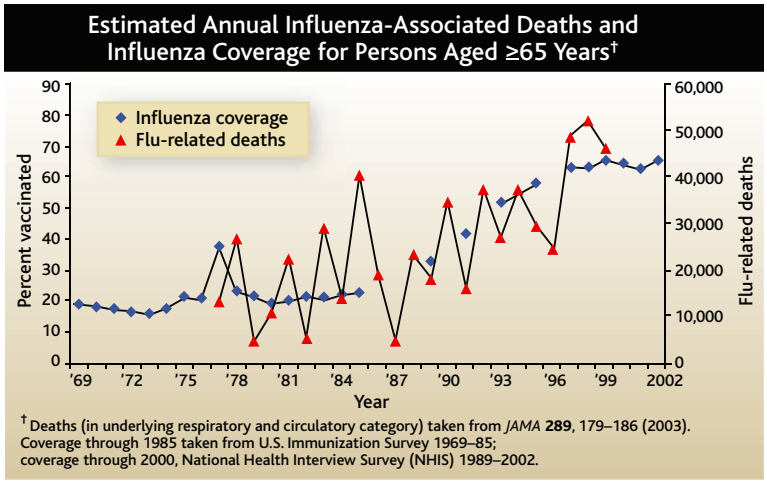

Discordant harmony. Why have U.S. influenza rates in the elderly risen in synchrony with vaccination rates?

The study has provoked starkly different reactions. "This is a very important, troubling study," says Walter Orenstein, the associate director of the vaccine center at Emory University in Atlanta, Georgia, and the former head of the National Immunization Program at the Centers for Disease Control and Prevention (CDC). "It is a paradigm shift." But CDC influenza expert William Thompson sharply disagrees: "I think it's extremely weak and overstates the results," says Thompson, who studies influenza-related disease and death in the United States. Thompson insists that his studies and others have accounted for the bias Simonsen points to in the selection of control groups.

The polar reactions in part speak to the difficulty of gauging the true impact of influenza. Both the observational studies and this new ecological study "raise interesting questions," says Kristen Nichol, an epidemiologist at the Veterans Administration in Minneapolis, Minnesota, who has published several observational studies that find a benefit from vaccinating the elderly, "but neither of us really knows what the baseline of mortality is in the absence of influenza." Specifically, Nichol notes that Simonsen's group measures influenza deaths by looking at "excess mortality" that occurs during the influenza season. But other respiratory illnesses that circulate during the same season can cause death. Cohort studies also have a shortcoming, she says: They rarely analyze blood to assess whether ailing people had influenza.

Whoever is correct, the Simonsen paper raises policy questions that promise to catalyze a hot debate. The current U.S. flu vaccine policy targets the elderly and the very young—but not school-age children. Yet several studies suggest that vaccinating school-age children, the main spreaders of flu, could provide a substantial indirect benefit to the elderly (*Science*, 12 November 2004, p. 1123).

In the United States, about 36,000 people, mostly elderly, die each year from influenza-related disease. "In a way, this study is good news: It says there's room for improvement," says Simonsen. "There's really a need to get to the bottom of this."

–JON COHEN

CREDIT: WALTER ORENSTEIN/EMORY UNIVERSITY

AVIAN FLU

First Human Case in Cambodia Highlights Surveillance Shortcomings

The confirmation last week that the H5N1 strain of avian influenza had claimed its first human victim in Cambodia has raised concerns about surveillance capabilities there and in nearby countries. The diagnosis was made not in Cambodia but in neighboring Vietnam, where the 25-year-old woman had sought treatment and died on 30 January. The Cambodian Ministry of Health and the World Health Organization (WHO) confirmed the case on 5 February. Cambodian health authorities subsequently learned that the woman's 14-year-old brother had died earlier of an apparent respiratory disease now suspected to be H5N1, but his remains were cremated before any samples were taken.

Health authorities believe the two were most likely infected by exposure to sick poultry. WHO and Cambodian health officials heard reports that the disease had wiped out small flocks of chickens in the vicinity of the woman's village in Kampot Province at the southern tip of Cambodia but were unable to confirm H5N1. Cambodia's Ministry of Agriculture later confirmed an outbreak of H5N1 among poultry in Kandal Province, about 100 kilometers away.

These incidents underscore the need to increase surveillance for H5N1 infections in both animals and humans in Cambodia, Laos, and Myanmar, says Klaus Stöhr, coordinator of WHO's Global Influenza Program. Because they have relatively small poultry populations, there is probably less H5N1 virus in circulation in these countries. But their underdeveloped surveillance capabilities also offer less chance of early detection of an outbreak. Especially if the virus becomes easily transmissible among humans, "the lead time we have to prepare vaccines or distribute antivirals to try to quell the outbreak at its source will depend on the sensitivity of surveillance," Stöhr says.

Cambodia and Laos reported minor outbreaks of H5N1 in poultry last year. Many international health experts assumed that additional outbreaks were dying out undetected and without intervention, given low poultry densities and the absence of large-scale commercial poultry operations, unlike Vietnam and Thailand, which have large and highly concentrated poultry farms.

Because viruses thrive in cooler weather, virologists had expected another wave of H5N1 outbreaks this winter. And since December, both Vietnam and Thailand have reported dozens of outbreaks among poultry. Vietnam has also reported 10 human cases and 9 deaths. International health experts suspected that the H5N1 virus must also be present in Cambodia and Laos, because they are sandwiched between countries with major outbreaks. Both the U.N. Food and Agriculture Organization (FAO) and WHO have been assisting Laos and Cambodia in building surveillance capabilities since last year. But Megge Miller, a WHO epidemiologist in Cambodia, says that country still relies on an informal disease reporting system.

False security? While Vietnam has reported widespread outbreaks of avian flu, Cambodia has confirmed just one human case and one infected farm.

Monitoring animal health seems equally sporadic. With FAO support, the Cambodian Ministry of Agriculture has been surveying chickens brought to markets. But WHO's Miller says this largely misses chickens families raise for their own consumption. Typically, she adds, these families eat diseased birds; preparing and cooking birds that have died of H5N1 is a suspected route of human infection. After the recent human case, Cambodian officials launched an advertising blitz, with leaflets and radio broadcasts warning of the dangers of contact with sick poultry. Similar efforts seem to have paid off in Thailand, says Supamit Chunsuttiwat, senior expert on communicable diseases at Thailand's Ministry of Public Health, where no human cases of H5N1 have been reported since last fall.

Meanwhile, FAO is planning to dispatch additional technical consultants to both Cambodia and Laos. Regional bird flu cooperation is likely to get a boost from a joint meeting on avian influenza control to be held by FAO and the World Organization for Animal Health 23 to 25 February in Ho Chi Minh City, Vietnam.

–DENNIS NORMILE

CREDIT (TOP TO BOTTOM): ADAPTED FROM FAO TECHNICAL TASK FORCE ON AVIAN INFLUENZA; NMFS

ScienceScope

Stem Cells Hit Snag in Massachusetts

A campaign in Massachusetts to smooth the path for stem cell research and explicitly sanction so-called therapeutic cloning suffered a setback last week when Republican Governor Mitt Romney declared himself opposed to all cloning.

Massachusetts is home to many leading stem cell researchers, but its laws on research with human embryonic stem cells are vague. Advocates are pushing for a state law that would allow research on surplus embryos generated at fertilization clinics and embryos created by cloning and would also set up a new ethics body to oversee the research. Although scientists and lawmakers had hoped for the governor's support, Romney declared that any law "should prohibit all human cloning and the creation of new human embryos for the purpose of research."

In response, Harvard stem cell researchers George Daley and Leonard Zon deplored efforts to "criminalize" what they characterized as vital research. "This throws everything up in the air," adds Robert Lanza of Advanced Cell Technologies Inc. in Worcester.

–CONSTANCE HOLDEN

Alaskan Coral Preserved

The North Pacific Fishery Management Council has voted to ban a destructive fishing practice called bottom trawling from 960,495 square kilometers of sea floor around Alaska's Aleutian Islands—the largest area ever afforded such protection.

Bottom trawling involves dragging heavy nets across the sea floor, a process that destroys coral, sponges, and other creatures. In 2002, researchers probing the deep waters around the Aleutians discovered rich gardens of corals, which they believe provide a habitat for many fish species. Last week's decision to protect that coral is "a significant advance in ocean management," says David Allison of Oceana, an advocacy group based in Washington, D.C.

The management council is one of several such regional bodies chartered by the National Oceanic and Atmospheric Administration to manage fisheries off United States' coasts. Later this year, the Pacific council will decide whether to vote for a similar ban for fish habitats off the West Coast thought to harbor similar coral gardens.

–ERIK STOKSTAD

BIOMEDICAL RESEARCH

Despite Protests, MRC to Move Its Largest Institute Into London

CAMBRIDGE, U.K.—Researchers at one of Britain's top biomedical centers learned last week that their months-long campaign to prevent the sale of the center's 19-hectare campus has failed. The National Institute for Medical Research (NIMR)—which has a staff of more than 700—will be relocated from the London suburb of Mill Hill to the city-center campus of University College London (UCL). The university intends to appoint an undetermined number of NIMR's 66 research leaders to its faculty.

The move represents a "unanimous decision" of the Medical Research Council, the government funding agency that runs the center, according to an MRC statement on 11 February. MRC chiefs had long argued that the suburban institute should sit alongside a medical school and hospital to advance "translational research" (*Science*, 4 February, p. 652). UCL beat out its rival King's College London to become NIMR's home because it has more depth in physics and chemistry, as well as greater "maturity" in clinical research, the MRC statement said.

Scientists at NIMR had mounted strong resistance to the planned move, with some even threatening to resign. Malcolm Grant, provost of UCL, immediately set out to reassure them. He hopes they will stay with NIMR because the partnership "will bring huge benefits on both sides," he says. The university already has strong collaborations with NIMR scientists, he notes, particularly in research on children's diseases. He proposes that the main part of NIMR's campus be set alongside the university's new medical complex on Gower Street. Grant planned to meet with NIMR researchers in person on 15 February.

New home. University College London has been chosen to host the U.K.'s National Institute for Medical Research.

There are still "a number of hurdles to be cleared" before the relocation can occur, Grant concedes. Among others, the project must win a large chunk of government funding. It must also receive approval for extensive renovation of buildings in the city and must find a home for NIMR's extensive animal lab—a tricky proposition in Britain, where animal-rights extremists have fought construction of animal facilities. And Grant fears UCL may not be able to duplicate one of the advantages the institute now enjoys: a category 4 biosafety research lab. "We will explore this," he says.

Some NIMR research leaders who had opposed the move from Mill Hill were not available for comment last week, but others were looking on the bright side. NIMR immunologist Dimitris Kioussis says, "This could be a very good thing for the institute," although he acknowledges that "we haven't heard about any detailed plans of what they are offering." Guy Dodson, head of structural biology at NIMR, also stressed that "there are a lot of positives" in MRC's decision, because "UCL is a very strong university."

An inquiry into the controversy by the House of Commons' science and technology committee, meanwhile, brushed aside allegations that MRC chief Colin Blakemore had improperly pressured NIMR staff to go along with the relocation. Released on 8 February, the report faulted some aspects of MRC's review of the move but concluded that Blakemore handled his part with "professionalism, objectivity, and competence."

—ELIOT MARSHALL

GENE THERAPY

As Gelsinger Case Ends, Gene Therapy Suffers Another Blow

Five years after 18-year-old Jesse Gelsinger died in a gene therapy experiment, the U.S. Department of Justice has reached a settlement with the researchers and with their institutions. The department announced last week that the University of Pennsylvania (U. Penn) will pay fines of $517,496, and Children's National Medical Center in Washington, D.C., will pay $514,622. The settlement also restricts the clinical research of the three investigators.

The Department of Justice alleged that toxic reactions in humans should have halted the trial earlier and that the lead investigators misrepresented clinical findings to the study's overseers, such as the National Institutes of Health (NIH) and the Food and Drug Administration (FDA). James Wilson of U. Penn, who had a financial interest in a company that stood to profit if the trial was successful, has agreed not to lead any FDA-regulated clinical trials for 5 years and be monitored for 3 years. Steven Raper of U. Penn and Mark Batshaw of Children's face less severe restrictions. Under the agreement, the scientists do not admit responsibility for Gelsinger's death. "Outrageous," responds Gelsinger family attorney Alan Milstein, who said the family had hoped for a formal apology and the release of the clinical trial documents.

While the Gelsinger case drew to a close, the field of gene therapy suffered another setback last month: A third child in a French trial for X-linked severe combined immunodeficiency (X-SCID) developed leukemia, French authorities reported on 24 January. Seventeen children have been successfully treated for SCID using gene therapy, making it the field's bright spot. But two patients in the French trial developed leukemia in late 2002 after a vector inserted near an oncogene; one child died last October. In response to the third leukemia case, the French trial has been halted again and FDA has suspended three U.S. SCID trials, but a trial in Britain continues.

The two previous leukemia cases in France occurred in infants treated at 3 months of age or less, which led to speculation that cells with the oncogene insertion proliferate more readily in very young children. But the third child was treated at 9 months, suggesting that older children may also be at risk, says Harry Malech of NIH, who heads one of the U.S. trials. Experts expect to discuss the case when FDA's gene therapy advisory committee and NIH's Recombinant DNA Advisory Committee meet in March.

—JENNIFER COUZIN AND JOCELYN KAISER

CREDIT: UNIVERSITY COLLEGE LONDON

GERMAN SCIENCE

Board Protest Stops a Shake-Up of the Dahlem Conferences

BERLIN—A crisis over the future of the prestigious Dahlem Conferences in Berlin that was brewing into a major furor has been calmed—at least for now. On 14 February, president Dieter Lenzen of the Free University in Berlin, which administers the conferences, agreed to reinstate a staff member whom the administration had dismissed and to protect the meetings from outside meddling with the scientific agenda.

Lenzen took these steps after he received a letter from members of Dahlem's scientific advisory board charging that the university was damaging the scientific reputation of the meetings and announcing their decision to resign. Several had said they would try to reestablish the conferences outside the university. But Lenzen's last-minute change of heart appears to have mollified at least some of the critics, who say they will give the university another chance.

The Dahlem conferences, named for the West Berlin neighborhood of villas and leafy boulevards where the conferences are held, were founded in 1974 as a way to boost the divided city's scientific reputation. Two or three conferences are held per year on broad topics such as "Genetic and Cultural Evolution of Cooperation" and "The Dynamics of Fault Zones." During the weeklong, invitation-only sessions, roughly 40 participants break into working groups to discuss position papers—often drafted to be as provocative as possible—and prepare a synthesis statement to be presented on the final day. The proceedings are published in book format.

More than 4000 scientists from around the world have taken part in 95 conferences over the past 3 decades. Fans of Dahlem say it offers a unique approach to tackling problems and making interdisciplinary connections. "The Dahlem format is such a great alternative" to the standard conference design, says Gerd Gigerenzer of the Max Planck Institute for Human Development in Berlin, who has led two Dahlem workshops.

In recent months scientists involved with the conferences charged that the university was undermining their scientific integrity. Specifically, they claimed that members of an International Advisory Board, established in 2003 to raise funds for the meetings, were attending scientific planning meetings uninvited and that the administration had pressured organizers to highlight Free University researchers instead of international experts in the lineup of participants. In early November, administration officials removed the longtime coordinator of the conferences, Julia Lupp, from her position and forbade her from speaking to anyone connected to the conferences. They said she was on sick leave.

Back from the brink. A feud over Dahlem's leadership has calmed.

Members of the scientific advisory board protested that the administration should have consulted them about such an important staffing change and that Lupp had done nothing to deserve firing. In January, an inquiry by a board member and the university found no fault in Lupp's job performance, but the administration refused to reconsider its decision.

By mid-February, nearly half of the advisory board had decided to resign, and organizers of three planned conferences had withdrawn their proposals and were looking for new venues. The international outcry apparently had an effect. Lenzen agreed on 14 February to reinstate Lupp and to draw up new guidelines to protect the science from fundraising or other pressures.

Observers say they are cautiously optimistic about Dahlem's future. Eörs Szathmáry of the Institute for Advanced Study in Budapest, who has been coordinating a conference scheduled for May, says he would reconsider his decision to withdraw the workshop if he received "an official, written" letter from the university confirming Lupp's reinstatement and "guaranteeing protection from nonacademic influences." Gigerenzer says he hoped the university would follow through on its promises. "The first Dahlem conference was one of the best I've ever organized," Gigerenzer says. "If the conflict is solved, that is good news."

–GRETCHEN VOGEL

BIOCHEMISTRY

Irresistible Lure for Cockroaches Determined

In search of mates, frogs croak, birds sing, and cockroaches wear their own special perfume. For almost 10 years, researchers have tried to decipher the chemical formula of the male-luring scent emitted by female German cockroaches. Now that formula is finally in hand. As a result, city dwellers may one day be less squeamish about turning on the light at night: The chemical may result in a "very powerful system" for pest control, says Walter Leal, a chemical ecologist at the University of California, Davis.

On page 1104, Satoshi Nojima, a chemist now at the Shin-Etsu Chemical Co. in Tokyo, Japan, and his colleagues describe the arduous path they took to characterize this chemical, one of several pheromones produced by cockroaches. They also show that a synthetic version of it is a potent attractant for the insects. "It was very difficult to do, very time-consuming," says Robert Kopanic Jr., an entomologist at S. C. Johnson and Son Inc. in Racine, Wisconsin.

German cockroaches are the bane of urban residents. As many as 100,000 can live in a single apartment or house; baits and sticky traps are only moderately effective, and insecticides are not environmental friendly.

Love is blind. A synthetic version of the female scent that attracts males (on female's back) may help with cockroach control.

So it was exciting news when Coby Schal, an urban entomologist at North Carolina State University in Raleigh, and Dangsheng Laing, now at Atex Bait Co. in Santa Clara, California, reported in 1993 that female cockroaches gave off a volatile compound, or pheromone, that attracts males from meters away. But taking the next step, identifying the pheromone, proved almost impossible. "Every time [we] tried to isolate it, it fell apart," recalls Wendell Roelofs, a ▶

CREDITS (TOP TO BOTTOM): THE MIT PRESS; S. NOJIMA *ET AL.*, *SCIENCE*

biochemist at the New York State Agricultural Experiment Station in Geneva.

Adding to the challenge, females produce so little pheromone that researchers needed to dissect 15,000 of them, removing the pheromone-producing gland from each, to extract enough material for analysis. And Nojima—who was working with Roelofs at the time—had to come up with new ways to pin down the attractant among the many compounds in the extracts.

Nojima joined a single detached cockroach antenna to electrodes and exposed it to the chemicals exiting a gas chromatograph, which had separated the roach extract into discrete components. If the antenna sent a signal to the electrodes, he knew he had a good candidate pheromone. The night before he flew back to Japan—his postdoc was ending—Nojima struck cockroach gold when his system recorded a hit. "After 10 years of work, it came down to one night," says Schal.

Fran Webster of Syracuse University in New York found that the newly isolated compound, called blattellaquinone after the cockroach's Latin name *Blattella*, has a novel structure. But it is similar enough to a commercial product that it is relatively inexpensive to synthesize. The compound clearly attracts male roaches: They prefer the dissolved synthetic pheromone over a control solvent about 93% of the time, on par with their preferences for the natural pheromone. Moreover, field tests at a cockroach-infested pig farm indicate that many males can't resist the synthetic version.

If the compound proves to be effective over long periods, it could be quite useful for pest control, says Kopanic. Even though blattellaquinone only attracts males, they are the wanderers among the two sexes. The new pheromone should lure males into traps or to poison laced with the compound. In the latter case, they would then transfer the poison, through their feces, to females and their young, suggests Schal. If so, for male roaches, the female scent may one day lead to poison, not procreation. **–ELIZABETH PENNISI**

AGRICULTURAL RESEARCH

Ag Schools Say They Can't Afford Budget Boost

Agricultural researchers have long been green with envy at the budgets of U.S. research agencies that fund their colleagues in other disciplines. So President George W. Bush's request last week for a 39% increase in the U.S. Department of Agriculture's (USDA's) signature competitive grants program would seem to be cause for celebration. Instead, university lobbyists have declared war on the proposal because it siphons money from a different program that assured some schools steady funding for infrastructure, salaries, and research on local problems.

At issue is the Administration's 2006 budget request for $250 million for the National Research Initiative (NRI). USDA officials say it will improve accountability and yield big dividends for agriculture. "We know that competitive grants usually bring out the better science," says Joseph Jen, USDA's undersecretary for research, education, and economics. USDA also wants to remove a mandated cap on the amount of overhead that institutions can receive for the cost of supporting federally funded research.

A larger NRI, Jen says, would include more research on obesity prevention and agricultural biosecurity, such as applying genomics to develop better diagnostic tests for animal and crop disease. That's an appealing vision, especially to officials at larger schools. "It's a good move," comments Peter Barry, director of the Center for Farm and Rural Business Finance at the University of Illinois, Urbana-Champaign. "Increased funding will take the program to a new level and significantly extend its capacity to address major societal problems."

Universities don't object to the boost for NRI, which has never come close to being the half-billion-dollar-a-year program recommended in a 1994 report from the National Academy of Sciences. But the 2006 request, they complain, takes a knife to a $550-million-a-year pot that funds agricultural experiment stations at so-called Land-Grant Colleges—mostly state universities—using a formula based on the number of small farmers in the state. The $104 million reduction "would be devastating," says Thomas Fretz, who heads the Northeastern Regional Association of State Agricultural Experiment Station Directors.

Plucked? Researchers worry that poultry flocks, livestock herds, and other research infrastructure, such as greenhouses, might be cut.

CREDIT: UNIVERSITY OF MARYLAND COLLEGE OF AGRICULTURE AND NATURAL RESOURCES

Deans at land-grant colleges worry about activities that don't typically get supported by grants, such as local applications of research. For example, researchers at Colorado State University support the state's $200 million potato industry by working with growers to breed resistance to particular diseases during growth or storage. "We are not likely to get national competitive grants" for such applied research, says Marc Johnson, dean of the College of Agricultural Sciences at Colorado State. Without another source of funding, Johnson and other deans say they will be forced to end applied research and shrink graduate programs.

Another concern is that the cut in formula funds will hurt infrastructure, such as greenhouses and herds of research animals. "Grant agencies in the past have not liked funding facilities," says Fretz. But these expenses are no less real, he notes: "You can't have breaks in funding and maintain a dairy herd."

To soften the blow, USDA has proposed fencing off $75 million for a competition among land-grant colleges. But department officials are still working out the details, leading to concern that these competitive grants won't be awarded in time to replace the cut in formula funding. "That will leave a pretty big hole for the year," says Johnson.

The next step is up to Congress, and lobbyists are already gearing up. "Our number one priority is to reinstate the formula funds," says Fred Cholick, dean of the College of Agriculture at Kansas State University and chair of the agriculture budget and advocacy committee for the National Association of State Universities and Land-Grant Colleges. Even advocates for NRI doubt that the president will get all that he wants. "I can't see [legislators] giving up their earmarks," says Karl Glasener, who tracks federal agricultural policy for three scientific societies.

–AMITABH AVASTHI AND ERIK STOKSTAD

A project backed by the World Bank aims to reverse the Aral Sea's rapid decline, but it could also increase traffic to an abandoned bioweapons testing site

To Save a Vanishing Sea

AKESPE, KAZAKHSTAN—Amid a parched landscape, Denis Zhakupov draws his hand across his chest, recalling how shoreside reeds grew "up to here" in his childhood. The air was full of birds, and the sea was full of fish. "We had everything," the 60-year-old medic recalls. But his community, like many other towns near the coast of the Aral Sea, has lost its shoreline and its easy fishing. They are victims of an avoidable environmental catastrophe that has devastated this region and given Akespe a problem all its own.

As the sea withdrew several kilometers to the south, it bared a bottom of fine, alluvial sand. The winds picked it up and blanketed the village, piling up dunes higher than houses that now make the place look like a Saharan oasis—without the palms. Some houses have collapsed under the pressure of drifts. "We have to dig ourselves out every day when the wind blows," Zhakupov complains.

Desiccation has been eating at the Aral Sea for 30 years, turning a bountiful source of fish into a salty, inhospitable body of water. The sea shrank by 75% and split into two parts joined by an isthmus: the Small Aral in the north, which includes Akespe, and the Big Aral in the south.

A regional governor in the north decided to do something about the crisis a dozen years ago and built a primitive dike to prevent the Small Aral from completely draining away. But the dike quickly breached. Workers rebuilt it again and again—seven times in all—finally giving up in 1999.

After years of monitoring the local efforts, the World Bank agreed to finance a properly engineered dike that includes a sluice to release excess water. The bank also committed to major works aimed at doubling the flow of the Syr Darya, the main river that feeds into the Small Aral. The $85 million project, now under way, "is the biggest attempt to repair a damaged lake that we've seen so far," says Philip Micklin, an Aral Sea specialist at Western Michigan University in Kalamazoo.

The new dike and sluice are to be completed this summer. Within 3 years, the Small Aral is expected to rise at least 3 meters and cover about 1000 square kilometers of now-dry former seabed, extending its surface by 25%.

The water's rise is also expected to increase rainfall, improve pastureland, and cut down on dust storms. The sea's salinity, now at 15 grams per liter, is predicted to fall to 10 grams, a third of the concentration of the ocean and roughly that of the Aral Sea before desiccation began. Fish and other freshwater aquatic life forms that retreated into the Syr Darya delta when the sea became too salty are expected to return, perhaps including the commercially valuable caviar-yielding ship sturgeon. If it succeeds, the restoration will partly undo the damage wrought by 3 decades of Soviet policy. But the dike may also decrease water flow to the south and expose land in the Big Aral that was partially submerged. This in turn is likely to increase traffic across a land link to Vozrozhdeniye (Renaissance) Island, a remote site where the Soviet military once did field tests of plague and other bacteria whose lethality had been artificially increased. Thus the paradox: Reviving the Small Aral could worsen problems around the Big Aral.

Beached. A Soviet decision to divert river water to cotton farming hastened the Aral Sea's retreat.

CREDITS: C. PALA

Sacrificed to cotton

The recent disruption of the Aral Sea began in the 1940s with Josef Stalin's decision that the Soviet Union needed to become self-sufficient in cotton production. This could be done, he declared, by massively increasing the amount of water diverted for irrigation from Central Asia's two big rivers, Uzbekistan's Amu Darya in the south and Kazakhstan's smaller Syr Darya in the north. The sea, which got most of its water from these, would shrink, and a 50,000-ton-a-year fishery would be lost, but the Kremlin calculated there was plenty of seafood coming in from its Pacific and Atlantic fisheries. Today, the skeleton of a huge fish cannery towers over the town of Aralsk, Kazakhstan, once the main port on the northern part of the sea, now 80 kilometers away.

Since the heavy irrigation began in 1961, the Aral Sea has dropped 22 meters and lost 90% of its volume (*Science*, 2 April 1999, p. 30). Dust storms have picked up millions of tons of salt and scattered it over neighboring areas, spurring desertification. Pesticides, herbicides, and chemical fertilizers used with abandon during the Soviet period were also picked up by winds, resulting in steep increases in respiratory diseases and cancers—one consequence the Soviets hadn't expected.

As the sea level dropped, the sea's only nature preserve, located on an island called Barsa Kelmes, became accessible by car in

2000. It had been a primary research center for Soviet-era university studies of desert botany and zoology. Hundreds of saiga antelopes once grazed there; poachers have decimated all but a few, and the park administration no longer bothers keeping wardens there. A summer visitor, after driving for hours on the caked mud of the former seabed, found the scientific station deserted and partly in ruins. Because the water table had dropped, even the sturdy saxaul trees that form the region's biggest vegetation were dying.

This wasn't the first time irrigation had damaged the Aral Sea region. The Zoroastrian civilization built a vast agricultural network that collapsed in the 3rd century. In the 16th century, the British traveler Anthony Jenkinson noted that abuse of irrigation by Islamic settlers had caused "the great destruction" of the Amu Darya. Both civilizations discovered a simple fact of nature: The region is steeped in plant-stunting calcium sulfate, which is why very little grows, even near rivers. This salt leaches to the surface when land is excessively irrigated and requires increasing amounts of water to wash it away. The modern ecosystem collapse differs from earlier ones in two ways: It happened faster and was accompanied by chemical contamination from fertilizers, herbicides, and pesticides.

As the crisis deepened, Soviet scientists and policymakers drew up grandiose plans for digging huge canals to divert and bring southward the waters of two of Siberia's northward-flowing great rivers. But when Mikhail Gorbachev came to power in 1985 with a mandate for change, he tossed out the plan as environmentally dangerous and ordered a reduction in the use of river water for irrigation. Uzbekistan, for whom cotton is the main export, ignored him.

The Amu Darya was still pouring some water into the Big Aral when Uzbekistan gained independence in 1991. To rescue the wetlands around its delta, Uzbek authorities, with international support, built a half-dozen more dikes. As a result, the Big Aral dropped another 7 meters and became so salty that today only brine shrimp survive in it.

The economic collapse brought one positive change, however: The use of agricultural chemicals plummeted. Residues seem to have settled or dissipated; the remaining fish in the Small Aral have fewer poisons in their fatty tissues than those in Europe, says Sergei Sokolov, a hydrochemist monitoring the project for the World Bank.

Crusader. Zoologist Nikolai Aladin points to where the first dike was built.

CREDIT: C. PALA

From Samizdat to Celebrity—and Back

Portly, pony-tailed, and richly opinionated, Russian zoologist Nikolai Aladin has been infatuated with the Aral Sea for nearly 3 decades. The affair began in 1978 when he decided to take a break after defending his thesis at the St. Petersburg Zoological Institute, a part of the Russian Academy of Sciences. Aladin's adviser suggested that he go diving in the Aral's exceptionally clear and pleasant water. But when the 25-year-old reached the port of Aralsk, the sea was nowhere in sight: It had receded more than 30 kilometers—something the adviser had failed to mention.

Aladin did eventually reach the water, though, and observed that its salinity had increased from 10 grams per liter to nearly 20 in just 18 years—possibly the fastest such rise on record. Yet the sea was alive. He set out to study how salinity impacts aquatic ecosystems.

But back in St. Petersburg, his proposals were met with evasive refusals. Soviet leaders had decided in the 1950s to sacrifice the fish-rich, closed sea by diverting its source waters to cotton irrigation; they did not wish to publicize the toll on the environment.

Aladin found a way around them. "My father was relatively well-off as a naval doctor," Aladin recalled in an interview. "He offered to pay for my field trips." But it wasn't easy to share his findings. "To publish my first paper in the *Soviet Journal of Hydrobiology*, which was the first paper on the subject ever, I had to wait for 4 years and agree that all precise geographical coordinates be deleted," Aladin recalled. He went on to read papers at scientific meetings but had to print and circulate them himself. "It was a soft form of samizdat," he said, referring to the underground literature of the Soviet days. During official hours, he studied how variations in salinity affect crustaceans in other seas.

Aladin's Aral research did not go unnoticed. "Not only is his scientific work impressive, but he has done more than anyone to make people aware of the problems in the region," says Dietmar Keyser, an Aral Sea specialist at the University of Hamburg in Germany. "He is something of a crusader."

Western scientists knew from satellite photographs that the sea was shrinking, but they were unable to gain access to it. "In 1987, I flew over the Aral Sea with a map on my knees," recalled Rene Letolle, then a professor of geochemistry at Pierre and Marie Curie University in Paris. "I asked my Russian colleagues when I got to Tashkent if it was possible to visit the sea. But they said no, it was a military zone." He didn't get there until 1995.

Things began to change in 1986 when Mikhail Gorbachev initiated a policy of glasnost (openness) to expose and improve the sort of policies that had led to the Aral Sea catastrophe. Outrage followed. "It was the Russians who made it a huge public issue, and that's what got the Western attention," recalled Philip Micklin, an Aral Sea specialist at Western Michigan University in Kalamazoo.

Aladin, his work now recognized, was handed his own lab, the Laboratory of Brackish Water Hydrobiology in St. Petersburg, which he still heads. He led or participated in many expeditions to the Aral, including one in 1988 involving 100 scientists and intellectuals and a major scientific trip in 1990. "I had lots of funding, and I thought I was making a difference," he says. He takes credit for impressing upon the Aralsk governor in 1992 the need for a dike to save the Small Aral and for bringing in World Bank officials to see it, which helped prompt the bank's current investment in the area (see main text).

But when the Soviet Union broke apart, the Russian Academy of Sciences stopped funding Aral Sea research on grounds that it might appear materialistic. International scientific and educational institutions, according to Micklin, also began to "feel that the Aral Sea is not in Russia, so why should we give money to Russians?" Aladin says he was "lucky" to get good support during the early 1990s, but donors since then have favored citizens of Kazakhstan and Uzbekistan.

For Aladin, there's a sense of déjà vu: "I feel in the same situation as I was in the '80s, except that my father passed away, and I now pay for my field trips from the salary I earn from research of other seas." **–C.P.**

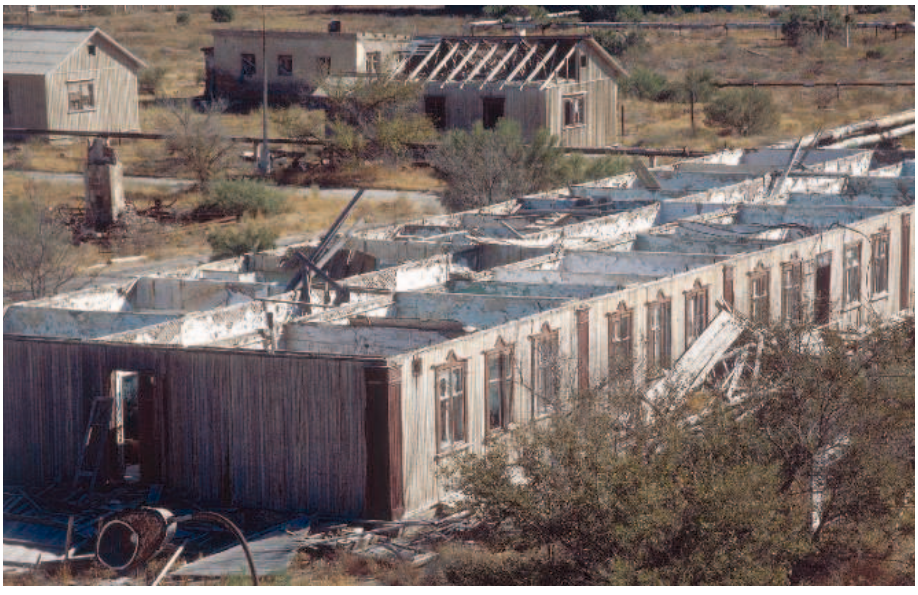

Grim legacy. Abandoned buildings on Vozrozhdeniye Island, a former bioweapons testing facility.

But the risk isn't gone, Sokolov says. As Kazakhstan's economy improves, the use of fertilizers has been rising. They flow into the river in the fall, after the harvests of rice and cotton, when farmers rinse the ground to wash out salt. "There needs to be a system under which, for 1 month a year, this water is not sent into the river but into special lakes," Sokolov argues. If not, he warns, "the Small Aral will become polluted." But Masood Ahmad, the World Bank official in charge of the project, disagrees: He says pollutants will be diluted to a safe level by the river's increased flow.

New prospects

Standing atop the smooth, new, 13-kilometer dike financed by the World Bank, most of which is already completed, Aitbai Kusherbayev, the dam's chief engineer and a former governor of the Aralsk region, says he's confident the barrier will work this time. It stands 6 meters high, 3 meters above the planned new sea level, and slopes gradually for about 120 meters toward the water. The seaside will be covered with gravel to resist the waves and the winter ice that dislodged the previous dike in 1999.

The structure will indisputably benefit the Small Aral. But the three-times-larger Big Aral will suffer as water from the Syr Darya is retained in the north for several years to raise the Small Aral by 3 meters.

Already, desiccation around the Big Aral has caused Vozrozhdeniye to grow from a 33-kilometer-long island into a 145-kilometer peninsula attached to the coast of Uzbekistan. Until last year, this southern end was too wet even in summer for any vehicle to pass. But access may soon be possible.

Because of its remoteness, Vozrozhdeniye was used as the main Soviet center for testing bioweapons, antidotes, and vaccines in complete secrecy. In the 1970s and 1980s, the only town, Kantubek, had a population of 2000 in the summer when experimenters were busy. Researchers exposed monkeys, horses, and other animals to weaponized anthrax, tularemia, brucellosis, plague, typhus, Q fever, smallpox, botulinum toxin, and Venezuelan equine encephalitis.

Biowarrior. Former lab supervisor Gennady Lepyoshkin worries that lethal plague bacteria may have survived among the island's rodents.

In 1992, Uzbekistan acquired the southern part of the deserted island; Kazakhstan, the northern part. But neither country bothered posting guards, so Kazakh scavengers were able to travel there episodically in small boats to take away pipes, wires, and other materials and sell them on the mainland.

To a visitor 2 years ago, Kantubek presented a rare glimpse of the world's biggest bioweapons program in ruins. Cages and lab equipment were piled haphazardly, and unused germ suits still could be found in boxes. Most of the equipment in the "hot zone" had been evacuated.

Russian and Kazakh scientists agree that one potential hazard remains: Military-grade, antibiotic-resistant plague bacteria—very different from the strain endemic in Central Asia—may have survived among the rodents in the testing range, 16 kilometers from Kantubek, despite attempts to minimize risk. Gennady Lepyoshkin, who spent 18 summers supervising a laboratory testing weaponized bacteria such as plague and brucellosis, recalls: "Before we tested, we would spray a poison over the area to kill all wildlife. Then we would bring in our testing animals and release the aerosol with the germs. But there's a good chance that some rodents had stayed in their burrows when the poison gas was released and came out when the germs were passing around them." Rodents and camels are natural carriers of plague; they don't die of it but spread it through fleas.

Lepyoshkin says Uzbeks will eventually cross the land bridge to Vozrozhdeniye, and the weapons-grade plague, if it has indeed survived, will spread when island and mainland populations of rodents begin to mingle. "An environmental catastrophe is inevitable," he claims.

There is a solution, according to Nikolai Aladin, a professor at the Zoological Institute of the Russian Academy of Sciences in St. Petersburg. Aladin, 51, has been studying the Aral Sea for 27 years, perhaps longer than any other scientist (see sidebar on p. 1033). He proposes building a dike from the northern part of Vozrozhdeniye to the Kazakh mainland that would cause the shallow water on the eastern side to rise and return the foot of the peninsula to marsh, making it impassible for vehicles.

"There has been talk about it," says the World Bank's Ahmad, "but so far no work has been done to investigate its feasibility or find financing for it."

Micklin, while acknowledging the bioweapons threat, calls the dike project backed by the World Bank "a reasonable approach" for now. He says, "You can't restore the whole sea, given the amount of water you have available now, so restoring the Small Sea and bringing back the fishery is a wise idea, even though it may speed up the decline of the Big Aral." It boils down to a tradeoff between the clear benefits of restoring part of a devastated ecosystem and the uncertain risks of resurrecting an old threat.

—CHRISTOPHER PALA

Christopher Pala is a writer based in Almaty, Kazakhstan.

CREDITS: C. PALA

A Devil of a Disease

Tasmanian devils are being wiped out by a deadly facial cancer that may spread when the animals fight each other

Geoff King, a farmer in Northwest Tasmania, sees a lot of fights at dinner. That's because he also runs a "devil restaurant," a tour in which customers watch the island's most famous animal, the Tasmanian devil, devour carcasses left out for it. Known as Taz in the cartoon incarnation of the marsupial, the Tasmanian devil is in reality a relatively shy scavenger. But at suppertime, and during the mating season, devils engage in the fighting and biting that have made them legendary. That violence may now be the death of the devils—but in a most unusual way.

A disfiguring and deadly facial cancer has slashed Tasmanian devil numbers by up to one-half in the past decade. "It's an aggressive cancer that is spreading rapidly and killing animals within 6 months," says Menna Jones, a zoologist at the University of Tasmania in Hobart. Although several hypotheses are still in the running, clues are emerging that the devils may be transferring tumor cells directly from animal to animal during fights. While research into the unusual cancer, known as devil facial tumor disease (DFTD), continues, biologists this month outlined a management strategy aimed at safeguarding the survival of the species.

In DFTD, tumors grow on an animal's face and muzzle so that the devil eventually cannot feed. Although the facial tumors were first recorded by a wildlife photographer in 1996, the true threat only became apparent in 2000 when the same tumors were found in statewide surveys. Research picked up momentum in November 2003, when the Tasmanian government dealt out a $1.8 million funding package to tackle DFTD.

Field research indicates that between one-half and one-third of the 150,000 devils that lived in Tasmania 10 years ago have been lost. According to a report released in January, the disease is now present across at least 65% of the island. And that may be a low estimate; with no diagnostic tests, scientists can only record the disease in obviously sick animals. Instead of breeding four to five times in their life, devils have been reduced to breeding only once before they succumb to the disease, says Jones.

Although there is no immediate threat of extinction, biologists fear that devils may become "functionally extinct" and no longer perform their role as a bush janitor. Already farmers are noting that dead stock is not cleaned up from their farms, says wildlife biologist Nick Mooney of the Department for Primary Industries, Water, and Environment (DPIWE). His biggest worry is that illegally introduced foxes, which were discovered on the island in 2001, may take over the devils' ecological niche.

The disease management strategy focuses on isolating devils that are already living in captivity—approximately 70 in zoos on the Australian continent and 100 in parks in Tasmania—from wild populations afflicted with the disease. So far there is no indication that devils in captivity are catching DFTD. Wildlife managers will also capture young, apparently healthy devils to establish further insurance populations. Should these devils develop tumors in quarantine, this would provide further opportunities to study the disease. Finally, scientists will experiment with strategies to suppress the disease's spread in the wild, such as removing affected animals in order to protect nearby healthy populations.

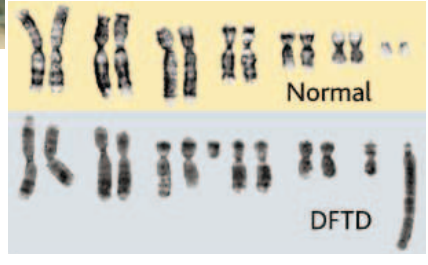

Cancer concern. The facial tumors killing Tasmanian devils have a characteristic abnormal karyotype.

"It's an excellent example of a sensible response to a new wildlife disease about which we know very little," says Andrew Dobson, a population ecologist at Princeton University who studies wildlife diseases.

At first, researchers assumed that a virus was behind the spread of DFTD, as similar viral conditions are known in cats and other animals. But efforts over the past year to detect virus particles in tumors have come up empty, prompting research into whether cancer cells themselves spread the disease. "Field observations are consistent with direct biting transmission, and we are waiting for the lab work," says Jones.

The lab work so far is provocative but not conclusive. The tumors have been characterized as a neuroendocrine cancer, and tumors studied so far have identical chromosomal rearrangements. That suggests that all the animals with DFTD are being affected by the same cancer cell line. "That's the hypothesis that I would put my money on," says Jonathan Stoye, a virologist at the National Institute for Medical Research in London, who is impressed by the chromosomal evidence.

Only one known cancer is spread in a similar fashion. Canine transmissible venereal tumor is passed among dogs during sex, sniffing, and licking. The similar karotypes of these canine tumors had led to the suggestion that the cancer cells themselves are infectious. Indeed, viral oncologist Robin Weiss and his student Claudio Murgia at University College London have recently carried out experiments—soon to be submitted for publication—that demonstrate that these tumors are caused by a single transmissible cancerous cell line. Weiss suggests that profiling the nuclear and mitochondrial genomes of DFTD tumor cells could confirm whether they, too, are a transmissible cell line.

If direct contact is required for transmission of DFTD, then removal of sick devils would be a very effective way of controlling the disease. But if a virus does turn out to be the culprit, other animals could be asymptomatic reservoirs for the disease. Researchers are continuing to investigate possible causes, from a virus to environmental and human-made toxins, says Stephen Pyecroft, a veterinary pathologist with DPIWE.

Tasmania's government and opposition parties have been quibbling over whether to list the devil as a threatened species, but with the data in hand, it is now expected that nomination to threatened species status will go ahead later this year. Worried Tasmanians have donated an additional $50,000 to study DFTD and to make sure the devil does not go the same way as the island's other iconic animal: the now-extinct Tasmanian tiger.

–ADAM BOSTANCI

Adam Bostanci is a science writer in Exeter, U.K.

CREDITS: CHRISTO BAARS; INSET SOURCE: DEPARTMENT OF PRIMARY INDUSTRIES, WATER, AND ENVIRONMENT

Will DNA Bar Codes Breathe Life Into Classification?

Biologists hope that a simple tag on all forms of life, and even a hand-held reader, will make classification a 21st century science

LONDON—The sometimes-dusty world of taxonomy and biological collections held a revival meeting here last week. In the imposing surroundings of the Natural History Museum, on Charles Darwin's birthday, more than 220 experts from 46 countries gathered to discuss a new technology that could change their profession and—some predict—energize the museums in which they work. It makes use of short but specific DNA tags, or "bar codes"—parts of genes present in all living things—to distinguish one species from another. Enthusiasts aim to create a portable device that will identify an anonymous specimen by species and link to a database crammed with biological information. Proponents say they're going to "bar code the planet."

The Consortium for the Barcode of Life (CBOL), which convened the meeting,* wants to tag every organism on Earth, starting with the 1.7 million species that have been named and moving on to the estimated 10 million to 20 million that have not. CBOL's leaders foresee many applications, from fundamental research on biodiversity to enforcement of food laws, protection of wildlife, and even biodefense (*Science*, 13 June 2003, p. 1692).

It's a grand vision, but the London museum's science chief Richard Lane says it's feasible. He told reporters that a "proof of principle" for DNA tagging has been demonstrated in a study of North American birds, recently published by a group led by Mark Stoeckle of the Rockefeller University in New York City and Paul Hebert of the University of Guelph in Canada. Hebert meanwhile leads a group that's tagging fish in the northern Atlantic Ocean. During the meeting, researchers announced a third major project—one that uses a novel bar code for plants—which will test the method on 8000 plant species in Costa Rica. Partners in this project include scientists from Costa Rica, the Royal Botanic Gardens at Kew, U.K., the University of Pennsylvania in Philadelphia, and the Smithsonian Institution in Washington, D.C. (where botanist John Kress is developing a new plant bar code).

Hebert, dubbed the "father of bar coding" by Lane and others, explained one reason for the current optimism among those in the field:

Muddled over your moths? Just check the bar code.

CREDIT: CHIP CLARK/SMITHSONIAN INSTITUTION

The price for reading bar codes is dropping. Hebert developed what has become a standard method for DNA-tagging animals. It uses a small part of the mitochondrial genome, 650 to 750 bases of the cytochrome *c* oxidase I gene (COI), to provide a unique fingerprint. For most eukaryotes, COI variation appears to be lower among individuals within a species than among those from different species; in the study of North American birds, it is about 18 times lower. Hebert said the cost of testing a specimen for COI variation is now about $2, not counting labor, or about 10% of what it was 2 years ago. This prompted Lane to predict that bar coding all of life would be "relatively cheap in terms of other big science projects": less than $1 billion.

CBOL's executive secretary, David Schindel of the Smithsonian, said that the push has already begun. The big genome databases—GenBank in the United States and its partners in Europe and Japan—"quietly" set up a bar codes section this month that includes the precise location the specimen came from, he says. About 1000 entries have been made so far, according to Scott Federhen of the National Center for Biological Information in Bethesda, Maryland. Guelph's Hebert and Bob Ward of Australia's Commonwealth Scientific and Industrial Research Organisation aim to supply tags for 15,000 marine and 8000 freshwater fish by 2010. During this time Stoeckle and a group of collaborators plan to bar-code 10,000 bird species. In an independent project, Ann Bucklin of the University of New Hampshire, Durham, and colleagues are gathering bar codes on ocean plankton.

Some big obstacles remain. One is technical: Experts are not sure that simple bar codes will work for all species. Plants, for example, cannot be tracked with the COI gene. Kress proposes to use a combination that includes a bit of highly variable DNA between two genes on the chloroplast genome. It worked well in a test on Plummer's Island near Washington, D.C., he says, and is now being tried in Costa Rica. Amphibians also pose a challenge because for many, the COI gene varies so much from one individual to the next that it cannot be used reliably to mark species, said Miguel Vences of the Institute for Biodiversity and Ecosystem Dynamics in Amsterdam, the Netherlands. Herpetologist James Hanken, director of Harvard University's Museum of Comparative Zoology, suggested that for certain species such as the amphibians he studies, COI variation may need to be supplemented by extra tests. And very young species—including orangutans—may not be easily distinguished by COI bar coding.

Another challenge is to find money. Jesse Ausubel of the Alfred P. Sloan Foundation in New York City has steered support to this area and helped launch CBOL, he said, ever since hearing Hebert describe the idea in 2002. Others have joined in, but so far foundations have helped pay for start-up work. To scale up, research groups will need to tap into government budgets, and it remains to be seen how much policymakers want to spend.

Ausubel said the field is gathering momentum and that funding will follow. He pointed out that several companies sent delegates to the meeting and have invested in the field, including the bioprospecting firm Diversa Corp. of San Diego, California, gene chip maker Affymetrix of Santa Clara, California, and enzyme supplier New England Biolabs of Beverly, Massachusetts. Government agencies, including the U.S. Food and Drug Administration and the U.S. Department of Homeland Security, are also jumping in. "Environmental genomics is going to be huge," says Ausubel. But the prediction—like many at this meeting—comes from a true believer.

—**ELIOT MARSHALL**

* The First International Barcoding of Life Conference, London, 7 to 9 February (www.nhm.ac.uk/science/BOL).

Linnaeus's Legacy Carries On

Following the tradition of its most famous taxonomist, Sweden aims to be the first country to complete an inventory and pictorial guide to its biodiversity

UPPSALA, SWEDEN—Nestled in the heart of this historic university city is a quiet garden with tidy rows of raised beds. It has been restored to the way it looked 260 years ago, when Carl Linnaeus occupied the adjacent house and paced the garden paths, formulating his influential *Systema Naturae*—a scheme for grouping and naming organisms according to their shared characteristics.

Linnaeus is a source of national pride for Swedes, many of whom share his appreciation of nature, says Ulf Gärdenfors, deputy director of the Swedish Species Information Center (SSIC), which compiles "red lists" of threatened flora and fauna that are used to guide national and international conservation policy. An entomologist, Gärdenfors is spearheading an effort that would continue the legacy of Linnaeus by making Sweden the first country to create a complete inventory of all of the multicellular species living within its borders. Known as Svenska Artprojektet, or the Swedish Taxonomy Initiative (STI), the project has just entered its fourth year and, Gärdenfors says, is on track to meet its goal of completing the inventory by 2021.

This is not the first attempt to create an all-taxa biodiversity inventory, as such catalogs are known. But although many biodiversity inventories, including the better-known INBio project in Costa Rica, have struggled to find secure funding (see sidebar), the Swedish project, headquartered at SSIC's woodsy campus just outside of Uppsala, seems to be picking up steam. Last fall, the Swedish government nearly doubled STI's budget to $9.3 million for 2005. If the money keeps coming, supporters say, it will not only fund the inventory but also help revitalize Sweden's natural history museums, train a new generation of taxonomists, and produce a lavishly illustrated set of encyclopedias-cum–field guides written for laypeople.

The project's two audiences, scientific and popular, are equally important, says STI co-founder Fredrik Ronquist, who's now on sabbatical from Uppsala University at Florida State University in Tallahassee. "There's a lot of emphasis in Sweden on the broader impact of scientific research," Ronquist says. "[We recognize] the importance of spreading scientific knowledge to the public and making sure it's used by policymakers."

Rich heritage. In this house 260 years ago, Linnaeus formulated his system for classifying organisms.

No rainforests

It's fair to say that Sweden is not a biodiversity hot spot. Its 450,000 square kilometers contain an estimated 60,000 species. The same number might be found in a few hundred square kilometers of tropical rainforest, says Daniel Janzen, an ecologist at the University of Pennsylvania in Philadelphia and INBio co-founder. Still, Janzen and others applaud the taxonomy effort. All-taxa inventories "are building blocks that can get us closer to understanding biodiversity," says

Taxonomy's Elusive Grail

A complete catalog of life on Earth ranks near the top of biologists' all-time wish list. To date, fewer than 2 million species have been described—perhaps a fifth of the planet's total.

In 2001 an ambitious group of Silicon Valley–types teamed up with several prominent researchers, including Harvard's E. O. Wilson and Peter Raven of the Missouri Botanical Garden in St. Louis, to launch the All Species Foundation, with the goal of cataloging every species on Earth in 25 years (*Science*, 26 October 2001, p. 769). Unfortunately, says Raven, the dream died when the dot-com bubble burst and donations dried up. A recent visit to the All Species Foundation Web site brought up a page simply titled: *Gone*.

Several other efforts are under way to inventory all of the species in a restricted area within some limited time frame—what's known as an all-taxa biodiversity inventory (ATBI). Three major projects are up and running, says Daniel Janzen, an ecologist at the University of Pennsylvania in Philadelphia.

The most recently launched ATBI, based in Uppsala, Sweden, aims to inventory that country's estimated 60,000 species within 20 years (see main text). Janzen helped set up the first in Costa Rica in 1989. The mandate of Costa Rica's Instituto Nacional de Biodiversidad (INBio), based outside San José, was to inventory all of that country's estimated 500,000 species. Janzen initially hoped to jump-start INBio with a 7-year project to inventory the species-rich Area de Conservación Guanacaste. But those plans fell apart amid political wrangling in 1997 (*Science*, 9 May 1997, p. 893).

The national survey continues today, Janzen says, but efforts are dispersed across the country with no definite time frame for completion. Part of the problem is inconsistent funding. INBio is not supported by the Costa Rican government; instead, it patches together money from a variety of sources, including contributions from foreign governments and ticket sales from its conservation theme park, INBioparque. In 2003, INBio raised $6.1 million.

The first project in the United States, the Great Smoky Mountains National Park All Taxa Biodiversity Inventory, started in 1999 (*Science*, 11 June 1999, p. 1747). It is run jointly by the National Park Service and a nonprofit organization called Discover Life in America. Work on the inventory reaches a fever pitch each summer when scores of scientists and thousands of volunteers converge on the park. Keith Langdon, the National Park Service's coordinator for the project, says it's hard to say how many species have been cataloged because each taxa goes into a separate database, but others say it's in the neighborhood of 12,000 to 15,000 of the 100,000 species estimated to live there. And the project may spark imitations: Langdon says several other parks and conservation areas in the United States have approached him for advice on setting up their own inventories.

But they may face an uphill battle for funding. The Great Smokies project has relied almost entirely on donations, which have totaled about $150,000 per year. This year, however, Langdon is optimistic that the project will get some money—perhaps as much as $200,000—from Congress. In the meantime, he says, "we're doing the best we can with the limited funding we have."

–G.M.

CREDIT: G. MILLER

Peter Raven, director of the Missouri Botanical Garden in St. Louis. "Whatever someone has the resources and funding to do is great."

A complete inventory of all the flora and fauna in any particular area would be a huge boon for ecologists, says Ronquist. Without the full cast of characters, it's impossible to determine how all the players in an ecosystem work together, he says.

Such inventories are also key for conservation and management. In Sweden, Ronquist says, only about 20,000 species have been considered for inclusion in the red lists: "There is a large number of species for which there's not enough information to even say whether they're threatened or not."

Even so, most of Sweden's flora and fauna have already been discovered, which gives STI a big head start. In 2003, SSIC published a list of 50,741 known species. But about two-thirds of these are described in obsolete scientific literature, using outdated criteria, says Gärdenfors.

Revising the descriptions to bring them up to date with modern naming conventions and species delimitations is a large part of STI's task and will ultimately occupy about 100 taxonomists. Another 40 or so researchers are working on filling in the gaps. Sweden has never had a good inventory of its marine species, Gärdenfors notes: "We had one in the 1920s, but it wasn't systematically done." Last summer, STI led a team of scientists and divers on a pilot survey of 80 locations off Sweden's west coast, and they are gearing up for a larger and more systematic survey of the west coast in 2006.

To survey terrestrial organisms, STI scientists are enlisting the help of Sweden's amateur naturalists. Many Swedes, especially among the older generations, pride themselves on being able to identify all of the plants and animals near their homes, says SSIC director Torleif Ingelög, and more than 1000 amateur naturalists contribute data used to compile the Swedish red lists.

The largest survey at the moment is of two relatively understudied groups: *Diptera* (flies) and *Hymenoptera* (ants, bees, and wasps). Amateur naturalists monitor a network of insect traps located at select points throughout the country, periodically emptying the trapped insects into an alcohol solution and mailing them off to a natural history museum, where professional taxonomists identify and catalog them. The estimated 100 million insect specimens collected in 2003 and 2004 may contain hundreds of species previously unknown to science, Gärdenfors says. He adds that 20 new species already have been identified in a single fly genus, *Megalesia*. As the major gaps in the inventory are filled in, additional surveys will be planned to address the remaining holes.

But even in the country that gave birth to taxonomy, there aren't always enough taxonomists to go around. A major goal of STI is to bolster this taxonomic infrastructure. STI's current funding supports four or five new taxonomy Ph.D. students each year, a rate that would more than double the number of Ph.D.s in the field in Sweden over the project's 20-year lifetime. And nearly $3 million a year will go to refurbishing another neglected but important part of Sweden's taxonomy infrastructure, its natural history museums, some of which house important collections that date back to Linnaeus's time.

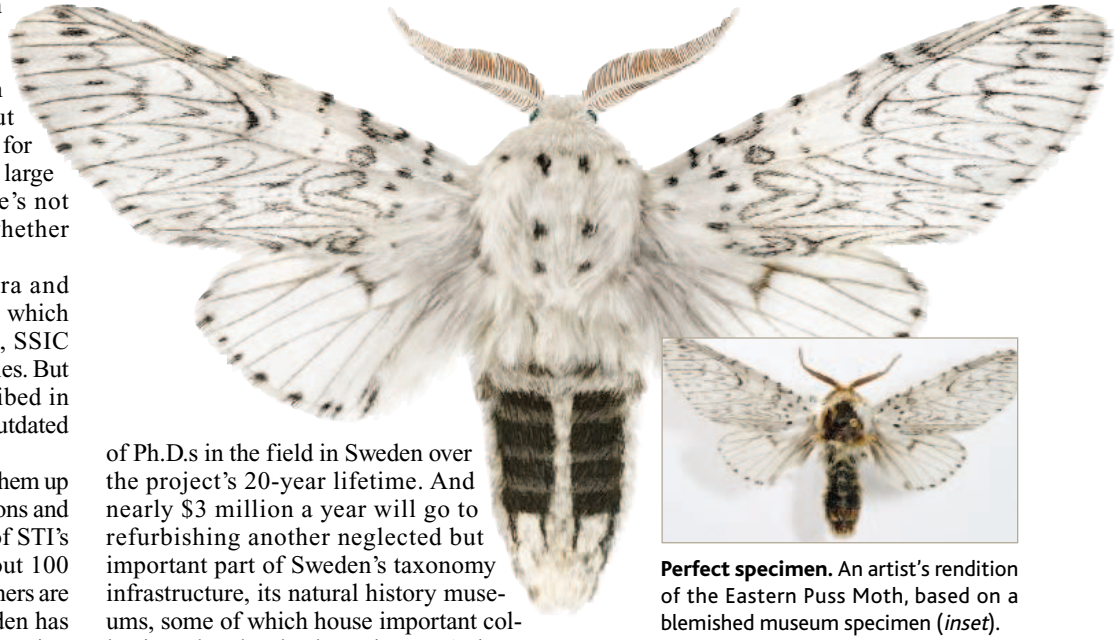

Perfect specimen. An artist's rendition of the Eastern Puss Moth, based on a blemished museum specimen (*inset*).

Pretty as a picture

While the scientists are busy collecting and cataloging, a team of illustrators is working hard to make the species look their best. Torbjörn Östman is one of nine Swedish artists STI has commissioned to work on the encyclopedias. In a 100-year-old schoolhouse near Lake Malvern that he's converted into his home and studio, Östman shows off a piece of recent work, a fantastically detailed rendering of the Eastern Puss Moth, *Cerura erminea*.

Back to nature. Ulf Gärdenfors oversees hundreds of scientists and amateur naturalists working on the all-taxa inventory.

To illustrate the moth, Östman worked from two museum specimens, both of which were in bad shape. Using a digital camera attached to a microscope, he captured a set of images of each specimen at different focal planes. He then merged those images and doctored the composite on a computer to create an archetypical example of the hairy black-and-white moth.

The illustrators working on the encyclopedias use a variety of techniques, but the images all end up looking more or less like watercolor paintings. That's partly because watercolor is a traditional medium for natural history illustrations, Gärdenfors says, and partly because it allows the artists to include all of the key markings and other characteristics for identification—a convergence that's rare in real-life specimens.

The first volume of the encyclopedia, on *Lepidoptera*, the order of insects that includes moths and butterflies, is scheduled for release in April, followed later this year by others on myriapods (centipedes and millipedes) and bryophytes (mosses and their relatives). In all, 120 volumes are planned and will include the roughly 30,000 species that can be identified easily by nonspecialists. The books will also contain distribution maps and identification keys.

Christer Engström, editor in chief of the series, envisions families passing the encyclopedias down through the generations, keeping the Swedish naturalist tradition alive. Indeed, there are signs that the naturalist spirit isn't lost on the younger generation. Sweden's popular Princess Victoria, 27, has given the project her blessing. Visiting the STI team last year, Victoria confided that biology was her favorite subject in school. "It's the best patronage we could have," says Engström. **–GREG MILLER**

CREDIT (TOP ILLUSTRATION AND PHOTO): TORBJÖR ÖSTMAN; (BOTTOM): G. MILLER

Random Samples

Edited by Constance Holden

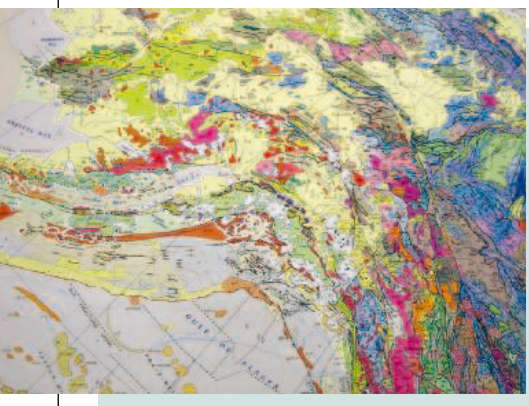

North America's Anatomy

Twenty-five years in the making, a new geologic map of North America was unveiled this month by the Geological Society of America. The map replaces a 1965 version that predated the widespread acceptance of plate tectonics. "It shows the grand architecture of the continent," says John Reed of the U.S. Geological Survey in Denver, Colorado, who helped compile it.

The map covers 15% of Earth's surface and incorporates a vast amount of information from radiometric dating, geologic mapping, ocean cores, and geophysical surveys. It includes more than 900 kinds of rock formations—seven times as many as its predecessor—and many other features such as faults, volcanoes, and impact craters. Some of the biggest scientific advances reflected in the new map concern the Canadian Shield, a vast expanse of ancient rock that underlies most of the continent. The map shows how the shield was assembled from many colliding continents. Alaska (above) has a similar history.

Sumatran Quake Supersized

Seismologists tracing Earth's shivers in the hours after the great tsunami of 26 December (*Science*, 14 January, p. 201) have found that they had overlooked fully two-thirds of the energy released.

By studying bell-like vibrations with periods up to almost an hour long, Seth Stein and Emile Okal of Northwestern University in Evanston, Illinois, discovered that the northern two-thirds of the 1600-kilometer-long fault that runs along the eastern side of the Indian Ocean and the Bay of Bengal must have ruptured slowly. That part of the rupture would have escaped detection when shorter-period waves were used to calculate a conventional magnitude of 9.0. Now the quake looks to have been three times as large, or magnitude 9.3.

The northward extension of the rupture—which meant a powerful tsunami would be directed at Sri Lanka—helps explain the extreme destruction, according to the researchers. The underestimate argues even more strongly for a tsunami-detecting network, scientists say.

Indeed, as far away as Washington state, where another offshore subduction zone spells vulnerability to underwater earthquakes, officials are plotting tsunami evacuation routes. Coastal cores show that tsunamis occur there every 500 years or so, the latest one having been 300 years ago.

Preserving New Zealand's Bats

Conservationists in New Zealand are hoping to engineer what they say will be the world's first successful transfer of bats to a new home. Bats are the country's only native land mammals. In the absence of other mammals, one species in particular, the lesser short-tailed bat, has evolved the habit of crawling around on the forest floor in search of food. This has made the species extremely vulnerable to introduced predators such as stoats, cats, and rats.

Hanging bat

Now 20 juvenile bats from a unique population of fewer than 300 living precariously in a North Island forest are this month being taken to Kapiti Island, 5 kilometers off the west coast. Over decades, officials have used shooting, trapping, and poisoning to rid the 2000-hectare sanctuary of introduced mammals from goats to rats. The island is already home to five transplanted endangered bird species.

The bats resisted a past attempt at transfer. They have a strong homing instinct and can fly long distances, says Brian Lloyd, a conservation biologist with the Department of Conservation in Wellington. To circumvent this problem, officials are transferring newly fledged bats born in captivity in the hope that they will be persuaded to imprint on roost boxes awaiting them on Kapiti. If the transfer is successful, Lloyd says more young bats will be brought to the island over the next 4 to 5 years.

Signals From Rubble

Latching onto a cell phone signal from someone trapped in the debris of a building that has just been bombed is no easy task. So engineers are wiring up buildings slated for demolition to track just how radio waves move through rubble.

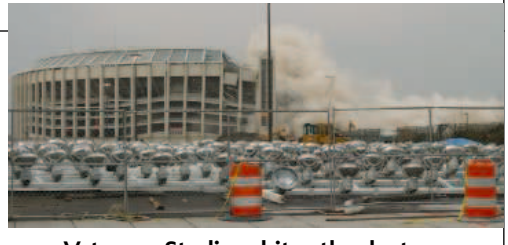

Veterans Stadium bites the dust.

Last year electrical engineers Chris Holloway and Kate Remley, who work at the National Institute of Standards and Technology in Boulder, Colorado, set up radio transmitters in Veterans Stadium in Philadelphia, Pennsylvania, just before it was demolished. Then in December, they did the same with Washington, D.C.'s old Convention Center before it was imploded. Early findings suggest that metal debris can boost a signal buried by a pile of wreckage. And with the help of noise-filtering techniques similar to those developed for deep-space communication, it was possible to pick up a simple preprogrammed Morse code message issuing from a transmitter in the rubble of the Convention Center, says Remley.

The work could improve urban radio networks designed for use after a terrorist attack and offer new strategies for finding faint radio or cell phone signals during an emergency, Remley adds. The next stage of the work is to study how modified hand-held radios could act as beacons after a collapse, perhaps by being designed to switch to a slow signal on a narrow wavelength.

CREDITS (CLOCKWISE FROM TOP): PHOTO COURTESY OF THE GEOLOGICAL SOCIETY OF AMERICA; CHRIS HOLLOWAY/NIST; BRIAN LLOYD

Edited by Yudhijit Bhattacharjee

JOBS

IRRI head. The International Rice Research Institute (IRRI) in Los Baños, the Philippines, has tapped one of its alumni to serve as its next director general. Robert Zeigler, an American plant pathologist who led research programs at the institute from 1992 to 1998, succeeds Ronald Cantrell, who retired in December.

The 54-year-old Zeigler earned his Ph.D. from Cornell University and has spent most of his career working on the challenges of developing-country agriculture. In addition to his stint at IRRI, he has worked at the International Center for Tropical Agriculture in Colombia, the Institut des Sciences Agronomique du Burundi in Burundi, and the International Maize and Wheat Improvement Center (CIMMYT) in Mexico.

Zeigler takes over the 45-year-old institute at a time when its donors—governments, agencies, and foundations—have been cutting support. "Maybe I'm a hopeless optimist, but I believe that if we demonstrate we can effectively apply science to real-world needs, we can reinvigorate donor interest in our activities," he says.

THEY SAID IT

"On average, students in grade 6 in this country spend less than 16 minutes per day on science. ... I'm glad that my grandsons have a scientist as a grandmother, because I can supplement that easily."

—Biologist and University of California Provost M. R. C. Greenwood, speaking last week in Washington, D.C., on the need to improve K–12 science education.

Got any tips for this page? E-mail people@aaas.org

DATA POINT

Faster entry. A year after receiving a congressional rap on the knuckles, the U.S. State Department says it has significantly reduced processing time for granting visas to students working on sensitive technologies. The extensive security check, called Visas Mantis, now takes less than 2 weeks, on average—a sharp drop from 67 days in mid-2003 (*Science*, 5 March 2004, p. 1453).

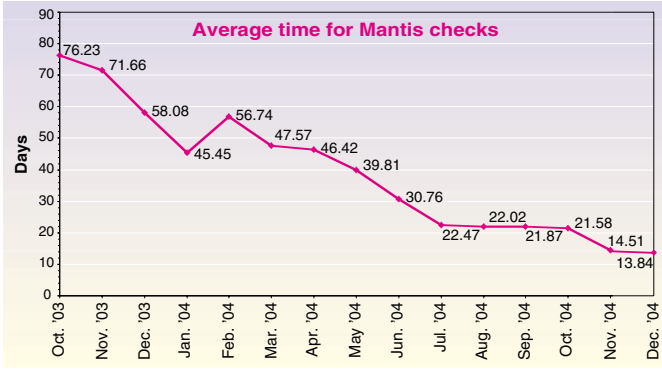

AWARDS

Arsenic challenge. The National Academy of Engineering (NAE) is offering a $1 million award to researchers who develop practical, inexpensive technologies for safe drinking water in arsenic-contaminated areas. The Grainger Challenge Prize for Sustainability, funded by the Grainger Foundation, will honor a household or community-scale water treatment system that removes arsenic from groundwater in Bangladesh, India, Nepal, and other developing countries. The winner(s) will be announced in February 2007. Details are at www.graingerchallenge.org. A list of 74 new members and 10 foreign associates, elected by the academy last week, is at www.nau.edu.

Chemistry prize. Stanford University's Richard Zare has won the $100,000 Wolf Prize in Chemistry. Zare, a chemical physicist, receives the award for applying laser techniques to the study of chemical reactions at the molecular level.

PIONEERS

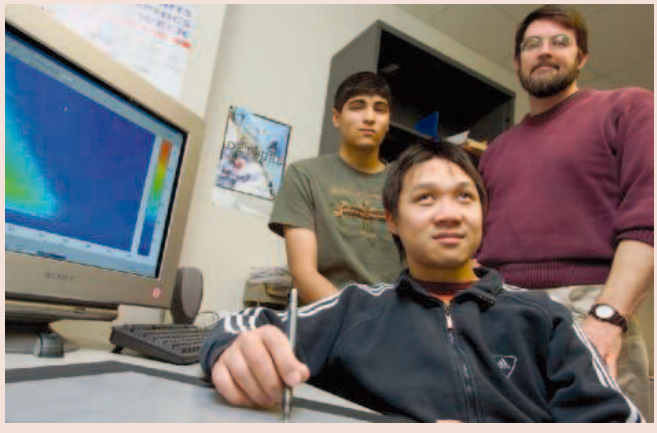

Mind's eye. Blind since the age of 7, Victor Wong faces a unique challenge as a graduate student at Cornell University: reading color-scaled maps for his research on space weather. Braille cannot address the problem, so he has developed a computer program to translate different colors on a map into distinct piano notes.

When Wong moves a stylus across the screen, the software speaks out the coordinates and generates notes for color codes representing parameters such as electron density. The sounds help provide a sense of what the data look like "when viewed visually," he says.

Wong, who developed the tool in collaboration with fellow student Ankur Moitra (far left) and research associate James Ferwerda, says the next step is telling the user when the stylus has crossed over from land to sea.

CREDITS (TOP TO BOTTOM): C. ZEIGLER; FRANK DIMEO/CORNELL UNIVERSITY

MERCK • AAAS

Undergraduate Science Research PROGRAM




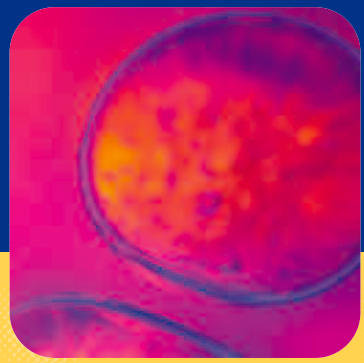

Congratulations to the Merck/AAAS USRP 2005 Award Winners

The Merck/AAAS Undergraduate Science Research Program (USRP) is a national competitive awards program available in all 50 states, the District of Columbia, and Puerto Rico.

Through 2009, up to 15 new awards will be made annually. Each award provides $60,000 ($20,000 per year over three years) for joint use by the biology and chemistry departments at each recipient institution.

The purpose is to promote interdisciplinary RESEARCH EXPERIENCE for undergraduate students in CHEMISTRY and BIOLOGY.

1. Bowdoin College
2. Fairleigh Dickinson University
3. Furman University
4. Harvey Mudd College
5. Hope College
6. McNeese State University
7. North Central College
8. Northern Kentucky University
9. Oakland University
10. Otterbein College
11. Seattle University
12. St. Olaf College
13. University of the Sciences in Philadelphia
14. Ursinus College
15. Vassar College

MERCK

AAAS
ADVANCING SCIENCE, SERVING SOCIETY

Send questions and requests for additional information to: **Merck@AAAS.org**
For full program details: **www.merckaaasusrp.org**

LETTERS

Letters to the Editor

Letters (~300 words) discuss material published in *Science* in the previous 6 months or issues of general interest. They can be submitted through the Web (www.submit2science.org) or by regular mail (1200 New York Ave., NW, Washington, DC 20005, USA). Letters are not acknowledged upon receipt, nor are authors generally consulted before publication. Whether published in full or in part, letters are subject to editing for clarity and space.

Gender Differences and Performance in Science

ON 14 JAN., HARVARD UNIVERSITY PRESIDENT Lawrence Summers, speaking at a meeting of the National Bureau of Economic Research, suggested that since fewer girls than boys have top scores on science and math tests in high school, genetic, rather than social, differences may explain why so few women are successful in these fields ("Summers's comments draw attention to gender, racial gaps," News of the Week, A. Lawler, 28 Jan., p. 492). Well-accepted, pathbreaking research on learning [for example, (*1*, *2*)] shows that expectations heavily influence performance, particularly on tests. If society, institutions, teachers, and leaders like President Summers expect (overtly or subconsciously) that girls and women will not perform as well as boys and men, there is a good chance many will indeed not perform as well. At the same time, there is little evidence that those scoring at the very top of the range in standardized tests are likely to have more successful careers in the sciences. Too many other factors are involved. Finally, well-documented evidence demonstrates that women's efforts and achievements are not valued, recognized, and rewarded to the same extent as those of their male counterparts (*3*).

> "[W]e are concerned by the suggestion that the status quo for women in science and engineering may be natural, inevitable, and unrelated to social factors."
>
> –*MULLER* ET AL.

As leaders in science, engineering, and education, we are concerned by the suggestion that the status quo for women in science and engineering may be natural, inevitable, and unrelated to social factors. Counterexamples to this suggestion are drawn from the fields of law and medicine. In 1970, women represented just 5% of law school students and 8% of medical school students (*4*). These low percentages have increased substantially in response to social changes and concerted institutional and individual effort and are now about 50% in each case. Obviously, the low rates of participation in 1970 were indicative of social, and not genetic, barriers to success.

We must continue to address the multitude of small and subtle ways in which people of all kinds are discouraged from pursuing interest in scientific and technical fields. Society benefits most when we take full advantage of the scientific and technical talent among us. It is time to create a broader awareness of those proven and effective means, including institutional policies and practices, that enable women and other underrepresented groups to step beyond the historical barriers in science and engineering.

CAROL B. MULLER, SALLY M. RIDE, JANIE FOUKE, TELLE WHITNEY, DENICE D. DENTON, NANCY CANTOR, DONNA J. NELSON, JIM PLUMMER, ILENE BUSCH-VISHNIAC, CAROLYN MEYERS, SUE V. ROSSER, LONDA SCHIEBINGER, ERIC ROBERTS, DAVID BURGESS, CRAIG BEESON, SUSAN STAFFIN METZ, LUCINDA SANDERS, BEVLEE A. WATFORD, ELIZABETH S. IVEY, MARY FRANK FOX, SHELDON WETTACK, MARIA KLAWE, WILLIAM A. WULF, JOAN GIRGUS, PHOEBE S. LEBOY, ELEANOR L. BABCO, BETTY SHANAHAN, CATHERINE DIDION, DARYL E. CHUBIN, MONIQUE FRIZE, SUSAN L. GANTER, E. ANN NALLEY, JUDY FRANZ, HÉCTOR D. ABRUÑA, MYRA H. STROBER, JANE ZIMMER DANIELS, EMILY A. CARTER, JEAN H. RHODES, IRIS SCHRIJVER, VIRGINIA A. ZAKIAN, BARBARA SIMONS, URSULA MARTIN, JO BOALER, KATHERINE ROSE JOLLUCK, PURNIMA MANKEKAR, ROBERT M. GRAY, MARGARET W. CONKEY, PETER STANSKY, AIHUA XIE, PINO MARTIN, LINDA P. B. KATEHI, JO ANNE MILLER, AMELIA TESS THORNTON, ANDREA LAPAUGH, DEBORAH L. RHODE, BARBARA C. GELPI, MARY JEAN HARROLD, CHERRILL M. SPENCER, CARLA SCHLATTER ELLIS, SUSAN LORD, HELEN QUINN, MARGARET MURNANE, PATRICIA P. JONES, FRANCES HELLMAN, GAIL WIGHT, RUTH O'HARA, MARY PICKERING, SHERI SHEPPARD, DAVID LEITH, ADINA PAYTAN, MATTHEW H. SOMMER, AUDREY SHAFER, DAVID GRUSKY, SHERRY YENNELLO, ASHIMA MADAN, DENISE L. JOHNSON, SYLVIA YANAGISAKO, JENNIFER M. CHOU-GREEN, SANDRA ROBINSON

Authors' affiliations are available in the Supporting Online Material at www.sciencemag.org/cgi/content/full/307/5712/1043b/DC1.

References

1. J. Bransford *et al.*, *How People Learn: Brain, Mind, Experience, and School: Expanded Edition* (National Academies Press, Washington, DC, ed. 1, 2000).
2. C. M. Steele, *Atlantic Monthly* **284** (no. 2), 44 (Aug. 1999).
3. V. Valian, *Why So Slow? The Advancement of Women* (MIT Press, Cambridge, MA, 1999).
4. Trends in Educational Equity of Girls and Women: 2004 (National Center for Education Statistics, Washington, DC, 2004) (available at http://nces.ed.gov/pubsearch/pubsinfo.asp?pubid=2005016).

Amazonian Deforestation Models

DEFORESTATION PREDICTIONS FOR AMAZONIA presented by W. F. Laurance *et al.* in 2001 (*1*) are based on the assumption that the road infrastructure is the prime factor driving deforestation. Much has already been said by the scientific community about their model—its apocalyptical results are based on simple extrapolation of past patterns, disregarding the region's enormous biophysical and socioeconomic heterogeneity (*2*, *3*)—but recently the authors reinforced their arguable results ("Deforestation in Amazonia," Letters, 21 May 2004, p. 1109), blaming planned infrastructure and the land speculation it provokes for the current high deforestation rates in the Amazon, which we consider an oversimplified view of current deforestation causes (*4*).

Deforestation rates have increased significantly in the last two years (*5*), but in spite of the ambitious infrastructure plans announced in the mid-1990s, very few federal investments on roads have been made since the 1980s. Therefore, this overall rate increase cannot be explained by those plans even if land speculation is one of the factors in areas such as BR-163. For instance, the municipality that has had the highest deforestation rates in recent years, São Felix do Xingu, Pará, is not even served by a paved road. São Felix is an entrée to the area between the Xingu and Iriri rivers, a recent deforestation hot spot, where cattle farmers and local municipal governments build unpaved roads themselves (*4*). The Laurence *et al.* model fails to capture this type of new frontier (see figure in Supporting Online Material) (*6*, *7*).

Although we do not dispute the fact that in the past most of the deforestation has happened along the major highways (*8*), there is an urgent need to understand the genesis of the new Amazon frontiers, and the hypothesis that they are more localized and much less dependent on federal government infrastructure investments than in the 1970s and 1980s (*9*). Even in the 1970s and 1980s, the effect of roads was not homogeneous across the region (*10*), depending on proximity to national markets in the south, climatic restrictions, official settlements sites, agrarian structure differences, and technology access.

Simplistic models such as that of Laurance *et al.* (*1*) may divert attention from real deforestation causes, being

potentially misleading in terms of deforestation control, even if, as proposed in (*2*), Brazilian infrastructure plans are completely undermined.

GILBERTO CÂMARA,[1]*† ANA PAULA DUTRA AGUIAR,[1]* MARIA ISABEL ESCADA,[1]* SILVANA AMARAL,[1]* TIAGO CARNEIRO,[1]* ANTÔNIO MIGUEL VIEIRA MONTEIRO,[1]* ROBERTO ARAÚJO,[2]* IMA VIEIRA,[2]* BERTHA BECKER[3]*

[1]Instituto Nacional de Pesquisas Espaciais (INPE), Avenida dos Astronautas 1758, São José dos Campos, SP, Brazil. [2]Museu Paraense Emílio Goeldi (MPEG), Avenida Magalhães Barata 376, Belém, PA, Brazil. [3]Universidade Federal do Rio de Janeiro (UFRJ), Cidade Universitária, Rio de Janeiro, RJ, Brazil.

*GEOMA Network, Ministry for Science and Technology

†To whom correspondence should be addressed. E-mail: gilberto@dpi.inpe.br

References

1. W. F. Laurance *et al.*, *Science* **291**, 438 (2001).
2. B. Becker, "Revisão das Políticas de Ocupação da Amazônia: é possível identificar modelos para projetar cenários?," *Parcerias Estratégicas*, Número 12, Setembro, pp. 135–159 (2001).
3. G. Câmara, "O Geoprocessamento e o Futuro da Amazônia," *InfoGeo*, Jan./Feb. 2001, p. 17.
4. S. Margullis, *Causas do Desmatamento na Amazônia Brasileira* (Banco Mundial, Brasília, ed. 1, Julho 2003).
5. INPE, The Amazon Deforestation Database, available at www.obt.inpe.br/prodes (INPE, São Jose dos Campos, 2004).
6. See Supporting Online Material on *Science* Online at www.sciencemag.org/cgi/content/full/307/5712/1043c/ DC1.
7. Figure and other supporting information also available at www.dpi.inpe.br/gilberto/lucc.html.
8. D. S. Alves, *Int. J. Remote Sens.* **23** (no. 14), 2903 (2002).
9. B. Becker, *Geopolítica na Virada do III Milênio - Amazônia* (Ed. Garamond, Brasilia, Brazil, 2004).
10. D. S. Alves, "O Processo de desmatamento na Amazônia," *Parcerias Estratégicas*, Número 12, Setembro, pp. 259–275 (2001).

Response

CÂMARA *ET AL.* CHALLENGE OUR assertion that the unprecedented, planned expansion of highways and other transportation projects in Amazonia that was originally proposed under the "Avança Brasil" (Advance Brazil) program is likely to lead to a dramatic increase in forest loss and degradation, and they argue that our earlier spatial models (*1*) were overly simplistic and "apocalyptic" in their projections. Three points about our models merit emphasis.

First, the projections of our models—that 28 to 42% of Brazilian Amazonia would be deforested by 2020 if all the Avança Brasil projects proceed immediately—are in fact very plausible and do not differ greatly from simple extrapolations using the current high rate of forest loss (*2*). Second, our models incorporated key components of regional heterogeneity in Amazonia, including spatial variability in forest vulnerability to fire, logging, and mining. Third, independently derived scenarios of future forest loss (*3*, *4*), including a recent model that incorporates much of the region's biophysical and economic heterogeneity (*5*), also indicate that new and planned highways are likely to play a central role in determining future patterns of Amazon deforestation.

If a new highway penetrates into a large forest tract and promotes spontaneous colonization by farmers, loggers, and ranchers, is the forest loss caused by the highway or the other drivers? Clearly, it is both—but the crucial point is that such transportation projects play a pivotal role in determining where forest destruction occurs. The truly alarming aspect of the Avança Brasil program is that it will crisscross the Amazon with some 7500 km of paved highways and many other transportation projects that will penetrate deep into the heart of the basin. The net effect will be not only increased deforestation, but also fragmentation of forests on an unprecedented spatial scale (*1*). Rather than concentrating development in the vast expanses of land that have already been deforested, the projects that promote frontier expansion will do precisely the opposite.

Contrary to the claim by Câmara *et al.*, the dramatic upsurge in Amazonian deforestation in 2002–03 includes many areas associated with highways and roads, including the notorious Santarém-Cuiabá Highway. Even the deforestation hot spot (São Félix do Xingu) emphasized by Câmara *et al.* is closely associated with privately financed roads (*6*). The point of our recent Letter is that Brazilian-government efforts to slow rampant Amazon deforestation are unlikely to succeed if the government proceeds with its most environmentally damaging transportation projects. We stand by this assessment.

The charred remains of logging slash in the Brazilian rainforest.

WILLIAM F. LAURANCE,[1]* PHILIP M. FEARNSIDE,[2] ANA K. M. ALBERNAZ,[3] HERALDO L. VASCONCELOS,[4] LEANDRO V. FERREIRA[3]

[1]Smithsonian Tropical Research Institute, Apartado 2072, Balboa, Panama. [2]Departamento de Ecologia, Instituto Nacional de Pesquisas da Amazônia, C.P. 478, Manaus, AM 69011-970, Brazil. [3]Museu Paraense Emílio Goeldi, Avenida Perimetral 190, Belém, PA 66077-530, Brazil. [4]Instituto de Biologia, Universidade Federal de Uberlândia, C.P. 593, Uberlândia, MG 38400-902, Brazil.

*To whom correspondence should be addressed. E-mail: laurancew@tivoli.si.edu

References and Notes

1. W. F. Laurance *et al.*, *Science* **291**, 438 (2001).
2. If the deforestation rate in 2002–03 (2.35 million ha year^{-1}) continues indefinitely, then 100 million hectares of forest will have disappeared by the year 2020. This is about 25% of the original forests in Brazilian Amazonia.
3. G. Carvalho, A. C. Barros, P. Moutinho, D. C. Nepstad, *Nature* **409**, 131 (2001).
4. B. Soares-Filho *et al.*, *Global Change Biol.* **10**, 745 (2004).
5. B. Soares-Filho *et al.*, "A spatially explicit simulation model of deforestation for the Amazon Basin" (3rd Scientific Conference of the LBA Program, Brasília, Brazil, 2004).
6. A. Alencar *et al.*, *Desmatamento na Amazônia: Indo Além da Emergência Crônica* (Instituto de Pesquisa Ambiental da Amazônia, Belém, Brazil, 2004).

A Delicate Balance in Amazonia

IN THEIR LETTER "DEFORESTATION IN AMAZONIA" (21 May 2004, p. 1109), W. F. Laurance *et al.* cogently summarize the threats that roads and other infrastructure development projects pose to Amazonian forests. However, their implicit suggestion that the best way to prevent forest loss is by halting these projects ignores important political and social constraints faced by the region (*1*), as well as evidence that land-use patterns can change when viable alternatives to deforestation are presented (*2*). There is no doubt that roads and other infrastructure projects are conduits for agents of forest loss. However, they also provide important benefits, such as access to markets without which community-based timber management, the extraction of non-timber forest products, and other strategies for slowing deforestation advocated by the conservation community would not be economically viable.

Laurance *et al.* argue that the Brazilian government should "curtail" their expansion, and we agree that without their doing so, the region's forest will certainly be degraded. However, we also believe that progress on the issue of balancing Amazonian infrastructure needs and environmental conservation will not be made by

CREDIT: STEPHANIE MAZE/CORBIS

advocating a sweeping rejection of further development, which is at best unrealistic and at worst counterproductive. Instead, the question must be rephrased as, "Given our goal of minimizing deforestation, what projects are necessary and will be most beneficial?"

EMILIO M. BRUNA* AND KAREN A. KAINER
Tropical Conservation and Development Program, The Center for Latin American Studies, University of Florida, Gainesville, FL 32611–5530, USA.
*To whom correspondence should be addressed.
E-mail: brunae@wec.ufl.edu

References
1. M. Schmink, C. H. Wood, *Contested Frontiers in Amazonia* (Columbia Univ. Press, New York, 1992).
2. D. Nepstad *et al.*, *Science* **295**, 629 (2002).

Response

BRUNA AND KAINER IMPLY THAT BRAZIL'S Amazonian road building could help to promote "community-based timber management, the extraction of nontimber forest products, and other strategies advocated for slowing deforestation." Our collective experience in Amazonia over the past quarter century suggests otherwise. Although their optimistic view may apply in a few, rather rare situations, it seems entirely foreign to the major hotbeds of deforestation.

For example, when completed, the Cuiabá-Santarém Highway (BR-163), one of the top priorities of the Brazilian federal government, is likely to create an 800-km-long swath of forest degradation across southern Amazonia. The highway will transport soybeans from Mato Grosso to the Amazon port of Santarém, almost entirely for the benefit of large corporations and landholders (*1*). The planned route is already swarming with land speculators, cut-and-run loggers, cattle ranchers, and soybean investors—hardly the cast of characters likely to promote a "community-based" utopia focused on maintaining forest for nontimber products. BR-163 typifies the ecological impacts that often accompany major new highways in the Amazonian frontier (*2–4*).

Moreover, we do not advocate a "sweeping rejection" of proposed transportation and infrastructure projects in Brazilian Amazonia. We do, however, believe that a limited subset of the proposed projects—particularly those that would create major corridors between densely populated areas and the remote Amazonian frontier—will be so damaging environmentally that their potential societal and economic benefits are clearly outweighed (*1–5*).

The notion that society has "needs" for new infrastructure, whereas it merely has concerns for the environment and its services, is a false dichotomy that implicitly will always lead to choices in favor of infrastructure. The implied conclusion that planned projects should never be rejected or delayed, but only "balanced" with environmental add-ons, would clearly imperil Amazonian forests (*5*). Current efforts to reduce rampant forest loss are likely to fail, we believe, unless the Brazilian government addresses one of the most fundamental causes of forest destruction: the dramatic proliferation of new transportation projects throughout the heart of the Amazon basin.

PHILIP M. FEARNSIDE,[1]* WILLIAM F. LAURANCE,[2] ANA K. M. ALBERNAZ,[3] HERALDO L. VASCONCELOS,[4] LEANDRO V. FERREIRA[3]
[1]Departmento de Ecologia, Instituto Nacional de Pesquisas da Amazônia, C.P. 478, Manaus, AM 69011-970, Brazil. [2]Smithsonian Tropical Research Institute, Apartado 2072, Balboa, Panama. [3]Museu Paraense Emílio Goeldi, Avenida Perimetral 190, Belém, PA 66077-530, Brazil. [4]Instituto de Biologia, Universidade Federal de Uberlândia, C.P. 593, Uberlândia, MG 38400-902, Brazil.
*To whom correspondence should be addressed.
E-mail: pmfearn@inpa.gov.br

References
1. P. M. Fearnside, *Environ. Conserv.* **28**, 23 (2001).
2. W. F. Laurance *et al.*, *Science* **291**, 438 (2001).
3. P. M. Fearnside, *Environ. Manage.* **30**, 735 (2002).
4. W. F. Laurance *et al.*, *J. Biogeogr.* **29**, 737 (2002).
5. W. F. Laurance, P. M. Fearnside, *Science* **295**, 1643 (2002).

Underlying Causes of Deforestation

IN THEIR LETTER "DEFORESTATION IN Amazonia" (21 May 2004, p. 1109), W. F. Laurance *et al.* present an outdated argument for some of the causes of deforestation in Amazonia. Although the expansion of highway infrastructure can explain part of the deforestation in the 1970s and 1980s, it does not explain deforestation in the 1990s, when this expansion basically came to an end, but the rates of deforestation remained high.

The current expansion in infrastructure is probably a consequence (rather than a cause) of the agricultural and agroindustrial expansions toward northern Brazil (*1*). Blaming the Brazilian government's plans to dramatically expand highways and other major infrastructure projects in the region hides the real causes behind the problem. The underlying forces behind deforestation in the region are complex and involve an interaction of cultural, demographic, economic, technological, political, and institutional issues (*2*–*4*).

The active and passive participation of the Brazilian government in deforestation occurs in many different ways: government investments and financing granted to the private sector for gross fixed capital formation, boosting production capacity over the long term; underwriting investments in areas that have been recently cleared for farming and ranching purposes; the lack of a firm policy for transferring unused government lands with lapsed titles to the private domain (along with complacency or even connivance in the takeover of vast tracts of these unused government lands with lapsed titles through claim jumping and counterfeit land titles); acceptance of large tracts of land lying fallow and property speculation; large-scale expropriations of land for agrarian reform; and the ineffectiveness of the Rural Land Tax (ITR) as a mechanism for regulating the land market.

For products involving high technology that have become competitive in international markets, such as soybeans, with significant expansion spurred by international demands, the easy availability of land makes Amazonia a natural setting for this expansion. For low-technology activities, such as open-range grazing, rising domestic beef demands are met largely through extending pasturelands rather than higher productivity, with severe direct consequences on deforestation. In brief, the underlying government policies (economic and environmental), as well as institutional (fragility), agritechnological and socioeconomic factors (i.e., population, income, food demands) interact among themselves and function together, driving deforestation in Amazonia (*5*).

ROBERTO SCHAEFFER AND RICARDO LEONARDO VIANNA RODRIGUES

Energy Planning Program, COPPE, Centro de Tecnologia, Bloco C, Sala C-211, Federal University of Rio de Janeiro, Cidade Universitaria, Ilha do Fundao, Rio de Janeiro 21941-972, Brazil.

References

1. S. Margullis, *Causas do Desmatamento da Amazonia Brasileira* (World Bank, Washington, DC, 2003).
2. H. J. Geist, E. F. Lambim, *BioScience* **52**, 143 (2002).
3. A. Angelsen, D. Kaimowitz, *World Bank Research Observer* **14** (no. 1), 73 (1999).
4. R. L. V. Rodrigues, Ph.D. dissertation, Federal University of Rio de Janeiro, Brazil (2004).
5. R. L. V. Rodrigues, R. Schaeffer, in preparation.

Response

Schaeffer and Rodrigues list a plethora of socioeconomic and societal factors that likely influence Amazonian deforestation, many of which we have previously assessed in detail (*1*–*9*). Nonetheless, despite the seeming complexity of deforestation driv-

ers, it is dangerous to obscure the central role of new highway and infrastructure expansion in promoting rapid forest loss.

New deforestation drivers in Amazonia (such as soybeans) have not replaced the "old" drivers that were promoting deforestation 25 or more years ago. Rather, they have been added to the list of existing drivers. Evidence indicates that the relationship between road building or paving and burgeoning forest loss along highway routes is as strong today as it was decades ago (*3*, *5*–*7*).

Moreover, Brazilian plans for infrastructure expansion in Amazonia are readily amenable to policy modification (*5*), whereas many of the endemic societal and institutional problems cited by Schaeffer and Rodrigues are less so. Despite weak frontier governance, the Brazilian federal government is pushing ahead with a dramatic expansion of Amazonian highways, roads, and other transportation projects. The net result, we believe, will be further acceleration of already rampant rates of forest loss and degradation.

In addition, Schaeffer and Rodrigues misunderstand the key role of highways and roads in promoting past deforestation, especially during the 1990s. Contrary to their claims, the 1990s did see significant expansion of highways and roads, such as paving of the 800-km-long Manaus-Boa Vista Highway (BR-174) that is promoting dramatic changes in central Amazonia, highway paving in Acre and Mato Grosso, and a proliferation of many secondary roads ramifying out from existing highways. Moreover, highway and road construction not only has an immediate impact on deforestation, as they imply, but also longer and more pervasive effects that persist for many years. Forest loss in the 1990s would certainly have been less severe were it not for the infrastructure created in preceding decades.

Finally, it is vital to emphasize that new highways and roads exacerbate many current development pressures. By continually opening up new frontiers for colonization, such projects promote land speculation, weakening incentives for more sustainable land uses, such as perennial crops and plantations (*3*, *5*, *6*). Abundant, cheap land means that destructive, fire-based agriculture, such as cattle ranching and slash-and-burn farming, will continue to thrive. In Brazilian Amazonia, an area the size of France has already been deforested, a large fraction of which is now degraded cattle pasture with minimal benefit for Brazilian society. A vital step in promoting more sustainable development is to intensify land-uses in these already degraded areas, rather than opening up immense new tracts of primary rainforest for exploitation.

WILLIAM F. LAURANCE,[1]* ANA K. M. ALBERNAZ,[2] PHILIP M. FEARNSIDE,[3] HERALDO L. VASCONCELOS,[4] LEANDRO V. FERREIRA[2]

[1]Smithsonian Tropical Research Institute, Apartado 2072, Balboa, Panama. [2]Museu Paraense Emílio Goeldi, Avenida Perimetral 190, Belém, PA 66077-530, Brazil. [3]Departamento de Ecologia, Instituto Nacional de Pesquisas da Amazônia, C.P. 478, Manaus, AM 69011-970, Brazil. [4]Instituto de Biologia, Universidade Federal de Uberlândia, C.P. 593, Uberlândia, MG 38400-902, Brazil.

*To whom correspondence should be addressed. E-mail: laurancew@tivoli.si.edu

References

1. P. M. Fearnside, in *The Future of Amazonia: Destruction or Sustainable Development?*, G. Goodman, A. Hall, Eds. (MacMillan, London, 1990), pp. 179–225.
2. P. M. Fearnside, *Ambio* **8**, 537 (1993).
3. W. F. Laurance, *Trends Ecol. Evol.* **13**, 411 (1998).
4. L. V. Ferreira *et al.*, *Áreas Protegidas ou Espaços Ameaçados?* (World Wide Fund for Nature, Brasília, Brazil, 1999).
5. W. F. Laurance *et al.*, *Science* **291**, 438 (2001).
6. P. M. Fearnside, *Environ. Conserv.* **28**, 23 (2001).
7. W. F. Laurance, A. K. M. Albernaz, C. Da Costa, *Environ. Conserv.* **28**, 305 (2001).
8. W. F. Laurance *et al.*, *J. Biogeogr.* **29**, 737 (2002).
9. P. M. Fearnside, *Environ. Manage.* **30**, 748 (2002).

FOOD

A Feast of Science for Food Lovers

Joe Schwarcz

"So, what came first, the chicken or the egg?" I recall the moment that question was posed to me some two decades ago as if it were yesterday. I had already been hosting a radio program on chemistry for a couple of years and was used to a variety of unusual queries, but this one stymied me. "I'll get back to you on that," I muttered, hoping that I would be able to come up with some sort of reasonable answer by the following week. Off I scooted to the library, as one was compelled to do in those pre-Google days, and searched the stacks for some publication that might address this classic riddle. And that is how I chanced upon Harold McGee's masterpiece, *On Food and Cooking: The Science and Lore of the Kitchen* (Scribner, New York, 1984). McGee, I learned from the book's dust jacket, had a Ph.D. in English literature of all things, and now "writes about science." As it turned out, that was tantamount to saying "and Tiger Woods plays golf."

The book was a masterful compilation of virtually everything you ever wanted to know about food. There were excellent and easy-to-follow scientific explanations about the chemistry of cooking along with historical anecdotes and discussions of the latest concepts in nutrition. From the first moment I glanced through the thick tome, it became a constant companion at my bedside and in the radio studio. You can then imagine how pleased I was to be asked to review the "completely revised and updated edition" of the book. I had been hoping that McGee would someday get around to producing this because the nutritional landscape of course has changed significantly in the last 20 years. We now have genetically modified foods, prion diseases, fish farming, rising obesity, and antioxidants to deal with, among many other things.

"Completely revised" is certainly an apt description of the new edition. The text has been expanded by nearly a third to reflect both recent developments in the field and, I suspect, McGee's expanded knowledge. For example, the leafy green vegetable purslane now receives mention for its content of linolenic acid, an omega-3 fatty acid that has been linked with a lower risk of heart disease. We even learn that it is nicknamed "pigweed" because the 19th-century Englishman William Cobbett said it was suitable only for pigs and the French. The book is replete with such fascinating factoids. Where else could you learn that our word "dairy" was originally "dey-ery," meaning the room in which the "dey," or woman servant, made milk into butter and cheese? Or that "pumpernickel" derives from a Westphalian expression for "devil's fart"? The salmon family of fish, we discover, is the only one that stores astaxanthin, a carotenoid derived from its crustacean prey, in muscle tissue. That's why farmed salmon without access to wild crustaceans have paler flesh unless their diet is supplemented with commercially produced carotenoids such as canthaxanthin. And isn't it delightful to know that camel's milk is much like cow's milk but the milk of the zebu, an Asian long-horned cow, is 25% richer in butterfat?

On Food and Cooking
The Science and Lore of the Kitchen. Completely Revised and Updated
by Harold McGee
Scribner, New York, 2004. 896 pp. $35, C$49.95. ISBN 0-684-80001-2.

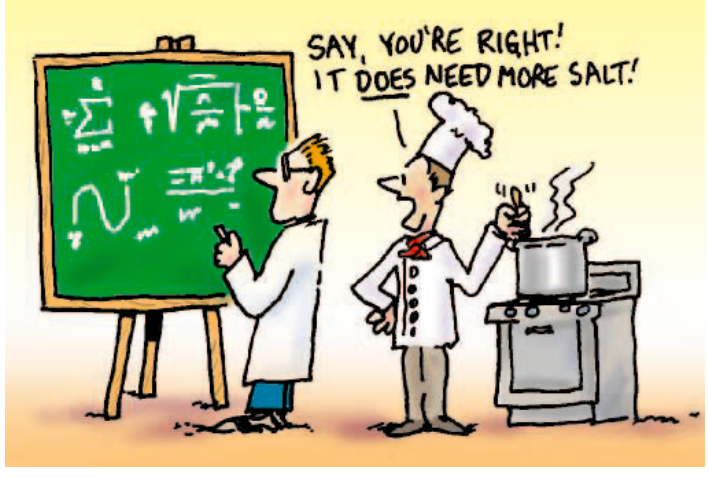

These trinkets, though, just add spice to the serious nature of the book. Speaking of spices, McGee devotes a whole chapter to them. Differences between black and pink peppercorns, artificial and natural vanilla flavorings, green and black teas are demystified. Meats, fish, breads, fruits, vegetables, sweets, sauces, eggs, and dairy products all have been granted their own chapters. We learn that soaking garlic in vinegar or lemon juice for several hours before storing it under oil helps prevent botulism poisoning and that crisp French fries are produced by initial gentle frying followed by boosting the temperature. When a cake is baked in the mountains according to a recipe tested at sea level, it will end up dry, coarse, and flat. Making mayonnaise with extra-virgin olive oil is not a good idea. Egg whites whip better in copper bowls, and green egg yolks can be prevented by rapidly cooling hard-boiled eggs. McGee of course does not just randomly spew out such bits of wisdom, he explains the underlying science with great lucidity. Green discoloration in eggs is caused by the reaction of hydrogen sulfide, formed as proteins break down, with iron in the yolk. Cooling the egg causes the hydrogen sulfide to gravitate toward the shell instead of the yolk.

There is plenty of myth-busting as well. Searing meat does not "seal in juices," but does produce flavorful compounds on the surface. Contrary to popular belief, hormone residues in beef are minute and probably of no significance. And, alas, the cannabinoids and amphetamine-like compounds in chocolate do not have any practical effect. It is the sensory experience of eating chocolate that is so appealing. Chocolate does, however, provide a good dose of antioxidants.

Although much of the information in the original work has been effectively expanded on, some chapters have been sacrificed in order to maintain a reasonable length. It is a pity that food additives, nutrition, and human physiology no longer have chapters devoted to them, although much of the information they contained is now sprinkled throughout the text. McGee tackles some controversial issues, such as food irradiation, the use of antibiotics in animal feed, mad cow disease, and genetically modified foods. Although he does this in a balanced, nonalarmist fashion, it would have been helpful to find a little more detail in his discussions. Genetic engineering is correctly

CREDIT: JOE SUTLIFF

The reviewer is in the Office for Science and Society and the Department of Chemistry, McGill University, 801 Sherbrooke Street West, Montreal, Quebec H3A 2K6, Canada. E-mail: joe.schwarcz@mcgill.ca

labeled as the "most far-reaching development in 20th-century agriculture," but McGee only devotes a page to it. A more elaborate discussion of the significant potential of the technology to improve nutritional status as well as more specific allusions to concerns such as producing herbicide-resistant weeds would have been welcome.

But this is minor bickering. The revised version of *On Food and Cooking* is an encyclopedic, relevant, well-written book, destined to be a classic like its predecessor. It should be on the bookshelf of anyone who eats. And, oh yes, McGee has no doubt that the egg came before the chicken. If you would like to know why, the answer can be found on page 69.

10.1126/science.1108292

MEDICINE

Sharp Critique of Industry's Influence

Eric G. Campbell

One of the most contentious topics in current medicine and science revolves around the nature, extent, and consequences of the relationships for-profit companies have with researchers and physicians in academia and government and with physicians in private practice. In recent months, a steady stream of newspaper articles, editorials in journals, books, and government reports have raised allegations of conflicts of interest, bias in scientific research, and inappropriate medical practices that result from links to industry.

On the Take
How Medicine's Complicity with Big Business Can Endanger Your Health
by Jerome P. Kassirer
Oxford University Press, New York, 2004. 271 pp. $28, £16.95. ISBN 0-19-517684-7.

Jerome P. Kassirer's *On the Take: How Medicine's Complicity with Big Business Can Endanger Your Health* further fuels this debate. Building on extensive evidence derived from empirical research, anecdotes, and inside information he obtained as a result of his tenure as the editor of the *New England Journal of Medicine*, Kassirer describes in detail the complex web of influence the pharmaceutical industry wields over biomedical research, medical education, and health care in the United States.

The author's account clearly shows that the pharmaceutical industry has developed deep inroads of influence into the research and health care communities. Through funding of research and perks such as paid consultancy positions (often for surprisingly little or no work), speaking engagements, and seats on corporate advisory boards, companies have established relations with many, if not the majority, of the leading members of the research community—including scientists in U.S. government agencies such as the National Institutes of Health and the Food and Drug Administration. Similarly, industry has built extensive ties to physicians through low-value gifts (such as pens, coffee mugs, mouse pads, and pizza) and more lavish enticements (such as free dinners at expensive restaurants, trips to exotic locations, and support for continuing medical education). At the institutional level, connections also link industry to physician associations, entire universities, and the leaders of prestigious government agencies.

The book casts a spotlight on the negative effects that relationships with industry sometimes have on the professional activities of those involved. In regard to researchers, empirical evidence suggests that ties to pharmaceutical companies are associated with greater chances of biased research, increased secrecy, inappropriate publication practices, and heightened risk for human subjects involved in clinical research. Considering physicians, Kassirer presents data suggesting that their prescription habits are influenced by relationships with industry, which sometimes lead doctors to prescribe drugs that are unnecessary, are more expensive but not more effective than readily available alternatives, or pose greater risks to patients without offering commensurate increases in efficacy.

Whereas Kassirer relentlessly pursues these various potential negative effects, he does not substantively discuss what many consider the possible benefits of relationships with industry. For example, through such arrangements scientists obtain resources to conduct research, write papers, attend conferences, sponsor students, and develop new products and services that likely would not be supported from nonindustrial sources. There can be little doubt that these activities lead to scientific advances and innovations in health care. Further, some believe that the personal compensation academic and government researchers receive as a result of their collaborations with industry acts to offset the salary differential between the public and private sectors, and thus that it helps academia and government recruit and retain star scientists. At the same time, relations between industry and physicians likely have some educational benefit—for example, through defraying the costs of continuing medical education for doctors (many of whom carry substantial debt as a result of their medical training).

The key question from a policy perspective is, what is the overall net effect of the relationships between the medical profession and industry? To what extent do the benefits outweigh the risks or vice versa? At present, the empirical data necessary to answer this question are not available—primarily because current, comprehensive data on the extent and influence of industry's ties to physicians have not been collected. As a result, for the near future at least, the debate is likely to be based primarily on ethical principles. Along such lines, Kassirer suggests a comprehensive set of policy and management recommendations that seek to promote patient safety, integrity of scientific information, physician accountability, and the full disclosure of industry relationships. It is difficult to assess—but extraordinarily relevant to the discussion—whether or not his suggestions would lead to the optimal balance of risks and benefits.

On the Take should be required reading for politicians, policy analysts, administrators, and members of the research and health care communities. Kassirer provides an invaluable resource for those seeking a complete survey of the literature along with previously untold examples of questionable behavior on the part of individual scientists and organizations. Although the book is likely to upset many readers, it highlights the need for additional debate, data, and perhaps policies regarding industry's influence on medical research and practice.

10.1126/science.1108501

The reviewer is at the Institute for Health Policy, Massachusetts General Hospital, 50 Stanford Street, Boston, MA 02114, USA. E-mail: ecampbell@partners.org

MEDICINE

Race and Reification in Science

Troy Duster

Alfred North Whitehead warned many years ago about "the fallacy of misplaced concreteness" (*1*), by which he meant the tendency to assume that categories of thought coincide with the obdurate character of the empirical world. If we think of a shoe as "really a shoe," then we are not likely to use it as a hammer (when no hammer is around). Whitehead's insight about misplaced concreteness is also known as the fallacy of reification. Recent research in medicine and genetics makes it even more crucial to resist actively the temptation to deploy racial categories as if immutable in nature and society.

Enhanced online at www.sciencemag.org/cgi/content/full/307/5712/1050

Hypertension and Heart Disease

In the last two decades, there has been extensive publication on the differences in hypertension and heart disease between Americans of European descent and Americans of African descent (*2*–*4*). Racial designations are frequently used in efforts to assess the respective influences of environmental and genetic factors.

In November, a study was published regarding a combination of isosorbide dinitrate and hydralazine (BiDil) that was originally found to be ineffective in treating heart disease in the general population but was then shown to work in a 3-year trial of a group of 1050 individuals designated as African Americans (*5*). BiDil is likely to get FDA approval this year and has been labeled "the first ethnic drug," although in medical practice, this becomes "the first racial drug." In presenting their justification for FDA approval of an ethnic/race–specific drug, the company (NitroMed) announced, "The African American community is affected at a greater rate by heart failure than that of the corresponding Caucasian population. African Americans between the ages of 45 and 64 are 2.5 times more likely to die from heart failure than Caucasians in the same age range" (*6*).

The author is director of the Institute for the History of the Production of Knowledge, New York University, 269 Mercer Street, New York, NY 10003–6687, USA. E-mail: troy.duster@nyu.edu

However, both age and survey population complicate this picture. The age group 45 to 64 only accounts for about 6% of heart failure mortality, and for those over 65, the statistical differences between "African Americans and Caucasians" nearly completely disappear (*7*). Researchers recently published a study that was explicitly designed to compare racial differences, by sampling whites from eight surveys completed in Europe, the United States, and Canada and contrasting these results with those of a sample of three surveys among blacks from Africa, the Caribbean, and the United States (*8*). Hypertension rates were measured in 85,000 subjects. The data from Brazil, Trinidad, and Cuba show a significantly smaller racial disparity in blood pressure than is found in North America (*8*).

Even within the category African American, the highly variable phenotype of skin color complicates the hypertension and race thesis. A classic epidemiological study on the topic also found differences within the African American population—with darker-skinned blacks generally having higher mean blood pressure than lighter-skinned blacks. The authors concluded that it was not the color of the skin that produced a direct causal outcome in hypertension, but that darker skin color in the United States is associated with less access to scarce and valued resources of the society. There is a complex feedback loop and interaction effect between phenotype and social practices related to that phenotype (*4*, *9*).

> "There is a complex feedback loop and interaction effect between phenotype and social practices related to that phenotype."
>
> —TROY DUSTER

Others have voiced concerns about the pitfalls of using race as anything but a temporary proxy: As the geneticist David Goldstein observed, "Race for prescription is only an interim solution to carry us through a period of ignorance until we find the underlying causes" (*10*). There is every evidence that these underlying causes interact with each other. However, race is such a dominant category in the cognitive field that the "interim solution" can leave its own indelible mark once given even the temporary imprimatur of scientific legitimacy by molecular genetics.

Studies of Human Genetic Diversity

The procedures for answering any inquiry into the empirical world determine the scientific legitimacy of claims to validity and reliable knowledge, but the prior question will always be: Why that particular question? The first principle of knowledge construction is, therefore, which question gets asked in the research enterprise.

A paper published in this week's issue of Science (*11*) is well-intentioned, well-crafted, and designed to help better understand the molecular basis of disease. The researchers were searching for and found patterns of SNPs differentially distributed in three population groups, formed from a total of 71 persons who were Americans of African, European, or Han Chinese descent.

Why was the question raised in this manner? The answer is a scientific Catch-22. This and other similar efforts (*12*) to create linkage disequilibrium and haplotype maps have a logic for choosing to study people from disparate geographic regions of the world. The purpose is to generate maps that can indicate subtle differences in the patterning or structuring of human genetic diversity across the globe. An increased understanding of these patterns of genetic diversity will help scientists doing gene-association studies by identifying new variants and reducing the likelihood of false-positive associations. The hope is that it may aid scientists to identify medically relevant genes for diseases

However, the particular groups of individuals chosen to represent each region of the world are often chosen because of their convenience and accessibility. Cell and tissue repositories are created to decrease the cost and difficulty of obtaining samples, and the archived samples will be extensively characterized and frequently utilized. Sample collections from repositories may be treated as populations in the narrow sense

of the term, even when there is little evidence that they represent a geographically localized, reproductively isolated group. These samples are often subtly portrayed as representing racially categorized populations. Finding a higher frequency of some alleles in one population versus another is a guaranteed outcome of modern technology, even for two randomly chosen populations. When the boundaries of those populations coincide with the social definition of race, a delicate tightrope needs to be better navigated between: (i) acknowledging race as a stratifying practice in societies that can lead to different frequencies of alleles in different modern populations but also to different access to health-related resources, and (ii) reifying race as having genetically sufficiently distinctive features, i.e., with "distinctive gene pathways," which are used to explain health disparities between racially categorized populations.

If we fall into the trap of accepting the categories of stored data sets, then it can be an easy slide down the slope to the misconceptions of "black" or "white" diseases. By accepting the prefabricated racial designations of stored samples and then reporting patterns of differences in SNPs between those categories, misplaced genetic concreteness is nearly inevitable.

SNP Patterns and Searches for a Biological Basis for Criminal Behavior

Several countries now have national DNA databases (*13*). Although I use the U.S. criminal justice system as an example, I have no doubt that the principles being considered are universal ones.

It is now relatively common for scholars to acknowledge the considerable and documented racial and ethnic bias in the criminal justice system, from police procedures, prosecutorial discretion, jury selection, and sentencing practices—of which racial profiling is but the tip of an iceberg (*14*–*16*). If the FBI's DNA database is primarily composed of those who have been touched by the criminal justice system and that system has engaged in practices that routinely select more from one group, there will be an obvious skew or bias toward this group in this database.

If we turn the clock back just 60 years, whites constituted about 77% of all prisoners in America, while blacks were only 22% (*17*). In just six decades, the incarceration rate of African Americans in relation to whites has gone up in a striking manner. In 1933, blacks were incarcerated at a rate about three times that of whites (*18*). In 1950, the ratio had increased to about four times; in 1970, it was six times; and in 1990, it was seven times that of whites.

Among humans, gene pools and SNP patterns cannot change much in 60 years, but economic conditions and the practices of the criminal justice system demonstrably do. The comparative explanatory power of SNP patterns surely pales before the analytic utility of examining shifting institutional practices and economic conditions. However, given the body of "ethnic-estimation" research being published on behalf of forensic applications (*19*, *20*) and the exponential growth of national DNA databases (*21*, *22*), it is not at all unreasonable to expect that a project that proposed to search for SNP profiles among sex offenders and felons convicted of violent crimes would meet with some success, both for funding and for finding "something." This could begin with the phenotype of "three populations," as in the study cited above (*11*), because that is the way these data are collected by the FBI and the contributing states. We must maintain vigilance to prevent SNP profiling from providing the thin veneer of neutral scientific investigation, while reinscribing the racial taxonomies of already collected data.

> **"allelic frequencies vary between any selected human groups—to assume that those variations reflect 'racial categories' is unwarranted."**
>
> —TROY DUSTER

Conclusions

As I have tried to show, a set of assumptions about race has animated the development of BiDil, genetic diversity analyses, "ethnic estimation" research, and the siren's call to do SNP research on the ever-expanding databases of DNA from the incarcerated. These elements are poised to exert a cascading effect—reinscribing taxonomies of race across a broad range of scientific practices and fields. Biomedical research must resist setting off the cascade and, while still moving forward in their efforts to identify the molecular correlates of disease, climb back on the tightrope to address racial disparities in health, in all their biosocial complexity.

The ability to use genomic knowledge to deliver effective pharmaceuticals more safely to special subpopulations that have some functional genetic markers holds promise. Thus, if the FDA approves BiDil, it should do so only under the condition that further research be conducted to find the markers that have the actual functional association with drug responsiveness—thus assuring that the drug be approved for everyone with those markers, regardless of their ancestry, or even of their ancestral informative markers.

The technology will be increasingly available to provide SNP profiles of populations. When the phenotype distinguishing these populations is race, the likelihood of committing the fallacy of misplaced concreteness, in science, is nearly overwhelming. For this reason, when geneticists report population data, they should always attach a caveat or warning label that could read something like this, "allelic frequencies vary between any selected human groups—to assume that those variations reflect 'racial categories' is unwarranted." Whereas this will not completely block the tendency to reify race, it will be an appropriately cautious intervention that tries to prevent science from unwittingly joining the current march toward a biological reinscription of the concept.

References and Notes

1. A. N. Whitehead, *Process and Reality* (Harper, New York, 1929), p. 11.
2. J. Kahn, *Yale J. Health Policy Law Ethics* **4**, 1 (2004).
3. R. S. Cooper, J. S. Kaufman, *Hypertension* **32**, 813 (1998).
4. M. J. Klag *et al.*, *JAMA* **265**, 599 (6 February 1991).
5. A. L. Taylor *et al.*, *N. Engl. J. Med.* **351**, 2049 (2004).
6. NitroMed, Inc., "BiDil® Named to American Heart Association's 2004 'Top 10 Advances' List; Only Cardiovascular Drug Recognized by AHA for Dramatically Improving Survival in African American Heart Failure Patients," PR Newswire US, 11 January 2005.
7. Jonathan Kahn, Jay Kaufman, personal communication.
8. R. S. Cooper *et al.*, *BMC Med.* **3**, 11 (2005).
9. V. Griffith, "FDA backs ethnically targeted drug," *Financial Times*, 9 March 2001, p. 13.
10. www.bioitworld.com/news/102904_report6447.html
11. D. A. Hinds *et al.*, *Science* **307**, 1072 (2005).
12. International HapMap Consortium, *Nature* **426**, 789 (2003); available at www.hapmap.org.
13. M. Jobling, P. Gill, *Nature Rev. Genet.* **5**, 739 (2004).
14. M. Mauer, *Race to Incarcerate* (New Press, New York, 1999).
15. J. Donohue, S. Levitt, *J. Law Econ.* **44**, 367 (2001).
16. J. Knowles, N. Persico, P. Todd, *J. Polit. Econ.* **109**, 203 (2001).
17. A. Hacker, *Two Nations: Black and White, Separate, Hostile, Unequal* (Scribner's, New York, 1992), p. 197.
18. T. Duster, in *DNA and the Criminal Justice System: The Technology of Justice*, D. Lazer, Ed. (MIT Press, Cambridge, MA, 2004), pp. 315–334.
19. M. D. Shriver *et al.*, *Am. J. Hum. Genet.* **60**, 957 (1997).
20. A. L. Lowe, A. Urquhart, L. A. Foreman, I. W. Evett, *Forensic Sci. Int.* **119**, 17 (2001).
21. D. Lazer, Ed., *DNA and the Criminal Justice System: The Technology of Justice* (MIT Press, Cambridge, MA, 2004), pp. 1–2.
22. T. Simoncelli, *Genewatch* **17** (March and April 2004).

10.1126/science.1110303

GENETICS

Harvesting Medical Information from the Human Family Tree

David Altshuler and Andrew G. Clark

A central goal of human genetics is to identify and understand causal links between variant forms of genes and disease risk in patients. To date, most progress has been made studying rare, Mendelian diseases in which a mutation in a single gene acts strictly in a deterministic manner, that is, the mutation causes the disease. The fact that such mutations strictly cosegregate with disease in families offers a shortcut to identifying the relevant chromosomal region, and means that the enrichment of mutations in patients with the disease compared with healthy controls can be convincingly documented in small numbers of individuals. In contrast, common diseases typically are caused by a complex combination of multiple genetic risk factors, environmental exposures, and behaviors. Because mutations involved in complex diseases act probabilistically—that is, the clinical outcome depends on many factors in addition to variation in the sequence of a single gene—the effect of any specific mutation is smaller. Thus, such effects can only be revealed by searching for variants that differ in frequency among large numbers of patients and controls drawn from the general population.

Limited knowledge about genetic variants in the human population, and the scarcity of technologies to score them accurately and at a reasonable cost, have been key impediments to performing this type of search. On page 1072 of this issue, Hinds *et al*. (*1*) describe dramatic progress toward overcoming these impediments. They describe a publicly available, genome-wide data set of 1.58 million common single-nucleotide polymorphisms (SNPs)—genome sequence sites where two alternative "spellings" exist in the population—that have been accurately genotyped in each of 71 people from three population samples. A second public data set of more than 1 million SNPs typed in each of 270 people has been generated by the International Haplotype Map (HapMap) Project (*2*). These two public data sets, combined with multiple new technologies for rapid and inexpensive SNP genotyping, are paving the way for comprehensive association studies involving common human genetic variations.

The rationale for genetic mapping by association to a dense map of common polymorphisms is based on two observations. The first is that most heterozygosity in the human population is due to a finite collection of common variants (on the order of 10 million and with a frequency exceeding 1%). The second is that nearby variants tend to correlate with one another in the population (known as linkage disequilibrium). Correlations among variants exist because when a mutation first arises, it does so on a single chromosome that carries a particular combination of alleles at flanking polymorphisms. Over time the mutation may spread to become common in a population, carrying with it the nearby flanking markers (see the figure). This correlation is eroded over the generations by recombination, just as in a pedigree study, except that the time scale may be thousands of generations, instead of one or two. In essence, genetic mapping with linkage disequilibrium treats the entire human population as a large family study with an unknown pedigree. The use of unrelated individuals makes it feasible to obtain sample sizes large enough to demonstrate modest relationships between genotype and phentoype through statistical associations.

Patterns of linkage disequilibrium are shaped by the local recombination rate, genealogical history, and chance. In the human genome, recombination is highly variable (*3*) and often clusters in regions of local high intensity or "hotspots" (*4*). Moreover, the human population has expanded recently from a much smaller founder pool, experiencing bottlenecks as well as expansions in its history. These forces combine to make human SNP patterns simpler and broader, such that they extend over longer distances than would otherwise be the case. Nevertheless, because the typical span of linkage disequilibrium is from thousands to more than 100,000 base pairs, genetic maps of very high density are needed to use linkage disequilibrium for mapping genes. These goals motivated the creation of the public human SNP map, which today contains more than 8 million variants (*5*). Developing genotyping assays for large numbers of these variants, determining their frequencies in population samples, and establishing their patterns of correlation have been the goals of both Perlegen—a private company whose work is described in the Hinds *et al*. (*1*) paper—and of the International HapMap Project.

In their study, Hinds *et al*. describe the genotyping of 1.58 million SNPs in each of 71 individuals. Critically, the authors document that the data are highly accurate. They identified 157,000 SNPs and nine individuals in their own data set that had also been collected and released by the public HapMap Project (*6*). Comparing these overlapping genotypes, the authors show that both data sets are of exceptionally high accuracy: 99.6% of genotype calls were identical in the two independent studies. High-quality data are extremely important because the goal is to identify associations among variants. Errors cause both an underestimation of correlation and an overestimation of diversity.

The SNPs genotyped by Hinds *et al*. are distributed across the genome, but as with all methods, certain biases of experimental design have shaped the data collected. Two major biases arise in the Perlegen study: One is caused by a desire to study variants that have appreciable frequency in the population (also shared by the HapMap project); the other is a particular technical aspect of the oligonucleotide chips used by Perlegen that limits analysis to unique (nonrepetitive) DNA sequences. A critical question is how completely this subset of SNPs allows prediction of the larger set of all common variants.

To answer this question, the authors cleverly included in their study a set of DNA samples in which a large collection of genes had been resequenced by a project at the University of Washington called SeattleSNPs (*7*). Hinds and colleagues measured the fraction of variants in this more complete data set that could be highly correlated with Perlegen's less complete set of genetic markers. The results are encouraging: 73% of all common variants in the SeattleSNP genes showed a strong correlation ($r^2 > 0.8$) with Perlegen's 1.58 million SNPs, and the mean correlation coefficient was 0.84. Moreover, the authors

D. Altshuler is at the Broad Institute of Harvard and Massachusetts Institute of Technology, and at the Massachusetts General Hospital, Boston, MA 02114, USA. E-mail: altshuler@molbio.mgh.harvard.edu A. G. Clark is in the Department of Molecular Biology and Genetics, Cornell University, Ithaca, NY 14853, USA. E-mail: ac347@cornell.edu

find that for future studies, an equivalent level of statistical power can be maintained by typing a selected set of just 300,000 SNPs in the samples with ancestry from Europe and Asia, and 500,000 SNPs in the African American sample. Because it is likely that the pairwise method of tagging used by the authors is conservative (*8*, *9*), even fewer markers would be likely to achieve a similar power.

In addition to the potential utility for disease research, such data are an excellent resource for population and evolutionary geneticists. Of particular interest is the inference of past natural selection. For example, if a mutation with a strong positive effect is "swept" to fixation, it leaves a footprint of low diversity and a skewed spectrum of allele frequencies nearby (*10*). Methods that incorporate information on this genomic scale are being devised to find these selective footprints. The hope is, of course, to locate genes that have evolved under positive selection in the recent history of humans, presumably because those changes were required for local adaptation to different environments. Some of these changes may cause differences in susceptibility to modern diseases in today's human populations.

Although the data described by Hinds *et al*. represent a major step forward, much more is needed to develop the resources for comprehensive genetic association studies. As the number and density of SNPs typed in reference samples become more complete, the power and efficiency of the markers selected will rise. In this regard, it is exciting that Perlegen and the public HapMap Project are now working together to generate an even denser map for the 270 HapMap samples. Integrating these SNP data with duplication, deletion, and inversion polymorphisms (*11*, *12*) will be required to fully capture all common sequence variations. It will be important to document how well allele frequencies and patterns of linkage disequilibrium observed in the 71 samples studied by Perlegen, and the 270 samples studied by the HapMap Project, will project over disease cohorts collected across the globe. Collecting data on diet, exercise, and relevant environmental exposures in long-term studies is key if we are ever to understand the confounding roles of genes and environment in influencing disease risk. Although there are many promising technologies for collecting genotype data, there is an acute need for improved methods to analyze these data for association with disease and to achieve robust results (*13*).

Ultimately, a complete description of each disease will require finding all variants, common and rare, and understanding their interactions with one another, with environmental exposures, and with multiple disease phenotypes. Association studies with common variants represent a screening method to find the most prevalent genetic risk factors. Although our population clearly contains common allelic variants that contribute to disease, the ultimate explanatory power of this approach depends critically on the unknown frequency distribution of genetic variants that contribute to disease risk, and on the magnitude of the effect of each allelic variant. There may be diseases for which there are no common alleles, presumably because the mutations that occurred long ago have been lost due to purifying selection, leaving only the more recent, rare mutations in the population. In such cases, because it is so hard to demonstrate association with rare variants, even direct resequencing data may be difficult to interpret. Where effects of common alleles are particularly weak, or if they are entangled in complex interactions with other genes and environmental factors, all methods will have correspondingly lower power. Suppose, for example, that a disease had the genetic architecture of the oil content of corn, where at least 50 genes, all of small effect, have been found to influence the trait (*14, 15*). Such a disease would demand an enormous amount of resources and yield little predictive information of use to public health—although the biological insights could still be of tremendous value. In short, we need to pick the targets for these approaches judiciously, and to modify the approach in light of what is learned.

Although population genetic theory has played a vital role in shaping our thinking about these problems (*16*), ultimately the contribution of common and rare variants in complex disorders is an empirical question that will only be answered by collecting data on an adequate scale. It is exciting to live in a time when the necessary tools are becoming available so that we can stop debating the hypothetical, and turn our attention to what we can learn from the data about real human diseases.

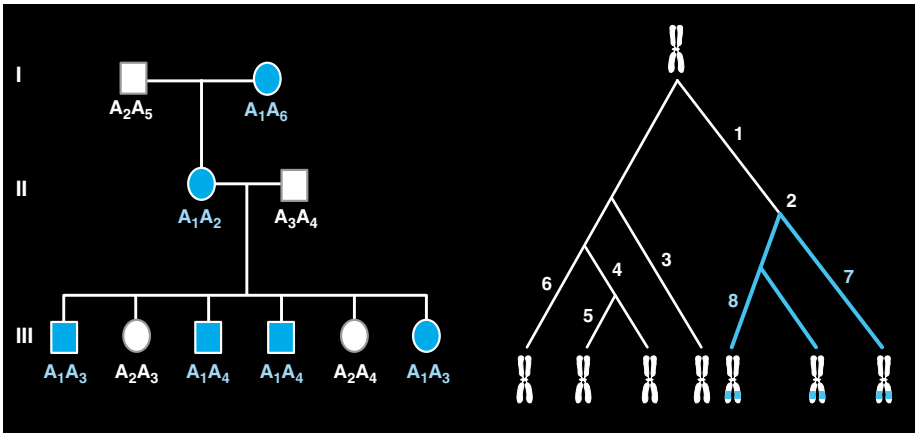

Gene mapping in families and in populations. (**Left**) The cotransmission of genes in families remains an important approach for the genetic mapping of human diseases. Pedigrees are collected, and genetic markers of many types (SNPs, microsatellites, insertions and deletions) are scored in each individual. Computer programs then calculate the probability that the pattern of transmission through the family is consistent with linkage of the disease and certain markers. (**Right**) For linkage disequilibrium mapping, the time scale is much longer, going back thousands of years. The diagram depicts a gene genealogy. At the top is an ancestral chromosome, with time flowing down the page, and the tips of the tree are individual chromosomes in the population today. Across a population sample, linkage is inferred if there is a statistical correlation (linkage disequilibrium) between the disease and a SNP marker. Numbers indicate mutations that generate SNP variations. A Mendelian disease is caused by mutation 2 (blue); all descendant chromosomes also carry mutation 1. Because recombination may occur over many generations, this correlation between variants is found only when the two are very close together (less than about 100 kb).

References

1. D. A. Hinds *et al. Science* **307**, 1072 (2005).
2. The International HapMap Consortium, *Nature* **426**, 789 (2003).
3. A. G. Clark *et al., Am. J. Hum. Genet.* **73**, 285 (2003).
4. G. A. McVean *et al., Science* **304**, 581 (2004) .
5. See www.ncbi.nlm.nih.gov/projects/SNP/.
6. See www.hapmap.org.
7. D. C. Crawford *et al., Am. J. Hum. Genet.* **74**, 610 (2004).
8. K. R. Ahmadi *et al., Nature Genet.* **37**, 84 (2005).
9. D. M. Evans, L. R. Cardon, A. P. Morris, *Genet Epidemiol.* **27**, 375 (2004).
10. Y. Kim, W. Stephan, *Genetics* **164**, 389 (2003).
11. J. Sebat *et al., Science* **305**, 525 (2004).
12. A. J. Iafrate *et al., Nature Genet.* **36**, 949 (2004).
13. J. N. Hirschhorn, K. Lohmueller, E. Byrne, K. Hirschhorn, *Genet. Med.* **4**, 45 (2002).
14. C. C. Laurie *et al., Genetics* **168**, 2141 (2005).
15. W.G. Hill, *Science* **307**, 683 (2005).
16. J. K. Pritchard, N. J. Cox, *Hum. Mol. Genet.* **11**, 2417 (2002).

10.1126/science.1109682

ATMOSPHERIC SCIENCE

Gamma Rays Made on Earth

Umran Inan

In 1994, Fishman *et al.* observed brief (>1 ms) bursts of intense gamma rays, called terrestrial gamma-ray flashes, with the Compton Gamma-Ray Observatory (CGRO) (*1*). Prior to this observation, intense transient bursts of gamma rays were only known to occur in an astrophysical context. The observed photon energies of more than 1 MeV suggested that the gamma rays were produced by "bremsstrahlung" radiation from high-energy electrons. (Such radiation is emitted when energetic electrons are scattered by nuclei.) The flashes—the most energetic natural photon phenomena on Earth—are caused by upward beams of electrons ("runaways") that are accelerated by thundercloud fields (*2*, *3*).

On page 1085 of this issue, Smith *et al.* (*4*) show, based on data from the Reuven Ramaty High Energy Solar Spectroscopic Imager (RHESSI) satellite, that terrestrial gamma-ray flashes are much more common than previously thought and that the photon energies can reach ~20 MeV. The CGRO and RHESSI data may be the first observational evidence of relativistic runaway breakdown, in which seed electrons at relativistic (>1 MeV) energies are accelerated by an electric field, followed by electrical breakdown as a result of their collision with air molecules. Relativistic runaway breakdown can proceed at much lower electric fields than conventional air breakdown (in which ambient thermal electrons must be accelerated to energies sufficient to ionize nitrogen). It may also be an important process in astrophysical plasmas. However, it has never been observed in the laboratory.

Computer models predict (*3*) that intense, transient electric fields associated with thunderclouds impose a total potential drop between 20- and 80-km altitude of more than 30 MV for large positive cloud-to-ground discharges of over 100 C (see the figure). These fields produce highly nonlinear runaway avalanches, in which accelerated electrons collide with molecules of air to strip even larger numbers of relativistic electrons. This process leads to a rapidly increasing number of relativistic electrons over large regions, with gamma-ray flashes emitted at altitudes of 30 to 70 km. The intense upward-driven relativistic electron beams eventually enter the radiation belts (the near-Earth space populated by energetic particles that are trapped in Earth's magnetic field). Here, some electrons may become trapped. A fraction of them may then precipitate in regions that are geomagnetically conjugate to intense lightning discharges (for example at the Southern Hemisphere termination of the magnetic field line that originates from a Northern Hemisphere thunderstorm). Here they interact with molecules in the increasingly dense atmosphere to produce optical emissions and x-rays, which are ultimately caused by the release of energy in a lightning discharge in the parent hemisphere.

A total of ~76 terrestrial gamma-ray flashes were observed with the CGRO over the 9-year mission. However, when the instrument was in an optimized energy trigger mode (>100 keV), ~1 event per week was observed. The instrument had a minimum trigger time resolution of 64, thus missing many terrestrial gamma-ray flashes, which have a typical duration of 1 ms (*5*). Smith *et al.* show that without this limitation, terrestrial gamma-ray flashes are observed much more often, ~15 to 20 per month, even with much smaller (and thus less sensitive) detectors (*4*).

There is clear evidence that terrestrial gamma-ray flashes are associated with lightning (*6*). For many of the flashes detected by CGRO and RHESSI, radio atmospherics (electromagnetic impulses produced by lightning discharges) were observed at the same time at Palmer Station, Antarctica. These radio atmospherics exhibit the slow tail characteristic of lightning flashes that lead to transient luminous high-altitude phenomena known as sprites (*6*, *7*).

Observations and modeling of sprites (*8*, *9*) confirm the existence of intense, slowly varying electric fields of up to 1 kV/m at altitudes of 30 to 80 km above thunderstorms. When integrated over altitudes of 20 to 80 km, these fields correspond to a total transient potential drop of more than 30 MV (see the figure). Such intense electric fields can produce runaway electron beams via avalanche acceleration (*10*–*13*), leading to the emission of bremsstrahlung gamma-ray flashes of an intensity consistent with the CGRO observations (*3*). However, models of this phenomenon depend strongly on the initial conditions (*3*, *14*, *15*), because the runaway process is highly nonlinear and the lightning electric fields vary widely.

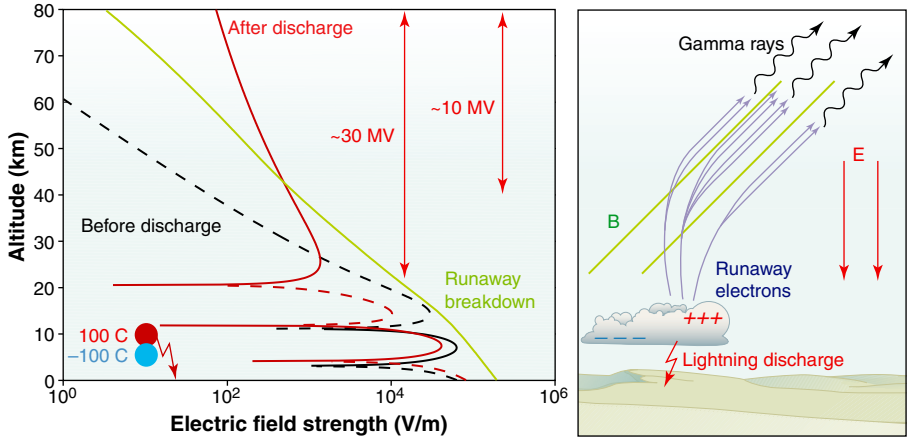

How terrestrial gamma-ray flashes form. (Left) The electric field before (black line) and after (red line) a positive lightning discharge that removes 100 C from the top of the cloud (at an altitude of 10 km). After the discharge, the relativistic runaway threshold field (green line) is exceeded above 40 km. Solid and dashed lines are downward and upward fields, respectively. **(Right)** Schematic of the relativistic electron avalanche and production of gamma rays after the lightning discharge. The scale roughly corresponds to the vertical scale on the left.

Hence, simultaneous measurements of terrestrial gamma-ray flashes and lightning discharges are needed to understand and quantify the mechanisms that cause the flashes. Observations over a broad range of geomagnetic latitudes are required to assess the role of the geomagnetic field orientation in the runaway breakdown process (*3*, *14*). With the observation of tens of terrestrial gamma-ray flashes per month on RHESSI (*4*), this objective may be within reach, especially given the increasing availability of lightning data from different parts of the globe (*16*).

The observations of terrestrial gamma-ray flashes imply the presence of electron beams with energies of more than 1 MeV; bremsstrahlung radiation from such electrons is the only viable source of gamma rays in Earth's atmosphere. Quantitative models indicate that a runaway beam of 100-keV to 10-MeV electrons radiates gamma

The author is in the Department of Electrical Engineering, Stanford University, Stanford, CA 94305, USA. E-mail: inan@stanford.edu

rays at altitudes of 30 to 70 km (*3*). For electrons >500 keV, the loss of energy due to scattering is insignificant above 70 km because of the low density of air at these altitudes. Therefore, most of these particles must escape upward along Earth's magnetic field lines into the radiation belts, constituting an injected beam with a total fluence of up to 10^6 to 10^7 electrons/cm^2 (*3*, *17*).

For cloud-to-ground discharges, the estimated transverse scale of the beam is about 10 to 20 km, whereas for horizontal intracloud discharges, the scale may be as large as ~100 km (*3, 12*). Direct satellite detection of such beams during injection is thus improbable: To observe the event, the satellite would have to be at just the right location during the ~1 ms of beam duration. However, some of the injected electrons are predicted to form (*17*) eastward-drifting "curtains" extending over ~70° in longitude within a few minutes of injection. Such spreading would substantially enhance the likelihood of in situ detection, especially shortly after injection, before the electrons drift around the planet and are precipitated into the atmosphere near the South Atlantic, where the Earth's magnetic field exhibits a minimum.

The satellite observations of hundreds of terrestrial gamma-ray flashes reported by Smith *et al.* (*4*) provide an excellent data set on these high-energy phenomena. Coupled with observations of sprites and elves and more comprehensive data on lightning occurrence, the data may allow us to quantitatively understand the mechanisms of runaway acceleration.

References

1. G. J. Fishman *et al.*, *Science* **264**, 1313 (1994).
2. C. T. R. Wilson, *Proc. Phys. Soc. London* **37**, 32D (1925).
3. N. G. Lehtinen, T. F. Bell, U. S. Inan, *J. Geophys. Res. A* **104**, 24699 (1999).
4. D. M. Smith *et al.*, *Science* **307**, 1085 (2005).
5. G. Fishman, personal communication.
6. U. S. Inan *et al.*, *Geophys. Res. Lett.* **23**, 1017 (1996).
7. S. C. Reising *et al.*, *Geophys. Res. Lett.* **23**, 3639 (1996).
8. D. D. Sentman *et al.*, *Geophys. Res. Lett.* **22**, 1205 (1995).
9. V. P. Pasko *et al.*, *J. Geophys. Res. A* **102**, 4529 (1997).
10. Y. N. Taranenko, R. A. Roussel-Dupré, *Geophys. Res. Lett.* **23**, 571 (1996).
11. N. G. Lehtinen *et al.*, *Geophys. Res. Lett.* **23**, 2645 (1996).
12. N. G. Lehtinen, U. S. Inan, T. F. Bell, *Geophys. Res. Lett.* **24**, 2639 (1997).
13. R. A. Roussel-Dupré, A. V. Gurevich, *J. Geophys. Res. A* **101**, 2297 (1996).
14. A. V. Gurevich *et al.*, *Radio Science* **31**, 1541 (1996).
15. G. Milikh, J. A. Valdivia, *Geophys. Res. Lett.* **26**, 525 (1999).
16. H. J. Christian *et al.*, *J. Geophys. Res. D* **108,** 4005 (2003).
17. N. G. Lehtinen, U. S. Inan, T. F. Bell, *Geophys. Res. Lett.* **27**, 1095 (2000).

10.1126/science.1109392

ARCHAEOLOGY

Patterns of Cultural Primacy

Richard A. Diehl

For more than 100 years, archaeologists have debated the impact of long-distance trade and exchange on the emergence of civilization. Nowhere has this issue been more sharply contested than in ancient Mesoamerica, especially with regard to the Olmecs during the Early Formative Period (1500 to 900 B.C.E.) at San Lorenzo in southern Mexico's Veracruz state.

San Lorenzo, the largest center in Mesoamerica from the Early Formative Period, covered 700 hectares and was home to several thousand residents. Some archaeologists have argued that San Lorenzo had a defining impact on societies in the neighboring Chiapas, Guerrero, and Oaxaca states and in central Mexico (*1*–*3*); others contend that each region witnessed the contemporaneous growth of complex societies that interacted with each other and with the Olmecs as equals (*4*, *5*). The terms "mother culture" and "sister cultures" are often applied to the extreme positions of the debate (*6*, *7*).

On page 1068 of this issue, Blomster *et al.* (*8*) provide powerful support for the mother culture school. They demonstrate that some of the Olmec-style pottery found throughout Mesoamerica was manufactured at San Lorenzo and traded over distances of hundreds of kilometers. San Lorenzo thus dominated in the commercial relationships and attendant spread of Olmec iconography and belief systems.

The author is in the Department of Anthropology, University of Alabama, Tuscaloosa, AL 35487, USA. E-mail: rdiehl@bama.ua.edu

San Lorenzo has been at the center of the Olmec mother culture debate since radiocarbon dates placed it centuries earlier (*9*) than had been postulated by some archaeologists on the basis of the sophistication of its stone sculptures, especially its famous colossal heads (*10*). Recent investigations show that in the Early Formative Period, San Lorenzo covered about 700 hectares, many times the area of any contemporary cities in Mesoamerica (*11*). Its known features include exquisitely carved colossal heads, thrones, and other two- and three-dimensional depictions of rulers, mythical and living animals, and deities (see the figure). The plateau it occupied overlooked the junction of several rivers, thus controlling transportation throughout the entire Coatzacoalcos river basin. Raised causeways led from the rivers across annually flooded ground to the plateau. Terraces holding commoner residences lined the ridge sides; the 100-hectare summit was reserved for elite housing, public architecture, and displays that included sets of stone sculptures. San Lorenzo's merchants imported jadeite, basalt, obsidian, Pacific coast shells, magnetite and other iron ores, and probably also more perishable materials.

San Lorenzo Monument 52. This water deity, carved from basalt, was found associated with a stone aqueduct. The down-turned mouth, almond-shaped eyes, headdress symbols, and cross-banded motif on the chest gorget are defining elements of the Olmec style and occur on ceramics found in many Mesoamerican centers from the Early Formative Period.

CREDIT: FELIPE DÁVALOS

The three major archaeological projects at San Lorenzo since 1946 (*12*) have revealed new and at times startling information and have resolved many questions. But each has also left numerous questions unresolved or subject to dispute while raising many new ones. Perhaps the most pervasive is the mother culture–sister cultures dispute. Did San Lorenzo's leaders maintain contacts with rulers in distant communities? If so, why? And what goods and other things did they seek?

Perhaps the most important question concerns the wide dispersal of Olmec iconic symbols and the belief systems they represent. The symbols are displayed on large stone sculptures, small portable greenstone objects, and pottery. Did all these symbols originate at San Lorenzo, or did societies in Chiapas, Oaxaca, Guerrero, and central Mexico contribute to the pool of what has been mistakenly attributed to the San Lorenzo style? Stone sculpture is rare outside Olman (the Olmec heartland), whereas pottery with Olmec-style iconography occurs frequently, and hence the debate has focused on the latter. One school holds that such vessels were exports from San Lorenzo; others argue that the different centers shared basic ideas but manufactured their

own Olmec-style wares, decorated with motifs of their own creation and meaning.

Blomster *et al.* (*8*) show that although the situation was much more complex than these extreme positions suggest, many vessels argued to be local products were in fact manufactured from clays native to the San Lorenzo area. In the past, scholars have depended primarily on stylistic analyses to support their positions. Style is an important and potentially very informative aspect of object analysis, but it has several deficiencies. First, style, like beauty, is almost impossible to quantify. This is especially true of Olmec designs, which tend to shape-shift into almost unrecognizable variants of a central theme. Second, the archaeological time periods used in Mesoamerican studies span at least a century. They cannot capture sporadic contacts between the elites of two societies separated by hundreds of kilometers that may have lasted less than a generation.

In the largest and most comprehensive study of this type ever done on Olmec pottery, Blomster *et al.* used instrumental neutron activation analysis, together with a conservative approach to statistical analyses. By comparing the chemical signatures of 725 ceramic pieces with those of clays collected from the various regions in question, they can determine which pottery vessels were manufactured from local clays and which were not. The results show that communities in Chiapas, Oaxaca, Guerrero, and the Basin of Mexico all imported vessels carrying Olmec iconography from San Lorenzo, and that potters at some of the foreign sites created imitations of Olmec pots with Olmec designs from local clays. They also show that trade relations emphasized direct contact between San Lorenzo and recipient groups, not complexly interwoven networks.

The study by Blomster *et al*. reveals complex patterns of social interaction that probably varied from place to place and through time. It documents the movement of Olmec pottery, along with an ideology reflected in its decoration, from San Lorenzo to foreign communities, and the integration of Olmec icons, beliefs, and practices into local indigenous systems. Later imitation of this pottery in local clays reflects the solidification of this transfer of ideas.

The study resolves some issues in the mother culture-sister culture debate, but others remain and new ones emerge. The exchanges apparently emphasized bipolar patron-client relationships between Olmec rulers and specific foreign lords, rather than the more diffuse trade networks posited by sister-culture proponents. These relations were hierarchical, with San Lorenzo Olmecs targeting specific foreign powers. How was this accomplished, and what motivated people on both ends? The archaeological evidence does not suggest conquest or proselytization. Were these truly commercial ventures, overlain with the power and mystery that adhered to Mesoamerica's largest and most complex culture of the time? Furthermore, what motivated the participants to behave as they did? Physical and social sciences, art analyses, and the humanities will all contribute to resolving these questions in the future.

References

1. M. D. Coe, in *Regional Perspectives on the Olmec*, R. J. Sharer, D. C. Grove, Eds. (Cambridge Univ. Press, Cambridge, 1989), pp. 68–82.
2. R. A. Diehl, M. D. Coe, in *The Olmec World: Ritual and Rulership*, J. Guthrie, Ed. (Art Museum, Princeton Univ., Princeton, NJ, 1995), pp. 11–25.
3. J. E. Clark, M. E. Pye, in *Olmec Art and Archaeology in Mesoamerica*, J. E. Clark, M. E. Pye, Eds. (National Gallery of Art, Washington, DC, 2000), pp. 217–251.
4. D. C. Grove, in (*1*), pp. 8–16.
5. A. Demarest, in (*1*), pp. 303–344
6. K. V. Flannery, J. Marcus, *J. Anthropol. Archaeol.* **19**, 1 (2000).
7. R. A. Diehl, *The Olmecs: America's First Civilization* (Thames and Hudson, London, 2004), pp. 126–180.
8. J. P. Blomster, H. Neff, M. D. Glascock, *Science* **307**, 1068 (2005).
9. M. D. Coe, R. A. Diehl, M. Stuiver, *Science* **155**, 1399 (1967).
10. C. R. Wicke, *Olmec: An Early Art Style in Precolumbian Mexico* (Univ. of Arizona Press, Tucson, AZ, 1971).
11. A. Cyphers, in *Población, Subsistencia y Medio Ambiente en San Lorenzo Tenochtitlán*, A. Cyphers, Ed. (Univ. Nacional Autónoma de México, Mexico, 1997), pp. 255–274.
12. R. A. Diehl, in (*7*), pp. 29–59.

10.1126/science.1109441

DEVELOPMENTAL BIOLOGY

Life After Deaf for Hair Cells?

Ruth Taylor and Andrew Forge

Disabling hearing impairments affect an estimated 250 million people worldwide (*1*), and deafness is the second most common disability in developed countries. Abnormalities in balance control contribute to disabling mobility problems and to falls in elderly people. The major cause of these hearing and balance functional deficits is the permanent loss of sensory hair cells in the inner ear epithelia. The inner ear comprises the cochlea, containing sensory epithelia for hearing, and the vestibular system, containing sensory epithelia that maintain balance by detecting changes in head position. The hair cells of the sensory epithelia are characterized by a bundle of projections at their apical pole—the stereocilia—that constitute the signal detection and transduction apparatus. Hair cells detect minute displacements of their stereocilia—which can be as small as 3×10^{-10} m—in response to sound or changes in head position, and convert them into neural signals.

A characteristic of many specialized, highly differentiated cells in mammals, including sensory hair cells, is that they are actively blocked from undergoing cell division, that is, they are held in mitotic arrest. As a consequence, when they die they cannot be readily replaced. Entry to and withdrawal from the cycle of events leading to cell division is tightly regulated (see the figure). Central to the complex network of interacting proteins that determines exit from the cell cycle is the retinoblastoma protein (pRb), which inhibits the expression of genes needed for cell cycle entry and thereby maintains cells in mitotic quiescence (*2*). On page 1114 of this issue, Sage and colleagues (*3*) identify pRb as a key mediator of mitotic arrest in sensory hair cells of the inner ear by demonstrating that suppression of its expression allows them to participate in cell division. The findings of Sage *et al*. suggest that modulating the expression of negative regulators of the cell cycle might be a way to regenerate damaged mammalian tissues.

Within the sensory epithelia, each hair cell is surrounded by and separated from its neighbor by intervening nonsensory supporting cells. In the auditory epithelium of mammals (the cochlea's organ of Corti), these two cell types are arranged in an orderly pattern along a spiraling strip (see the figure, A). Hair cells at a particular place along the spiral detect sounds of only a specific frequency. Therefore, loss of only a few hair cells (see the figure, B) can cause significant hearing impairment. Hair cells and supporting cells are born during embryonic life. Cells in the presumptive sensory epithelium exit the cell cycle and then differentiate into either hair cells or supporting cells (*4*, *5*). Normally, these differentiated cells remain mitotically quiescent throughout life. A negative regulator of cell cycle progression, $p27^{Kip1}$, has been found to mediate exit of precursor cells from the cell cycle (*6*, *7*), which in mice occurs at about embryonic day 13. Expression of $p27^{Kip1}$ in supporting cells is maintained into adulthood, and ablation of the gene encoding $p27^{Kip1}$ leads to a continuation of cell division, presumably of precursor cells in the organ of Corti. However, expression of $p27^{Kip1}$ is down-regulated in hair cells as they begin to differentiate from about embryonic day 14 and so is unlikely to be involved in

The authors are at the Centre for Auditory Research, UCL Ear Institute, University College London, London WC1X 8EE, UK. E-mail: a.forge@ucl.ac.uk

maintaining the mitotic arrest of these cells.

In an initial screen of genes expressed during development of the mouse inner ear, Sage *et al*. identified pRb as a candidate for maintaining cell cycle arrest in hair cells. Then they detected the protein's appearance in precursor cells as they began to differentiate into hair cells, and its retention in hair cells of the mature epithelia. Next, they explored the function of pRb in mice by genetically engineering animals lacking the *Rb* gene in the inner ear and a limited number of other tissues. Although these animals died perinatally, presumably due to defects in tissues other than those of the inner ear, it was still possible to examine the inner ear of mouse embryos and the mice at birth. The authors found an increase in the number of hair cells, both in the utricular maculae (one of the vestibular sensory tissues) and, even more dramatically, in the organ of Corti in mice that lacked pRb in the inner ear. Because these hair cells were labeled with markers of cell division, which was not seen in the hair cells of age-matched littermate controls, the authors were able to confirm that pRb is needed for maintenance of mitotic arrest. In addition, they found that in utricular maculae that had developed normally, and in which postmitotic arrest had occurred, subsequent ablation of pRb induced proliferation and production of extra hair cells. This provides some proof of principle that manipulating pRb expression could be used to generate new hair cells in damaged, mature inner ear tissue.

One of the most surprising findings of the Sage *et al*. work is that hair cells divide while still maintaining their differentiated state. Cells that were labeled with markers of proliferation retained several different proteins characteristic of hair cell differentiation. Furthermore, transduction currents could be recorded from these extra (supernumerary) hair cells, indicating that they were functional. In many tissues that are able to regenerate, such as those in the newt, differentiated postmitotic cells first have to dedifferentiate, losing many of their characteristic specializations, before being able to re-enter the cell cycle (*8*). Indeed, differentiated multinucleate muscle cells (myotubes) from Rb-deficient mice—which, unlike their normal counterparts, can be induced to reenter the cell cycle—dedifferentiate into mononucleate cells before reentry (*9*). Thus, the Sage *et al*. finding that functional differentiated hair cells can directly enter the cell cycle and divide is unexpected.

The most immediate practical benefit of this work is the potential to obtain large numbers of hair cells of particular types in vitro. This should enable identification of their molecular and biochemical characteristics and the growth factors that regulate their differentiation. Such work has been hampered by the relatively small number of hair cells in the sensory patches (only about 13,000 in a human cochlea).

Much less immediate is a therapy for deafness that uses suppression of pRb activity to induce hair cell division and restore a functional auditory epithelium. Any such therapy would depend on the ability to reactivate pRb in order to halt proliferation—inactivation of pRb is a feature of many tumors—and to do so when the correct number of hair cells has been restored in order to reestablish appropriate neural connections. In mice with targeted ablation of $p27^{Kip1}$, supernumerary hair cells are produced, but these animals are deaf (*6*). Furthermore, when pRb expression was suppressed in mice in the Sage *et al*. study, hair cell production exceeded that of supporting cells, and the orientation of the hair cell stereocilia was random. Sufficient numbers of supporting cells are necessary for mechanical maintenance of the sensory epithelium. In the *mind bomb* zebrafish mutant, all of the precursor cells differentiate into hair cells, and in the absence of supporting cells, the hair cells detach from the epithelium (*10*). The precise orientation of the stereocilia in one particular direction (see the figure, A) is essential for effective stimulation of hair cells in situ. We require a more detailed understanding of how the patterning of the organ of Corti is generated.

Another concern is that the inner ear tissues examined in this work, although past the age at which mitosis has normally been arrested, are still quite immature. In the organ of Corti, hair cells undergo further differentiation in parallel with changes in

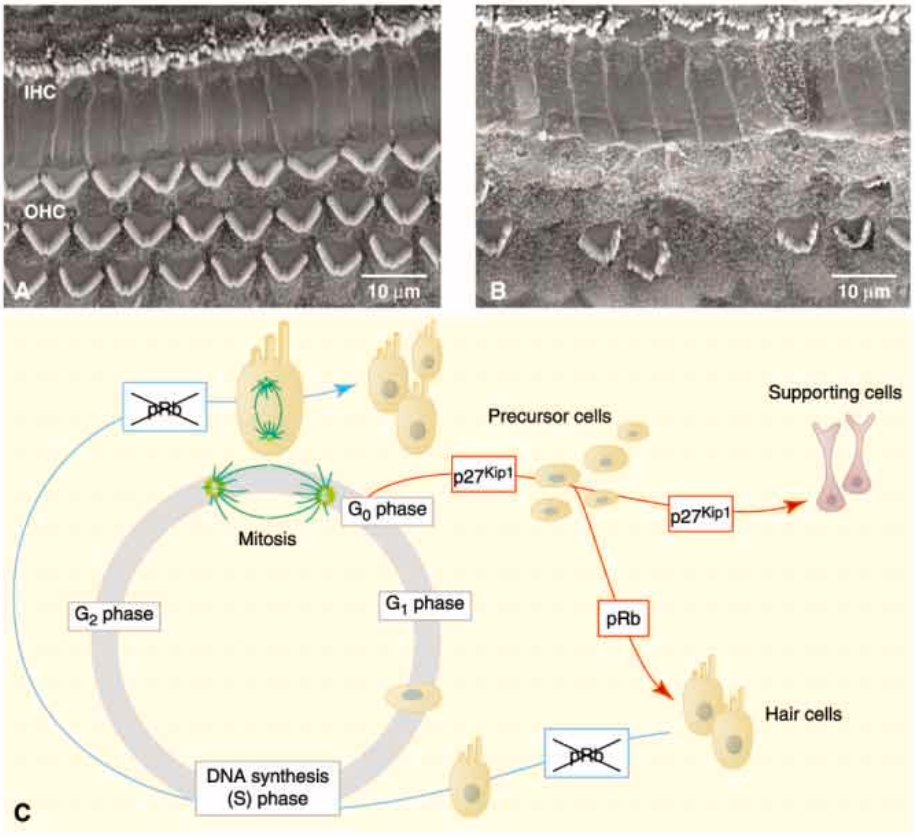

A sound basis for hair cell renewal. (**A**) The auditory epithelium (organ of Corti) of the mouse cochlea. Hair cells and supporting cells are laid out in a regular pattern. There is a single row of inner hair cells (IHC) and three rows of outer hair cells (OHC). Each hair cell is separated from its neighbors by intervening supporting cells. The hair bundles (stereocilia) on each hair cell are oriented in a precise relationship to each other. Movement of the stereocilia in response to sound results in the firing of neurons. (**B**) Hair cell loss in the mouse organ of Corti induced by exposure to an ototoxic aminoglycoside antibiotic. Supporting cells expand to close the lesions created by loss of hair cells. (**C**) During the cell cycle (gray), DNA synthesis takes place in S phase and then the cell passes through G_2 phase, entering mitosis and dividing into two daughter cells. Unless stopped from doing so in G_0/G_1 phase, cells will continue progressing through the cell cycle. In the developing inner ear, however, after the final round of division, precursor cells exit the cell cycle and begin to express $p27^{Kip1}$, a negative regulator of mitosis (red arrows). These precursor cells differentiate into hair cells and supporting cells, which are held in postmitotic arrest. $p27^{Kip1}$ continues to be expressed in supporting cells. In contrast, hair cells express pRb as they begin to differentiate, which prevents their reentry into the cell cycle. The absence of pRb allows hair cells to reenter the cell cycle and progress through mitosis, resulting in the generation of supernumerary hair cells (blue arrow).

supporting cell specialization and with innervation patterns (*11*). In fully mature tissue, the effects of suppressing pRb function may not be so pronounced or may have different consequences. In mice lacking the cyclin-dependent kinase inhibitor Ink4d, which is expressed by hair cells and regulates maintenance of the postmitotic state and of differentiation, the organ of Corti develops normally to maturity, but then hair cell death is triggered as mitosis is initiated (*12*). Although the hair cells generated in the absence of pRb in the immature organ of Corti apparently do not undergo programmed cell death, it is not yet known whether this is the case in the mature tissue.

Despite these caveats, the results of Sage *et al*. represent an important milestone. Other recent studies have shown that a population of stem cells with the potential to differentiate into hair cells exists in vestibular organs (*13*) and that it is possible to induce nonsensory cells in the mature cochlea to differentiate into hair cells by transfection with the gene encoding the Math-1 transcription factor, which specifies that a cell should become a hair cell (*14*). These studies together with the encouraging findings of Sage *et al.* place therapies to restore lost inner ear hair cells on a sounder footing.

References

1. World Health Organization (www.who.int/pbd/deafness/en).
2. M. V. Frolov, N. J. Dyson, *J. Cell Sci.* **117**, 2173 (2004).
3. C. Sage *et al.*, *Science* **307**, 1114 (2005); published online 14 January 2005 (10.1126/science.1106642).
4. R. J. Ruben, *Acta Otolaryngol. Suppl.* **220**, 1 (1967).
5. D. M. Fekete, *et al., J. Neurosci.* **18**, 7811 (1998).
6. P. Chen, N. Segil, *Development* **126**, 1581 (1999).
7. H. Lowenheim *et al., Proc. Natl. Acad. Sci. U.S.A.* **96**, 4084 (1999).
8. J. P. Brockes, *Science* **276**, 81 (1997).
9. J. W. Schneider *et al., Science* **264**, 1467 (1994).
10. C. Haddon *et al., J. Neurocytol.* **28**, 837 (1999).
11. A. Forge *et al., Semin. Cell Dev. Biol.* **8**, 225 (1997).
12. P. Chen *et al., Nature Cell Biol.* **5**, 422 (2003).
13. H. Li *et al.,, Nature Med.* **9**, 1293 (2003).
14. K. Kawamoto *et al., J. Neurosci.* **23**, 4395 (2003).

10.1126/science.1109680

OCEAN SCIENCE

Ironing Out Biosphere Oxidation

Lee Kump

Iron is the most abundant element on Earth. It plays a critical role in a wide range of Earth system processes, from generation of the magnetic field in Earth's outer core to the production in the cell of a variety of compounds essential for life. Investigations into the biogeochemical behavior of other elements have benefited from slight differences in the chemical behavior of different stable isotopes of the same element. Yet, despite iron's importance, almost nothing was known about the natural variability of the stable iron isotopes until about a decade ago (*1*) and only now are researchers beginning to use iron isotopes in biogeochemical and Earth-system evolution studies. The latest application of iron isotopes to major questions in Earth history appears on page 1088 in this issue, in which Rouxel and colleagues (*2*) show that a progressive change in iron cycling during the Precambrian (from 3.5 to 0.5 billion years ago) was associated with the establishment of an oxygen-rich biosphere.

The gap in our knowledge of iron isotopes was in part due to analytical problems, but it also reflected the common belief that there was little likelihood of fractionation of such heavy isotopes during natural processes, despite indications to the contrary (*3*, *4*). Painstaking work in thermal ionization mass spectrometry, the development of the inductively coupled plasma mass spectrometer, and mounting curiosity about trace-metal stable-isotope behavior have led to a rapid accumulation of data on the iron isotopes in the past few years and a clear demonstration of natural iron isotopic variability (*5*). Recently, Dauphas and colleagues reported that iron isotopes indicate that some of Earth's oldest rocks are of water-laid origin (*6*). Now Rouxel *et al.* use the observation that Fe-oxides concentrate ^{56}Fe to interpret a new geochemical record of iron isotope variability in terms of the oxygenation of the oceans through time.

There are three chemical elements whose redox chemistry controls the oxygenation of the surface environment: sulfur, carbon, and iron. Weathering of rocks that contain their reduced forms consumes oxygen, whereas oxygenic photosynthesis generates oxygen by reducing carbon with water. The oxygen accumulates in the atmosphere if the organic matter is buried in sediments. Temporal changes in carbon and sulfur isotopic composition, as captured in marine minerals, record imbalances in the rates of input and removal of carbon and sulfur in the ocean, and thus reveal how rates of oxygen production and consumption have varied over time. A complementary record of the third redox element, iron, has been awaiting construction.

To meet this need, Rouxel *et al*. (*6*) analyzed the iron isotopic composition of rather ubiquitous Precambrian marine pyrites. These are iron sulfide minerals that form readily under reducing conditions in marine sediments and euxinic (hydrogen sulfide–rich) water columns, and are thought to faithfully record the isotopic composition of the dissolved iron in the ocean at the time, presuming that the iron was completely used to form the pyrite in the sediments. They found that pyrites older than about 2.3 billion years exhibit low ratios of the iron isotopes $^{56}Fe/^{54}Fe$ (expressed as the standardized value $\delta^{56}Fe$ with permil notation, ‰) relative to younger materials, and that pyrites from

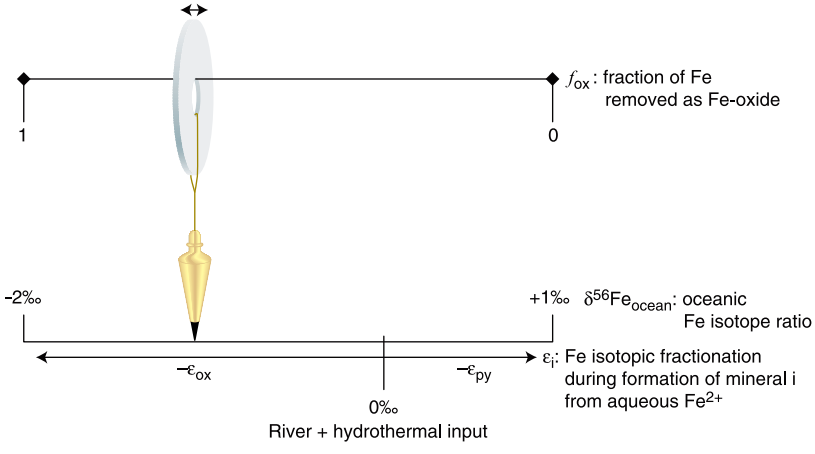

Iron-cycling in the ocean. The steady-state iron (Fe) isotopic composition of the ocean is set by the Fe-oxide fraction of the total sedimentary flux from the ocean (f_{ox}). If most of the Fe is removed as Fe-oxides (for example, during intervals of banded iron formation), $f_{ox} \rightarrow 1$, and $\delta^{56}Fe \rightarrow -2‰$. At the other extreme, if most Fe is removed as pyrite, $f_{ox} \rightarrow 0$ and $\delta^{56}Fe \rightarrow +1‰$. The average $\delta^{56}Fe$ of the weathering and hydrothermal inputs has an approximate value of 0‰. This model is only appropriate for times when the deep ocean was iron-rich and thus hydrogen sulfide- and oxygen-poor (in other words, greater than 1.8 billion years ago). [$\varepsilon_{py} = \delta^{56}Fe_{pyrite} - \delta^{56}Fe_{ocean} \approx -1‰$; $\varepsilon_{ox} = \delta^{56}Fe_{Fe\text{-}oxides} - \delta^{56}Fe_{ocean} \approx +2‰$. At steady state, $\delta^{56}Fe_{ocean} = -\varepsilon_{py} - f_{ox}(\varepsilon_{ox} - \varepsilon_{py})$.]

The author is in the Department of Geosciences, Pennsylvania State University, University Park, PA 16802, USA. E-mail: lkump@psu.edu

CREDIT: PRESTON HUEY/*SCIENCE*

~2.3 to 1.8 billion years ago display relatively large ratios compared to either older or younger pyrites. This breakdown of Earth history is particularly interesting because it coincides with current views of the redox evolution of the biosphere: Stage 1 (more than ~2.3 billion years ago), in which the atmosphere and much of the ocean were free of oxygen; Stage 2 (from ~2.3 to ~1.8 billion years ago), when the atmosphere became oxidized but the ocean remained anoxic and perhaps mildly sulfidic; Stage 3a, characterized by deep-ocean euxinia (from ~1.8 to ~0.75 billion years ago); and Stage 3b (from ~0.75 billion years ago to the present), during which, with the exception of brief "oceanic anoxic events" (*7*), both the ocean and atmosphere were oxygenated (*8*, *9*). During Stage 1, the oceans became enriched in iron during periods of submarine volcanism. At the same time, iron was being removed from the ocean as both iron oxides [including the voluminous banded iron formations (BIFs) upon which much of the world's steel production depends] and pyrite. Iron oxides were formed in the water column either by anaerobic oxidation or by small amounts of oxygen that accumulated in regions of the surface ocean with high cyanobacterial productivity. BIF was demonstrably enriched in ^{56}Fe; its deposition drove the ocean toward lower values of $\delta^{56}Fe$, as recorded in the pyrites (see the figure). Stage 2 witnessed a waning of volcanism and associated BIF, and thus a shift toward a dominance of the pyrite-removal mechanism for iron and higher oceanic values of $\delta^{56}Fe$. Renewed BIF at 1.8 billion years ago lowered the marine iron isotope ratio at the beginning of stage 3a. Subsequent sulfidic (*8*, *9*) or oxygenated (*10*) conditions in the deep sea ensured that aqueous iron did not accumulate in the ocean but rather was removed as an insoluble component of the sediment, thus retaining the isotopic composition of the Fe inputs to the ocean at very close to the crustal average ($\delta^{56}Fe \approx 0‰$).

As is always the case during the early development of paleoenvironmental proxies, more observations are needed before firm, globally relevant interpretations can be made. If the trends do persist, though, a number of outstanding questions may eventually be answered: Was iron an important component of the Precambrian oxygen balance? Was BIF deposition a major sink for iron throughout the Precambrian before 2.3 billion years ago, or was its deposition more episodic, separated by long intervals of non-BIF deposition (*11*)? Was the end of BIF deposition the result of the establishment of oxygenated (*10*) or sulfidic (*8*, *9*) deep-ocean conditions? Did Phanerozoic (since 542 million years ago) oceanic anoxic events leave tell-tale iron-isotope signatures? Ultimately, we will be able to use the iron isotopes, as we've used carbon and sulfur isotopes, to put quantitative constraints on rates of Precambrian iron cycling, and thus on the extent to which iron provided a source or sink for oxygen during this critical interval of Earth history.

References and Notes

1. G. E. Valley, H. H. Anderson, *J. Am. Chem. Soc.* **69**, 1871 (1947).
2. O. J. Rouxel *et al.*, *Science* **307**, 1088 (2005).
3. K. Rankama, *Isotope Geology* (Pergamon, London, 1954).
4. G. Bluth, L. R. Kump, *Eos* **69**, 515 (1988).
5. B. L. Beard *et al.*, *Science* **285**, 1889 (1999).
6. N. Dauphas *et al.*, *Science* **306**, 2077 (2004).
7. M. A. Arthur, B. Sageman, *Annu. Rev. Earth Planet. Sci.* **22**, 499 (1994).
8. D. E. Canfield, *Nature* **396**, 450 (1998).
9. The stage designations are those of (*2*), except that Stage 3 is divided into euxinic (3a) and oxygenated (3b) substages. According to (*10*), there was no stage 3a (interval of oceanic euxinia); the oceans became oxygenated at 1.8 billion years ago.
10. H. D. Holland, *The Chemical Evolution of the Atmosphere and Ocean* (Princeton Univ. Press, Princeton, NJ, 1984).
11. A. E. Isley, D. H. Abbott, *J. Geophys. Res.* **104**, 15461 (1999).

10.1126/science.1107482

NEUROSCIENCE

Adaptive Coding

K. Richard Ridderinkhof and Wery P. M. van den Wildenberg

A century ago, psychologists considered cognitive control to be a major player in decision-making (*1*, *2*). Yet, the study of how perception and action are mediated by instructions and intentions entered a twilight zone during the middle part of last century as behaviorists turned their backs on mental processes that they could not directly observe. It was not until the turn of the millennium that psychologists and neuroscientists regained their interest in understanding how the human brain regulates the flow of information to achieve intended goals. Notably, this resurgence of interest in cognitive control (*3*) coincided with methodological innovations such as functional magnetic resonance imaging (fMRI) and electrical recordings from single neurons. Such techniques enable dissection of the brain activities that underlie mental operations. Two studies, on pages 1121 (*4*) and 1118 (*5*) of this issue, nicely illustrate another development that may boost investigation of cognitive control beyond its renaissance. The new work was inspired by the notion that neurons in the frontal region of the brain (or neuronal ensembles, or even brain areas) may dynamically and adaptively switch between multiple functions rather than statically accomplishing preset tasks.

In their study, Machens and colleagues (*4*) inserted tiny electrodes into the prefrontal cortex of monkey brains to record the firing rates of single neurons while the monkeys performed a dynamic decision-making task. The task involved the comparison of two quantities (two frequencies of vibration presented to a fingertip), separated by a brief delay. The mental operations involved in this quantity-comparison task included (i) perceiving the first signal (S1), (ii) holding it in working memory for several seconds, and (iii) perceiving the second signal (S2) and deciding whether it was of lower or higher quantity than the first.

Some monkey neurons expressed a clear preference for the low vibration frequency (quantity), whereas others fired preferentially in response to the higher quantity. Although neurons in the secondary somatosensory cortex of monkey brain remained silent in the delay interval between S1 and S2, their preferences for the low versus the high quantity remained invariant. Neurons in the prefrontal cortex, by contrast, showed differential preferences for the low versus the high quantity not only during the presentation of S1, but throughout the delay interval, during which they sustained their preferential firing patterns. In the decision phase, however, prefrontal cortex neurons no longer encoded information about high versus low quantities, but rather encoded information for "S2 < S1" or "S2 > S1", respectively. Thus, the firing rates of single neurons in the prefrontal cortex first encode the quantity of S1, then represent the active maintenance of that quantity in working memory, and finally reverse sign to encode the appropriate decision. Computer simulations of firing in a neural network, which capitalize on mutual inhibition between opposing units, confirmed the firing patterns produced by real neurons as observed by Machens and coworkers. Their study provides a fruitful synthesis of real-world neurophysiological data with the nonlinear modeling of dynamic systems. The Machens *et al.* results clearly show that networks of prefrontal cortex neurons

K. R. Ridderinkhof is in the Department of Psychology, University of Amsterdam and Leiden University, the Netherlands. E-mail: k.r.ridderinkhof@uva.nl W. P. M. van den Wildenberg is in the Laboratory of Neurobiology and Cognition, Centre National de la Recherche Scientifique and Université de Provence, Marseille, France. E-mail: wery@dds.nl

can dynamically adapt and reconfigure the encoding functions represented in their firing patterns as the cognitive flow develops, without changing their connectivity.

Nevertheless, the question remains: How do neurons "know" when to encode a particular activity? A larger scale implementation of adaptive coding, like that introduced by Brown and Braver (*5*) in their new study, may provide some answers. Cognitive control should not simply be considered a basic mental function supported by static, dedicated neural systems. Instead, instantiations of cognitive control should be envisioned as emergent properties of the neural network configuration, with more elementary mechanistic processes being tailored to allow new and unique functions to emerge (*3*). The notion of "adaptive coding" applies not only to within-trial changes in the firing patterns of prefrontal cortex neurons, but also to the emergence of cognitive control through learning. For example, the specialized higher order nature of a process called performance-error monitoring may be a new function that emerges from more basic neural mechanisms for conflict detection. Such conflict-detection mechanisms usually reside in medial frontal cortex (MFC) neurons, which detect the simultaneous activation of competing correct and incorrect responses (*6*). Brown and Braver (*5*) take this notion one step further with their proposal that both error detection and conflict monitoring are special cases of a more fundamental computational process in which activation of MFC neurons is proportional to the perceived likelihood of an error taking place.

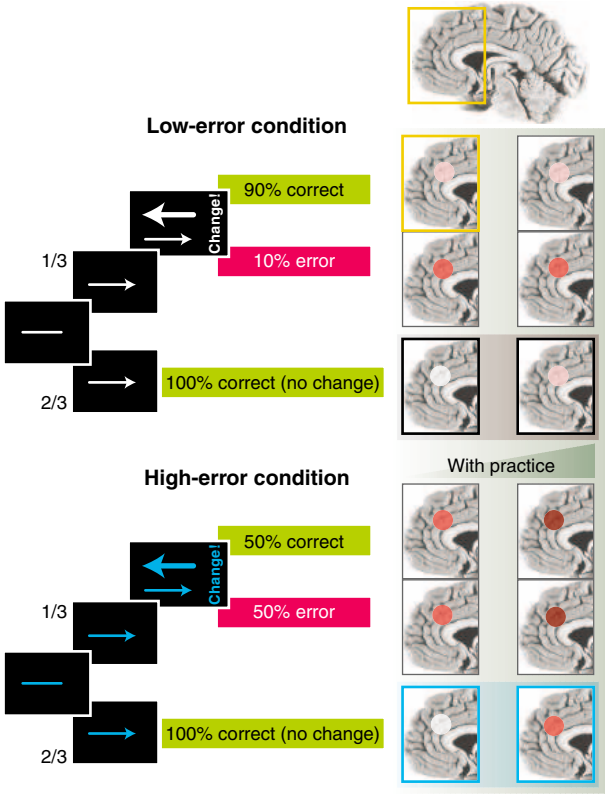

Predicting error likelihood. In Brown and Braver's fMRI study, human volunteers undertook a stop-change task. In this task, a rapid left- or right-hand button-press response is designated by the direction of an arrow; this response must be reversed when a second arrow pointing in the opposite direction is presented (*5*). The task uses a tracking algorithm that adjusts the time of presentation of the change-signal (opposite arrow) and hence controls the likelihood of making an error. On each trial, the error likelihood is indicated in advance by a color cue (blue for high error, white for low error). With blue-color cues, human volunteers had a harder time changing their response after a change signal (50% errors) than with white-color cues (10%). Brain areas highlighted in red indicate MFC regions that are activated by the stop-change task (the greater the MFC activation, the deeper the red color). Most importantly, during no-change trials (which lack error-inducing tactics and thus lack conflict), MFC activity increased with practice, especially in response to blue color cues, reflecting an improved ability to predict the likelihood of making an error.

Brown and Braver assume that representations of the likelihood of error by the MFC develop through experience. Such representations build on reinforcement-learning processes that are mediated by phasic decreases in midbrain dopamine projections to the MFC when ongoing events turn out worse than expected (*7*, *8*). To test their assumption, the investigators invited human volunteers to perform a stop-change task (*9*) in which a rapid left- or right-hand button-press response is designated by the direction of an arrow (see the figure). This response requires reversing in one-third of the trials when a second arrow pointing in the opposite direction is presented at a later time point. The second arrow is presented at variable time intervals after the first, calibrated so as to produce error rates of 10% or 50% unchanged responses (low-error and high-error conditions, respectively). On each trial, the error likelihood is indicated in advance by a color cue (blue for high-error likelihood, white for low-error likelihood). During execution of the stop-change task, fMRI revealed greater activity in the MFC during the high-error change trials compared with low-error change trials. This was the case even when only correct responses to change trials were considered and failure-to-change errors were excluded from the analysis. Moreover, the effects of error likelihood were seen even on no-change trials, when no second (change) arrow was presented at all. Blue color cues, which came to be associated with a high likelihood of failure-to-change errors, elicited greater activity in the MFC during no-change trials than did white color cues, which were associated with low-error likelihood. The authors cleverly captured these data together with the observation that MFC activity gradually emerged over the course of the experimental session. They did this by conducting simulations with a nonlinear neural-network model that computationally implemented their assumptions about the prediction of error likelihood. After individuals gradually learned the associations between color cue and error likelihood, presentation of the high-error color cue was sufficient to increase activity in the MFC, even in the absence of other features that might cause conflicting responses or errors (see the figure).

Thus, the MFC determines that goals may not be achieved or rewards may not be obtained unless the level of cognitive control is subsequently increased. This increase in cognitive control takes place not only when a response conflict indicates a reduced probability of obtaining a reward, or when errors signal the loss of an anticipated reward, but also when the context *predicts* the likelihood of imminent errors (*5*). Together, these patterns of neural firing confirm that the principal task of the MFC is to monitor performance, that is, to compute and signal the likelihood of obtaining or losing rewards in response to particular actions (*10*). The MFC thus guides decisions about which actions are worth taking (*11*). One challenge of the error-likelihood model that needs to be addressed is the incorporation of transient disengagements of MFC activity that foreshadow errors (*12*). Occasional lapses and other forms of variability are characteristic of all cognitive processes. Such baroque characteristics should be accomodated in our models of cognitive control as we move beyond the era of the renaissance.

References

1. W. James, *The Principles of Psychology* (Dover Publications, New York, 1890).
2. N. Ach, *Über den Willensakt und das Temperament* (Quelle & Meyer, Leipzig, Germany, 1910).
3. B. Hommel *et al.*, *Psychol. Res.* **66**, 215 (2002).
4. C. K. Machens *et al.*, *Science* **307**, 1121 (2005).
5. J. W. Brown, T. S. Braver, *Science* **307**, 1118 (2005).
6. N. Yeung *et al.*, *Psychol. Rev.* **111**, 931 (2004).
7. W. Schultz, *Neuron* **36**, 241 (2002).
8. C. B. Holroyd, M. G. H. Coles, *Psychol. Rev.* **109**, 679 (2002).
9. G. D. Logan, J. Burkell, *J. Exp. Psychol. Hum. Percept. Psychophys.* **12**, 549 (1986).
10. K. R. Ridderinkhof, *et al.*, *Science* **306**, 443 (2004).
11. M. F. S. Rushworth *et al.*, *Trends Cogn. Sci.* **8**, 410 (2004).
12. K. R. Ridderinkhof *et al.*, *Neurosci. Lett.* **348**, 1 (2003).

10.1126/science.1109837

Editing at the Crossroad of Innate and Adaptive Immunity

Priscilla Turelli and Didier Trono*

Genetic information can be altered through the enzymatic modification of nucleotide sequences. This process, known as editing, was originally identified in the mitochondrial RNA of trypanosomes and later found to condition events as diverse as neurotransmission and lipid metabolism in mammals. Recent evidence reveals that editing enzymes may fulfill one of their most essential roles in the defense against infectious agents: first, as the mediators of antibody diversification, a step crucial for building adaptive immunity, and second, as potent intracellular poisons for the replication of viruses. Exciting questions are raised, which take us to the depth of the intimate relations between vertebrates and the microbial underworld.

Compared with alternative splicing, a process in which fragments of RNA transcripts are differentially cut and pasted, editing seems a rather subtle fine-tuning of the coding capacity of genomes. Yet the power of this process for genetic diversification is overwhelmingly illustrated by its crucial role in allowing B lymphocytes to generate high-affinity antibodies against an almost infinite variety of antigens. In mammals, there are two main classes of editing enzymes, both of which deaminate encoded nucleotides: one generates inosine (I) from adenine (A), the other uridine (U) from cytidine (C). Both classes of proteins are characterized by the presence of closely homologous zinc-coordinating catalytic domains, and phylogenetic analyses indicate that this now diversified family of proteins evolved from an ancestral cytosine deaminase involved in pyrimidine metabolism (*1*). Activation-induced deaminase (AID) likely was the first editing deaminase to appear in vertebrates, as this subphylum emerged from the chordata and started to develop an adaptive immunity (*2*). The pattern of chromosomal distribution and the degree of homology of the 11 AID-related cytidine deaminase genes found so far in humans and other primates indicate that the other members of the family arose through a series of gene transpositions and duplications (*3*–*6*) (Fig. 1). It is interesting that this process appears to have undergone a sharp acceleration in primates, because the genome of rodents, for instance, contains only four AID-related cytidine deaminase genes.

APOBEC1 [apolipoprotein B (apoB)–editing catalytic subunit 1] was the first identified mammalian cytidine deaminase (*7*). Like its paralogs, APOBEC1 exhibits a narrowly tissue-specific distribution. Expressed in enterocytes, it is responsible for introducing a premature nonsense codon in the *apoB* mRNA by changing cytidine 6666 to uridine. The resulting truncated form of apoB and its liver-specific full-length counterpart play distinct roles in lipid metabolism. RNA editing by APOBEC1 critically depends on its homodimerization and on its recruitment by ACF (APOBEC1 complementation factor), an RNA-binding protein that recognizes a mooring sequence in the *apoB* mRNA. An "editosome" is thereby formed, the activity of which is modulated by auxiliary components (*8*).

Cytidine Deamination and the Emergence of Adaptive Immunity

When mature B lymphocytes migrate to secondary lymphoid organs, such as spleen and lymph nodes, and encounter antigens, they become activated and rapidly proliferate. At the same time, their genome undergoes two kinds of alterations at the immunoglobulin gene locus: class switch recombination (CSR) and somatic hypermutation (SHM). CSR replaces the constant region of the immunoglobulin heavy chain gene (C_H), which triggers a switch of immunoglobulin isotype from the original IgM to IgG, IgE, or IgA. SHM introduces point mutations in the variable (V), antigen-binding region of both heavy and light chain genes and thus creates a repertoire of B cells from which producers of high-affinity antibodies are then selected (*9*). Although apparently dissimilar, these two genetic events both depend on activation-induced deaminase. In birds, diversification of the antigen-binding site of antibodies is accomplished by another mechanism, gene conversion (GC), but it too requires AID. Even though it was initially suggested that AID might act by editing the RNA encoding for some DNA-modifying enzyme, several lines of recent evidence support a model whereby CSR, SHM, and GC all result from the initial conversion by AID of cytidine to uridine in the immunoglobulin locus DNA in a transcription-dependent and strand-biased fashion (*10*, *11*). It is noteworthy that the enzyme uracil DNA glycosylase (UNG), a DNA repair enzyme that removes uracil from single- and double-stranded DNA, is also required for all three AID-dependent processes. This has been interpreted by most as supporting the DNA-editing model of antibody diversification. However, the recent demonstration that catalytically inactive *ung2* mutants are functional in tissue culture–based systems of CSR adds a level of complexity that precludes definitive conclusions regarding the mechanism of AID action (*12*).

A Viral Shield Reveals a Cellular Weapon

After the human immunodeficiency virus (HIV) was first isolated in the early 1980s, the sequencing of its genome rapidly delineated nine genes, the products of which were soon assigned a variety of structural, enzymatic, or regulatory functions. All but one, *vif* (virion infectivity factor, initially called *sor*), would largely elude the perspicacity of researchers for close to another 20 years. It did not take long to demonstrate that the ~200–amino acid–long Vif protein, which accumulates in the cytoplasm of infected cells late in the viral life cycle, is important for virion infectivity (*13*), but more tedious efforts were required to reveal first that *vif*-mutated virions can enter cells normally but yield markedly reduced levels of proviral DNA (the integrated form of the reverse-transcribed RNA genome) and, second, that this defective phenotype is entirely

School of Life Sciences, Ecole Polytechnique Fédérale de Lausanne, CH-1015 Lausanne, Switzerland, and "Frontiers in Genetics" National Center for Competence in Research, and Department of Microbiology and Molecular Medicine, School of Medicine, University of Geneva, 1211 Geneva 4, Switzerland.

*To whom correspondence should be addressed. E-mail: Didier.Trono@medecine.epfl.ch

conditioned by the cell releasing the virus, not by its next target cell (*14*, *15*). ΔVif-permissive and ΔVif-restrictive cells were thus distinguished from each other, the latter, not surprisingly, was composed of the cells normally infected by HIV in vivo, namely, primary T lymphocytes and macrophages. An important breakthrough came with the demonstration that ΔVif restrictiveness is a dominant phenotype and, hence, reflects an intracellular antiviral activity specifically countered by Vif (*16*, *17*). Finally, through DNA subtraction, an approach requiring much patience, a member of the human cytidine deaminase family, APOBEC3G, was identified as this intracellular restriction factor (*18*). This discovery immediately set up intense efforts to elucidate the mechanisms of APOBEC3G action against HIV and of its blockade by Vif. It ended up unveiling a far broader defense system than was initially suspected.

Cytidine Deamination as a Broad Line of Defense Against Exogenous Retroelements

APOBEC3G is a cytoplasmic protein, the product of one of the eight APOBEC3 genes found on human chromosome 22 (*3*) (Fig. 1). In the absence of Vif, it is packaged into HIV particles during assembly, apparently through formation of a complex with the RNA-recruiting nucleocapsid (NC) region of the Gag viral protein, an interaction possibly strengthened by the nonspecific binding of RNA to NC (*19*–*21*). APOBEC3G subsequently associates with the viral reverse-transcription complex, where it deaminates cytidine residues to uridine in the nascent minus-strand viral DNA (Fig. 2, upper left). These dU-rich transcripts are then either degraded or serve as templates for the synthesis of plus-strand DNA, thus yielding proviruses that are largely nonfunctional due to G-to-A hypermutation (*22*–*25*). Vif counters this antiviral defense by connecting APOBEC3G with a poly-ubiquitinating complex comprising elongin B/C, Cul5, and Rbx1 (*26*). This prevents the virion incorporation of the deaminase and triggers its proteasomal degradation, which allows the production of HIV particles that can fully express their infectious potential.

The antiretroviral spectrum of human APOBEC3G extends well beyond HIV, because it can also block other lentiviruses, such as the simian immunodeficiency virus (SIV) and equine infectious anemia virus (EIAV), as well as the gammaretrovirus murine leukemia virus (MLV) (*23*, *25*) (Table 1). APOBEC-mediated editing thus constitutes a barrier to the cross-species transmission of several retroviral pathogens.

Additional members of the human APOBEC3 family are endowed with activity against HIV, for instance, APOBEC3F, which is largely coexpressed and perhaps coregulated, with APOBEC3G. The two enzymes, however, can be distinguished by their target sequence consensus: APOBEC3G favors the 5′-CC dinucleotide (underline marks the target), whereas APOBEC3F prefers 5′-TC (*27*–*30*). Human APOBEC3B also exhibits moderate levels of activity against HIV, with an APOBEC3F-like consensus, but is resistant to the action of Vif (*27*). However, the immediate relevance of this finding is unclear, because this protein is at best weakly antiviral and is expressed in small amounts in the natural targets of HIV. Future drugs aimed at blocking the interaction between Vif and APOBEC3G and APOBEC3F may thus have the potential to constitute valid additions to current AIDS therapies.

The editing of retroviral reverse transcripts by APOBEC family members suggested that these enzymes might also act on other types of retroelements. Like retroviruses, hepatitis B virus (HBV) replicates through reverse transcription. However, although the retroviral RNA genome is copied into DNA, for the most part, once the virus enters target cells, HBV and other hepadnavirus particles contain a partially double-stranded DNA genome, synthesized from a pregenomic RNA by the viral reverse transcriptase within subviral core particles in the cytoplasm of virus producer cells. Recent experiments demonstrate that this process can be efficiently inhibited by human APOBEC3G and APOBEC3F (*31*, *32*) (Fig. 2, bottom). However, the editing function of the cellular enzymes is dispensable for this effect, which rather reflects either an inhibition of HBV pregenomic RNA packaging or a destabilization of the viral reverse transcription complex, precluding HBV DNA accumulation. In the HepG2 hepatoma cell line, the same phenomenon prevails, but some APOBEC3G-mediated HBV DNA editing can also be detected (*33*).

These data raise at least three questions. First, do antiviral cytidine deaminases participate in the noncytopathic clearance of HBV that takes place in most patients acutely infected with this virus? APOBEC3 family members are expressed at only low levels in hepatocytes, but they could be induced by HBV infection, for instance, under the influence of cytokines. HBV replication is rapidly abolished in the liver of HBV transgenic mice treated with an interferon-inducing agent; this inhibition reflects primarily loss of capsids containing

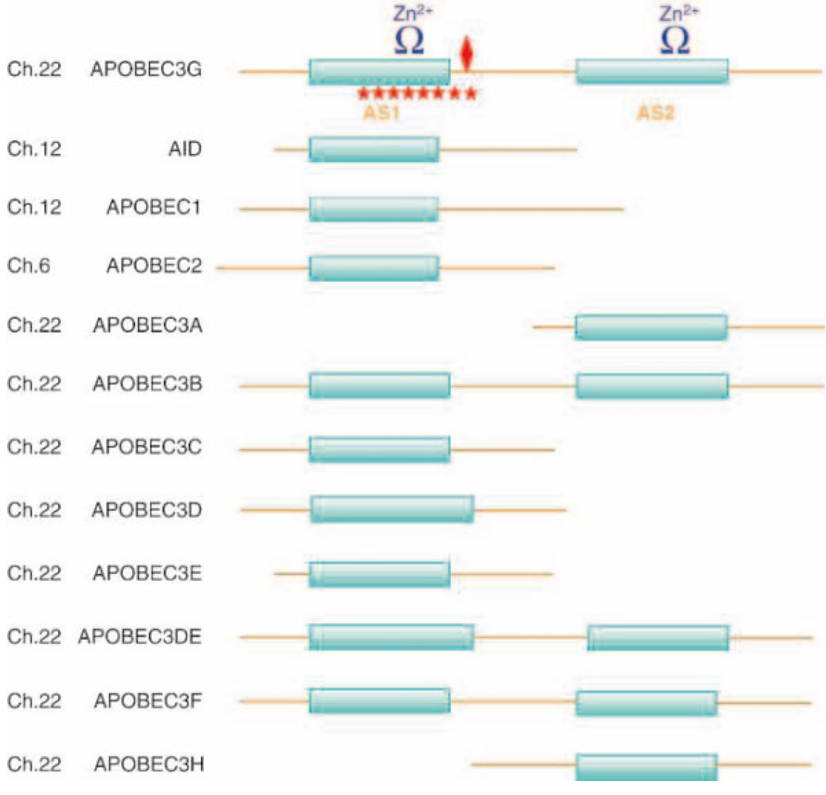

Fig. 1. The primate cytidine deaminases family. Schematic representation of the 12 known cytidine deaminases, with chromosomal location of corresponding gene indicated on left. All family members share at least one zinc-dependent cytidine deaminase active site (AS). APOBEC3B, -3G, and -3F are the result of a further duplication; APOBEC3DE is encoded by a predicted splicing variant. Also indicated is the domain implicated in HIV-1 Vif binding (red stars), including the critical Asp^{128} residue (red diamond) responsible for its species specificity.

pregenomic RNA, reminiscent of the observed effect of APOBEC3G in tissue culture (*31*, *34*). Also, recent data indicate that stimulation of the protein kinase C (PKC)/mitogen-activated protein kinase kinase (MEK)/extracellular signal–regulated kinase (ERK) pathway enhances APOBEC3G expression (*35*). A second question is: Would it be possible to induce the expression of antiviral cytidine deaminases in the liver of individuals chronically infected with HBV, either pharmacologically or by gene transfer, in order to eradicate the virus? Whereas the constitutive expression of wild-type forms of these proteins might carry the risk of introducing mutations in the cellular DNA (*36*), catalytically inactive variants fully conserving their antiviral potential would be devoid of such a side effect. Finally, does cytidine deamination explain the occasional emergence of G-to-A mutated HBV isolates, including HbeAg-negative strains and vaccine escape variants (*37*)?

Human antiviral cytidine deaminases can thus inhibit retroelements by at least two distinct mechanisms: single-stranded DNA editing (for retroviruses) and noncatalytic blockage of DNA accumulation (for hepadnaviruses). A third mode of antiviral action for this class of proteins was discovered by examining how rat APOBEC1 interferes with HIV replication: In that case, the editing process targeted not only the virus minus-strand DNA but also its genomic RNA (*38*) (Fig. 2, top right). This raises the possibility that APOBEC-mediated C-to-U editing might affect some of the innumerable viruses that replicate entirely through RNA. Accordingly, the spectrum of innate antiviral resistance conferred by cytidine deaminases might be of considerable breadth.

Mechanisms of Viral Escape

Pathogenic retroviruses seem a relatively new entry in the realm of factors that can cause human diseases. Nevertheless, the brutality of the AIDS epidemic cruelly illustrates the limits of our resistance to this class of pathogens. Evolution allows viruses to overcome host defenses, and retroviral inhibition by cytidine deamination has been no exception to this rule. The acquisition of a *vif* gene is the best-documented viral countermeasure against APOBEC proteins, but, interestingly, it is effective in an almost completely species-specific manner. *Vif*-defective HIV-1, for instance, is blocked by APOBEC3G from human, chimpanzee, rhesus macaque, and African green monkey (AGM) and by mouse APOBEC3. However, the Vif protein of HIV-1 can only counter human and chimpanzee APOBEC3G and is ineffective against the rhesus macaque, AGM, and mouse orthologs of the enzyme. Conversely, Vif from SIV_{AGM} is active against AGM but not against human APOBEC3G (*39*). Remarkably, a single amino acid difference at position 128 of these two highly homologous proteins governs their virus-specific binding to Vif, hence, their inactivation by the viral protein (*40*–*42*) (Fig. 1).

The *vif*-devoid MLV is efficiently blocked by human APOBEC3G but resists APOBEC3F and APOBEC3B through unknown mechanisms (Table 1). Unsurprisingly, MLV also escapes the action of murine APOBEC3, the antiviral cytidine deaminase found in its normal host (*27*), seemingly by avoiding the packaging of the enzyme during virion assembly (*43*). This raises questions about how other viruses might protect themselves against cytidine deaminases. For instance, does EIAV, which again does not contain a *vif* gene, proceed similarly in order to spread in its equine host, if one assumes that there is a horse antiviral cytidine deaminase? Alternatively, does this lentivirus hide a *vif*-like function in some other of its genes or does it avoid replicating in cell types that express the cellular enzyme?

What about human T cell leukemia virus (HTLV), another *vif*-less retrovirus that happens to infect the same CD4-positive T lymphocytes as HIV, that is, it targets cells expressing APOBEC3G and APOBEC3F? Has this virus evolved alternative strategies to counter the antiviral cytidine deaminases, for instance, by modulating their expression at the transcriptional level, or does it tolerate

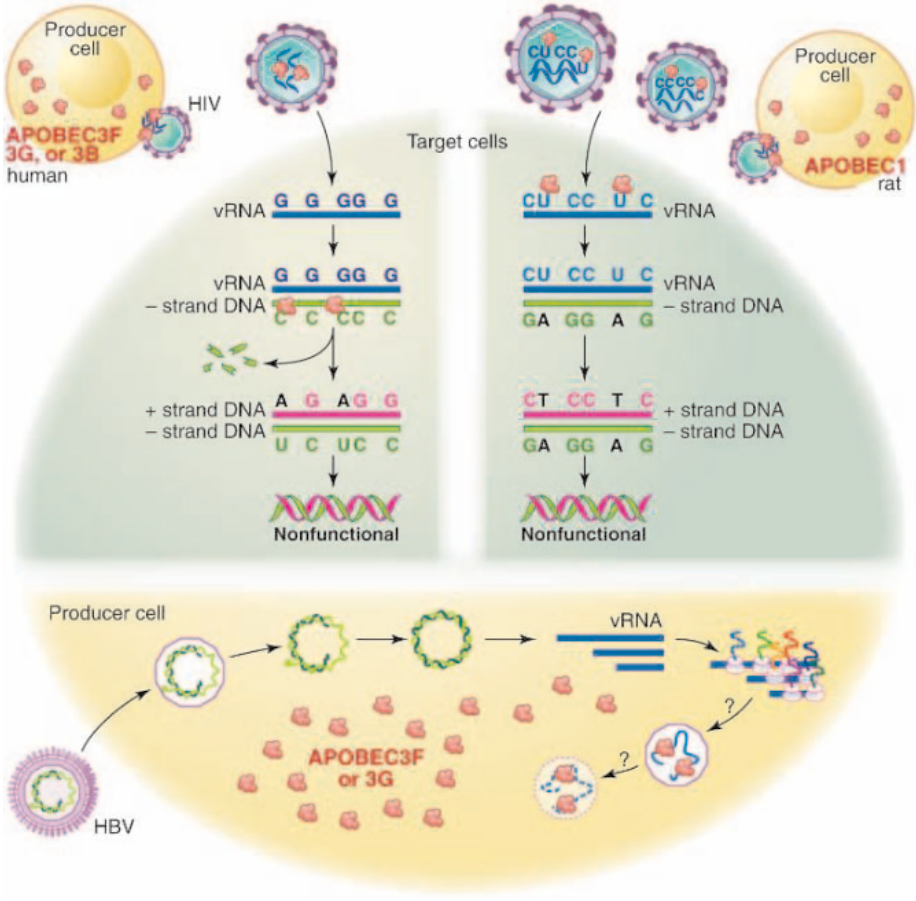

Fig. 2. One family of proteins, three antiviral mechanisms. (**Top left**) When expressed in HIV producer cells in the absence of Vif, huAPOBEC3F, -3G, or -3B is packaged in outgoing virions. In target cells, APOBEC3F, -3G, and, to a lesser extent, -3B deaminate cytidines to uridines in the growing minus-strand DNA reverse-transcribed from the viral genomic RNA. Many of these dU-rich reverse transcripts are degraded (*52*). The others serve as templates for the synthesis of G-to-A hypermutated plus-strand DNA. The resulting proviruses are nonfunctional. (**Top right**) Rat APOBEC1, possibly packaged in the outgoing virions, can also deaminate cytidines in the HIV viral genomic RNA. This leads to G-to-A changes in the minus-strand DNA and, hence, to C-to-T mutations in the plus-strand DNA. The resulting hypermutated proviral DNAs can integrate but are defective. (**Bottom**) After infection of APOBEC3G- or APOBEC3F-expressing cells, the partially double-stranded DNA HBV genome is repaired by cellular enzymes, and the various viral RNAs are transcribed and translated normally. However, there is a defect either in the assembly of capsids containing pregenomic RNA or in the stability of the viral reverse transcription complex. The end result is a sharp drop in the production of HBV DNA-containing virions. [Illustration: Katharine Sutliff/*Science*]

T cells, which it ultimately transforms, as dead ends for its replication? HTLV exhibits notoriously low levels of infectivity in tissue culture, but the basis of this phenotype likely depends on multiple factors.

Discovering the full antiviral spectrum of APOBEC family members may be a complicated task. Indeed, viruses that replicate in a given species will generally have evolved ways to escape inhibition by the editing cytidine deaminases expressed in this host. So far, the antiviral potential of this class of innate resistance factors was revealed by testing viruses that were either invalidated by specific mutations (as for ΔVif HIV) or confronted with noncognate APOBEC proteins (as for MLV and human APOBEC3G).

Endogenous Targets for APOBEC-Mediated Editing? Evolutionary Considerations

The nature of the physiological targets of APOBEC1 and AID suggests that at least some other members of the family edit cellular genes, whether at the RNA or DNA level. However, evolutionary data support a model whereby most APOBEC proteins play a major role at the interface between hosts and pathogens. The mouse genome encodes orthologs of AID, APOBEC1 and APOBEC2, but contains only one APOBEC3 gene, compared with eight in primates. This recent expansion of the APOBEC gene cluster was further modulated by repeated episodes of positive selection during primate evolution, as indicated by the accumulation of nonsynonymous nucleotide changes in several of these genes, particularly at positions coding for charged residues likely to participate in protein-protein interactions (*5*, *6*). Although only human APOBEC3B, -3F, and -3G have so far been demonstrated to carry antiviral activity, a sequence comparison between the genomes of *Homo sapiens* and other primates indicates that APOBEC1, -3C, -3D, and -3E have also been subjected to this type of positive selection, hence, have likely participated, at least occasionally, in host defense (*5*). Only the heart- and muscle-restricted APOBEC2 and the keratinocyte-specific APOBEC3A seem to have escaped this process and thus may have cellular sequences as their exclusive targets.

Identifying the genetic conflicts that have shaped the APOBEC family is a task of great interest. The apparent antagonistic coevolution of these proteins with invading genetic elements started long before the appearance of modern lentiviruses (*5*, *6*), which points to additional pressures and is consistent with the demonstrated effect of these antivirals on other types of retroelements. The presence of a single APOBEC3 protein in the mouse may reflect the development of an alternative, yet unidentified, form of innate antiviral immunity in this species. However, there is a striking evolutionary coincidence between the expansion of the APOBEC gene cluster and the abrupt drop in retrotransposon activity that took place in primates, compared with rodents (*44*).

Retrotransposons cumulatively account for about one-third of the human genome and are commonly classified as those that bear long terminal repeats (LTRs), also known as endogenous retroviruses, and those that do not, of which only L1 elements (LINE-1, long interspersed nucleotide element–1) are autonomous (by contrast with SINE elements and Alu repeats) (*45*). Retrotransposons actively participate in genome remodeling and, as such, may facilitate adaptation. However, they also represent genetic threats, because they can disrupt genes by insertional mutagenesis, promote translocations and other rearrangements by recombination, generate aberrant cellular transcripts from their promoter, and exert antisense effects. The mouse genome contains up to 3000 active L1 elements and shows evidence for ongoing LTR retrotransposition. By comparison, only 40 to 60 L1 elements are active in humans, and all human endogenous retroviruses (HERVs) appear lethally incapacitated. The presence of human-specific HERV proviruses and their absence in corresponding loci of other primates, nevertheless, indicate that a subset of these LTR retrotransposons has been active during the recent evolution of hominoids.

Although transcriptional silencing via cytosine methylation of CpG dinucleotides is a major mechanism of retrotransposon control, one can speculate that destabilization or hypermutation of their reverse transcripts by cytidine deamination also participates in this process. Particularly intriguing are the high levels of human APOBEC3G and APOBEC3F detected in testes and ovaries (*3*) and the extensive level of genome demethylation that prevails during the preimplantation phase of embryonic development, two settings in which expression of retroelements is thought to occur. APOBEC3G has been shown not to inhibit human L1 retrotransposition in a tissue culture–based assay (*46*), which is perhaps not too surprising considering that L1 reverse transcription occurs in the nucleus, whereas APOBEC3G is a cytoplasmic protein. In contrast, HERVs carry strong functional homologies with exogenous retroviruses and, as such, could be sensitive to APOBEC-mediated cytidine deamination. Short of the identification of active HERVs and of a tissue culture–based assay for measuring their retrotransposition ability, a careful comparison of the A/G content of endogenous retroviruses with that of related exogenous retroelements might give hints regarding their past exposure to cytidine deaminases. In strong support of a protective role for cytidine deaminases against genome destabilization by endogenous retro-

Table 1. Genetic and functional characteristics of human and rodent cytidine deaminases. Extensive comparisons between primate and human genomes reveal that AID, APOBEC2, and APOBEC3A have been submitted to purifying rather than positive selection. Reported patterns of expression; antiviral activity against HIV, HBV, and MLV; and sensitivity to HIV-1 Vif action are indicated for each member of the family. ND, not determined.

Cytidine deaminase	Positive selection	Reported expression	Antiviral activity			Vif sensitivity
			HIV	MLV	HBV	
Human						
APOBEC1	+	Small intestine, spleen	–	–	ND	ND
APOBEC2	–	Heart and muscles	ND	ND	ND	ND
AID	–	Activated B cells	–	–	ND	ND
APOBEC3A	–	Keratinocytes	–	–	ND	ND
APOBEC3B	+	PBLs, many tumor cell lines	±	–	ND	–
APOBEC3C	+	PBLs, hear, spleen, testes, ovary, prostate, thymus … many tumor cell lines	–	–	ND	ND
APOBEC3D	+	None found so far	ND	ND	ND	ND
APOBEC3E	+	Pseudogene?	ND	ND	ND	ND
APOBEC3DE	+	None found so far	ND	ND	ND	ND
APOBEC3F	+	PBLs, macrophages, spleen, testes, ovary	+	–	+	±
APOBEC3G	+	PBLs, macrophages, spleen, lung, testes, ovary	+	+	+	+
APOBEC3H	ND	Lymphoid tissue, placenta	ND	ND	ND	ND
Mouse						
muAPOBEC1	ND	Spleen> liver, brain, kidney, lungs, testes, oocytes, ovary, embryonic stem cells	–	ND	ND	ND
muAPOBEC2	ND	Heart	–	ND	ND	ND
muAID	ND	Lymph nodes, oocytes, ovary > thymus, spleen	–	ND	ND	ND
muAPOBEC3	ND	Spleen, lungs > testes, PBLs?	+	–	ND	–

elements, recent experiments with murine intracisternal A-particles and MusD elements indicate that at least some murine endogenous retroviruses are sensitive to murine APOBEC3 and human APOBEC3G (*47*, *48*).

When Viruses Utilize the Host Deaminases

Even though Vif efficiently counters the antiviral action of APOBEC3G and APOBEC3F, some level of G-to-A mutation can be detected when wild-type HIV is produced in the presence of high levels of the deaminases. This apparent flaw may actually serve the virus by increasing its genetic diversity, thus enabling escape from adaptive immune responses or antiviral drugs. Even though the error-prone reverse transcriptase is likely to be the major factor driving HIV diversification, G-to-A hypermutation has been documented in proviral DNA sequences isolated from peripheral blood lymphocytes of HIV-infected individuals. In many cases, these nucleotide changes were extensive and clearly resulted in complete virus inactivation. However, specific G-to-A changes, often in sequences fitting the APOBEC3F and, more rarely, the APOBEC3G consensus, have been shown to govern resistance to protease inhibitors used in AIDS therapies (*49*). Because it is slightly less sensitive than APOBEC3G to Vif action, APOBEC3F may be a more important factor for HIV hypermutation in vivo (*28*).

An even more convincing case for the hijacking of deaminating enzymes by viral pathogens is provided by adenosine deaminases. These enzymes seem to act exclusively on free adenosine or on RNA. ADARs (adenosine deaminases that act on RNA) can induce codon changes (inosine is read as guanosine, G, during translation); alter splicing; or modify the subcellular localization of their substrate (*50*). Such editing was first shown to account for isoforms of the glutamate and serotonin receptors in the central nervous system. However, many inosine-containing RNAs have been detected, in particular in the brain, where ADARs most likely exert broad regulatory influences. ADARs are also interferon-inducible proteins that can target a wide array of viral RNAs with a variety of consequences, often beneficial to the virus. For minus-strand RNA viruses such as measles, A-to-I hypermutation has been proposed to promote persistence. For the DNA polyomavirus, ADAR-mediated editing facilitates the sequential expression of early and late viral transcripts. Finally, for the agent of hepatitis D, an A-to-I change at a specific position of the antigenomic RNA is essential to remove an amber codon and to allow synthesis of the viral capsid.

Many More Questions for the Curious Mind

Although defining the range of antiviral activities of editing enzymes certainly represents a most exciting challenge, many other questions need to be addressed. The biochemistry of APOBEC-mediated retroviral editing is still, in many regards, a black box. Is an editosome at play, as for APOBEC1? If so, are its additional components of cellular or viral origin? A unique opportunity to characterize the determinants of this reaction may be provided by the possibility of its completion within purified HIV-1 virions (*24*). What is the noncatalytic mechanism that underlies the blockade of HBV by several APOBEC family members? What regulates the expression of these antiviral proteins, in particular, in organs targeted by APOBEC-sensitive viruses? Do polymorphisms in APOBEC genes shape interindividual susceptibilities to human pathogens (*51*)? What is the tridimensional structure of the APOBEC-Vif interface, and does it open a window for the design of pharmacological inhibitors that could complement current AIDS therapies? Answers to these and other questions will take us to new frontiers in understanding the fine balance between vertebrates and their genetic invaders.

References and Notes

1. A. P. Gerber, W. Keller, *Trends Biochem. Sci.* **26**, 376 (2001).
2. K. Azumi *et al.*, *Immunogenetics* **55**, 570 (2003).
3. A. Jarmuz *et al.*, *Genomics* **79**, 285 (2002).
4. J. E. Wedekind, G. S. Dance, M. P. Sowden, H. C. Smith, *Trends Genet.* **19**, 207 (2003).
5. S. L. Sawyer, M. Emerman, H. S. Malik, *PLoS Biol.* **2**, E275 (2004).
6. J. Zhang, D. M. Webb, *Hum. Mol. Genet.* **13**, 1785 (2004).
7. B. Teng, C. F. Burant, N. O. Davidson, *Science* **260**, 1816 (1993).
8. V. Blanc, N. O. Davidson, *J. Biol. Chem.* **278**, 1395 (2003).
9. Z. Li, C. J. Woo, M. D. Iglesias-Ussel, D. Ronai, M. D. Scharff, *Genes Dev.* **18**, 1 (2004).
10. M. S. Neuberger, R. S. Harris, J. Di Noia, S. K. Petersen-Mahrt, *Trends Biochem. Sci.* **28**, 305 (2003).
11. J. Chaudhuri, C. Khuong, F. W. Alt, *Nature* **430**, 992 (2004).
12. N. A. Begum *et al.*, *Science* **305**, 1160 (2004).
13. A. G. Fisher *et al.*, *Science* **237**, 888 (1987).
14. D. H. Gabuzda *et al.*, *J. Virol.* **66**, 6489 (1992).
15. U. von Schwedler, J. Song, C. Aiken, D. Trono, *J. Virol.* **67**, 4945 (1993).
16. N. Madani, D. Kabat, *J. Virol.* **72**, 10251 (1998).
17. J. H. Simon, N. C. Gaddis, R. A. Fouchier, M. H. Malim, *Nature Med.* **4**, 1397 (1998).
18. A. M. Sheehy, N. C. Gaddis, J. D. Choi, M. H. Malim, *Nature* **418**, 646 (2002).
19. T. M. Alce, W. Popik, *J. Biol. Chem.* **279**, 34083 (2004).
20. S. Cen *et al.*, *J. Biol. Chem.* **279**, 33177 (2004).
21. E. S. Svarovskaia *et al.*, *J. Biol. Chem.* **279**, 35822 (2004).
22. D. Lecossier, F. Bouchonnet, F. Clavel, A. J. Hance, *Science* **300**, 1112 (2003).
23. B. Mangeat *et al.*, *Nature* **424**, 99 (2003).
24. H. Zhang *et al.*, *Nature* **424**, 94 (2003).
25. R. S. Harris *et al.*, *Cell* **113**, 803 (2003).
26. X. Yu *et al.*, *Science* **302**, 1056 (2003).
27. K. N. Bishop *et al.*, *Curr. Biol.* **14**, 1392 (2004).
28. M. T. Liddament, W. L. Brown, A. J. Schumacher, R. S. Harris, *Curr. Biol.* **14**, 1385 (2004).
29. H. L. Wiegand, B. P. Doehle, H. P. Bogerd, B. R. Cullen, *EMBO J.* **23**, 2451 (2004).
30. Y. H. Zheng *et al.*, *J. Virol.* **78**, 6073 (2004).
31. P. Turelli, B. Mangeat, S. Jost, S. Vianin, D. Trono, *Science* **303**, 1829 (2004).
32. P. Turelli, S. Jost, B. Mangeat, D. Trono, *Science* **305**, 1403 (2004).
33. C. Rösler, J. Köck, M. H. Malim, H. E. Blum, F. von Weizsäcker, *Science* **305**, 1403 (2004).
34. S. F. Wieland, L. G. Guidotti, F. V. Chisari, *J. Virol.* **74**, 4165 (2000).
35. K. M. Rose, M. Marin, S. L. Kozak, D. Kabat, *J. Biol. Chem.* **279**, 41744 (2004).
36. R. S. Harris, S. K. Petersen-Mahrt, M. S. Neuberger, *Mol. Cell* **10**, 1247 (2002).
37. S. L. Ngui, R. Hallet, C. G. Teo, *Rev. Med. Virol.* **9**, 183 (1999).
38. K. N. Bishop, R. K. Holmes, A. M. Sheehy, M. H. Malim, *Science* **305**, 645 (2004).
39. R. Mariani *et al.*, *Cell* **114**, 21 (2003).
40. B. Mangeat, P. Turelli, S. Liao, D. Trono, *J. Biol. Chem.* **279**, 14481 (2004).
41. B. Schrofelbauer, D. Chen, N. R. Landau, *Proc. Natl. Acad. Sci. U.S.A.* **101**, 3927 (2004).
42. H. P. Bogerd, B. P. Doehle, H. L. Wiegand, B. R. Cullen, *Proc. Natl. Acad. Sci. U.S.A.* **101**, 3770 (2004).
43. M. Kobayashi *et al.*, *J. Virol.* **78**, 8238 (2004).
44. R. H. Waterston *et al.*, *Nature* **420**, 520 (2002).
45. E. T. Prak, H. H. Kazazian Jr., *Nature Rev. Genet.* **1**, 134 (2000).
46. P. Turelli, S. Vianin, D. Trono, *J. Biol. Chem.* **279**, 43371 (2004).
47. M. Dewannieux, A. Dupressoir, F. Harper, G. Pierron, T. Heidmann, *Nature Genet.* **36**, 534 (2004).
48. C. Esnault *et al.*, *Nature* **433**, 430 (2005).
49. B. Berkhout, A. de Ronde, *AIDS* **18**, 1861 (2004).
50. B. L. Bass, *Annu. Rev. Biochem.* **71**, 817 (2002).
51. P. An *et al.*, *J. Virol.* **78**, 11070 (2004).
52. J. H. Simon, M. H. Malim, *J. Virol.* **70**, 5297 (1996).

53. We apologize to the investigators whose work could not be cited due to space limitations. Research in our laboratory is supported by the Swiss National Science Foundation, the European Union, and the Institut Clayton de la Recherche.

10.1126/science.1105964

Entropically Driven Helix Formation

Yehuda Snir and Randall D. Kamien*

In the crowded environment of the cell, long molecular chains frequently adopt ordered, helical conformations. Not only does this enable information to be tightly packed, as in chromatin, but it also allows the machines of transcription and repair to grapple on to a regular track. Though geometrically motivated models of folding (*1*) with nonlocal interactions corroborate detailed models of proteins (*2*), foldamers (*3*), and DNA, here we suggest a purely entropic approach to understanding the folding of helices that arises from a local and homogeneous interaction with depleting spheres. This depletion interaction (*4*) can be used as a surrogate for hydrophobicity, for polymer-polymer interactions, and for boundary layers in elastica and liquid crystals. For a broad range of depletors, maximizing entropy leads to a universal polymer geometry; as the depletors grow large on the scale of the polymer, this leads to the favoring of sheetlike folding.

We modeled our polymer as a solid, impenetrable tube (with radius t) immersed in a solution of hard spheres (with radius r) (*5*). The tube renders a region of space inaccessible to the depleting spheres (Fig. 1A). The spheres' entropy increases as this excluded volume decreases by the overlap volume, V_{overlap}. Though the size of the excluded region is fixed by r and t, the geometry can vary, allowing overlap of the inaccessible volumes from different parts of the polymer, thus increasing the entropy of the depleting spheres. If the tube takes on a regular helix, the excluded volumes from adjacent turns and the central region will overlap (Fig. 1B). For small spheres, the tube will bend into a helix with a pitch (P) to radius (R) ratio $c^* = 2.5122$. This optimal ratio is comparable to that seen, for instance, in many α helices of commonly found proteins (*1*) where $c \approx 5.4$ Å/2.7 Å = 2 is a lower bound. The optimal ratio decreases as the colloid size grows, tending toward zero (Fig. 1C). As r/t grows large, the helix radius will grow, causing a fixed length of tube to unwind. This limit of infinite helix radius is equivalent to a β sheet, because this geometry is equivalent to straight tubes lying in parallel.

As the colloid concentration increases, the tendency to form a helix will grow strong enough to bend stiff polymers. The persistence length l_{P} measures the relative stiffness of a rod and is the length scale over which the rod can bend. If a stiff rod of length L bends into a helix with curvature κ, the total change in free energy ΔF, including the entropy of the colloids at concentration n, will be $\Delta F \propto \frac{1}{2} L l_{\mathrm{P}} \kappa^2 - n V_{\mathrm{overlap}}$. Because the geometry of the helix relates V_{overlap}/L to the curvature, we can determine when $\Delta F < 0$; that is, when the depletion interaction dominates the bending stiffness. In Fig. 1D, we plot the value of the dimensionless control parameter $\theta = nr^3/(l_{\mathrm{P}}/t)$ at which the fully collapsed helix is degenerate with a straight tube for a variety of colloid radii. For segments of tube on the order of a few l_{P} that cannot bend back on themselves, the helix should be the tightest packing, as with packing spheres in tubes (*6*).

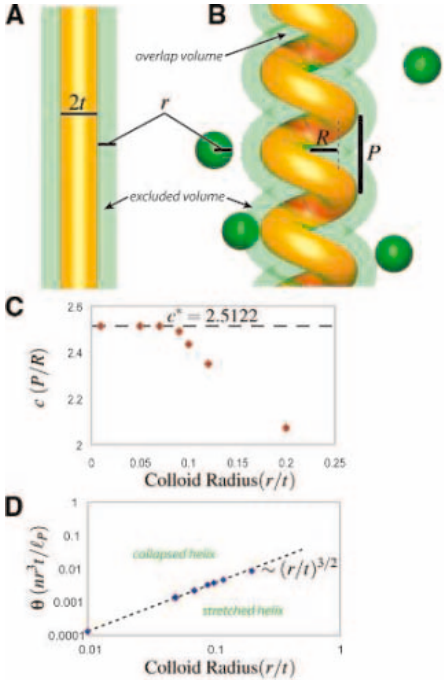

Fig. 1. (**A**) Excluded volume (green) for a straight tube (orange). (**B**) When the tube takes on a helical conformation, the excluded volume overlaps itself, reducing the total depleted volume. (**C**) The ratio $c = P/R$, which maximizes V_{overlap} versus r/t. The points were calculated by numerical integration of the overlap volume. As r/t goes to 0, the value of c approaches c^* (dashed line). (**D**) The value of θ at which $\Delta F = 0$ versus r/t. As nr^3 grows, the tube will go from a stretched helix to a collapsed (optimal) helix. The points fall on the curve $(r/t)^{3/2}$, consistent with the geometry (fig. S1).

Our results suggest an explanation for the helical conformations at the onset of protein folding, the helical fiberlike growth of one liquid crystalline phase into another, and the helical supermolecular scaffold in condensed chromatin, for instance. It is straightforward to generalize this work to the induced interaction between tubes. In order to maximize the entropy of the colloidal depletants, the two tubes would form helices of opposite handedness to achieve the tight packing known in liquid crystalline systems. Applied to the chromatin scaffold, the stereoconformations of sister chromatids in mitosis (*7*) may be attributed to crowding in the cell. As the density of polymers is increased, l_{P}/t controls their liquid crystalline ordering, while the volume fraction nr^3 of the colloids measures the intensity of the inter- and intratube attractions. The interplay of these competing interactions, controlled by θ, will lead to a rich phase diagram to explore through additional theory and experiment.

It has been observed that the helix content of polypeptides changes in response to solvent (*8*). Though our model predicts trends and lends understanding, the details of complex interactions are encoded in effective values of r and t, much as effective masses and spring constants are used to fit the modes of crystals. Our approach yields the same optimal geometry as equating the tube thickness to its global radius of curvature (*9*) and thus provides a physical approach to studying the conformations of knotted and linked tubes.

References and Notes

1. A. Maritan, C. Micheletti, A. Trovato, J. R. Banavar, *Nature* **406**, 287 (2000).
2. K. F. Lau, K. A. Dill, *Macromolecules* **22**, 3986 (1989).
3. S. H. Gellman, *Acc. Chem. Res.* **31**, 173 (1998).
4. S. Asakura, F. Oosawa, *J. Chem. Phys.* **22**, 1255 (1954).
5. J. R. Banavar, A. Maritan, *Rev. Mod. Phys.* **75**, 23 (2003).
6. G. T. Pickett, M. Gross, H. Okuyama, *Phys. Rev. Lett.* **85**, 3652 (2000).
7. E. Boy de la Tour, U. K. Laemmli, *Cell* **55**, 937 (1988).
8. J. Bello, *Biopolymers* **33**, 491 (1993).
9. O. Gonzalez, J. H. Maddocks, *Proc. Natl. Acad. Sci. U.S.A.* **96**, 4769 (1999).
10. We thank G. Grason and D. Wu for discussions. Supported by NSF grant nos. DMR01-02459 and DMR01-29804 and by the Pennsylvania Nanotechnology Institute.

Supporting Online Material
www.sciencemag.org/cgi/content/full/307/5712/1067/DC1
Fig. S1

12 October 2004; accepted 29 December 2004
10.1126/science.1106243

Department of Physics and Astronomy, University of Pennsylvania, Philadelphia, PA 19104, USA.

*To whom correspondence should be addressed. E-mail: kamien@physics.upenn.edu

Olmec Pottery Production and Export in Ancient Mexico Determined Through Elemental Analysis

Jeffrey P. Blomster,[1]* Hector Neff,[2] Michael D. Glascock[3]

The first Mesoamerican civilization, the Gulf Coast Olmec, is associated with hierarchical society, monumental art, and an internally consistent ideology, expressed in a distinct style and salient iconography. Whether the Olmec style arose in just one area or emerged from interactions among scattered contemporaneous societies remains controversial. Using elemental analysis, we determined the regional clay sources of 725 archaeological ceramic samples from across Mesoamerica. Exported Olmec-style ceramics originated from the San Lorenzo region of the Gulf Coast, supporting Olmec priority in the creation and spread of the first unified style and iconographic system in Mesoamerica.

More than 3000 years ago, the first civilization in ancient Mexico, the Olmec, coalesced along the Mexican Gulf Coast. Much of modern Mexico, along with Guatemala, Belize, Honduras, and El Salvador, constitutes the cultural region known as Mesoamerica (Fig. 1). Elements of the Olmec art style and associated iconography—the first coherent iconographic system in Mesoamerica—that emerged were depicted on stone monuments in the Gulf Coast, as well as on portable ceramic objects that have been found at sites throughout Mesoamerica (*1*, *2*). Because this iconography has been linked with the dissemination of the social, political, and religious institutions of the Olmec, analyzing its origin and spread is central to understanding the development of complex society in Mesoamerica. The Olmec style's appearance at select sites outside the Gulf Coast has been used to argue that it arose in one area only and was exported or, alternatively, emerged from interactions among scattered regional chiefdoms (*3*). Here, we use instrumental neutron activation analysis (INAA) on archaeologically excavated or collected ceramics to fingerprint their provenience and exchange during the later half of the Early Formative period [~3450 to 2850 years before the present (yr B.P.), or 1500 to 900 B.C.E.].

The Olmec and Olmec style in Mesoamerica. Not all features referred to as the Olmec style may be linked with the archaeological Gulf Coast Olmec; thus, we distinguish between the terms Olmec culture and Olmec style. Two views have emerged on the relationship of the Olmec with other contemporaneous cultures, characterized as the ''mother culture'' and ''sister culture'' perspectives (4). Proponents of the mother-culture perspective see the Olmec as more sociopolitically complex than coeval cultures, playing a central role in the dissemination of key elements of Mesoamerican civilization. Sister-culture advocates characterize the Olmec as at the same sociopolitical level as other contemporaneous chiefdoms; while engaged in competitive interaction, the Olmec had no priority in the development of the Olmec style and its distribution. Here, we endeavor to move beyond this dichotomy, which obscures understanding the complex nature of the Olmec and its relationships with its neighbors.

In terms of Early Formative complexity, recent investigations by Ann Cyphers and her collaborators at the first Olmec capital, San Lorenzo, Veracruz (*5*), emphasize the higher sociopolitical level that the Olmecs achieved relative to contemporaneous groups in Mesoamerica (Fig. 1). While leaders, for example, at the emerging chiefdom of San José Mogote in the Valley of Oaxaca lived in somewhat better made wattle-and-daub huts than other villagers (*6*), San Lorenzo leaders probably lived in the so-called Red Palace, where they used basalt brought in from 60 km away to provide columns, step coverings, and drainage channels for their residence. Rather than engage in the typological argument as to whether the Olmec constituted a state or a chiefdom, we simply note the more complex level of sociopolitical organization achieved by the Olmec compared with that of other contemporaneous societies (*7*).

The ''San Lorenzo horizon'' from 3150 to 2800 yr B.P. (1200 to 850 B.C.E., or 1350 to 1000 calibrated B.C.E.) refers to the earliest spread of Olmec-style ceramic vessels and figurines across Mesoamerica (*3*, *8*, *9*). As defined at San Lorenzo (*9*), some Olmec ceramic types (such as Calzadas Carved pottery) have excised designs that may express ideological concepts through iconography (Fig. 2, A and B). Two additional San Lorenzo horizon pottery types have a fine kaolin clay body: Xochiltepec White and Conejo Orange-on-White (Fig. 2, C and D). Xochiltepec White has long been recognized as a possible export ware across Mesoamerica, although of uncertain provenance (*6*, *9*).

The lack of the full repertoire of Olmec-style motifs at any one site and the apparent regional differences in expression of the Olmec style have been cited as evidence that each

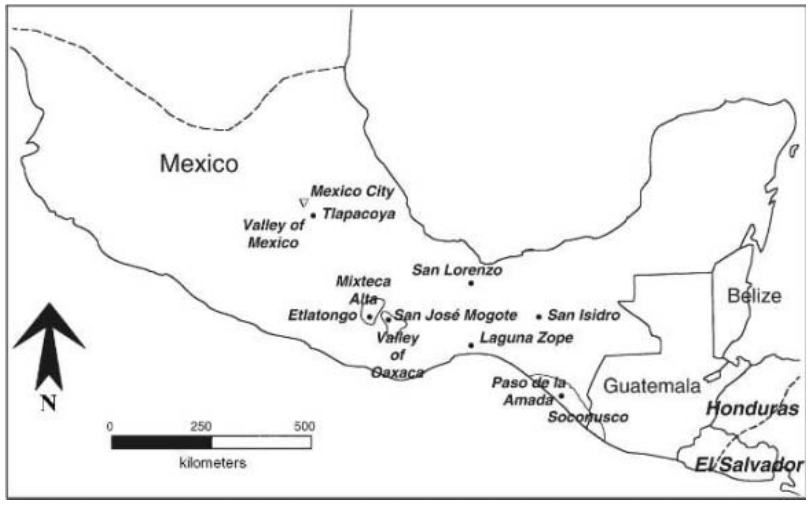

Fig. 1. Map of Early Formative regional centers, showing modern national borders and Mexico City for reference. Dashed lines show approximate boundaries of Mesoamerica.

[1]Department of Anthropology, George Washington University, Washington, DC 20052, USA. [2]Department of Anthropology, California State University, Long Beach, CA 90840, USA. [3]Research Reactor Center, University of Missouri, Columbia, MO 65211, USA.

*To whom correspondence should be addressed. E-mail: blomster@gwu.edu

region contributed to the style, with no central origin of imagery (*3*). Ceramic data from Oaxaca have shaped this debate for the past 30 years, as archaeologists have used stylistic analysis, as well as limited microscopic study of select sherds, to assert that villagers created their own local set of Olmec-style symbols (*6*, *10*). This model concludes that, rather than importing Gulf Coast pottery and iconography, Valley of Oaxaca potters produced and exported Olmec-style symbols made in distinctive gray-ware pottery, referred to as Delfina Fine Gray and Leandro Gray, across Mesoamerica; recipients of this Oaxaca-made pottery supposedly included the Gulf Coast Olmec (*6*, *11*). To test this model, the first author excavated Early Formative ceramics at the site of Etlatongo, in the Nochixtlán Valley of the Mixteca Alta, northwest of the Valley of Oaxaca (Fig. 1). Previously explored by Roberto Zárate Morán, the site, with little prior occupation, grew to be as large as contemporaneous San José Mogote during the San Lorenzo horizon, serving as the center of a small chiefdom comparable to that in the Valley of Oaxaca (*7*).

Ceramic data. Since the mid-1990s, a wide variety of Early Formative ceramic samples from regions of Mesoamerica have been submitted to the University of Missouri Research Reactor (MURR) for INAA (*7*, *12*). Although the 80 samples detailed in table S1 come primarily from Etlatongo and San Lorenzo, the larger database includes a total of 725 sourced archaeological pottery samples from Tlapacoya (Basin of Mexico), San José Mogote and other Valley of Oaxaca sites, Laguna Zope (Pacific Coast, Isthmus of Tehuantepec), Paso de la Amada and other Mazatán area sites (Soconusco region, Pacific Coast of Chiapas), and San Isidro (Chiapas Central Depression) (table S2). Samples of raw clay include 160 clay samples from San Lorenzo, 25 from Oaxaca (*12*–*14*), 203 from the Mazatán zone, 244 from the Basin of Mexico, and 196 samples of raw clay and modern/historic examples of pottery collected from pottery-making towns in the Valley of Oaxaca. Our data have been compared with an additional 527 archaeological samples from later sites in the Valley of Oaxaca.

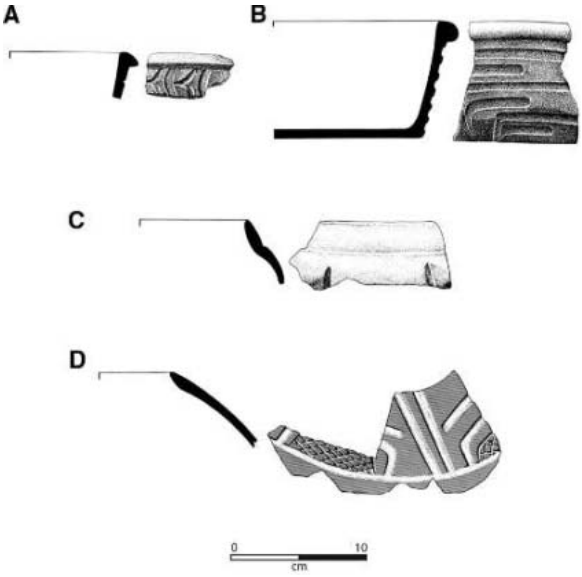

Fig. 2. Profile and exterior views of Olmec pottery types produced at San Lorenzo. (**A** and **B**) Calzadas Carved pottery. [(A) is sample BLM060.] (**C**) Xochiltepec White (sample BLM042). (**D**) Conejo Orange-on-White (sample BLM041). Adapted from (*9*); drawings courtesy of M. Coe.

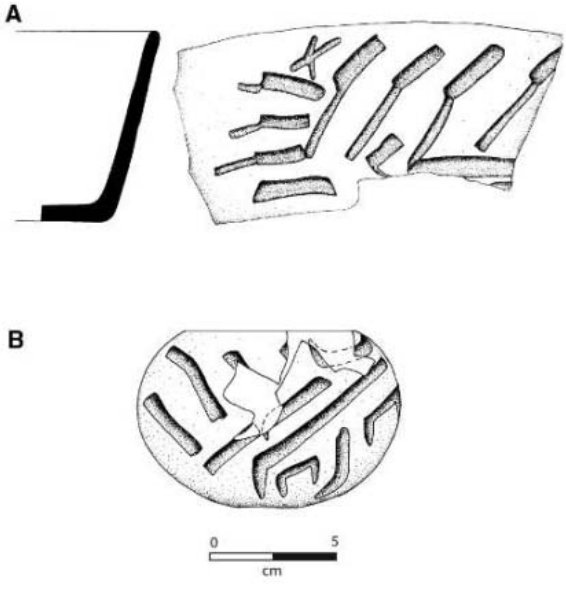

Fig. 3. Olmec-style pottery excavated at Etlatongo. (**A**) Profile and exterior of a bowl made with San Lorenzo clay (sample BLM003). (**B**) Reconstruction of a locally produced neckless jar (sample BLM006).

Clays are useful in sourcing analysis because they reflect the composition of local geology. The clay available for pottery has been documented in the three regions on which we focus: San Lorenzo, the Valley of Oaxaca, and the Nochixtlán Valley (*9*, *13*–*16*). Located in the Isthmian Saline Basin, San Lorenzo sits on a salt dome located in Miocene sedimentary rocks, adjacent to Pleistocene and Holocene alluvium deposited during flooding. The sedimentary rocks provide excellent pottery clays, including white-firing clay (kaolin). Precambrian metamorphic rock, Cretaceous limestone, and Miocene volcanic ignimbrite are exposed in the Valley of Oaxaca, along with Quaternary alluvium derived from these rocks. Clay was likely obtained from weathered Precambrian gneiss, schists, and the associated alluvium; kaolinite clays appear in scattered pockets (*6*). Similar rocks are exposed in the Nochixtlán Valley, although Cretaceous limestone is more abundant. Tertiary volcanic rocks, alluvial clays, and residual clays (with a high calcium carbonate content formed from the decomposition of limestone parent materials) are available in the Etlatongo vicinity.

All 80 pottery samples in table S1 have been recorded with photography and/or drawings, with all Etlatongo (n = 42) and San Lorenzo (n = 21) samples from well-documented archaeological contexts. Most of the ceramics in the larger database (table S2) have not been illustrated, and some lack archaeological provenience information (*13*). The sampling procedure was not random. Sherds were selected that would show both local production and possible imports, including samples similar to Xochiltepec White and Conejo Orange-on-White. Thus, Olmec-style sherds are overrepresented at most sites in the sample. In selecting samples from Etlatongo, special attention was paid to the gray wares that may have been exported by the Valley of Oaxaca (Fig. 3A).

Analysis. Sample preparation, INAA, and quantitative techniques (*17*, *18*) are detailed in online materials (*19*). We used a variety of pattern-recognition techniques to discern compositionally homogeneous groups in the data and then tested the effectiveness of elemental discrimination between the groups by calculating individual ceramics and clay-sample Mahala-

nobis distances from all group centroids. All Mahalanobis distances were cross-validated; that is, each specimen was removed from its presumed group before calculating its own Mahalanobis distance from the group's centroid (*12*, *20*). This is a conservative approach to group evaluation that may exclude true group members but minimizes the chances of erroneous attribution. Such a conservative approach minimizes chances that Olmec-style sherds found outside the Gulf Coast will be incorrectly identified as imports rather than local production. Sherds that could fall into more than one group from the same region were not used in group definition (such as "San Lorenzo Local/White" in table S1); excluding them from specific group membership means that they play no role in defining the centroid and variance-covariance structure of those groups.

Production and consumption of Olmec-style ceramics. The majority (n = 725) of more than 1000 Early Formative archaeological and clay samples separate into 15 regionally specific compositional groups; the remainder fall into 3 unassigned groups (table S3). These 15 groups are discriminated well by the 32 elements retained for analysis according to the Mahalanobis distance–based probabilities of group membership. Several elements, such as chromium, thorium, tantalum, cesium, and calcium, are particularly useful as discriminators of ceramics made in different regions. For example, the Mazatán samples are all low in chromium, whereas the Tlapacoya samples are all enriched in chromium (Fig. 4).

Three groups—Etlatongo-1, Etlatongo-2, and Oaxaca-1—can be associated with highland Oaxaca production. Although we have numerous clay samples from the Valley of Oaxaca, local production at Etlatongo was primarily sampled by selecting highly friable utilitarian wares that would be in need of frequent replacement (*7*). The Etlatongo-1 and Etlatongo-2 groups represent the varied nature of the clays available in the Etlatongo vicinity. The data demonstrate that the same clays used for utilitarian vessels could also be used for serving vessels with Olmec-style motifs (Fig. 3B). Potters thus produced Olmec-style ceramics using local clays in both the Nochixtlán and Oaxaca Valleys.

Three groups—San Lorenzo White, San Lorenzo Local, and San Lorenzo Local/White—clearly derive from San Lorenzo region clays, even though the finished vessels are found at villages across Mesoamerica. The ceramics in the combined San Lorenzo Local/White group were produced with San Lorenzo region clays, but it was not possible to distinguish among these groups; a similar problem precludes sample BLM009 from being firmly placed in the San Lorenzo Local group. All examples of Conejo Orange-on-White, and virtually all Xochiltepec White and La Mina White ceramics in the sample, were evidently produced with San Lorenzo clay.

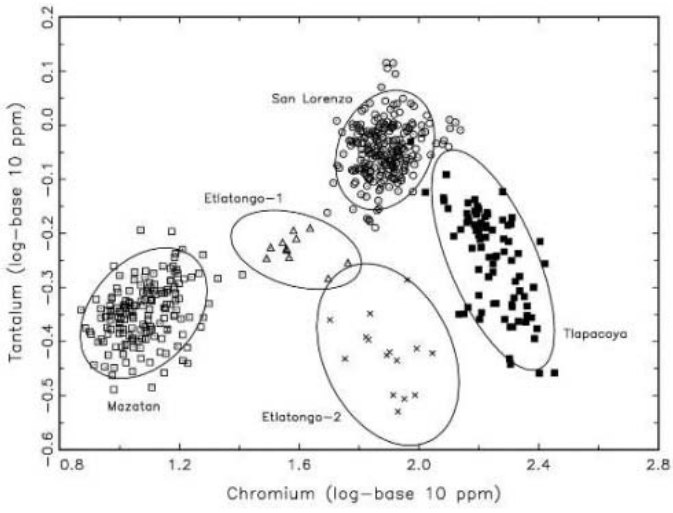

Fig. 4. Bivariate plot of chromium and tantalum concentrations in pottery samples assigned to five well-defined reference groups in the Early Formative pottery database. Ellipses represent 90% confidence level for group membership, with unique symbols for the samples of each group.

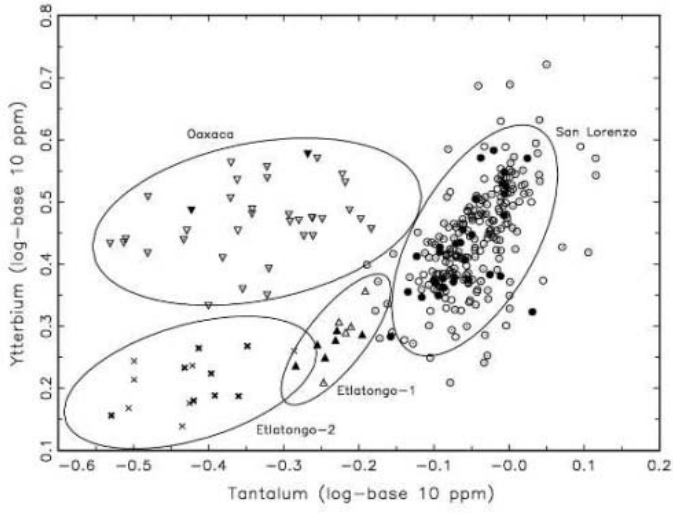

Fig. 5. Bivariate plot of tantalum and ytterbium shows the high concentration of tantalum in San Lorenzo samples. Shaded/bold symbols represent the samples detailed in table S1. Ellipses represent 90% confidence level for group membership, with unique symbols for the samples of each group.

One white-ware group, White-2, cannot be associated with a specific region. All nine White-2 samples in table S3 appear similar to Xochiltepec White pottery or a similar type. The chemistry of Xochiltepec White pottery clearly indicates that it was produced in the Gulf Coast, but all White-2 group archaeological samples have been found in the Valley of Oaxaca. Although this occurrence could represent a kaolin source in the Valley of Oaxaca, approximately half of the specimens assigned to the group exceed 1% probability of membership in the San Lorenzo White group. Thus, there remains the possibility that the clay may be derived from slightly anomalous clays local to the San Lorenzo region.

The results of the INAA demonstrate that the Olmec produced luxury white wares, particularly Conejo Orange-on-White and Xochiltepec White, at San Lorenzo. Other regions included in the study evidently imported this pottery, which explains its widespread distribution. Although some regions produced local variants, these were not exported between regions; no non–Gulf Coast–produced white ware was exported to San Lorenzo. Xochiltepec White, which first appears at San Lorenzo prior to the San Lorenzo horizon (*9*), and Conejo Orange-on-White were Olmec products exported to select sites throughout Mesoamerica.

In terms of decorated pottery, the San Lorenzo Local group contains most of the Olmec-style ceramics with iconography in the database, especially as expressed in gray-ware pottery. A problem did emerge early in the analysis in segregating pottery produced at San Lorenzo from certain Oaxaca gray wares. Generally, Gulf Coast clays contain low concentrations of calcium, whereas those from highland Oaxaca generally have high concentrations. Some samples of Gulf Coast pottery and clay, however, have calcium concentrations similar to examples of later Oaxacan gray wares, as well as ethnographic samples of Valley of Oaxaca pots and clay (*12*). A multivariate perspective resolves this problem; when all 32 elements retained from

Table 1. Secure regional assignments for Early Formative pottery

Archaeological context	Region as identified by INAA							
	Gulf Coast	Mazatán	Valley of Oaxaca	Nochixtlán Valley	Valley of Mexico	Chiapas Central Depression	Isthmus of Tehuantepec	Total
San Lorenzo (Gulf Coast)	203	0	0	0	0	0	0	203
Mazatán (various sites)	23	177	0	0	0	0	0	200
Valley of Oaxaca (various sites)	12	0	42	0	0	0	0	54
Etlatongo (Nochixtlán Valley)	35	0	0	26	0	0	0	61
Tlapacoya (Valley of Mexico)	17	0	0	0	87	0	0	104
San Isidro (Chiapas Central Depression)	1	0	0	0	0	41	0	42
Laguna Zope (Isthmus of Tehuantepec)	3	0	0	0	0	0	58	61
								725

the analysis are considered, the discrimination into groups is unambiguous. For example, just a bivariate plot of tantalum and ytterbium segregates archaeological samples from Oaxaca, Etlatongo, and San Lorenzo (Fig. 5).

In Oaxaca, Delfina and Leandro Gray pots with Olmec-style motifs have been interpreted as expressing local variants of the Olmec style manufactured in the Valley of Oaxaca and exported to other Formative centers (*6*, *11*). Our data document the presence of compositionally different gray wares in the Valley of Oaxaca; it seems that both local manufacture and Olmec imports are represented at sites such as San José Mogote. Valley of Oaxaca–produced gray wares were not exported to the nearby Nochixtlán Valley; instead, Etlatongo imported Olmec-style gray wares from the more distant Gulf Coast (Fig. 3B). Indeed, all nonlocally produced Olmec-style gray pottery samples found outside the Gulf Coast appear to be San Lorenzo exports (Table 1).

The INAA data thus contradict the model that regional exports can be identified simply by style in assemblages of Olmec-style pottery (*6*). At least one supposed "Oaxaca-style" Calzadas Carved gray ware excavated at San Lorenzo (sample BLM050) was analyzed by INAA; it was produced with San Lorenzo clay.

The Olmec produced and exported a wide variety of Olmec-style iconography, often on gray-ware pottery, across Mesoamerica. Local production of Olmec-style motifs also occurred in all regions involved in this interaction. At Tlapacoya, a Basin of Mexico village known for pottery with elaborate profile views of cleft-headed creatures (*21*), Olmec-style designs occur on gray pottery with both San Lorenzo (BLM039) and local (BLM062) origins. Once again, none of the decorated and undecorated gray pottery analyzed from Tlapacoya was imported from Oaxaca.

Olmec and Early Formative interaction. The San Lorenzo Olmec produced both fine white-paste pottery and decorated Olmec-style ceramics. The Olmec exported this pottery to other regional centers across Mesoamerica, where many centers created local variants of it; indeed, we suspect Gulf Coast Xochiltepec White served as the inspiration for local ceramic emulations throughout Mesoamerica. None of the locally produced Olmec-style pottery in the sample from the Valley of Oaxaca, the Nochixtlán Valley, the Valley of Mexico, the Isthmus of Tehuantepec, the Chiapas Central Depression, and the Mazatán region was exported to the Gulf Coast (Table 1). Contra to the sister-culture perspective, our analysis implies that the Olmec at San Lorenzo did not receive foreign-made variants of the Olmec style; the Olmec were its sole exporters. Despite the size of the San Lorenzo sample (n = 203), not a single analyzed sherd was imported. Rather than expressing regional styles from across Mesoamerica at San Lorenzo, the INAA data emphasize the diversity of Calzadas Carved pottery produced by the Olmec. Furthermore, the conservative approach used to assign members to the compositional groups may underestimate the numbers of San Lorenzo–derived specimens exported outside the Gulf Coast. Because sampling was not random, the data in Table 1 do not represent frequencies of imported pottery for each region.

Our data present several implications for understanding the Olmec and their relationships with contemporaneous groups. Olmec pottery and symbols associated with the Olmec were valued by elites at some of the largest chiefly centers in Early Formative Mesoamerica. It does not appear that these other regions contributed substantially to the assemblage of Olmec-style symbols employed beyond each region. Not only did the Olmec not import any foreign pottery with Olmec-style symbols, none of the regions in Table 1 exchanged pottery with each other. Etlatongo and San José Mogote, in adjacent regions of highland Oaxaca, received pottery from the more distant San Lorenzo rather than from each other. This appears to be a stark repudiation of the view of mutual exchange and production of these symbols, and it contradicts the claim that Oaxacan Delfina Fine gray pottery was as popular an export ware as Xochiltepec White (*6*). The regions outside the Gulf Coast appear to be primarily consumers and emulators rather than exporters and innovators of Olmec-style motifs.

We propose that the San Lorenzo Olmec played a central role in synthesizing a distinct style and associated iconography, disseminating it across Mesoamerica. The mechanisms for exchange of Olmec-style pottery and symbols probably varied on a regional basis. Rather than being imposed by the Olmec, these symbols were received by people, probably leaders, at regional centers, who used, manipulated, and reproduced them in different ways. Exchange of these symbols formed an important component of communication and negotiation between communities on both intra- and interregional levels; non–Gulf Coast groups may have moved Olmec-produced objects between regions rather than locally produced pottery. The local impact of this interaction on communities varied. While this interaction may have had a transformative effect on the local population of the Mazatán region (*22*), the impact in the Nochixtlán Valley appears to be substantially different and less profound. Despite the high frequency of imported Olmec pottery in Table 1, the total quantity of Olmec-style pottery, both imported and locally made, probably never exceeded 5 to 10% of the total ceramic assemblage excavated at Etlatongo (*7*).

Olmec priority in the creation of the Olmec style emphasizes their important role in Early Formative social developments throughout much of Mesoamerica. Understanding the Olmec role in disseminating this style and associated iconography invokes more dynamic models of interregional interaction that explore the interests of both producers and consumers of Olmec-style pottery. This multifaceted interaction anticipates the increasingly complex nature of Olmec networks in the following Middle Formative Period, when La Venta became the Gulf Coast's largest Olmec center.

References and Notes

1. M. Coe, in *Handbook of Middle American Indians*, Vol. 3: *Archaeology of Southern Mesoamerica*, part 2, R. Wauchope, G. Willey, Eds. (Univ. Texas Press, Austin, 1965), pp. 739–775.
2. E. Benson, B. de la Fuente, Eds., *Olmec Art of Ancient Mexico* (National Gallery of Art, Washington, DC, 1996).

3. R. Sharer, D. Grove, Eds., *Regional Perspectives on the Olmec* (Cambridge Univ. Press, New York, 1989).
4. D. Grove, *J. World Prehistory* **11**, 51 (1997).
5. A. Cyphers, in *Olmec to Aztec: Settlement Patterns in the Ancient Gulf Lowlands*, B. Stark, P. Arnold III, Eds. (Univ. of Arizona Press, Tucson, AZ, 1997), pp. 96–114.
6. K. Flannery, J. Marcus, *Early Formative Pottery of the Valley of Oaxaca, Mexico*, Memoirs of the Museum of Anthropology 27 (Univ. of Michigan, Ann Arbor, MI, 1994).
7. J. Blomster, *Etlatongo: Social Complexity, Interaction, and Village Life in the Mixteca Alta of Oaxaca, Mexico* (Wadsworth, Belmont, CA, 2004).
8. J. Blomster, *Ancient Mesoamerica* **9**, 171 (1998).
9. M. Coe, R. Diehl, *In the Land of the Olmec*, Vol. 1: *The Archaeology of San Lorenzo Tenochtitlán* (Univ. of Texas Press, Austin, TX, 1980).
10. K. Flannery, in *Dumbarton Oaks Conference on the Olmec*, E. Benson, Ed. (Dumbarton Oaks, Washington, DC, 1968), pp. 79–117.
11. K. Flannery, J. Marcus, *J. Anthropol. Archaeol.* **19**, 1 (2000).
12. H. Neff, M. Glascock, "Report on Instrumental Neutron Activation Analysis of Olmec Pottery" (Research Reactor Center, Univ. of Missouri, Columbia, MO, 2002).
13. R. Herrera, H. Neff, M. Glascock, J. Elam, *J. Archaeol. Science* **26**, 967 (1999).
14. M. Thieme, in *Procesos de Cambio y Conceptualización del Tiempo: Memoria de la Primera Mesa Redonda de Monte Albán*, N. Robles García, Ed. (Instituto Nacional de Antropología e Historia, Mexico City, 2001), pp. 341–349.
15. J. Lorenzo, *Rev. Mex. Estud. Antropol.* **16**, 49 (1960).
16. M. Kirkby, *The Physical Environment of the Nochixtlán Valley, Oaxaca*, Vanderbilt University Publications in Anthropology 2 (Vanderbilt Univ., Nashville, TN, 1972).
17. M. Glascock, in *Chemical Characterization of Ceramic Pastes in Archaeology*, H. Neff, Ed. (Prehistory Press, Madison, WI, 1992), pp. 11–26.
18. H. Neff, in *Modern Analytical Methods in Art and Archaeology*, E. Ciliberto, G. Spoto, Eds. (Wiley, New York, 2000), pp. 81–134.
19. Materials and methods are available as supporting material on *Science* Online.
20. R. Bishop, H. Neff, in *Archaeological Chemistry IV*, R. Allen, Ed. (American Chemical Society, Washington, DC, 1989), pp. 576–586.
21. P. Joralemon, *A Study of Olmec Iconography*, Studies in Pre-Columbian Art and Archaeology 7 (Dumbarton Oaks, Washington, DC, 1971).
22. J. Clark, M. Pye, in *Olmec Art and Archaeology in Mesoamerica*, J. Clark, M. Pye, Eds. (National Gallery of Art, Washington, DC, 2000), pp. 217–251.

23. We thank the technicians at MURR and the archaeologists in Mexico who provided samples for this study, as well as funding agencies that made their collections possible. The support and permissions of the Instituto Nacional de Antropología e Historia—especially L. Mirambell, M. Serra Puche, J. García-Bárcena, E. López Calzada, and N. Robles Garcia—have been invaluable. Funding for the 80 samples in table S1 came primarily from the Charles J. MacCurdy Endowment, Yale University; the non-Etlatongo samples were provided by M. Winter and M. Coe. The research at the MURR Archaeometry Lab has been supported by NSF (no. SBR-9802366). We are grateful for the support of the Sainsbury Research Unit, University of East Anglia. We thank R. Diehl, A. Joyce, G. Lau, and an anonymous reviewer for comments.

Supporting Online Material
www.sciencemag.org/cgi/content/full/307/5712/1068/DC1
Materials and Methods
Tables S1 to S3
References

16 November 2004; accepted 6 January 2005
10.1126/science.1107599

Whole-Genome Patterns of Common DNA Variation in Three Human Populations

David A. Hinds,[1] Laura L. Stuve,[1] Geoffrey B. Nilsen,[1] Eran Halperin,[2] Eleazar Eskin,[3] Dennis G. Ballinger,[1] Kelly A. Frazer,[1] David R. Cox[1]*

Individual differences in DNA sequence are the genetic basis of human variability. We have characterized whole-genome patterns of common human DNA variation by genotyping 1,586,383 single-nucleotide polymorphisms (SNPs) in 71 Americans of European, African, and Asian ancestry. Our results indicate that these SNPs capture most common genetic variation as a result of linkage disequilibrium, the correlation among common SNP alleles. We observe a strong correlation between extended regions of linkage disequilibrium and functional genomic elements. Our data provide a tool for exploring many questions that remain regarding the causal role of common human DNA variation in complex human traits and for investigating the nature of genetic variation within and between human populations.

Single-nucleotide polymorphisms (SNPs) are the most abundant form of DNA variation in the human genome. It has been estimated that there are ~7 million common SNPs with a minor allele frequency (MAF) of at least 5% across the entire human population (*1*). Most common SNPs are to be found in most major populations, although the frequency of any allele may vary considerably between populations (*2*). An additional 4 million SNPs exist with a MAF between 1 and 5%. In addition, there are innumerable very rare single-base variants, most of which exist in only a single individual.

The relationship between DNA variation and human phenotypic differences (such as height, eye color, and disease susceptibility) is poorly understood. Although there is evidence that both common SNPs and rare variants contribute to the observed variation in complex human traits (*3*, *4*), the relative contribution of common versus rare variants remains to be determined. The structure of genetic variation between populations and its relationship to phenotypic variation is unclear. Similarly, the relative contribution to complex human traits of DNA variants that alter protein structure by amino acid replacement, versus variants that alter the spatial or temporal pattern of gene expression without altering protein structure, is unknown. In some cases, these issues have been studied in limited genomic intervals, but comprehensive genomic analyses have not been possible.

Genome-wide association studies to identify alleles contributing to complex traits of medical interest are currently performed with subsets of common SNPs, and thus they rely on the expectation that a disease allele is likely to be correlated with an allele of an assayed SNP. Although studies have shown that variants in close physical proximity are often strongly correlated, this correlation structure, or linkage disequilibrium (LD), is complex and varies from one region of the genome to another, as well as between different populations (*5*, *6*). Selection of a maximally informative subset of common SNPs for use in association studies is necessary to provide sufficient power to assess the causal role of common DNA variation in complex human traits. Although a large fraction of all common human SNPs are available in public databases, lack of information concerning SNP allele frequencies and the correlation structure of SNPs within and between human populations has made it difficult to select an optimal subset.

Here we examine the SNP allele frequencies and patterns of LD between 1,586,383 SNPs distributed uniformly across the human genome in unrelated individuals of European, African, and Asian ancestry. Our primary aim was to create a resource for further investigation of the structure of human genetic variation and its relationship to phenotypic differences.

A dense SNP map. To characterize a panel of markers that would be informative in whole-genome association studies, we selected a total of 2,384,494 SNPs likely to be common in individuals of diverse ancestry (*7*). We identified the majority (69%) of the SNPs by performing array-based resequencing

[1]Perlegen Sciences Inc., 2021 Stierlin Court, Mountain View, CA 94043, USA. [2]International Computer Science Institute, Berkeley, CA 94704, USA. [3]Department of Computer Science and Engineering, University of California–San Diego, La Jolla, CA 92093, USA.

*To whom correspondence should be addressed. E-mail: david_cox@perlegen.com

of 24 human DNA samples of diverse ancestry (*5*). These SNPs were supplemented with SNPs chosen from public databases to obtain a more uniform physical distribution across the human genome. Further details of the SNP ascertainment are given in the supporting online material (*7*). We designed 49 high-density oligonucleotide arrays for genotyping these SNPs (*8*, *9*) and roughly 300,000 long-range polymerase chain reaction (PCR) primer pairs covering the selected SNPs, with an average of eight SNPs per individual region being amplified by PCR. The amplicons had an average length of 9 kb and covered ~92% of the available human genome. An average of 6250 amplicons derived from a single individual were pooled and hybridized to a single high-density oligonucleotide array, producing genotypes for ~48,000 SNPs.

We genotyped 71 unrelated individuals from three populations: 24 European Americans, 23 African Americans, and 24 Han Chinese from the Los Angeles area. The 71 individuals genotyped here were not related to the individuals previously used for SNP discovery. DNA samples were selected from the Coriell Cell Repositories' Human Variation Collection, and we relied on Coriell's determinations of sample populations. We complied with all Coriell policies for research use DNA of samples from named populations.

Each SNP was scored with a combination of metrics that had been shown to correlate with genotype quality on our platform, and data for poorly performing SNPs was rejected. These metrics included the call rate; the number of observed genotype clusters; the existence of near-perfect matches for SNP flanking sequences elsewhere in the genome; the presence of other known SNPs in probe-flanking sequences; and consistency with Hardy Weinberg equilibrium. Tests for Hardy Weinberg equilibrium are very effective for identifying some types of genotyping artifacts (*10*); however, because we used these tests for quality control, our genotype data are unsuitable for investigating biologically interesting true deviations from Hardy Weinberg equilibrium. Further details of our genotype quality control are described in the supporting online material (*7*).

A subset of 1,586,383 SNPs was successfully genotyped based on our quality criteria, with two alleles each observed at least once among the 71 individuals. In total, more than 112 million individual genotypes were determined for these SNPs. There were no missing genotypes for 64% of these SNPs, and 92% of these SNPs had less than 5% missing data. The overall frequency of successful genotype calls was 98.6%. SNP assay details and individual genotypes have been deposited in the National Center for Biotechnology Information (NCBI)'s SNP database (dbSNP, build 123, accession nos. ss23145044 to ss24731426). Genotypes for 156,757 SNPs for nine of the European-American individuals that were part of this project had been previously determined by the International HapMap Project, using a variety of genotyping platforms (*11*). Our data for these 1.6 million genotypes is 99.54% concordant with the HapMap project data. The distribution of discordant genotypes is very nonrandom; only 0.3% of the SNPs account for 50% of all the discrepancies, and we estimate that 90% of the SNPs in the complete data set have no incorrect genotypes. Haplotype analyses in particular will generally benefit from this error distribution, because accurate inference of haplotypes requires consistent genotypes across large groups of nearby markers.

The distribution of the 1.6 million high-quality genotyped SNPs (table S1) is similar to that of a previously reported map of 1.42 million SNPs (*12*). More than 95% of the genome is in inter-SNP intervals of less than 50 kb, and roughly two-thirds of the sequenced genome is covered by inter-SNP intervals of 10 kb or less (table S2). The average distance between adjacent SNPs is 1871 base pairs (bp). Although repetitive elements are underrepresented in our collection, we genotyped 269,611 SNPs within repetitive elements where the SNP flanking sequences could be uniquely mapped. There are 735,094 SNPs (46%) in genic regions of the genome, which we define as being within 10 kb of the transcribed intervals for 22,904 protein-coding genes in release 3 of NCBI's build 34 annotations. At least one SNP is present in 78% of all transcripts. When the 10-kb region of DNA upstream and downstream of each transcript is included, 93% of all the protein-coding genes contain at least one SNP. A total of 20,165 SNPs (1.3%) are present in amino acid coding sequences and 9370 of these SNPs are nonsynonymous, leading to an amino acid change (table S3). Although our SNP ascertainment is not random, this subset of SNPs is quite uniformly distributed throughout the human genome with respect to annotated protein-coding genes as well as physical distance.

Common SNPs in three populations. Table 1 illustrates our success in obtaining a set of common SNPs that are informative in human populations of diverse ancestry. Most of the 1,586,383 SNPs with high-quality genotypes are polymorphic in each of the three population samples genotyped in this study. Ninety-four percent of the SNPs (1,483,594 SNPs) have two alleles in the African-American sample; 81% (1,286,277 SNPs) have two alleles in the European-American sample; and 74% (1,168,029 SNPs) have two alleles in the Han Chinese sample. In each population, the majority of the segregating SNPs have a MAF greater than 10%, ranging from 68% of all segregating SNPs in the African-American sample to 57% of all segregating SNPs in the Han Chinese sample. Only 263,029 of the 1,586,383 SNPs (17%) have a MAF of less than 10% in all three of the population samples. The distributions of MAFs we see in the three populations is very similar for the European-American and Han Chinese samples, with a higher frequency of rarer alleles in the African-American sample (fig. S1). Consistent with previous studies (*2*, *13*), we observed the greatest genetic diversity in individuals of African descent. Our SNP ascertainment strategy makes it difficult to make more definitive statements regarding the precise distribution of SNP allele frequencies in different populations.

Although the small sample sizes in this study preclude any definite conclusion regarding the complete absence of a particular allele in any given population, we observed 291,012 SNPs (18%) that were segregating in only one population sample (''private SNPs''). Most of these private SNPs (75%) were segregating in the African-American sample, although private SNPs were observed for each of the three population samples (Table 1). Although private SNPs tend to have lower MAFs than other SNPs in our collection, a substantial fraction are common: 106,404, or 37%, have MAF > 0.10.

To quantify genetic variation within and between populations, we calculated F_{ST} for each SNP in each pair of populations, as well as combined values across all three popula-

Table 1. SNPs segregating in the three genotyped populations. Percentages are of 1,586,383 genotyped SNPs or of 291,012 private SNPs.

Population	Segregating		MAF > 0.05		MAF > 0.10	
	SNPs	%	SNPs	%	SNPs	%
All SNPs						
African-American	1,483,594	93.5	1,267,594	79.9	1,083,652	68.3
European-American	1,286,277	81.1	1,123,765	70.8	991,046	62.5
Han Chinese	1,168,029	73.6	1,027,109	64.7	910,451	57.4
Private SNPs						
African-American	218,500	75.1	139,536	47.9	88,525	30.4
European-American	44,555	15.3	18,284	6.3	8,062	2.8
Han Chinese	27,957	9.6	15,946	5.5	9,817	3.4

tions (*14*). F_{ST} measures the genetic variance between populations as a fraction of the total genetic variance. Because African Americans are a relatively admixed population with substantial but heterogeneous European genetic contributions (*15*), the F_{ST} estimates for comparisons with this group will be more variable but should generally underestimate the results that would be obtained with a native African sample. The distribution of pairwise F_{ST} is very similar for the African-American versus European-American and European-American versus Han Chinese samples, with more large F_{ST} values between the African-American and Han Chinese samples (fig. S2). These findings are consistent with prior studies (*16*, *17*) showing that most common DNA variation is shared across human populations, with differences in allele frequencies between populations.

Markers with large between-population variance will be useful for admixture mapping studies to identify genetic variants causing phenotypic differences (*18*). Admixture mapping exploits relatively long-range allelic correlations in a recently admixed population to identify functional variants that have different prevalences in the ancestral populations, whether because of genetic drift or local natural selection. The technique requires selection and genotyping of limited numbers of "ancestry-informative markers." Our identification of large numbers of such markers removes one of the major barriers to practical use of this promising but largely untested technique.

Evidence for natural selection between populations. It has been suggested that natural selection distorts the observed distribution of F_{ST} across the human genome and that large F_{ST} values can be used to identify candidate loci likely to have undergone local selection (*13*, *19*). If this is true, then larger F_{ST} values should be found near functional genetic elements. We looked at the distribution of F_{ST} for SNPs that were genic or nongenic, coding or noncoding, and synonymous or nonsynonymous. We performed the analysis within subsets of SNPs grouped by MAF, so that effectively, we looked at the fraction of between-population variance for SNPs with the same total genetic variance (fig. S3). Common SNPs in genic regions do have slightly but significantly higher F_{ST} values than nongenic SNPs with the same MAF [analysis of variance (ANOVA), $P = 1.8 \times 10^{-46}$], and common coding SNPs have slightly higher F_{ST} values than noncoding SNPs in genic regions (ANOVA, $P = 1.1 \times 10^{-4}$). We did not see a significant difference in F_{ST} between synonymous and nonsynonymous coding SNPs, but our sensitivity is limited by the small sample sizes and expected correlations among SNPs within the same transcript. These results are consistent with local selection changing the distribution of F_{ST} near functional sequences. However, because the distributions of F_{ST} among genic and nongenic SNPs are very similar, large F_{ST} values by themselves appear to be very weak evidence of selection.

We performed a similar analysis to see if there is also an association between private SNPs and functional genetic elements. When conditioned on MAF, we saw no difference in frequency of private SNPs among genic and nongenic SNPs or among coding and noncoding SNPs (fig. S4). This indicates that the SNPs responsible for evidence of local selection in the F_{ST} analysis tend not to be private and instead are segregating in multiple populations. Although there are known examples linking population-specific SNP alleles to phenotypic differences (*20*–*22*), our results are more consistent with the conclusion that most functional human genetic variation is not population-specific.

Correlation structure of common SNPs. DNA variants in physical proximity along a chromosome tend to be correlated, and these correlations are known as linkage disequilibrium. LD results from a combination of processes, including mutation, natural selection, and genetic drift. It can initially extend over very long genomic distances but is steadily broken down over time by recombination. The observed structure of LD in any particular genomic interval thus depends on a complex interplay of demographic history, stochastic events, and functional constraints. Several metrics exist for measuring LD between pairs of SNPs; we used r^2, the squared correlation coefficient for a 2 by 2 table of haplotype frequencies (*23*).

We have used a modification of a previously described algorithm to identify bins of common SNPs that are in very strong LD, where each bin has at least one "tag SNP" with an r^2 of at least 0.8 with every other SNP in the bin (*24*). This "greedy" algorithm works by iteratively identifying the largest possible subset with these properties from a list of available SNPs, then removing those SNPs from the list used in the next iteration. By assaying a reduced set of tag SNPs, the genotyping burden of an association study may be substantially reduced while retaining most of the power to discover disease associations of the entire SNP set. Unlike haplotype blocks, which are defined as contiguous groups of SNPs, the SNPs that make up a bin may be interdigitated with SNPs that are part of other bins.

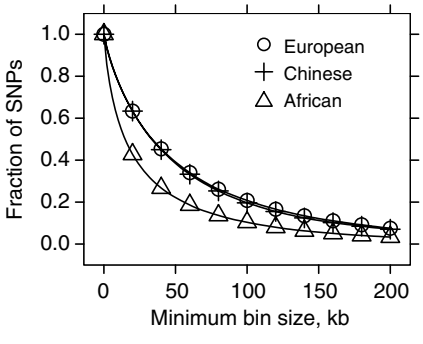

Fig. 1. Size distribution of LD bins. We show, for a given minimum bin size, the fraction of SNPs in bins of that size or larger. The size distributions for the European-American and Han Chinese LD maps are essentially identical.

Table 2 summarizes bin characteristics across the genome, excluding the Y chromosome, for each of the three population samples. We focused on common SNPs with MAF > 10% in this analysis, because estimates of LD for variants with lower MAF are unreliable unless large numbers of individuals are genotyped (*23*). Although most LD bins contained just one SNP, these isolated SNPs were a small proportion of all SNPs, and most SNPs were tightly correlated with multiple other SNPs. In the European-American data, 52.3% of 293,677 bins contained one SNP; however, these constituted only 15.5% of the 991,185 common SNPs. A substantial portion of all SNPs qualified as tag SNPs by having a high r^2 value with every other bin member, indicating that the bins are generally quite densely connected. For the African-American sample, there were substantially fewer bins made up of large numbers of SNPs extending over large distances (Fig. 1). It should be kept in mind that the LD structure we observed is based on an analysis of only 25% of all common SNPs in the genome. Although the sizes of longer intervals of LD should be relatively robust to our incomplete ascertainment, the proportion of all common SNPs in high LD with other SNPs may be substantially underestimated from our data.

LD and functional elements. We observed a strong relationship between extended intervals of LD and functional genomic fea-

Table 2. LD bin statistics in three populations. Bins were classified by the number of SNPs they contained.

Size*	Bins	% Bins	kb†	SNPs	% SNPs
			African-American		
1	362,465	67.4	0.0	362,465	33.5
2 to 4	131,737	24.5	12.4	337,877	31.2
5 to 9	32,081	6.0	37.2	202,512	18.7
≥10	11,530	2.1	78.4	180,556	16.7
Total	537,813			1,083,410	
			European-American		
1	153,511	52.3	0.0	153,511	15.5
2 to 4	84,890	28.9	14.6	226,172	22.8
5 to 9	33,745	11.5	37.3	218,491	22.0
≥10	21,531	7.3	89.5	393,011	39.7
Total	293,677			991,185	
			Han Chinese		
1	129,759	50.8	0.0	129,759	14.3
2 to 4	74,232	29.1	13.2	198,422	21.8
5 to 9	30,569	12.0	34.8	198,429	21.8
≥10	20,708	8.1	83.7	383,580	42.1
Total	255,268			910,190	

*The number of SNPs per LD bin. †Average distance spanned by the SNPs in each LD bin, in kb.

tures (Table 3). Large bins were significantly overpopulated with genic versus nongenic SNPs (trend test, $P \approx 0$), and in genic regions, coding SNPs were significantly enriched over noncoding SNPs (trend test, $P = 1.9 \times 10^{-26}$). Large bins were also overrepresented for nonsynonymous versus synonymous SNPs (trend test, $P = 5.3 \times 10^{-4}$). This result is consistent with the hypothesis of an association between selection and some regions of extended LD (*25*, *26*) and suggests that some genomic regions of extended LD may play a particularly important role in determining the genetic basis of human phenotypic differences.

We identified five bins of more than 200 SNPs each and 17 genomic intervals containing bins that span more than 1000 kb in one or more populations (tables S4 and S5). Several of these large bins spanned similarly large genes. The bin with the most SNPs was on chromosome 17 in the European-American map and had an unusual pattern of variation, with two previously reported haplotypes extending across 518 SNPs and spanning a distance of 800 kb (*27*). The rarer haplotype had a frequency of 25% in the European-American sample and a 9% frequency in the African-American sample and was absent in the Han Chinese sample. This bin includes the gene for microtubule-associated protein tau, mutations of which are associated with a variety of neurodegenerative disorders; a gene coding for a protease similar to presenilins, mutations of which result in Alzheimer's disease; and the gene for corticotropin-releasing hormone receptor, which mediates immune, endocrine, autonomic, and behavioral responses to stress (*27*–*29*).

Large-scale patterns of LD. The distribution of SNPs and LD across the entire human genome is shown in Fig. 2 and can be examined in more detail online. The top track illustrates the relative uniformity of coverage of the analyzed SNPs apart from intervals of centromeric and telomeric heterochromatin. The middle track shows the fraction of common SNPs that are in high LD with at least one other SNP. In most regions, we observed a high level of redundancy for the European-American and Han Chinese samples and somewhat less redundancy in the African-American sample. The bottom track shows the fraction of common SNPs observed to be in relatively large LD bins in each population. This track shows substantial structure on a scale of megabases. Although there is generally good agreement between populations, there are also intervals where there is substantial divergence.

Our whole-genome analysis reveals that the large-scale structure of LD across the genome is correlated with large-scale differences in recombination rates, consistent with previous findings for a single chromosome (*30*). In particular, regions of very strong LD are mostly located in regions of low recombination (fig. S5). This correlation of large-scale LD structure with recombination rate and the finding that regions of extended LD show evidence of selection provide strong support for the hypothesis that the LD structure of the human genome has functional significance and is not simply a byproduct of random genetic drift and population demographics.

SNP subsets capture most common variation. As only a fraction of all common SNPs in human populations have been characterized to date, association studies based on available subsets of SNPs rely on the expectation that an undiscovered, disease-associated variant is likely to be correlated with an allele of an assayed SNP. The statistical power to detect an unassayed, disease-associated allele indirectly with a correlated allele of an assayed SNP is related to r^2. Specifically, the power to detect an association indirectly in N individuals is equivalent to the power to detect it directly in Nr^2 individuals (*31*). The actual power to detect a particular causal variant depends on that variant's mode of action and penetrance as well as details of the study design. Thus, r^2 can only be used to answer the narrower question of what is the sample size penalty, in an otherwise appropriately designed study, for not directly assaying a causal variant.

To determine our ability to detect unassayed, disease-associated variants with this SNP collection, we took advantage of the fact that the European-American and African-American individuals genotyped in this study were also sequenced across selected genes by the SeattleSNPs Program for Genomic Applications (PGA) (*32*). For these individuals, this data provides an essentially complete assessment of genetic variation in the sequenced regions, allowing us to estimate the fraction of all variation contained in our SNP set. In addition, the data allows us to determine the coverage of our genotyped SNPs for the sites we did not directly assay.

We evaluated data for 16,601 sequence variants identified in 152 genes, of which 2465 were part of our SNP set. The concordance between our genotype data and the PGA data for these 2465 SNPs was 99.2%. Our SNP set contained ~24% of all SNPs with a MAF ≥ 10% for these 152 genes in the African-American and European-American samples. SNPs with low MAF are underrepresented in our data compared to the PGA data, because our SNPs were typically discovered with sequence data from fewer distinct chromosomes. These rarer variants account for relatively small fractions of the total nucleotide diversity. In the PGA data for the European Americans, 45% of SNPs have MAF < 10% but account for only 15% of nucleotide diversity; for the African Americans, 58% of SNPs have MAF < 10% and account for 23% of nucleotide diversity.

Table 4 shows the average r^2 and the fraction of r^2 values exceeding thresholds, for

Table 3. Distribution of genic, synonymous, and nonsynonymous coding SNPs spanned by bins of extended LD in any of the three population samples. Genic SNPs are defined as within 10 kb of a protein-coding gene annotation.

Longest spanning LD bin (kb)	SNPs	Genic		Synonymous		Nonsynonymous	
		SNPs	%	SNPs	%	SNPs	%
<500	1,536,094	707,950	46.1	10,330	0.67	8,898	0.58
500 to 1000	42,432	22,189	52.3	347	0.82	302	0.71
≥1000	7,857	4,955	63.1	120	1.52	171	2.17

Table 4. LD statistics for common SNPs genotyped in this study, with common variants identified by complete resequencing in 152 genes.

Subset*	Yield (%)†	r^2‡	$r^2 > 0.5$ (%)§	$r^2 > 0.8$ (%)	$r^2 = 1.0$ (%)
African-American					
All	23.3	0.715	70.9	53.7	41.5
Tag	12.3	0.698	70.1	51.9	33.2
European-American					
All	25.0	0.841	86.5	72.6	62.4
Tag	8.1	0.810	85.6	69.7	44.8

*SNPs from the current study: either all common SNPs or a minimal tagging subset. †Percentage of all SeattleSNPs PGA variants that were in the selected set. ‡Across all PGA variants, the mean maximum r^2 with a selected SNP in the same locus. §Percentages of PGA variants having an r^2 greater than the specified threshold with any selected SNP in the same locus.

Fig. 2. Distribution of SNP positions and LD structure across the genome. For each chromosome, the top track shows SNP density per kb, with a window size of 500 kb. The middle track shows, for each population, the fraction of common SNPs with MAF > 10% that are in high LD ($r^2 > 0.8$) with at least one other common SNP, with a window size of 500 kb. The bottom track shows, for each population, the fraction of common SNPs that are in an LD bin extending over at least 50 kb, with a window size of 1000 kb.

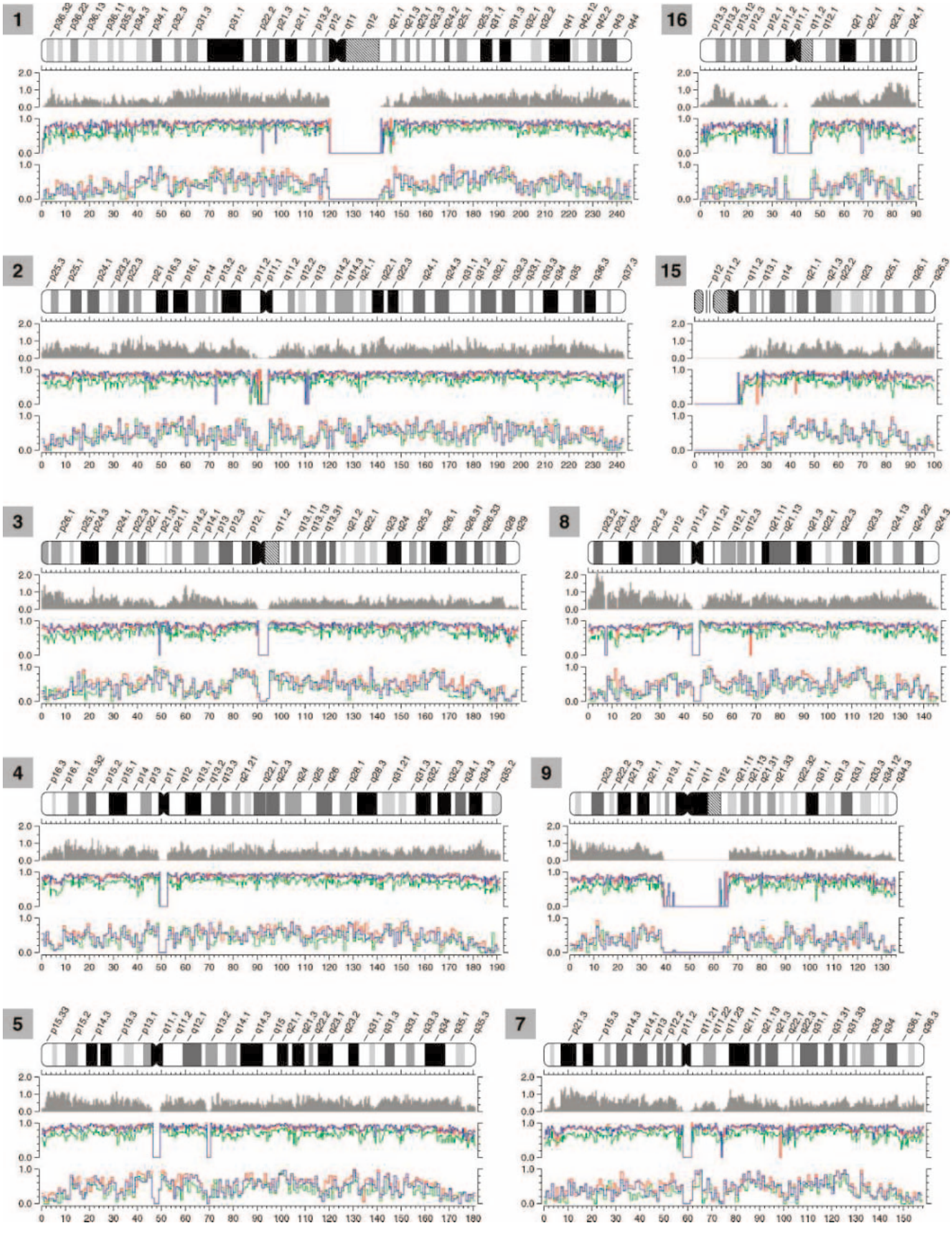

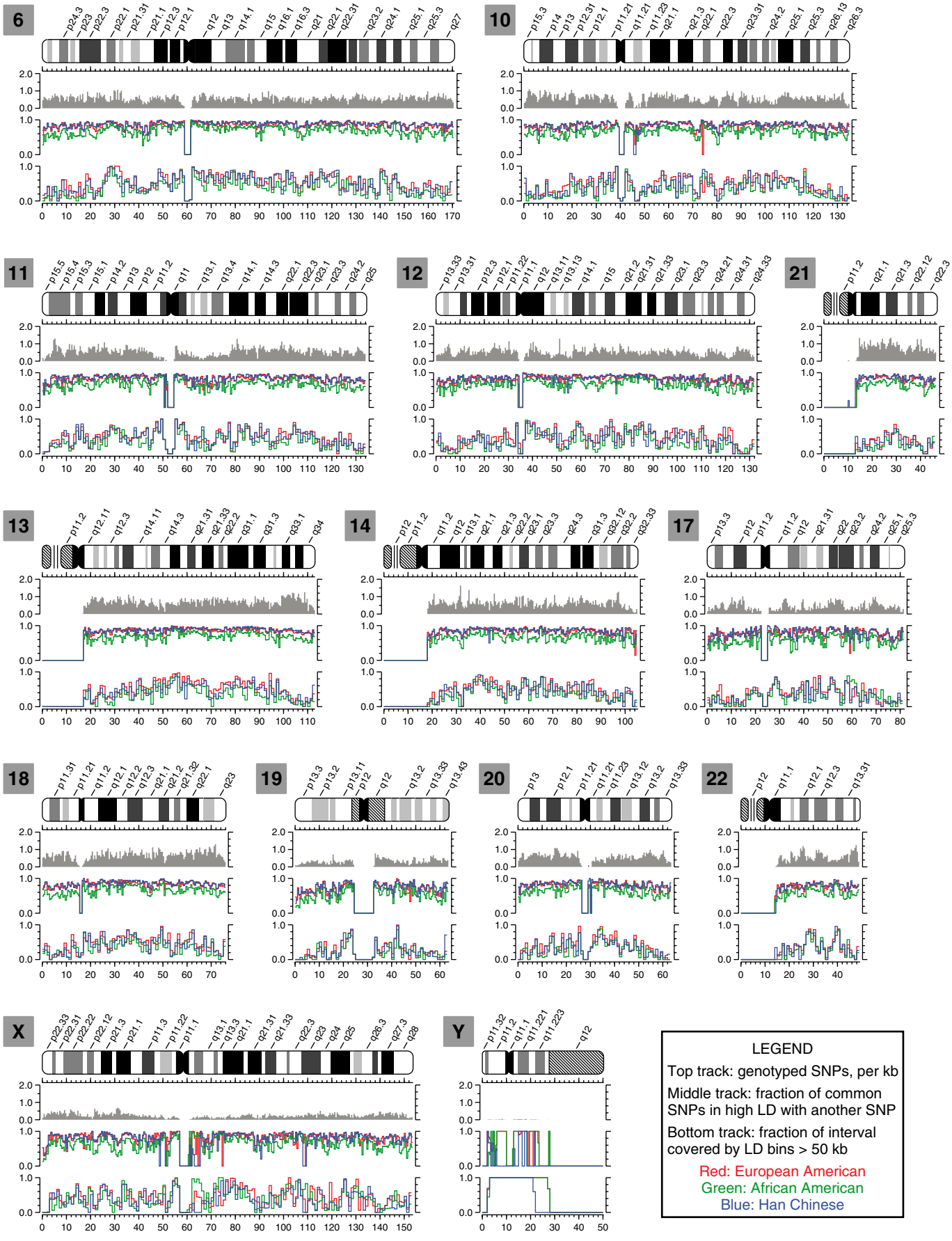
6
10
11
12
21
13
14
17
18
19
20
22
X
Y
LEGEND
Top track: genotyped SNPs, per kb
Middle track: fraction of common SNPs in high LD with another SNP
Bottom track: fraction of interval covered by LD bins > 50 kb
Red: European American
Green: African American
Blue: Han Chinese

any PGA SNP with the most-correlated SNP in the same region that was included in our SNP set. These results indicate that, with the stringent threshold of $r^2 > 0.8$, our SNP set ascertains ~73% of common variation in the European-American sample and ~54% of common variation in the African-American sample. These values are similar to those previously predicted if 2.7 million SNPs from public databases were developed into genotyping assays (*17*). This analysis sets a very conservative lower bound on coverage, because it treats SNPs below the threshold of $r^2 = 0.8$ as completely uncovered and does not reward coverage that exceeds the threshold. Using a less stringent threshold of $r^2 > 0.5$, coverage would improve to 86% in the European-American sample and 71% in the African-American sample. The skewed distribution of r^2 toward high values is apparent in the mean values of 0.84 for the European-American sample and 0.72 for the African-American sample. These numbers are especially impressive considering that we did not genotype 75% of all the common SNPs in these intervals.

Selection of one tag SNP from each LD bin for the three population samples yielded 296,313 of the 991,398 SNPs segregating in the European-American sample (30%); 256,766 of the 909,824 SNPs segregating in the Han Chinese sample (28%); and 540,533 of the 1,083,638 SNPs segregating in the African-American sample (50%). When tag SNPs from European Americans and African Americans were used to assess common variation in the PGA data, for MAF ≥ 10%, the amount of all common variation ascertained was reduced very little compared to that ascertained with the complete sets of common SNPs (Table 4). These tag SNP numbers are smaller than have previously been predicted with a similar selection strategy (*24*); however, we did not attempt to achieve 100% coverage as in that work. Although choosing subsets of SNPs based on bin relationships reduces the genotyping burden for a comprehensive whole-genome scan to some degree in all populations, these data indicate that even taking advantage of such tag SNP selection, a comprehensive whole-genome association study requires genotyping each individual for at least several hundreds of thousands of SNPs.

Haplotype block structure. LD maps and haplotype maps represent somewhat different aspects of the local structure of genetic variation. The genetic architecture of a particular phenotype will determine which representation is most powerful for the identification of functional variants (*33*). In parallel with our LD analysis, we used the HAP program (*34*) to infer haplotypes from our diploid genotype data. We partitioned these reconstructed haplotypes into blocks with limited diversity, separately for each of the three population samples. These blocks were defined as sets of SNPs for which at least 80% of the inferred haplotypes could be grouped into common patterns with population frequencies of at least 5%.

Table 5 summarizes the structure of the three resulting haplotype maps for the whole genome, excluding the Y chromosome. The haplotype map statistics across the three populations appear qualitatively similar to the LD maps, with substantially more blocks in the map derived from the African-American sample than in the maps from the European-American and Han Chinese samples. The numbers of SNPs required to represent frequencies of common haplotype patterns were similar to the numbers of tag SNPs identified in the LD maps. Substantial fractions of LD bins of two or more SNPs crossed haplotype block boundaries, ranging from 33% in the Han Chinese map to 48% in the African-American map.

The bin structure for SNPs in the region of the *CFTR* gene on chromosome 7 (Fig. 3) demonstrates some of the differences between the LD bin and haplotype block maps and further illustrates that there can be substantial population differences in local map structure. In this interval, the European-American and African-American LD maps have similar complexity, with multiple overlapping bins, but the Han Chinese map is dominated by two disjoint bins of highly correlated SNPs. Conversely, a break point near the 116,790-kb position is shared in the African-American and Han Chinese LD maps but is bridged by multiple LD groupings in the European-American map. All three haplotype maps share this break point. However, the African-American map contains many more distinct haplotype blocks than the maps for the other two population samples.

Common genetic variation and human health. Our focus on common genetic variation has several motivations. Common variants account for a larger share of human nucleotide diversity than rare variants and are more experimentally tractable. For the same allelic effect, a common variant represents a larger fraction of phenotypic variance and population attributable risk than a rare one, so common variants are more valuable from the perspective of diagnostics and intervention. Finally, detecting and characterizing effects of rare variants requires very large sample sizes to obtain statistically meaningful numbers of individuals carrying

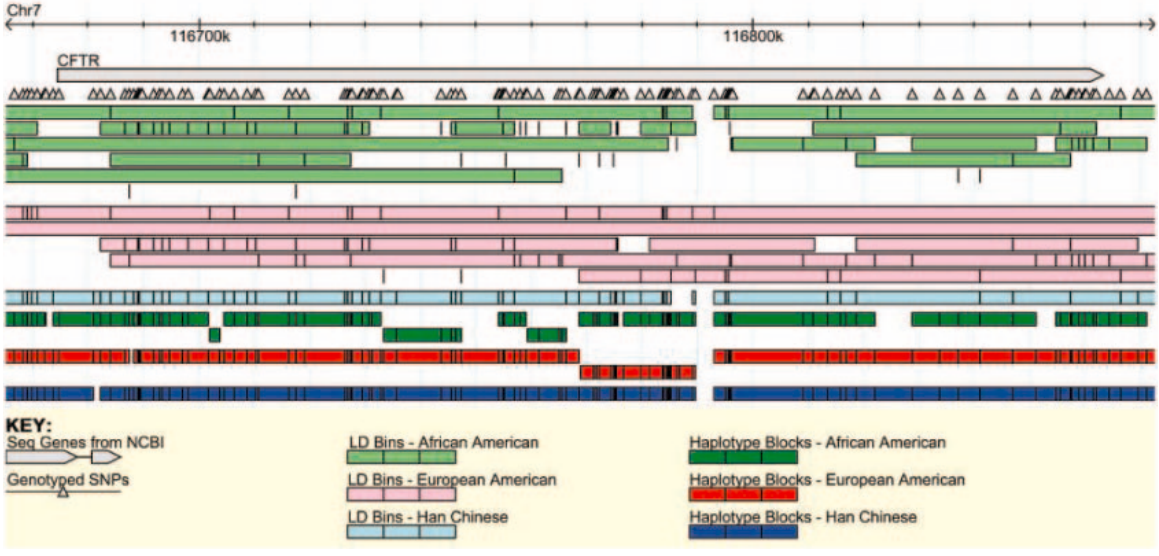

Fig. 3. Extended LD bin and haplotype block structure around the *CFTR* gene. LD bins, where each bin has at least one SNP with $r^2 > 0.8$ with every other SNP, are depicted as light horizontal bars, with the positions of constituent SNPs indicated by vertical tick marks as well as the extreme ends of the bars. Isolated SNPs are indicated by plain tick marks. Haplotype blocks, within which at least 80% of observed haplotypes could be grouped into common patterns with frequencies of at least 5%, are depicted as dark horizontal bars. Unlike haplotype blocks that are by design sequential and nonoverlapping, SNPs in one LD bin can be interdigitated with SNPs in multiple other overlapping bins.

a rare allele. There is no doubt that rare variants play a role in the etiology of common disease, but pursuit of common variants is more tractable with available technologies.

Common human diseases, such as cardiovascular disease and psychiatric illness, are caused by the interplay of multiple genetic and environmental factors. The bounded nature of the human genome and the availability of the complete human genome sequence have resulted in extensive efforts to define the genetic basis of a wide variety of complex human traits. One approach for identifying such genetic risk factors is the case-control association study, in which a group of individuals with disease is found to have an increased frequency of a particular genetic variant compared to a group of control individuals. A number of genetic risk factors for common disease have been identified by such association studies (*3*, *4*, *35*, *36*). These studies suggest that many different genes distributed throughout the human genome contribute to the total genetic variability of a particular complex trait, with any single gene accounting for no more than a few percent of the overall variability of the trait (*37*). Case-control study designs that include on the order of 1000 individuals can provide adequate power to identify genes accounting for only a few percent of the overall genetic variability of a complex trait, even using the very stringent significance levels required when testing large numbers of common DNA variants (*37*). Using such study designs in conjunction with the detailed description of common human DNA variation presented here, it may be possible to identify a set of major genetic risk factors contributing to the variability in a complex disease and/or treatment response. Although knowledge of a single genetic risk factor can seldom be used to predict the treatment outcome of a common disease, knowledge of a large fraction of all the major genetic risk factors contributing to a treatment response or common disease could have immediate utility, allowing existing treatment options to be matched to individual patients without requiring additional knowledge of the mechanisms by which the genetic differences lead to different outcomes.

In our analyses, we selected representations of the data, including pairwise LD as well as a haplotype-based approach, that we felt would be most useful for an initial characterization of this resource. We focused attention on pairwise LD analyses because they provide a particularly simple framework for evaluating coverage and information content of different SNP collections. The optimal representation of genetic variation data remains an area of active research. Although we have determined example haplotype maps of the human genome in these three populations, the most appropriate representation of the data depends substantially on the specific questions to be answered. There will be many maps of human genetic variation, each tailored for specific uses.

Public data availability. We have implemented an instance of the Generic Genome Browser (*38*) at http://genome.perlegen.com for viewing the SNP, LD, and haplotype data reported here; this data will also be available from *Science* upon request. More detailed haplotype analysis results are available at http://research.calit2.net/hap/wgha/ and through dbSNP. The data reported here represent a massive increase in the available number of SNPs characterized in multiple populations. For comparison, although the public SNP database, dbSNP build 122, contained map positions for more than 8.1 million human SNPs, frequencies were available for only 797,000 of these SNPs, mostly in just one population, and genotypes were available for only 210,000 SNPs. Our data also complement the results of the International HapMap Project (*11*), by providing data for many more SNPs across fewer individuals.

This work enables detailed analyses of the structure of human genetic variation on a whole-genome scale. We examined genetic variation in individuals from three populations with substantially different histories and describe general features of variation within and between populations. Because these samples do not capture the full genetic diversity of the populations from which they were selected, our data are not suitable for answering many questions about the detailed genetic structure of human populations (*39*). However, the public availability of these data will enable a wide variety of additional analyses to be carried out by scientists investigating the structure of human genetic variation as well as the genetic basis of human phenotypic differences.

Table 5. Haplotype block partition results for the three populations.

Population	Blocks	Average size, kb*	Required SNPs†
African-American	235,663	8.8	570,886
European-American	109,913	20.7	275,960
Han Chinese	89,994	25.2	220,809

*Average distance spanned by segregating sites in each block. †Minimum number of SNPs required to distinguish common haplotype patterns with frequencies of 5% or higher.

References and Notes

1. L. Kruglyak, D. A. Nickerson, *Nature Genet.* **27**, 234 (2001).
2. C. Romualdi *et al.*, *Genome Res.* **12**, 602 (2002).
3. J. P. Hugot *et al.*, *Nature* **411**, 599 (2001).
4. A. D. Roses, *Neurogenetics* **1**, 3 (1997).
5. N. Patil *et al.*, *Science* **294**, 1719 (2001).
6. S. B. Gabriel *et al.*, *Science* **296**, 2225 (2002).
7. Materials and methods are available as supporting material on *Science* Online.
8. D. A. Hinds *et al.*, *Am. J. Hum. Genet.* **74**, 317 (2004).
9. D. A. Hinds *et al.*, *Hum. Genom.* **1**, 421 (2004).
10. L. Hosking *et al.*, *Eur. J. Hum. Genet.* **12**, 395 (2004).
11. International HapMap Consortium, *Nature* **426**, 789 (2003), available at www.hapmap.org.
12. International SNP Map Working Group, *Nature* **409**, 928 (2001).
13. A. M. Bowcock *et al.*, *Proc. Natl. Acad. Sci. U.S.A.* **88**, 839 (1991).
14. B. S. Weir, C. C. Cockerham, *Evolution* **38**, 1358 (1984).
15. E. J. Parra *et al.*, *Am. J. Hum. Genet.* **63**, 1839 (1998).
16. N. A. Rosenberg *et al.*, *Science* **298**, 2381 (2002).
17. C. S. Carlson *et al.*, *Nature Genet.* **33**, 518 (2003).
18. N. Patterson *et al.*, *Am. J. Hum. Genet.* **74**, 979 (2004).
19. J. M. Akey, G. Zhang, K. Zhang, L. Jin, M. D. Shriver, *Genome Res.* **12**, 1805 (2002).
20. Q. Xiao, H. Weiner, D. W. Crabb, *J. Clin. Invest.* **98**, 2027 (1996).
21. P. Duggal *et al.*, *Genes Immun.* **4**, 245 (2003).
22. K. Nakayama *et al.*, *J. Hum. Genet.* **47**, 92 (2002).
23. B. Devlin, N. Risch, *Genomics* **29**, 311 (1995).
24. C. S. Carlson *et al.*, *Am. J. Hum. Genet.* **74**, 106 (2004).
25. G. A. Huttley, M. W. Smith, M. Carrington, S. J. O'Brien, *Genetics* **152**, 1711 (1999).
26. P. C. Sabeti *et al.*, *Nature* **419**, 832 (2002).
27. A. M. Pittman *et al.*, *Hum. Mol. Genet.* **13**, 1267 (2004).
28. G. Van Gassen, W. Annaert, *Neuroscientist* **9**, 117 (2003).
29. E. R. De Kloet, *Ann. N.Y. Acad. Sci.* **1018**, 1 (2004).
30. E. Dawson *et al.*, *Nature* **418**, 544 (2002).
31. J. K. Pritchard, M. Przeworski, *Am. J. Hum. Genet.* **69**, 1 (2001).
32. SeattleSNPs, National Heart, Lung, and Blood Institute Program for Genomic Applications, University of Washington–Fred Hutchinson Cancer Research Center, Seattle, WA, available at http://pga.gs.washington.edu.
33. J. S. Bader, *Pharmacogenomics* **2**, 11 (2001).
34. E. Halperin, E. Eskin, *Bioinformatics* **20**, 1842 (2004).
35. D. Altshuler *et al.*, *Nature Genet.* **26**, 76 (2000).
36. L. A. Pennacchio *et al.*, *Science* **294**, 169 (2001).
37. N. J. Risch, *Nature* **405**, 847 (2000).
38. L. D. Stein *et al.*, *Genome Res.* **12**, 1599 (2002).
39. D. Serre, S. Pääbo, *Genome Res.* **14**, 1679 (2004).

40. We thank B. Margus and S. Fodor for many helpful discussions, S. Ptak for comments on the manuscript, and the following individuals for expert technical assistance: high throughput genotyping, C. Chen, P. Chu, D. Dalija, J. Doshi, P. Jain, A. Johnson, L. Kamigaki, J. Karbowski, C. Kautzer, V. Mendoza, M. Morenzoni, B. Nguyen, C. Owyang, N. Patil, K. Perry, R. Patel, C. Pethiyagoda, T. L. Pham, C. Sanders, A. Sparks, R. Stokowski, D. Telman, R. Vergara, P. Vu, and P.-H. Wang; bioinformatics design, W. Barrett, H. Huang, M. Jen, X. Li, B. Mooney, and S. Pitts; data analysis, A. Berno, K. Konvicka, A. Ollmann, K. Pant, and J. Sheehan; laboratory information management, R. Gupta, E. Jacobs, C. Radu, and P. Starink; engineering and instrumentation, R. Hartlage, M. Norris, G. Park, and A. Yee; computer systems and operations, T. Fleury, R. Galvez, R. Gordon, P. Hickey, C. LaPlante, J. Nordhal, T. Ogi, and J. VandenHengel. E.E. is supported by the California Institute for Telecommunications and Information Technology.

Supporting Online Material

www.sciencemag.org/cgi/content/full/307/5712/1072/DC1
Materials and Methods
Figs. S1 to S5
Tables S1 to S5
References and Notes

20 September 2004; accepted 14 January 2005
10.1126/science.1105436

Oxidative Addition of Ammonia to Form a Stable Monomeric Amido Hydride Complex

Jing Zhao,[1] Alan S. Goldman,[2] John F. Hartwig[1]*

The insertion of an iridium complex into an N-H bond in ammonia leads to a stable monomeric amido hydride complex in solution at room temperature. This reaction advances the transition-metal coordination chemistry of ammonia beyond its role for more than a century as an ancillary ligand. The precursor for this insertion reaction is an iridium(I) olefin complex with an aliphatic ligand containing one carbon and two phosphorus donor atoms. Kinetic and isotopic labeling studies indicate that olefin dissociates to give a 14-electron iridium(I) fragment, which then reacts with ammonia. This cleavage of the N-H bond under neutral conditions provides a foundation on which to develop future mild catalytic transformations of ammonia, such as olefin hydroamination and arene oxidative amination.

The field of coordination chemistry began when Alfred Werner isolated and elucidated the structures of ammonia complexes of transition metals in the late 19th century (*1*). To this day, the reactions of ammonia with most transition-metal complexes generate simple Lewis acid-base complexes similar to Werner's. In contrast to this simple binding of ammonia, transition-metal complexes react with many other small molecules by inserting into otherwise generally unreactive X-H bonds. This insertion process, termed oxidative addition, is useful for chemical synthesis, because it enables the catalysis of reactions of H_2 (hydrogenation and hydroformylation), H-SiR_3 (hydrosilation), H-BR_2 (hydroboration), and H-C (hydroarylation and alkane dehydrogenation) that yield products ranging from chemical feedstocks to pharmaceuticals. Similarly, oxidative addition of the N-H bond of ammonia, if achieved, would have the potential to initiate valuable new catalytic reactions. For example, the catalytic addition of ammonia to olefins and the coupling of ammonia with arenes are considered to be two of the ten greatest current challenges for catalytic chemistry (*2*).

To accomplish the oxidative addition of ammonia, one must alter its classical transition-metal chemistry. An amido hydride complex formed by cleavage of the N-H bond must be favored over the isomeric ammonia coordination complexes of Werner (Fig. 1). Although no terminal amido complexes have previously been prepared by the oxidative addition of ammonia (*3*–*5*), several terminal amido complexes of the late transition metals have been prepared by other routes during the past several years (*6*–*9*). The reaction chemistry of these terminal amido complexes is beginning to unfold and, thus far, encompasses reactions with electrophiles, weak acids, nonpolar reagents such as hydrogen, and unsaturated reagents such as CO (*9*–*13*). Development of the reaction chemistry of these amido complexes, in combination with the ability to prepare these complexes directly from ammonia under neutral conditions, should give rise to new catalytic processes. We report making a long stride toward this end: the identification of an iridium complex that undergoes oxidative addition of ammonia rapidly at room temperature to form a monomeric terminal amido hydride complex.

To prepare a complex that would insert into the N-H bond of ammonia, we built upon existing iridium chemistry. Iridium complexes with tridentate "pincer" ligands can insert into a variety of X-H bonds under mild conditions (*14*, *15*). In past experiments, we showed that the hydridoiridium amido complex **1**, containing an aromatic pincer ligand, rapidly forms the N-H bond in ammonia complex **2** by reductive elimination, the opposite of oxidative addition (Scheme 1) (*16*). From these observations, we inferred that an appropriate modification of iridium complexes with pincer ligands might tip the thermodynamic balance from rapid formation to rapid cleavage of the N-H bond in ammonia.

Although many factors control the rates and thermodynamics of oxidative addition (*17*), the thermodynamics of oxidative addition tend to be favored by increasing electron density at the metal center. We reasoned that a pincer ligand with an aliphatic backbone (*18*) would be more electron donating than

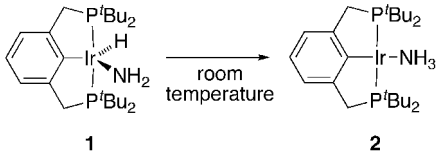

1 **2**

Scheme 1.

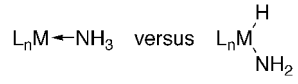

Fig. 1. Ammine versus amido hydride complexes.

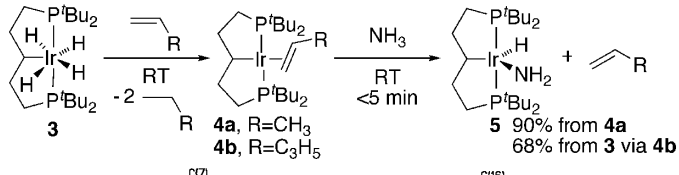

3 **4a**, R=CH$_3$ **4b**, R=C$_3$H$_5$ **5** 90% from **4a** 68% from **3** via **4b**

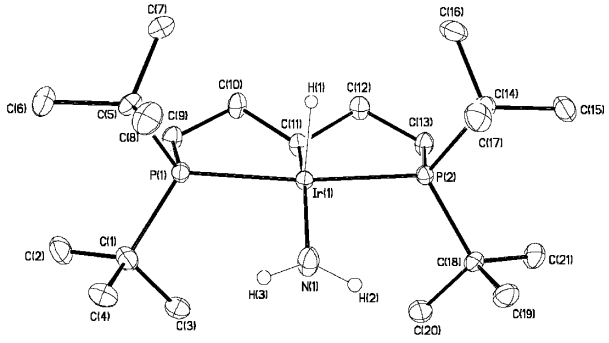

ORTEP diagram of **5**

Scheme 2.

[1]Department of Chemistry, Yale University, Post Office Box 208107, New Haven, CT 06520–8107, USA. [2]Department of Chemistry, Rutgers University, 610 Taylor Road, Piscataway, NJ 08854–8087, USA.

*To whom correspondence should be addressed. E-mail: John.Hartwig@yale.edu

the aromatic ligand in **1** and would, therefore, favor N-H insertion over the coordination of ammonia; the coordination of ammonia would transfer substantial electron density to an already electron-rich metal center. To that end, we treated iridium tetrahydride complex **3** (*19*) with propene and pentene to prepare the olefin complexes **4a** and **4b** (Scheme 2) (*20*).

Treatment of propene complex **4a** with four equivalents of ammonia, at 25°C in cyclohexane, generated the monomeric amido hydride complex **5** in 90% yield within 5 min. Free propene (57%) was observed in the solution phase by ^{1}H nuclear magnetic resonance (NMR) spectroscopy. Similarly, addition of ammonia to the pentene complex **4b**, generated in situ from the precursor **4** and pentene, led to the amido hydride **5** in 68% yield for the two-step process.

Complex **5** was characterized by standard NMR spectroscopic methods, combustion analysis, and x-ray diffraction. We further confirmed the identity of this amido hydride complex by an independent synthesis (Scheme 3). Reaction of the 16-electron hydrido chloride complex **6** with ammonia, followed by addition of the strong base $KN[Si(CH_3)_3]_2$ to deprotonate the coordinated ammonia and eliminate KCl, generated the 16-electron amido hydride complex **5**.

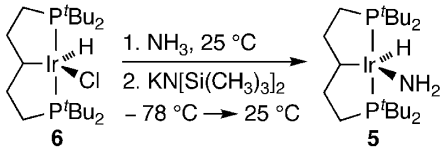

Scheme 3.

X-ray diffraction showed that amido hydride **5** [Oak Ridge thermal ellipsoid plot (ORTEP) diagram in Scheme 2] possesses a geometry between trigonal bipyramidal and square pyramidal. The three angles of the equatorial plane (±estimated standard deviation) are 139.4°(13°) for H-Ir-N, 153.69°(17°) for C-Ir-N, and 66.8°(13°) for C-Ir-H. According to earlier calculations on related iridium complexes (*21*), this geometry results from π bonding between the electron pair on nitrogen and the lowest unoccupied molecular orbital on the metal, which lies in the equatorial plane. The nitrogen in compound **5** could be either cis or trans to the hydrogen on the methine carbon of the ligand backbone. We detected only one isomer by NMR spectroscopy in solution. In the solid state, the nitrogen was cis to this hydrogen.

To investigate the thermodynamics of the oxidative addition, we determined the stability of the amido hydride **5**, relative to the olefin complex **4b**. We combined ammonia, pentene, and the complex **4b** (0.03 M in diethyl ether-d_{10}) in a 15:30:1 ratio. The resulting equilibrium distribution was a 3.9:1 ratio of amido hydride **5** to pentene complex **4b** (Scheme 4) and a 1:2.3 ratio of dissolved ammonia to pentene. Addition of the same ratio of ammonia and pentene to a 0.03 M solution of amido hydride **5** led to the same ratio of **5a** and **4b**. These experiments yield an equilibrium constant of 9 for the conversion of olefin complex **4b** to amido hydride **5**.

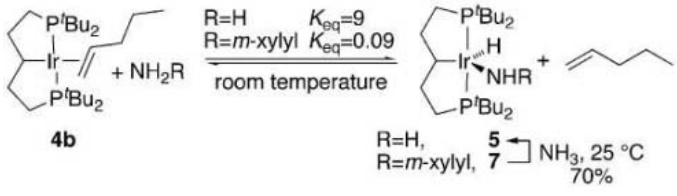

Scheme 4.

We also compared the oxidative addition of ammonia to **4b** with the oxidative addition of aromatic amines, which are typically more reactive toward cleavage of the N-H bond by transition metals (*22*–*24*). Like ammonia, 3,5-dimethylaniline underwent rapid oxidative addition to **4a** and **4b** at room temperature (71% from **4a** with an excess of arylamine), in this case to form arylamido hydride **7** (Scheme 4). However, the conversion of the olefin complex to the hydrido arylamide **7** was thermodynamically less favorable than the reaction with ammonia. Despite the lower N-H bond strength and greater acidity of the aromatic amine, the equilibrium constant for the oxidative addition of 3,5-dimethylaniline to **4b** was only 0.09. In accordance with the more favorable oxidative addition of ammonia, the reaction of **7** with ammonia fully consumed the arylamide and generated free 3,5-dimethylaniline and amido hydride **5** in 70% yield (Scheme 4). These results contrast with the typically greater stability of adducts generated from more acidic protic reagents (*25*). The smaller size of the parent amide ligand relative to the arylamido ligand, the greater π donation by the parent amide ligand, or both may account for the unusual stability of **5** relative to that of **7**.

The formation of **5** from the reaction of ammonia with the olefin complexes **4a** and **4b** need not occur by a simple insertion of the iridium into an N-H bond. For example, insertion of iridium(I) into the C-H bonds of alkyl ligands (*26*) and the α elimination from related pincer ligands in related iridium compounds (*27*, *28*) are precedented. If these reactions occur with **4b**, then the overall oxidative addition of ammonia might occur by addition of ammonia's N-H bond across the iridium-carbon single bond in **8** or the iridium-carbon double bond in **9** of Scheme 5. To investigate whether these mechanisms are operating, we treated **4b** with isotopically labeled ammonia-d_3. In the product of this reaction, **5**-d_3, there was no evidence by ^{2}H NMR spectroscopy for the presence of deuterium in the pincer ligand (*29*). We thereby ruled out reaction through potential intermediates **8** and **9**; all data are consistent with insertion of an iridium(I) complex into the N-H bond of ammonia.

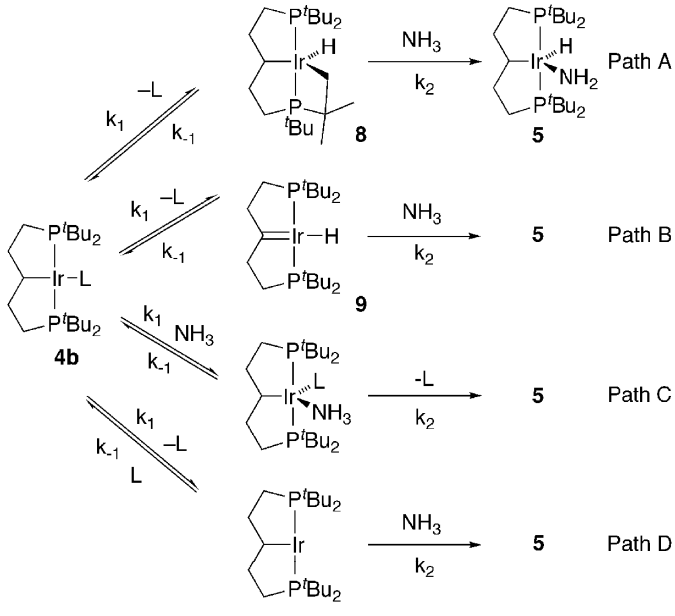

Scheme 5.

Kinetic studies allowed us to distinguish between an associative path C, in which

ammonia would react directly with compounds **4a** and **4b**, and a dissociative path D, in which ammonia would react with a 14-electron complex formed after dissociation of olefin (Scheme 5). The rates of decay of the pentene complex **4b** were measured by ^{31}P NMR spectroscopy with varied amounts of olefin and ratios of ammonia to olefin (data and plot are shown in figs. S1 and S2 and table S1). The observable rate constants, k_{obs}, predicted for reaction by associative path C (Eq. 1) and dissociative path D (Eq. 2), were derived with the steady state approximation. For path C, the observed rate constant would be independent of the concentration of olefin, but for path D, a plot of $1/k_{obs}$ versus the ratio of olefin to ammonia is predicted to be linear with a nonzero intercept. The reactions were clearly slower at higher concentrations of olefin, and a plot of $1/k_{obs}$ versus the ratio of olefin to ammonia was found to be linear with a positive slope ($0.20 \times 10^{-4} \pm 0.01 \times 10^{-4}$ s^{-1}) and a nonzero y intercept ($0.65 \times 10^{-4} \pm 0.16 \times 10^{-4}$ s). These data suggest that olefin dissociation is the first step in the reaction, and, if so, the y intercept of this double reciprocal plot would correspond to the inverse of the rate constant for dissociation of olefin.

$$\frac{1}{k_{obs}} = \frac{k_{-1}}{k_1 k_2[\text{ammonia}]} + \frac{1}{k_1[\text{ammonia}]} \quad (1)$$

$$\frac{1}{k_{obs}} = \frac{k_{-1}[\text{pentene}]}{k_1 k_2[\text{ammonia}]} + \frac{1}{k_1} \quad (2)$$

Because substitution reaction of square-planar d^8 complexes typically proceed associatively, and because the reactions could occur by more complex pathways with multiple equilibria preceding N-H bond cleavage, we conducted further experiments to test whether the reaction was initiated by dissociation of olefin. The pentene in complex **4b** is displaced by ethylene to form ethylene complex **4c**. If the reactions of **4b** occur dissociatively, then the rate constants for dissociation of pentene obtained from the reaction of **4b** with ethylene and from the reaction of **4b** with ammonia should be the same.

Consistent with dissociative reactions of **4b**, the reaction of **4b** with ethylene was independent of the concentration of ethylene or 0.03 to 0.3 M added pentene; all reactions occurred with rate constants within 3% of the mean value of 1.6×10^{-3}. Moreover, this mean value is well within experimental error of the value of k_1 (1.5×10^{-3}) measured for the reaction of ammonia with **4b**.

The identification of an iridium complex that undergoes oxidative addition of ammonia and the elucidation of key thermodynamic and mechanistic aspects of the reaction advance our understanding of how to cleave N-H bonds under mild conditions. We anticipate that this understanding will accelerate the development of catalytic chemistry that parallels the existing reactions of hydrogen, hydrocarbons, silanes, and boranes but begins with oxidative addition of the N-H bond of abundant and inexpensive ammonia.

References and Notes

1. G. B. Kauffman, in *Coordination Chemistry: A Century of Progress*. (American Chemical Society Symposium Series, Washington, DC, 1994), vol. 565, pp. 3–34.
2. Two reactions of ammonia are among the top 10 challenges for catalysis listed in this article: J. Haggin, *Chem. Eng. News*. **71**, 23 (1993).
3. For a reaction of an Ir(I) complex with ammonia to form an insoluble product containing hydrides and bridging amides, as characterized by solid-state IR and ^1H NMR spectroscopy and derivatization, see A. L. Casalnuovo, J. C. Calabrese, D. Milstein, *Inorg. Chem.* **26**, 971 (1987).
4. For the protonolysis of a hydride ligand on a group IV metal complex, presumably after coordination of the ammonia ligand, see G. L. Hillhouse, J. E. Bercaw, *J. Am. Chem. Soc.* **106**, 5472 (1984).
5. For an example of a reaction of ammonia with a cluster to form a product in low yield that was formulated by ^1H NMR spectroscopy to contain a bridging hydride and bridging amide, see E. G. Bryan, B. F. G. Johnson, J. Lewis, *J. Chem. Soc. Dalton Trans.* **1977**, 1328 (1977).
6. F. L. Joslin, M. P. Johnson, J. T. Mague, D. M. Roundhill, *Organometallics* **10**, 2781 (1991).
7. A. W. Kaplan, J. C. M. Ritter, R. G. Bergman, *J. Am. Chem. Soc.* **120**, 6828 (1998).
8. J. Campora, P. Palma, D. del Rio, M. M. Conejo, E. Alvarez, *Organometallics* **23**, 5653 (2004).
9. D. Conner, K. N. Jayaprakash, T. R. Cundari, T. B. Gunnoe, *Organometallics* **23**, 2724 (2004).
10. H. E. Bryndza, W. Tam, *Chem. Rev.* **88**, 1163 (1988).
11. J. R. Fulton, A. W. Holland, D. J. Fox, R. G. Bergman, *Acc. Chem. Res.* **35**, 44 (2002).
12. J. R. Fulton, S. Sklenak, M. W. Bouwkamp, R. G. Bergman, *J. Am. Chem. Soc.* **124**, 4722 (2002).
13. D. J. Fox, R. G. Bergman, *Organometallics* **23**, 1656 (2004).
14. M. Kanzelberger, B. Singh, M. Czerw, K. Krogh-Jespersen, A. S. Goldman, *J. Am. Chem. Soc.* **122**, 11017 (2000).
15. D. Morales-Morales, D. W. Lee, Z. Wang, C. M. Jensen, *Organometallics* **20**, 1144 (2001).
16. M. Kanzelberger *et al.*, *J. Am. Chem. Soc.* **125**, 13644 (2003).
17. K. Krogh-Jesperson *et al.*, *J. Am. Chem. Soc.* **124**, 10797 (2002).
18. N. A. Al-Salem, H. D. Empsall, R. Markham, B. L. Shaw, B. Weeks, *J. Chem. Soc. Dalton Trans.* **1979**, 1972 (1979).
19. M. A. McLoughlin, R. J. Flesher, W. C. Kaska, H. A. Mayer, *Organometallics* **13**, 3816 (1994).
20. Materials and methods, including the details of the synthesis of the olefin complexes, are available as supporting material on *Science* Online.
21. J. F. Riehl, Y. Jean, O. Eisenstein, M. Pelissier, *Organometallics* **11**, 729 (1992).
22. J. F. Hartwig, R. G. Bergman, R. A. Andersen, *J. Am. Chem. Soc.* **113**, 3404 (1991).
23. J. Ruiz, V. Rodriguez, G. Lopez, P. A. Chaloner, P. B. Hitchcock, *J. Chem. Soc. Dalton Trans.* **1997**, 4271 (1997).
24. M. Kanzelberger *et al.*, *J. Am. Chem. Soc.* **125**, 13644 (2003).
25. P. L. Holland, R. A. Andersen, R. G. Bergman, J. K. Huang, S. P. Nolan, *J. Am. Chem. Soc.* **119**, 12800 (1997).
26. H. A. Y. Mohammad *et al.*, *Organometallics* **21**, 5775 (2002).
27. H. D. Empsall *et al.*, *J. Chem. Soc. Chem. Commun.* **1977**, 589 (1977).
28. C. Crocker *et al.*, *J. Chem. Soc. Dalton Trans.* **1982**, 1217 (1982).
29. This method would detect deuterium in the ligand if it were present in 10% of the sample.

30. We thank the Department of Energy for funding. Structural data for compounds **4a** and **5** have been deposited in the Cambridge Crystallographic Data Centre under CCDC 260224 (**4a**) and 260225 (**5**), and can be obtained free of charge at www.ccdc.cam.ac.uk/conts/retrieving.html. We thank L. Bienen for editing of the manuscript.

Supporting Online Material

www.sciencemag.org/cgi/content/full/307/5712/1080/DC1
Materials and Methods
Figs. S1 to S5
Tables S1 to S6
References and Notes

1 December 2004; accepted 12 January 2005
10.1126/science.1109389

Efficient Bipedal Robots Based on Passive-Dynamic Walkers

Steve Collins,[1] Andy Ruina,[2]* Russ Tedrake,[3] Martijn Wisse[4]

Passive-dynamic walkers are simple mechanical devices, composed of solid parts connected by joints, that walk stably down a slope. They have no motors or controllers, yet can have remarkably humanlike motions. This suggests that these machines are useful models of human locomotion; however, they cannot walk on level ground. Here we present three robots based on passive-dynamics, with small active power sources substituted for gravity, which can walk on level ground. These robots use less control and less energy than other powered robots, yet walk more naturally, further suggesting the importance of passive-dynamics in human locomotion.

Most researchers study human locomotion by observing people as they walk, measuring joint angles and ground reaction forces (*1*). Our approach is different: We study human locomotion by designing and testing walking machines that we compare to humans in terms of morphology, gait appearance, energy use, and control.

Previous bipedal robots with humanlike forms have demonstrated smooth, versatile motions (*2–5*). These impressive robots are based on the mainstream control paradigm, namely, precise joint-angle control. For the study of human walking, this control paradigm is unsatisfactory, because it requires actuators with higher precision and frequen-

cy response than human muscles have (*6*) and requires an order of magnitude more energy. To address these issues, passive-dynamic walkers (Fig. 1) were proposed as a new design and control paradigm (*7*). In contrast to mainstream robots, which actively control every joint angle at all times, passive-dynamic walkers do not control any joint angle at any time. Although these walkers have no actuation or control, they can walk downhill with startlingly humanlike gaits (*8*).

To demonstrate that the humanlike properties of passive-dynamic machines are not dependent on gravitational power, but rather extend to level-ground walking, we built three powered walking robots (Fig. 2) at three institutions, substituting gravitational power with simple actuation. The Cornell biped (Fig. 2A) is based on the passive device in Fig. 1D and is powered by electric motors with springs that drive ankle push-off. It has five internal degrees of freedom (two ankles, two knees, and a hip), each arm is mechanically linked to the opposite leg, and the small body is kinematically constrained so that its midline bisects the hip angle. The Delft biped (Fig. 2B) has a similar morphology, but it is powered by pneumatic hip actuation and has a passive ankle. The Massachusetts Institute of Technology (MIT) learning biped (Fig. 2C) is based on the simpler ramp-walkers in Fig. 1, A and B. It has six internal degrees of freedom (two servo motors in each ankle and two passive hips), each arm is mechanically linked to the opposite leg, the body hangs passively, and it uses reinforcement learning to automatically acquire a control policy. The supporting online movies show these robots walking and the supporting online text describes their construction details (*9*).

The Cornell biped is specifically designed for minimal energy use. The primary energy losses for humans and robots walking at a constant speed are due to dissipation when a foot hits the ground and to active braking by the actuators (negative work). The Cornell design demonstrates that it is possible to completely avoid this negative actuator work. The only work done by the actuators is positive: The left ankle actively extends when triggered by the right foot hitting the ground, and vice versa. The hip joint is not powered, and the knee joints only have latches. The average mechanical power (*10*) of the two ankle joints is about 3 W, almost identical to the scaled gravitational power consumed by the passive-dynamic machine on which it is based (*8*). Including electronics, microcontroller, and actuators, the Cornell biped consumes 11 W (*11*).

To compare efficiency between humans and robots of different sizes, it is convenient to use the dimensionless specific cost of transport, c_t = (energy used)/(weight × distance traveled). In order to isolate the effectiveness of the mechanical design and controller from the actuator efficiency, we distinguish between the specific energetic cost of transport, c_{et}, and the specific mechanical cost of transport, c_{mt}. Whereas c_{et} uses the total energy consumed by the system (11 W for the Cornell biped), c_{mt} only considers the positive mechanical work of the actuators (3 W for the Cornell biped). The 13-kg Cornell biped walking at 0.4 m/s has $c_{et} \approx 0.2$ and $c_{mt} \approx 0.055$. Humans are similarly energy effective, walking with $c_{et} \approx 0.2$, as estimated by the volume of oxygen they consume (V_{O_2}), and $c_{mt} \approx 0.05$ (*12*–*14*). Measurement of actuator work on the Delft biped yields $c_{mt} \approx 0.08$. Based on the small slopes that it descends when passive, we estimate the MIT biped to have $c_{mt} \geq 0.02$. Although the MIT and Delft bipeds were not specifically designed for low-energy use, both inherit energetic features from the passive-dynamic walkers on which they are based. By contrast, we estimate the state-of-the-art Honda humanoid Asimo to have $c_{et} \approx 3.2$ and $c_{mt} \approx 1.6$ (*15*). Thus Asimo, perhaps representative of joint-angle controlled robots, uses at least 10 times the energy (scaled) of a typical human.

Control algorithms for state-of-the-art, level-ground walking robots are typically complex, requiring substantial real-time computation. In contrast, the Delft and Cornell bipeds walk with primitive control algorithms. Their only sensors detect ground contact, and their only motor commands are on/off signals issued once per step. In addition to powering the motion, hip actuation in the Delft biped also improves fore-aft robustness against large disturbances by swiftly placing the swing leg in front of the robot before it has a chance to fall forward (*16*, *17*).

The MIT biped (Fig. 2C) is designed to test the utility of motor learning on a passive-dynamic mechanical design. The goal of the learning is to find a control policy that

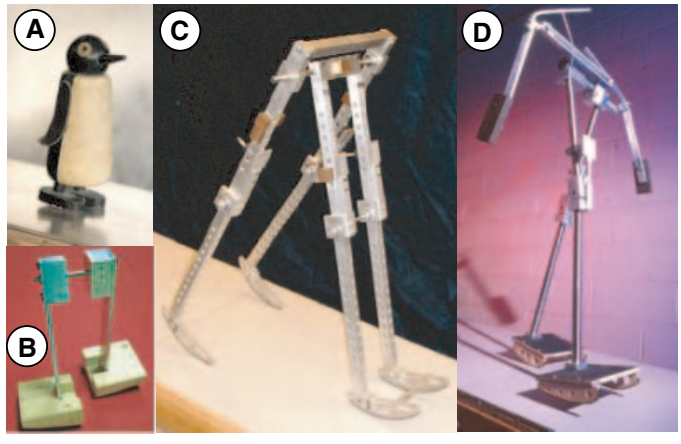

Fig. 1. "Ramp-walking," "downhill," "unpowered," or "passive-dynamic" machines. Our powered bipeds are based on these passive designs. (**A**) The Wilson "Walkie" (*27*). (**B**) MIT's improved version (*28*). Both (A) and (B) walk down a slight ramp with the "comical, awkward, waddling gait of the penguin" (*27*). (**C**) Cornell copy (*29*) of McGeer's capstone design (*7*). This four-legged "biped" has two pairs of legs, an inner and outer pair, to prevent falling sideways. (**D**) The Cornell passive biped with arms [photo: H. Morgan]. This walker has knees and arms and is perhaps the most humanlike passive-dynamic walker to date (*8*).

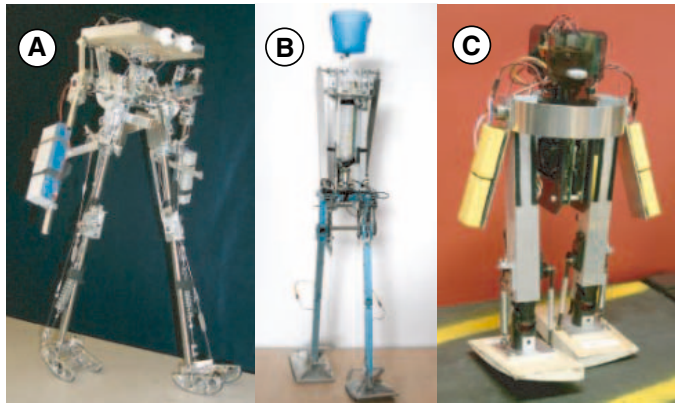

Fig. 2. Three level-ground powered walking robots based on the ramp-walking designs of Fig. 1. (**A**) The Cornell biped. (**B**) The Delft biped. (**C**) The MIT learning biped. These powered robots have motions close to those of their ramp-walking counterparts as seen in the supporting online movies (movies S1 to S3). Information on their construction is in the supporting online text (*9*).

[1]Mechanical Engineering, University of Michigan, Ann Arbor, MI 48104, USA. [2]Theoretical and Applied Mechanics, Cornell University, Ithaca, NY 14853, USA. [3]Brain and Cognitive Sciences and Center for Bits and Atoms, Massachusetts Institute of Technology, Cambridge, MA 02139, USA. [4]Mechanical Engineering, Delft University of Technology, NL-2628 CD Delft, Netherlands.

*To whom correspondence should be addressed. E-mail: ruina@cornell.edu

stabilizes the robot's trajectory on level terrain using the passive ramp-walking trajectory as the target. The robot acquires a feedback control policy that maps sensors to actions using a function approximator with 35 parameters. With every step that the robot takes, it makes small, random changes to the parameters and measures the change in walking performance. This measurement yields a noisy sample of the relation between the parameters and the performance, called the performance gradient, on each step. By means of an actor-critic reinforcement learning algorithm (*18*), measurements from previous steps are combined with the measurement from the current step to efficiently estimate the performance gradient on the real robot despite sensor noise, imperfect actuators, and uncertainty in the environment. The algorithm uses this estimate in a real-time gradient descent optimization to improve the stability of the step-to-step dynamics (Fig. 3). The robot's actuators are mounted so that when they are commanded to their zero position, the robot imitates its passive counterpart. Starting from this zero policy, the learning system quickly and reliably acquires an effective control policy for walking, using only data taken from the actual robot (no simulations), typically converging in 10 min or ~600 steps. Figure 3 illustrates that the learned control policy not only achieves the desired trajectory but is also robust to disturbances. The robot can start, stop, steer, and walk forward and backward at a small range of speeds. This learning system works quickly enough that the robot is able to continually adapt to the terrain (e.g., bricks, wooden tiles, and carpet) as it walks.

Each of the robots here has some design features that are intended to mimic humans. The Cornell and Delft bipeds use anthropomorphic geometry and mass distributions in their legs and demonstrate ankle push-off and powered leg swinging, both present in human walking (*14*, *19*). They do not use high-power or high-frequency actuation, which are also unavailable to humans. These robots walk with humanlike efficiency and humanlike motions (Fig. 4 and movies S1 to S3). The motor learning system on the MIT biped uses a learning rule that is biologically plausible at the neural level (*20*). The learning problem is formulated as a stochastic optimal feedback control problem; there is emerging evidence that this formulation can also describe biological motor learning (*21*).

The Cornell and Delft bipeds demonstrate that walking can be accomplished with extremely simple control. These robots do not rely on sophisticated real-time calculations or on substantial sensory feedback such as from continuous sensing of torques, angles, or attitudes. This implies that steady-state human walking might require only simple control as well; the sequencing of human joint-angles in time might be determined as much by morphology as by motor control. We note that no other robots have done particularly better at generating humanlike gaits even when using high-performance motors, a plethora of sensors, and sophisticated control.

In theory, pushing off just before heel-strike requires about one-fourth the energy of pushing off just after heel-strike (*22*, *23*), so the Cornell robot was initially designed with this preemptive push-off strategy. Initial push-off resulted in both higher torque demands on the motor and a high sensitivity to push-off timing that our primitive control system could not reliably stabilize. Humans seem to solve both of these problems without a severe energy penalty by using a double support phase that overlaps push-off and heel-strike. These issues must also be addressed in the design of advanced foot prostheses.

The success of the Delft robot at balancing using ankles that kinematically couple

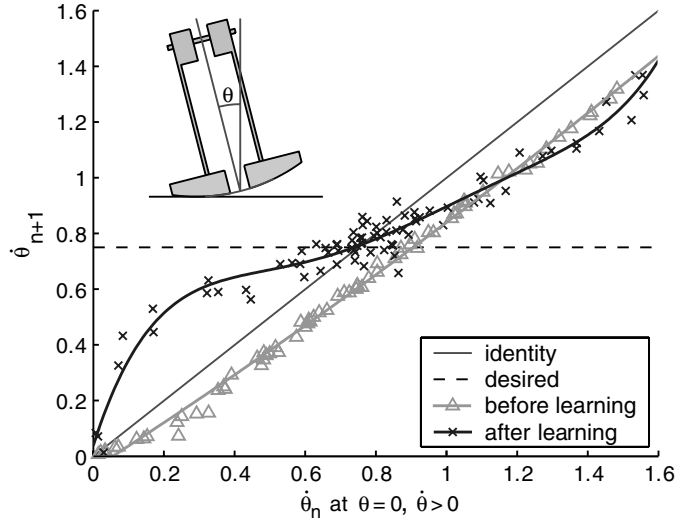

Fig. 3. Step-to-step dynamics of the MIT biped walking in place on a level surface, before (△) and after (x) learning. Shown is the roll angular velocity when the right foot collides with the ground ($\theta = 0$, $\dot{\theta} > 0$) at step $n + 1$ versus step n. Intersections of the plots with the solid identity line are fixed points. The horizontal dashed line is the theoretical ideal; the robot would reach $\dot{\theta} = 0.75\ s^{-1}$ in one step. This ideal cannot be achieved due to limitations in the controllability of the actuation system. On a level surface, before learning, the robot loses energy on every step ($\dot{\theta}_{n+1} < \dot{\theta}_n$), eventually coming to rest at $\dot{\theta} = 0$. After learning, the robot quickly converges near $\dot{\theta} = 0.75\ s^{-1}$ for $0 \le \dot{\theta}_0 \le 1.7\ s^{-1}$.

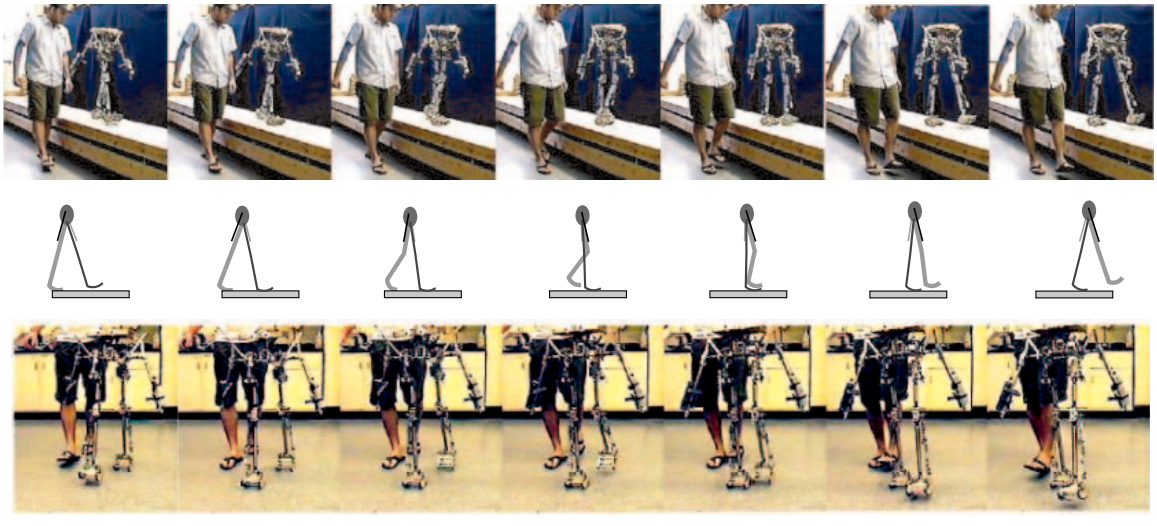

Fig. 4. Two sets of video stills of the Cornell ankle-powered biped walking on a level surface next to a person. A little less than one step is shown at 7.5 frames/s. Both the robot and the person are walking at about 1 step/s. The stick figure indicates the leg angles for the corresponding video stills; the right arm and leg are darker than the left.

leaning to steering hints that humans could similarly use a simple coupling between lean and lateral foot placement to aid balance. Furthermore, simulations used in the development of the Delft robot showed that the swift swing-leg motion not only increased fore-aft stability but also increased lateral stability. Indeed, the physical robot was not able to balance laterally without sufficient fore-aft swing-leg actuation. This highlights the possible coupling between lateral and sagittal balance in human walking.

The MIT biped shows that the efficiency of motor learning can be strongly influenced by the mechanical design of the walking system, both in robots and possibly in humans. Previous attempts at learning control for bipedal robots have required a prohibitively large number of learning trials in simulation (*24*) or a control policy with predefined motion primitives on the robot (*25*). By exploiting the natural stability of walking trajectories on the passive-dynamic walker, our robot was able to learn in just a few minutes without requiring any initial control knowledge. We also found that it was possible to estimate the walking performance gradient by making surprisingly small changes to the control parameters, allowing the robot to continue walking naturally as it learns. This result supports the use of actor-critic reinforcement learning algorithms as models for biological motor learning.

The conclusion that natural dynamics may largely govern locomotion patterns was already suggested by passive-dynamic machines. A common misconception has been that gravity power is essential to passive-dynamic walking, making it irrelevant to understanding human walking. The machines presented here demonstrate that there is nothing special about gravity as a power source; we achieve successful walking using small amounts of power added by ankle or hip actuation.

We expect that humanoid robots will be improved by further developing control of passive-dynamics–based robots and by paying closer attention to energy efficiency and natural dynamics in joint-controlled robots (*26*). Whatever the future of humanoid robots, the success of human mimicry demonstrated here suggests the importance of passive-dynamic concepts in understanding human walking.

References and Notes

1. D. A. Winter, *The Biomechanics and Motor Control of Human Gait* (Univ. of Waterloo Press, Waterloo, Ontario, Canada, 1987).
2. I. Kato *et al.*, *Proc. CISM-IFToMM Theory and Practice of Robots and Manipulators* (Udine, Italy, 1973), pp. 12–24.
3. Y. Sakagami *et al.*, *Proc. IEEE/Robotics Society of Japan (RSJ) Int. Conf. Intell. Robots Syst.* (IEEE/RSJ, Lausanne, Switzerland, 2002), pp. 2478–2483.
4. C. Chevallereau *et al.*, *IEEE Control Syst. Mag.* **23**, 57 (2003).
5. F. Pfeiffer, K. Löffler, M. Gienger, *Proc. IEEE Int. Conf. Robotics Automation* (IEEE, Washington, DC, 2002), pp. 3129–3135.
6. F. Zajac, *Crit. Rev. Biomed. Eng.* **17**, 359 (1989).
7. T. McGeer, *Int. J. Robotics Res.* **9**, 62 (1990).
8. S. H. Collins, M. Wisse, A. Ruina, *Int. J. Robot. Res.* **20**, 607 (2001).
9. Supporting online movies and text are available at *Science* Online.
10. Mechanical power is defined here as net positive mechanical work at the joints $= \int_0^T \sum [\omega_j M_j]^+ dt/T$ where T is the period of one step, ω_j is the relative angular velocity at one joint, M_j is the torque across that joint, $[x]^+ = x$ if $x > 0$ and 0 otherwise, and the sum is over all the joints. Because only the ankle does positive work on the Cornell robot, this can be measured by measuring the foot force as the ankle extends during push-off.
11. For the Cornell robot, total power was measured by averaging the voltage across a 1-ohm resistor put in series with the battery.
12. E. Atzler, R. Herbst, *Pflueg. Arch. Gesamate Physiol.* **215**, 291 (1927).
13. N. H. Molen, R. H. Rozendal, W. Boon, *Proc. K. Ned. Akad. Wet. Ser. C* **75**, 305 (1972).
14. J. M. Donelan, R. Kram, A. D. Kuo, *J. Exp. Biol.* **205**, 3717 (2002).
15. Honda's ASIMO can walk at a variety of speeds, kick balls, and even climb stairs. It weighs 510 N, can walk at speeds up to 1.6 km hour^{-1}, and drains a 38.4-V, 10–A-hour battery in about 30 min (http://world.honda.com/ASIMO/). Using these numbers, we estimate $c_{et} \approx 3.2$ and, assuming a 50% drive train efficiency, $c_{mt} \approx 1.6$.
16. M. Wisse, J. van Frankenhuyzen, *Proc. Conf. Adaptive Motion Anim. Machines* (Kyoto, Japan, 2003).
17. M. Wisse, A. L. Schwab, R. Q. van der Linde, F. C. T. van der Helm, *IEEE Trans. Robot.*, in press.
18. R. Tedrake, T. W. Zhang, M. Fong, H. S. Seung, *Proc. IEEE/RSJ Int. Conf. Intell. Robots Syst.* (IEEE/RSJ, Sendai, Japan, 2004).
19. T. McGeer, *J. Theor. Biol.* **163**, 277 (1993).
20. H. Seung, *Neuron* **40**, 1063 (2003).
21. E. Todorov, *Nature Neurosci.* **5**, 1226 (2002).
22. A. D. Kuo, *J. Biomech. Eng.* **124**, 113 (2002).
23. A. Ruina, J. Bertram, M. Srinivasan, *J. Theor. Biol.*, in press.
24. H. Benbrahim, J. A. Franklin, *Robot. Auton. Syst.* **22**, 283 (1997).
25. A. Kun, W. T. Miller III, *Proc. IEEE Int. Conf. Robotics Automation* (IEEE, Minneapolis, MN, 1996).
26. J. Pratt, thesis, Massachusetts Institute of Technology (2000).
27. J. E. Wilson, U.S. Patent 2,140, 275; available at www.tam.cornell.edu/~ruina/hplab/.
28. R. Tedrake, T. W. Zhang, M. Fong, H. S. Seung, *Proc. IEEE Int. Conf. Robotics Automation* (IEEE, New Orleans, LA, 2004).
29. M. Garcia, A. Chatterjee, A. Ruina, *Dyn. Stabil. Syst.* **15**, 75 (2000).

30. The Cornell robot was developed by S.C. with suggestions from A.R.; the Delft robot was developed by M.W. and J. van Frankenhuyzen on an Stichting Technische Wetenschappen grant, with help from A. Schwab; and the MIT robot was developed by R.T. and T. Weirui Zhang with help from M.-f. Fong and D. Tan in the lab of H. Sebastian Seung. A.R. and S.C. were funded by an NSF Biomechanics grant. R.T. was funded by the Packard Foundation and the NSF. The text was improved by comments from N. Agnihotri, C. Atkeson, J. Burns, A. Chatterjee, M. Coleman, J. Grizzle, P. Holmes, I. ten Kate, A. Kun, A. Kuo, Y. Loewenstein, S. van Nouhuys, D. Paluska, A. Richardson, S. Seung, M. Srinivasan, S. Strogatz, and N. Sydor.

Supporting Online Material

www.sciencemag.org/cgi/content/full/307/5712/1082/DC1
Materials and Methods
SOM Text
Movies S1 to S3
References and Notes

22 November 2004; accepted 26 January 2005
10.1126/science.1107799

Terrestrial Gamma-Ray Flashes Observed up to 20 MeV

David M. Smith,[1]* Liliana I. Lopez,[2] R. P. Lin,[3] Christopher P. Barrington-Leigh[4]

Terrestrial gamma-ray flashes (TGFs) from Earth's upper atmosphere have been detected with the Reuven Ramaty High Energy Solar Spectroscopic Imager (RHESSI) satellite. The gamma-ray spectra typically extend up to 10 to 20 megaelectron volts (MeV); a simple bremsstrahlung model suggests that most of the electrons that produce the gamma rays have energies on the order of 20 to 40 MeV. RHESSI detects 10 to 20 TGFs per month, corresponding to ~50 per day globally, perhaps many more if they are beamed. Both the frequency of occurrence and maximum photon energy are more than an order of magnitude higher than previously known for these events.

Terrestrial gamma-ray flashes (TGFs) were unexpectedly detected from Earth's atmosphere by the Burst and Transient Source Experiment (BATSE) on the Compton Gamma-Ray Observatory (CGRO), a NASA satellite in low-Earth orbit between 1991 and 2000. Each BATSE TGF (*1*) lasted between a fraction of a millisecond and several milliseconds, shorter than all other transient gamma-ray phenomena observed from space. Since they were first detected, it has also been noticed that TGFs had a harder energy spectrum (higher average energy per photon) than any of these other phenomena (*1*).

Fishman *et al.* (*1*) immediately interpreted the TGFs as high-altitude electrical discharges and found a correlation with thunderstorms.

[1]Physics Department and Santa Cruz Institute for Particle Physics, University of California, Santa Cruz, 1156 High Street, Santa Cruz, CA 95064, USA. [2]Astronomy Department and Space Sciences Laboratory, University of California, Berkeley, Berkeley, CA 94720, USA. [3]Physics Department and Space Sciences Laboratory, University of California, Berkeley, Berkeley, CA 94720, USA. [4]University of British Columbia, 2329 West Mall Vancouver, BC V6T 1Z4 Canada.

*To whom correspondence should be addressed. E-mail: dsmith@scipp.ucsc.edu

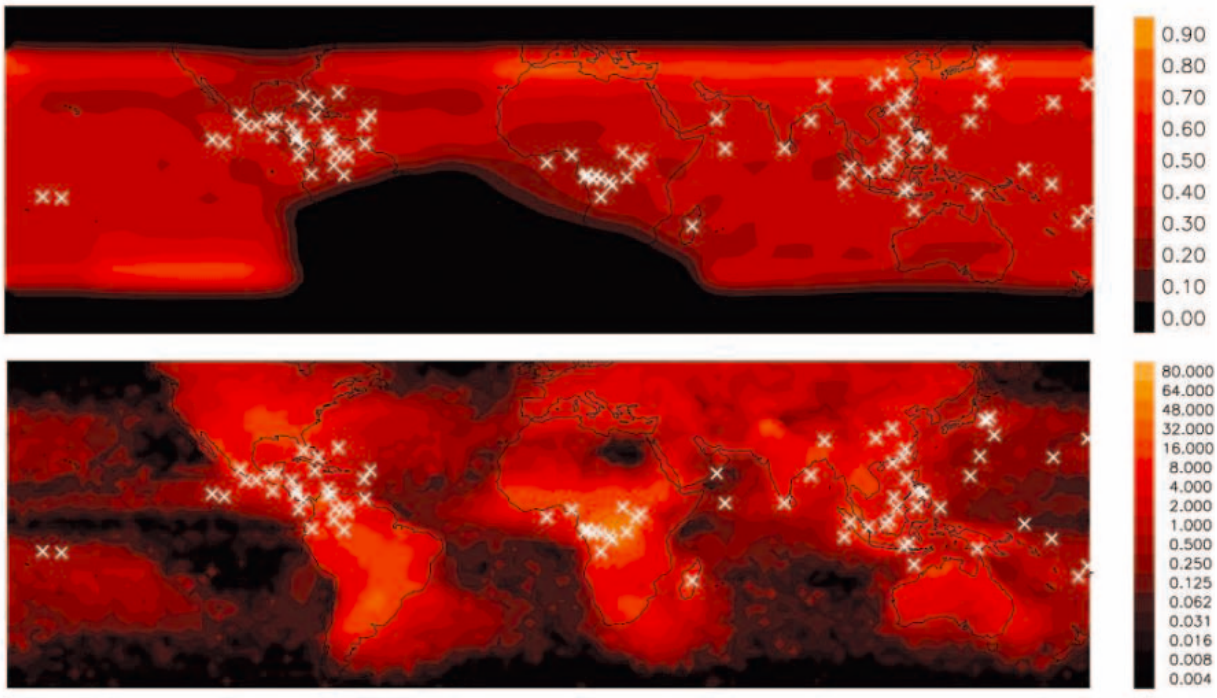

Fig. 1. RHESSI position during each recorded TGF, plotted over (i) the expected distribution of observed TGFs if the population were evenly distributed over the globe, with the scale in fraction of maximum exposure (**top**); and (ii) long-term lightning frequency data (*29*), with the scale in flashes per square kilometer per year (**bottom**).

Hard x-rays and/or gamma rays have also been detected in thunderclouds and at ground level from natural and triggered lightning strokes (*2*–*5*). Acceleration of electrons to high energies in electric fields above thunderstorms was predicted in 1925 by Wilson (*6*), and this runaway process was recently shown (*7*) to be capable of avalanche multiplication, making its variants (*8*–*10*) good candidates for the TGF parent process.

Runaway breakdown is one of several candidate mechanisms for the production of red sprites and blue jets, transient luminous events (TLEs) in the upper atmosphere above thunderstorms (*11*). The production of upward-going, relativistic electrons, necessary for TGFs, is not necessary for sprites, a few of which have been observed in high-altitude electric fields of the opposite polarity (*12*); other sorts of breakdown such as streamer formation (*13*) may be at work in sprites. There is no direct evidence linking TGFs to any of the family of TLEs. In 1996, Inan *et al*. (*14*) reported a burst of radio noise ("sferic"), typical of lightning, at Palmer Station, Antarctica, from the direction of CGRO's position during one of the BATSE TGFs. This sferic showed positive cloud-to-ground polarity and a slow tail, features typical of sprite-producing lightning. Recently, sferics were seen with five out of six additional BATSE TGFs for which data were available at Palmer (*15*).

The high-energy electron beams that cause TGFs may also produce some secondary phenomena if they escape the atmosphere and travel along field lines in the magnetosphere: They may interact in the magnetically conjugate point of Earth's atmosphere (*16*), may populate the inner radiation belt (*17*), and may be directly detectable from satellites.

BATSE recorded somewhat less than one TGF per month, when a trigger criterion was met on board (*1*) that initiated data collection at high time resolution in four energy channels, the highest of which collected all pulses above 300 keV. The spectra were consistent with power laws having photon indices between −0.6 and −1.5 (*18*). Interpreted as bremsstrahlung, this result suggested electron energies of ~1 MeV or higher, but could not distinguish between that and much higher energies; only by observing the cutoff of the bremsstrahlung at high energies can the maximum electron energy be determined.

The Reuven Ramaty High Energy Solar Spectroscopic Imager (RHESSI) (*19*) is a NASA Small Explorer spacecraft designed to study x-rays and gamma rays from solar flares. It was launched on 5 February 2002, into an orbit of inclination 38° and of altitude 600 km, which covers most of Earth's thunderstorm zones and reaches geomagnetic latitudes up to ~50°. RHESSI's germanium detectors (*20*) detect photons from any direction in the sky and record each photon individually, so that no on-board trigger is necessary.

We present 86 TGFs from 6 months of RHESSI data, two near the beginning of the mission (April and May 2002) and four recent (July to October 2004). Data are available from the entire mission, and the analysis is ongoing. The RHESSI TGFs range from 0.2 to 3.5 ms in duration and contain from 17 to 101 detected photons. Sometimes two RHESSI flashes are detected from a single geographic region, either during one satellite pass (in one case 15 s apart) or separated by a full spacecraft orbit (about 96 min). These clusters suggest activity from a single storm.

Figure 1 shows the position of RHESSI during each of the TGFs. The color scale in the top plot is the product of the time spent above each position and the sensitivity to TGFs at those times, giving the number of TGFs expected at each position if they were uniformly distributed on the globe. When the spacecraft passes through Earth's inner radiation belt at the South Atlantic Anomaly, no data are taken. RHESSI's TGFs, like BATSE's, congregate where lightning (bottom plot) is common; note the region of central Africa that has the highest rate of lightning and the tightest cluster of RHESSI TGFs. There is a notable lack of TGFs in the southern United States, where RHESSI's magnetic latitude is highest and there is a lot of lightning, despite theoretical expectations that it should be easier to accelerate electrons upwards at high altitudes when Earth's magnetic field is further from horizontal (*21*, *22*). With only 6 months of data, however, it is premature to declare that TGFs do not occur in this region.

With its high energy resolution and broad energy range, RHESSI is able to study the spectra of TGFs in detail. Figure 2, left panel,

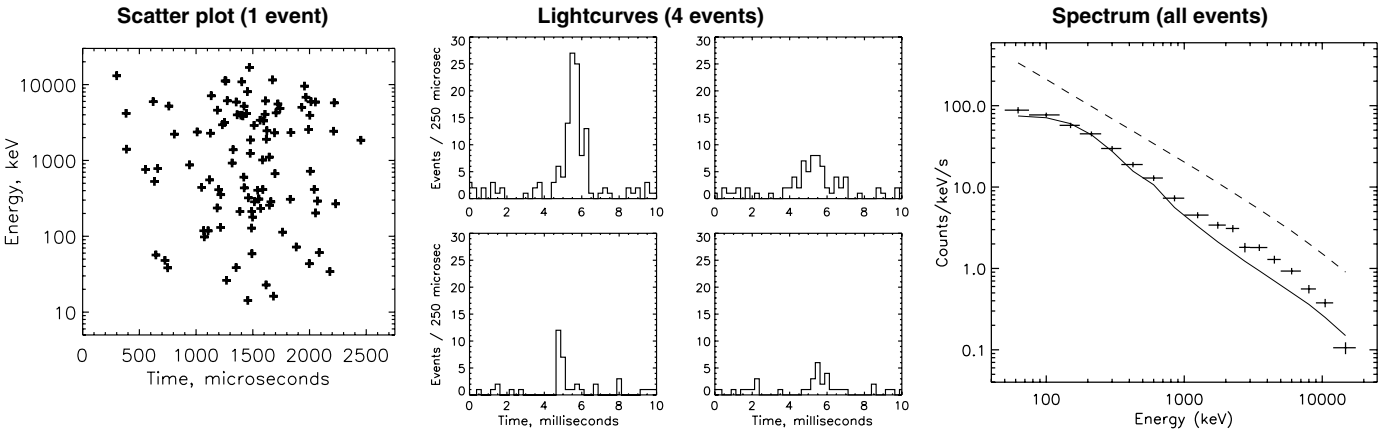

Fig. 2. (**Left**) Scatter plot of energy versus time for the brightest RHESSI TGF. (**Center**) Histograms of count rate versus time for the brightest, longest, faintest, and shortest (clockwise from upper left). RHESSI TGF detected so far. (**Right**) Summed energy spectrum of all the RHESSI TGFs, shown with the expected instrumental response (solid curve) to isotropic thin-target bremsstrahlung from 35 MeV electrons (dashed line).

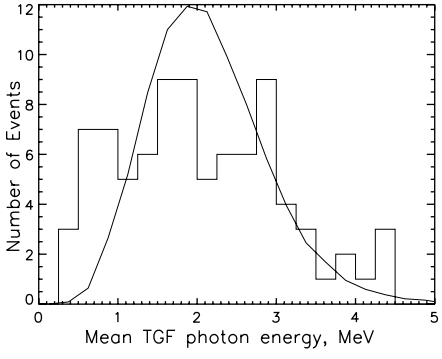

Fig. 3. Distribution of average energy for the RHESSI TGFs (histogram) along with a simulation assuming that each TGF has exactly the spectrum shown in Fig. 2.

shows count energies versus arrival time for the largest TGF. The center panels show four representative lightcurves, and the right panel shows the summed energy spectrum of the whole population. The background gamma-ray spectrum has been subtracted.

The position of the high-energy cutoff suggests that the energy of the electrons responsible for the bulk of the bremsstrahlung is on the order of 20 to 40 MeV. The spectrum is reminiscent of that seen once at ground level by Dwyer *et al.* (*5*) from triggered lightning. The right panel of Fig. 2 also shows the expected signal from isotropic, thin-target bremsstrahlung of 35-MeV monoenergetic electrons. This is not, of course, a realistic model, but it demonstrates that the correct electron spectrum will be extremely hard. The dashed curve is the model spectrum itself, and the solid curve is its convolution with the instrumental response for comparison with the data. An unmodeled excess at several MeV is apparent, which is expected for beamed TGFs viewed along the beam axis, due to the peaking of the bremsstrahlung cross section at high energies and small angles (*23*).

The flattening of the spectrum below 200 keV is consistent with absorption in materials surrounding the detectors. The BATSE data down to 25 keV were consistent with a power law when corrected for the instrumental response (*18*). These results suggest that TGFs occur relatively high in the atmosphere and are probably not from the same source that produces gamma rays seen on the ground (*4*, *5*). Assuming that the intrinsic TGF spectrum does not rise suddenly just where the atmospheric cross sections rise below 100 keV, and assuming that all the photons come from a single altitude, we can constrain that altitude to be >25 km by noting that the lowest RHESSI energy point shown (about 60 keV) does not have an extra *e*-folding of absorption compared to the points at several hundred keV. Monte Carlo simulations of electron and gamma-ray propagation in the atmosphere will produce stronger altitude constraints and address other scenarios that might fit the data, such as a hard electron spectrum below 25 km combined with a softer spectrum at higher altitudes. Future orbiting detectors sensitive to lower energies (~10 keV) would give even better constraints, due to the much higher cross sections for atmospheric absorption at lower energies.

The TGFs that make up the composite spectrum may have different spectra (*18*). Although each TGF has too few photons for a good spectral fit, the mean photon energy for each TGF can be compared (Fig. 3). The smooth curve is a larger set of artificial TGFs, each one having the mean spectrum in Fig. 2 and the same number of counts as one randomly selected real TGF. The width of this curve indicates that some, but not all, of the spectral variation we see is due to the small number of photons per TGF. Nemiroff *et al.* (*18*) and Feng *et al.* (*24*) found that BATSE TGF spectra evolved from hard to soft within each flash, and that the bursts were somewhat longer at low energies. We see both effects in the RHESSI flashes, but at a low level; more detailed analyses will be forthcoming.

Individual photons greater than 10 MeV appear in 60 of the 86 TGFs. Summing all the TGFs, we find 47 photon events that exceed one detector's threshold of ~18 MeV and 9 photon events that, because they deposited energy in more than one detector, we can be certain were above 20 MeV. The expected values of these numbers at normal background rates would be 16.5 and 2.8 photon events, respectively. The electron accelerator responsible for TGFs may thus work to higher energies than any other natural accelerator in Earth's atmosphere or magnetosphere. If the acceleration is by a DC electric field, it requires a potential drop of at least 30 MV (higher when taking frictional energy losses into account). This is comparable to predicted potentials between cloudtops and the ionosphere (*25*).

To estimate the global average rate of TGFs, we need RHESSI's footprint for TGF detection. Although RHESSI has a line of sight to the horizon at 2700 km, only an extremely bright flash at that distance would be detected above background. Assuming that TGFs are isotropic emitters and equally luminous, and considering the dynamic range of our events, we estimate an effective footprint of radius ~1000 km. Then the observed TGF rate of 86 events in 183 days corresponds to ~50 events per day summed over the latitudes RHESSI covers. Upward beaming of the photons would reduce the radius of detectability. One model predicted a ~100-km beam (*21*), in which case the true global rate could be two orders of magnitude higher. Even 5000 TGFs per day is only 0.1% of the global lightning rate, which the space-based Optical Transient Detector recently measured to be 44 ± 5 per second (*26*). We cannot rule out an even larger population of TGFs below RHESSI's detection threshold.

The average number of relativistic electrons in each flash can be estimated. Assuming monoenergetic 35-MeV electrons (Fig. 2), an average photon energy of 2.5 MeV, thick-target bremsstrahlung, isotropic emission, a distance

of 600 km to the source, total bremsstrahlung production efficiency of 13% (*27*), 30 photons detected for an average TGF, and an instrumental effective area of 250 cm^2, we require $\sim 3 \times 10^{15}$ 35-MeV electrons, for a total energy of ~20 kJ or a power of ~40 MW over 0.5 ms. Beaming would make these numbers lower, even as it made the inferred number of TGFs higher. Although thin-target bremsstrahlung gives a better fit, the electron content in the thin-target case is unconstrained and could be much higher. For upward-beamed electrons, ignoring Earth's magnetic field, the transition between thin and thick target would take place at ~30 km.

TGFs near geomagnetic latitude 45° have been considered as a source of ~1-MeV electrons in Earth's inner radiation belt by Lehtinen *et al.* (*17*). Inner-belt electrons above 10 MeV are more relevant to our results and were detected by Mariya-2 on the Mir station (*28*). The RHESSI TGFs, however, have an average geomagnetic latitude of 14°, and for these the electrons would be tied to magnetic field lines that skim the atmosphere and could not become trapped. As we analyze the whole RHESSI data set—almost 3 years and counting—we will either measure or place limits on high-latitude TGFs that may contribute to the inner-belt electrons above 10 MeV.

We are searching with a number of groups for coincidences between RHESSI TGFs and different kinds of lightning and TLEs. With TGFs for the whole RHESSI mission, we will compare these populations statistically as well.

References and Notes

1. G. J. Fishman *et al.*, *Science* **264**, 1313 (1994).
2. G. K. Parks, B. H. Mauk, R. Spiger, J. Chin, *Geophys. Res. Lett.* **8**, 1176 (1981).
3. K. B. Eack, W. H. Beasley, W. D. Rust, T. C. Marshall, M. Stolzenburg, *Geophys. Res. Lett.* **23**, 2915 (1996).
4. C. B. Moore, K. B. Eack, G. D. Aulich, W. Rison, *Geophys. Res. Lett.* **28**, 2141 (2001).
5. J. R. Dwyer *et al.*, *Geophys. Res. Lett.* **31**, L05119 (2004).
6. C. T. R. Wilson, *Proc. Phys. Soc. London* **37**, 32D (1925).
7. A. V. Gurevich, G. M. Milikh, R. Roussel-Dupré, *Phys. Lett. A* **165**, 463 (1992).
8. R. Roussel-Dupré, E. Symbalisty, Y. Taranenko, V. Yukhimuk, *J. Atmos. Sol. Terr. Phys.* **60**, 917 (1998).
9. G. M. Milikh, J. A. Valdivia, *Geophys. Res. Lett.* **26**, 525 (1999).
10. A. V. Gurevich, G. M. Milikh, *Phys. Lett. A* **262**, 457 (1999).
11. For a review of TLEs, see T. Neubert, *Science* **300**, 747 (2003).
12. C. P. Barrington-Leigh, U. S. Inan, M. Stanley, S. A. Cummer, *Geophys. Res. Lett.* **26**, 3605 (1999).
13. V. P. Pasko, U. S. Inan, T. F. Bell, *Geophys. Res. Lett.* **25**, 2123 (1998).
14. U. S. Inan, S. C. Reising, G. J. Fishman, J. M. Horack, *Geophys. Res. Lett.* **23**, 1017 (1996).
15. U. S. Inan, personal communication.
16. N. G. Lehtinen, U. S. Inan, T. F. Bell, *J. Geophys. Res.* **106**, 28841 (2001).
17. N. G. Lehtinen, U. S. Inan, T. F. Bell, *Geophys. Res. Lett.* **27**, 1095 (2000).
18. R. Nemiroff, J. T. Bonnell, J. P. Norris, *J. Geophys. Res.* **102**, 9659 (1997).
19. R. P. Lin *et al.*, *Solar Phys.* **210**, 1 (2002).
20. Materials and methods are available as supporting material on *Science* Online.
21. N. G. Lehtinen, T. F. Bell, U. S. Inan, *J. Geophys. Res.* **104**, 24699 (1999).
22. L. P. Babich, R. I. Il'kayev, A. Yu. Kudryavtsev, I. M. Kutsyk, R. A. Roussel-Dupré, *Dokl. Earth Sci.* **381**, 994 (2001).
23. R. Roussel-Dupré, personal communication.
24. H. Feng, T. P. Li, M. Wu, M. Zha, Q. Q. Zhu, *Geophys. Res. Lett.* **29**, 1036 (2002).
25. P. T. Tonev, P. I. Y. Velinov, *Adv. Space Res.* **31**, 1443 (2003).
26. H. J. Christian *et al.*, *J. Geophys. Res.* **108**, 4005 (2003).
27. H. W. Koch, J. W. Motz, *Rev. Mod. Phys.* **31**, 920 (1959).
28. A. M. Galper *et al.*, *J. Geophys. Res.* **104**, 28685 (1999).
29. The v1.0 gridded satellite lightning data were produced by the NASA Lightning Imaging Sensor/Optical Transient Detector Science Team (Principal Investigator, H. J. Christian, NASA/Marshall Space Flight Center) and are available from the Global Hydrology Resource Center (http://ghrc.msfc.nasa.gov).

30. We thank R. Roussel-Dupré, S. Mende, S. Frey, U. Inan, S. A. Cummer, Y. Zhai, C. J. Rodger, Y. Yair, Y. Takahashi, and D. Fargion for helpful discussions and NASA for supporting this work under contract NAS5-98033.

Supporting Online Material

www.sciencemag.org/cgi/content/full/307/5712/1085/DC1
Materials and Methods
References and Notes

12 November 2004; accepted 31 December 2004
10.1126/science.1107466

Iron Isotope Constraints on the Archean and Paleoproterozoic Ocean Redox State

Olivier J. Rouxel,[1]* Andrey Bekker,[2] Katrina J. Edwards[1]

The response of the ocean redox state to the rise of atmospheric oxygen about 2.3 billion years ago (Ga) is a matter of controversy. Here we provide iron isotope evidence that the change in the ocean iron cycle occurred at the same time as the change in the atmospheric redox state. Variable and negative iron isotope values in pyrites older than about 2.3 Ga suggest that an iron-rich global ocean was strongly affected by the deposition of iron oxides. Between 2.3 and 1.8 Ga, positive iron isotope values of pyrite likely reflect an increase in the precipitation of iron sulfides relative to iron oxides in a redox stratified ocean.

The rise of atmospheric oxygen, which began by about 2.3 Ga (*1*–*3*), was one of the most important changes in Earth's history. Because Fe, along with C and S, are linked to and maintain the redox state of the surface environment, the concentration and isotopic composition of Fe in seawater were likely affected by the change in the redox state of the atmosphere. The rise of atmospheric oxygen should have also led to dramatic changes in the ocean Fe cycle because of the high reactivity of Fe with oxygen. However, deposition of banded iron formations (BIFs) during the Paleoproterozoic era suggests that the deep ocean remained anoxic, at least episodically, until about 1.8 Ga, which allowed high concentrations of Fe(II) to accumulate in the deep waters (*4*).

Here we use Fe isotope systematics (*5*) to provide constraints on the redox state of the Archean and Paleoproterozoic oceans and to identify direct links between the oxidation of the atmosphere and the Fe ocean cycle. Laboratory and field studies suggest that Fe isotope variations are associated mainly with redox changes (*6*, *7*). Lithogenic sources of Fe on the modern oxygenated Earth, such as weathering products, continental sediments, river loads, and marine sediments, have isotopic compositions similar to those of igneous rocks (*8*, *9*). In contrast, seafloor hydrothermal sulfides and secondary Fe-bearing minerals from the altered oceanic crust span nearly the entire measured range of δ^{56}Fe values (*5*) on Earth, from –2.1 to 1.3 per mil (‰) (*10*, *11*). Large variations of δ^{56}Fe (from –2.5 to 1.0‰) in Late Archean to Early Paleoproterozoic BIFs have been also reported (*12*), which highlight the roles of ferrous Fe oxidation, fluid-mineral isotope fractionation, and potentially microbial processes in the fractionation of Fe isotopes.

Study of S isotope composition of sedimentary pyrite over geological time has placed important constraints on the S cycle and the evolution of ocean chemistry (*13*). Here we apply a similar time-record approach in order to explore potential changes in Fe isotope compositions. Pyrite formation in modern organic-rich marine sediments is mediated by sulfate-reducing bacteria and proceeds essentially through the dissolution and reduction of lithogenic Fe oxides and Fe silicates to Fe(II), either below the sediment-water interface or in stratified euxinic bottom waters (*14*–*16*). During reduction of Fe oxides, diagenetic fluids with isotopically light Fe(II) may be produced (*17*, *18*). However, the Fe

[1]Marine Chemistry and Geochemistry Department, Geomicrobiology Group, Woods Hole Oceanographic Institution, Mail Stop 8, Woods Hole, MA 02543, USA. [2]Geophysical Laboratory, Carnegie Institution of Washington, 5251 Broad Branch Road NW, Washington, DC 20015, USA.

*To whom correspondence should be addressed. E-mail: orouxel@whoi.edu

isotope composition of sedimentary pyrite from Phanerozoic organic-rich sediments studied so far (Fig. 1 and table S2) (*19*) suggests that such processes are unlikely to produce sedimentary pyrite with $\delta^{56}Fe < -0.5‰$. It is presumed that most of reactive Fe is scavenged to form pyrite, minimizing Fe isotope fractionation regardless of the isotope effect during Fe reduction (*17*) and precipitation (*20*). In contrast, when high concentrations of Fe(II) accumulate under anoxic conditions and low sulfide concentrations, large $\delta^{56}Fe$ variations (*10*–*12*) may occur because of partial Fe(II) oxidation, Fe(III) reduction, and distillation processes during mineral precipitation. We thus hypothesize that Fe isotope variations in sedimentary pyrite are particularly sensitive to the concentration of dissolved Fe(II) and can be used to place important constraints on the sources and sinks of the Fe(II) reservoir.

We analyzed Fe isotope composition of sulfides in black shales ranging in age from Precambrian to Late Cretaceous, specifically focusing on Late Archean to early Paleoproterozoic time (Fig. 1) (*21*). The emerged general pattern of Fe isotope variations suggests that Earth's history may be divided into three stages, which are strikingly similar to the stages defined by multiple sulfur isotope and carbon isotope records, as well as other indicators of the redox state of the atmosphere and ocean (*2*, *3*, *13*, *22*).

Stage I extends from before 2.8 Ga to about 2.3 Ga and is characterized by highly variable and negative $\delta^{56}Fe$ values. The range of $\delta^{56}Fe$ values between 0.5 and –3.5‰ is often observed within a single section of black shales, but individual pyrite nodules from the same stratigraphic level have similar $\delta^{56}Fe$ values (Fig. 2). Because dissimilatory Fe(III) reduction has been suggested to be important on early Earth (*23*) and is known to produce large Fe isotope fractionations (*6*, *24*), it can be hypothesized that these extreme Fe isotope fractionations were produced by this metabolic activity. However, three independent observations argue against this hypothesis. First, Fe isotope fractionation during single-step bacterial reduction of Fe oxides (with an initial $\delta^{56}Fe$ value of 0‰) is unlikely to produce Fe(II) with $\delta^{56}Fe$ less than –1.3‰ (*17*). Second, if a $\delta^{56}Fe$ value as low as –3.5‰ can be generated through multiple steps of Fe oxidation and reduction, then the evidence for these processes should be evident in younger sediments, but they are not documented (Fig. 1). In addition, bacterial Fe(III) reduction is expected to produce pyrite with locally highly variable negative $\delta^{56}Fe$ values, depending on the extent of Fe(III) reduction and Fe(II) reoxidation. Our samples (Fig. 2 and table S2) do not show great variability between individual sulfide nodules and suggest a common source of Fe(II). Third, the amount of biogenically produced Fe(II) would need to be unrealistically high during the Archean to swamp the global influence of hydrothermally derived Fe(II) with $\delta^{56}Fe$ values between 0 and –0.5‰ (*8*) delivered to the deep ocean.

Values of $\delta^{56}Fe$ as low as –2.3‰ have been observed in Fe-rich groundwater springs that precipitate isotopically heavy ferrihydrite along a fluid-flow path (*25*) and yield low $\delta^{56}Fe$ values in a residual Fe(II) pool. Adsorption of Fe(II) onto Fe oxide particles may also provide an additional means to produce an isotopically negative Fe(II) pool through the preferential sorption of ^{56}Fe onto Fe oxide surfaces (*24*). In a similar manner, low $\delta^{56}Fe$ values for Archean oceans may reflect preferential sequestration of ^{56}Fe on Fe oxides (*26*, *27*). Indeed, magnetite and hematite in BIFs are often characterized by positive $\delta^{56}Fe$ values (*12*), for example, $\delta^{56}Fe$ values up to 1.6‰ in iron formations of the ~2.7 Ga

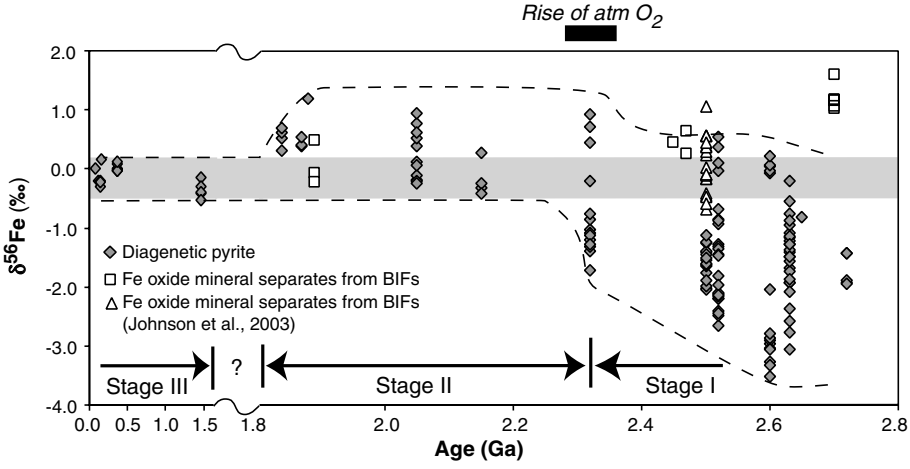

Fig. 1. Plot of $\delta^{56}Fe$ values versus sample age for Fe sulfides from black shales and Fe oxides from BIFs. On the basis of the $\delta^{56}Fe$ values, the Fe ocean cycle can be roughly divided into three stages: (i) stage I is from >2.8 to 2.3 Ga, (ii) stage II is from 2.3 to 1.8 Ga, and (iii) stage III is less than 1.7 Ga. Note the scale change between 1.5 to 1.8 Ga. The gray diamonds correspond to Fe isotope composition of pyrite from black shales (table S2), and open squares and triangles correspond to Fe isotope composition of magnetite- and hematite-rich samples from BIFs [table S3 and (*12*), respectively]. The gray area corresponds to $\delta^{56}Fe$ values of Fe derived from igneous rocks (at 0.1‰) and hydrothermal sources (about –0.5‰) (*8*). Dashed lines represent the contour lines of maximum and minimum Fe isotope compositions of sedimentary sulfides used to define Stages I to III. The rise of atmospheric oxygen (atm O_2) is defined by multiple sulfur isotope analyses of pyrite in the same samples as analyzed for Fe isotopes (*3*).

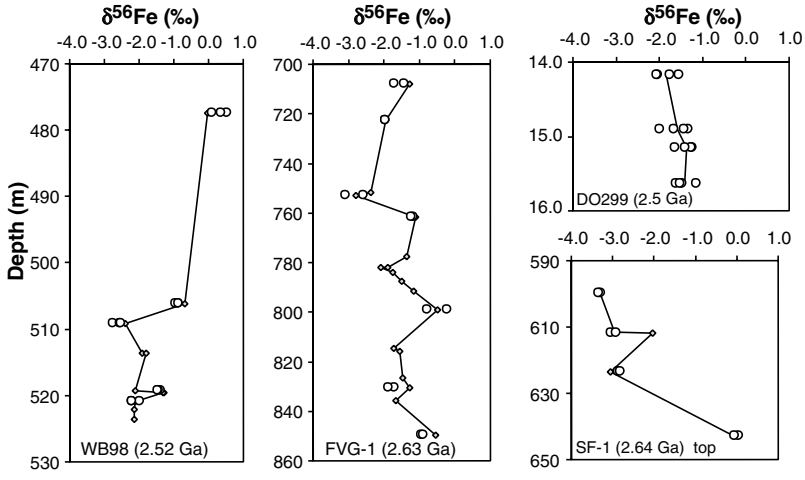

Fig. 2. Fe isotope composition of pyrite plotted along stratigraphic sections of black shales. $\delta^{56}Fe$ values of individual diagenetic pyrite nodules and pyrite grains (open circles) are plotted together with bulk pyrite values (gray diamonds) to illustrate possible Fe isotope heterogeneity within samples. Samples were selected from drill cores WB98 (Gamohaan Formation, Campbellrand Subgroup, Griqualand West Basin, South Africa, about 2.52 Ga); FVG-1 (Roy Hill Member of the Jeerinah Formation, upper part of the Fortescue Group, Hamersley Basin, Western Australia, about 2.63 Ga); DO299 (Mount McRae Shale, Mount Whaleback Mine, Newman, Hamersley Basin, Western Australia, about 2.5 Ga); and SF-1 (Lokammona Formation, Schmidtsdrift Group, Griqualand West Basin, South Africa, about 2.64 Ga).

Belingwe Belt, Zimbabwe (Fig. 1). Large stratigraphic variations in δ^{56}Fe of sedimentary pyrites in ~2.7- to ~2.5-Ga black shales, up to 3‰ over tens to hundreds meters of section (Fig. 2), suggest changes in Fe isotope composition of seawater over short periods of time on the order of a few million years. This implies a nonsteady state of the Archean Fe cycle with variable Fe concentrations caused by the competitive effect of Fe oxide precipitation and Fe supply from hydrothermal sources. These rapid changes of Fe concentrations are consistent with the idea that Fe oxide deposition in BIFs resulted from the episodic upwelling of Fe-rich deep waters accompanied by partial biological and/or abiological oxidation (*26*) in shallow waters (*28*). Alternatively, Fe oxide deposition within marine sediments on continental shelves or in the deep ocean may have also provided an important sink for Fe between periods of large BIF deposition.

We used a simple Rayleigh distillation model to explore the influence of Fe oxide deposition on the Fe isotope composition of seawater (*29*). Fe is delivered to the ocean from rivers and from seafloor hydrothermal systems with δ^{56}Fe values ranging from 0.0 to –0.5‰ (*8*). Fe is then removed by precipitation of Fe oxides. δ^{56}Fe values as low as –3.5‰ are only reached when more than 90% of the Fe from the initial Fe pool is precipitated as Fe oxides. δ^{56}Fe values of –1.5 to –2.0‰, which are more typical of Late Archean sulfides, correspond to about 50% of the Fe precipitated as oxides. This value is similar to the estimates of Fe sink in BIFs based on P adsorption (*30*).

Stage II, which covers the time interval from about 2.3 to about 1.7 Ga, is characterized by the disappearance of negative δ^{56}Fe values and the emergence of positive δ^{56}Fe values up to 1.2‰. Major perturbations in biogeochemical and climatic record occurred during the beginning of stage II. These include the following: (i) negative and positive carbon isotope excursions in carbonates sandwiched between glacial diamictites, (ii) Earth's earliest global glaciations, and (iii) oxidation of Earth's atmosphere as suggested by increasing seawater sulfate content inferred from the δ^{34}S record and appearance of sulfate evaporites; disappearance of nonmass-dependent S isotope fractionation; appearance of red beds, oxidized paleosols, hematitic oölites, and pisolites; Mn oxide deposits; and Ce anomalies in chemical sedimentary deposits (*3*, *13*, *22*, *31*). The appearance of positive δ^{56}Fe values, which persisted until about 1.7 Ga, together with the disappearance of strongly negative δ^{56}Fe values, occurred during the period when the most sensitive indicators for the rise of atmospheric oxygen first appeared. All these observations suggest that the oxidation of the surface environment in the early Paleoproterozoic was relatively rapid and that it directly affected the Fe isotope composition of the ocean.

How the change in the Fe isotope record about 2.3 Ga corresponds with change of the oceanic Fe cycle and the redox state of the ocean is not straightforward. Large BIF deposits are almost entirely lacking between 2.3 and 2.1 Ga (*32*), which is consistent with the lack of negative δ^{56}Fe values during this period. However, BIF deposition returned at about 2.1 Ga, and major BIFs were deposited in North America and Australia (*32*). If δ^{56}Fe values of pyrites in black shales that were deposited between 2.1 and 1.8 Ga are representative of the whole ocean, then BIF deposition mechanisms were different from those prevailing during the Archean. We infer that late Paleoproterozoic BIFs were deposited in an oxygenated layer of the ocean, and complete precipitation of Fe from Fe-rich plumes upwelling from the deep ocean did not affect the Fe isotope composition of the deep ocean. Despite the limited number of analyses, the narrow range of δ^{56}Fe values of hematite and magnetite from the 1.88-Ga Biwabik and Tyler formations compared with Archean BIFs (Fig. 1 and table S3) is consistent with this assumption.

An important consequence of the rise of atmospheric oxygen levels was the initiation of oxidative weathering and an increase in sulfate delivery to seawater (*13*). Consequently, the formation of Fe sulfides in the water column of pericratonic basins may have became the dominant part of the global ocean Fe cycle and may have prevented deposition of large BIFs, except during periods of intense submarine volcanic activity followed by high hydrothermal input of Fe. The effect of the increased role of sulfide production on the Fe isotope record is presently uncertain because reliable estimates of equilibrium Fe isotope fractionation during pyrite formation are lacking (*20*). One plausible hypothesis is that the positive δ^{56}Fe values in 2.3 to 1.8 Ga sedimentary sulfides might be related to sulfide precipitation from an Fe-rich pool with δ^{56}Fe composition around 0‰ and a pyrite-Fe(II) fractionation factor of up to 1‰ as suggested in previous studies (*10*, *33*). This hypothesis indicates that sulfide produced by sulfate-reducing bacteria during this period has been completely titrated by dissolved Fe species in the Fe-rich and sulfide-poor ocean.

The disappearance of major BIFs after about 1.8 Ga is thought to indicate that the deep ocean became either progressively oxic or euxinic (*4*). Because the solubility of Fe sulfides and Fe oxides was low, most of the hydrothermally derived Fe(II) was likely rapidly precipitated in the deep ocean, allowing few possibilities to produce Fe isotope fractionation. The lack of substantial δ^{56}Fe value variations in sulfides from black shales younger than 1.5 Ga is thus consistent with the general picture that the whole ocean was Fe-poor after about 1.6 Ga. But the lack of variation does not place constraints on the oxic versus sulfidic nature of the deep ocean. More data that cover the Phanerozoic, Mesoproterozoic, and Neoproterozoic time intervals are required to understand fully the change in the ocean Fe cycle at about 1.8 Ga.

Our Fe isotope record provides new insights into the Archean and Paleoproterozoic ocean chemistry and redox state. Fe isotopes suggest that the Archean oceans were globally Fe rich and that their Fe isotope composition and Fe content were variable in response to the episodic establishment of an Fe-rich pool supplied by hydrothermal activity and the deposition of Fe oxides, either in BIFs or dispersed throughout sediments on continental shelves and in the deep sea. After the rise of atmospheric oxygen by about 2.3 Ga, the Paleoproterozoic ocean became stratified and characterized by an increase of sulfide precipitation relative to Fe oxide precipitation. During this period, BIFs were likely deposited by upwelling of Fe(II)-rich plumes and rapid oxidation in the oxygenated layer of the ocean. Conducting Fe isotope analyses of sedimentary sulfides in conjunction with S isotope analyses should enable a more refined understanding of the origin of the positive Fe isotope excursion and the biogeochemical cycles of Fe and S during the Paleoproterozoic era.

References and Notes

1. H. D. Holland, *The Chemical Evolution of the Atmosphere and Oceans* (Princeton Univ. Press, Princeton, NJ, 1984).
2. J. Farquhar, H. Bao, M. Thiemens, *Science* **289**, 756 (2000).
3. A. Bekker *et al.*, *Nature* **427**, 117 (2004).
4. The disappearance of BIFs after about 1.8 Ga had been initially thought to indicate the transition to the oxygenated ocean (*1*), but a growing body of evidence suggests that sulfide, rather than oxygen, could have been responsible for removing Fe from deep ocean waters (*13, 34–36*).
5. Data are reported using the delta notation relative to the Institute for Reference Materials and Measurements (IRMM)–14 Fe isotope reference standard defined as $\delta^{56}Fe = 1000 \times [(^{56}Fe/^{54}Fe)_{sample}/(^{56}Fe/^{54}Fe)_{IRMM\text{-}14} - 1]$. External precision of δ^{56}Fe values are estimated at 0.10‰ (2σ level). Analytical procedures, sample descriptions, and Fe isotope composition of various georeference materials, black shales, and BIF are available as supporting materials on *Science* Online.
6. C. M. Johnson, B. L. Beard, E. E. Roden, D. K. Newman, K. H. Nealson, *Rev. Mineral. Geochem.* **55**, 359 (2004).
7. B. L. Beard, C. M. Johnson, *Rev. Mineral. Geochem.* **55**, 319 (2004).
8. B. L. Beard, C. M. Johnson, K. L. VonDamm, R. L. Poulson, *Geology* **31**, 629 (2003).
9. The range of Fe isotope composition of hydrogenic ferromanganese deposits in modern oceanic basins is large [between –0.8 and –0.1‰ (*37*)], but it is unclear whether the variability is caused by changes of Fe isotope composition in the water column or by secondary effects.
10. O. Rouxel, Y. Fouquet, J. N. Ludden, *Geochim. Cosmochim. Acta* **68**, 2295 (2004).
11. O. Rouxel, N. Dobbek, J. Ludden, Y. Fouquet, *Chem. Geol.* **202**, 155 (2003).
12. C. M. Johnson, B. L. Beard, N. J. Beukes, C. Klein, J. M. O'Leary, *Contrib. Mineral. Petrol.* **144**, 523 (2003).
13. D. E. Canfield, *Science* **396**, 450 (1998).
14. D. E. Canfield, *Geochim. Cosmochim. Acta* **53**, 619 (1989).
15. J. W. M. Wijsman, J. J. Middelburg, P. M. J. Herman, M. E. Bottcher, C. H. R. Heip, *Mar. Chem.* **74**, 261 (2001).
16. T. F. Anderson, R. Raiswell, *Am. J. Sci.* **304**, 203 (2004).
17. Experimental studies suggest that Fe isotope fractionations during bacterial reduction of Fe oxides is

dependent on reduction rates (*6*). At high reduction rates, rapid formation and sorption of Fe(II) to ferric oxide substrate produced fractionations as large as –2.3‰, but this value corresponds to an extreme case and fractionation of –1.3‰ between biogenic Fe(II) and ferric oxide is more representative (*6*).
18. S. Severmann, J. McManus, C. M. Johnson, B. L. Beard, *Eos* **84**, *Ocean Sci. Meet. Suppl.*, abstract OS31L-09 (2003).
19. A. Matthews *et al.*, *Geochim. Cosmochim. Acta* **68**, 3107 (2004).
20. Theoretical calculations predict that pyrite (FeS_2) is an isotopically heavy phase relative to Fe(II) with a fractionation factor similar to magnetite (*33*). However, experimental precipitation of mackinawite (Fe_9S_8) produces a kinetic isotope fractionation of 0.3‰ (*38*), suggesting that the fractionation of pyrite is poorly constrained from –0.3 to 1.0‰ relative to dissolved Fe(II).
21. Samples from different black shale units of similar ages were selected to distinguish between local and global effects on Fe isotope composition of seawater. We extracted between 10 and 20 sulfide grains to obtain a best estimate for the average δ^{56}Fe value for each sample. For comparison and to evaluate heterogeneity, we also analyzed several individual sulfide nodules from the same samples (table S2).
22. J. A. Karhu, H. D. Holland, *Geology* **24**, 867 (1996).
23. M. Vargas, K. Kashefi, E. L. Blunt-Harris, D. R. Lovley, *Nature* **395**, 65 (1998).
24. G. A. Icopini, A. D. Anbar, S. S. Ruebush, M. Tien, S. L. Brantley, *Geology* **32**, 205 (2004).
25. T. D. Bullen, A. F. White, C. W. Childs, D. V. Vivit, M. S. Schulz, *Geology* **29**, 699 (2001).
26. Because the atmosphere was still reducing during this period, the mechanisms by which oxidation of ferrous Fe sources occurred are extensively debated. Biogeochemical evidence for oxygenic photosynthesis exists in sediments as old as 2.7 Ga (*39*) and may have contributed to ferrous iron oxidation with O_2. Alternatively, a direct mechanism for Fe oxidation by anoxygenic phototrophic bacteria has been suggested (*40*), and abiotic photochemical oxidation may have also contributed to Fe oxidation in the Archean (*41*).
27. A magnetite-Fe(II) fractionation factor of about 2.4‰ has been inferred from BIFs data (*12*), which is slightly less than the equilibrium Fe(III)-Fe(II) fractionation factor of 2.9‰ at 22°C (*42*). The fractionation between ferrihydrite and Fe(II) of 1.5‰ measured during anaerobic photosynthetic Fe(II) oxidation by bacteria (*43*) is slightly larger than the 0.9‰ fractionation measured during abiotic oxidation of Fe(II) to ferrihydrite (*25*).
28. N. J. Beukes, C. Klein, A. J. Kaufman, J. M. Hayes, *Precambrian Res.* **85**, 663 (1990).
29. In our model, we assumed that an initial pool of Fe(II) supplied by hydrothermal activity was depleted through Fe oxidation and precipitation of Fe oxides. The isotope composition of residual Fe(II) is linked to *F*, the ratio of remaining to initial Fe(II), following the distillation equation

$$\delta^{56}\mathrm{Fe} = (1000 + d^{56}\mathrm{Fe}_i) \times F^{(\alpha_{BIF} - 1)} - 1000$$

where $\delta^{56}Fe_i$ is the initial value of hydrothermally derived Fe(II) at –0.5‰ (*8*) and α_{BIF} is the fractionation factor during Fe oxidation and Fe oxide precipitation, ranging between 1.0015 and 1.0023 (*6*).
30. C. J. Bjerrum, D. E. Canfield, *Nature* **417**, 159 (2002).
31. A. Bekker, A. J. Kaufman, J. A. Karhu, K. A. Eriksson, *Precambrian Res.*, in press.
32. A. E. Isley, D. H. Abbott, *J. Geophys. Res.* **104**, 15461 (1999).
33. V. B. Polyakov, S. D. Mineev, *Geochim. Cosmochim. Acta* **64**, 849 (2000).
34. Y. Shen, A. H. Knoll, M. R. Walter, *Nature* **423**, 632 (2003).
35. G. L. Arnold, A. D. Anbar, J. Barling, T. W. Lyons, *Science* **304**, 87 (2004).
36. A. D. Anbar, A. H. Knoll, *Science* **297**, 1137 (2002).
37. S. Levasseur, M. Frank, J. R. Hein, A. N. Halliday, *Earth Planet. Sci. Lett.* **224**, 91 (2004).
38. I. B. Butler, C. Archer, D. Rickard, D. Vance, A. Oldroyd, *Geochim. Cosmochim. Acta* **67**, A51 (2003).
39. R. E. Summons, L. L. Jahnke, J. M. Hope, G. A. Logan, *Nature* **400**, 554 (1999).
40. F. Widdel *et al.*, *Nature* **362**, 834 (1993).
41. P. S. Braterman, A. G. Cairns-Smith, R. W. Sloper, *Nature* **303**, 163 (1983).
42. S. A. Welch, B. L. Beard, C. M. Johnson, P. S. Braterman, *Geochim. Cosmochim. Acta* **67**, 4231 (2003).
43. L. R. Croal, C. M. Johnson, B. L. Beard, D. K. Newman, *Geochim. Cosmochim. Acta* **68**, 1227 (2004).
44. We gratefully acknowledge B. Krapež, M. Barley, D. Winston, B. Rasmussen, F. Gauthier-Lafaye, P. Medvedev, N. Beukes, L.-L. Coetzee, E. N. Berdusco, R. Ruhanen, M. Köhler, M. Jirsa, M. J. Severson, J. Brouwer, R. Shapiro, G. L. LaBerge, B. Peucker-Ehrenbrink, S. Petsch, and H. Baioumy for advice and access to sample collections and L. Ball and J. Blusztajn for technical assistance. O.J.R. is grateful to M. Bickle and A. Galy from the University of Cambridge for the access to Belingwe Iron Formation samples and analytical support of the Nu Plasma. A.B.'s fieldwork in South Africa and Western Australia was supported by NASA and Petroleum Research Fund grants to H. D. Holland and by Australian Research Council and Minerals Energy Research Institute of Western Australia grants to M. Barley and B. Krapež. We thank J. M. Hayes, H. D. Holland, and two anonymous reviewers for constructive comments. The Fe isotope work was supported by NASA Astrobiology Institute Award NNA04CC04A From Early Biospheric Metabolisms to the Evolution of Complex Systems (K.J.E.). Support for O.J.R. was provided by a postdoctoral fellowship from the Deep Ocean Exploration Institute at Woods Hole Oceonagraphic Institue (WHOI). This is WHOI contribution number 11275.

Supporting Online Material
www.sciencemag.org/cgi/content/full/307/5712/1088/DC1
Materials and Methods
Fig. S1
Tables S1 to S3
References

27 September 2004; accepted 6 January 2005
10.1126/science.1105692

Stem Lagomorpha and the Antiquity of Glires

Robert J. Asher,[1]* Jin Meng,[2] John R. Wible,[3] Malcolm C. McKenna,[2,4] Guillermo W. Rougier,[5] Demberlyn Dashzeveg,[6] Michael J. Novacek[2]

We describe several fossils referable to *Gomphos elkema* from deposits close to the Paleocene-Eocene boundary at Tsagan Khushu, Mongolia. *Gomphos* shares a suite of cranioskeletal characters with extant rabbits, hares, and pikas but retains a primitive dentition and jaw compared to its modern relatives. Phylogenetic analysis supports the position of *Gomphos* as a stem lagomorph and excludes Cretaceous taxa from the crown radiation of placental mammals. Our results support the hypothesis that rodents and lagomorphs radiated during the Cenozoic and diverged from other placental mammals close to the Cretaceous-Tertiary boundary.

Rodents and lagomorphs, collectively known as Glires, represent much of the modern diversity of mammals and have played an important role in understanding the timing of placental mammal diversification. On paleontological grounds, the origin of Glires is hypothesized to have taken place close to the Cretaceous-Tertiary boundary (*1*–*3*), a result compatible with some recent estimates from molecular studies (*4*,*5*). In contrast, other molecular estimates of Glires divergence have suggested a much older date, extending to 80 (*6*) or even more than 110 (*7*) million years ago (Ma). Paleontological support for an older date for Glires divergence has been proposed by studies supporting a close relationship between fossil zalambdalestids and Glires (*8*–*10*). Zalambdalestids are an extinct central Asian group of eutherian mammals (*11*, *12*); their first appearance 85 to 90 Ma (*10*), coupled with a sister-taxon relationship with lagomorphs and/or rodents, would imply the presence of a Glires stem lineage more than 20 million years before the first appearance of any undisputed placental mammal. Until recently, stem lagomorphs (*13*, *14*) were known from fragmentary craniodental remains (*15*), with few specimens associated with postcrania (*16*). Here we describe fossils of *Gomphos elkema*, including a specimen with an articulated skull and skeleton (Fig. 1), from the Nemegt Basin, Mongolia, and re-evaluate the origin of Glires.

G. elkema was first described as a paramyid-like rodent on the basis of lower-cheek teeth from deposits overlying Paleocene rocks at Gashato, Mongolia (*17*–*19*). The specimens discussed here are older and were recovered from a number of localities near Tsagan Khushu, Mongolia (*19*, *20*), from the base of the Bumban Member of the Naran Bulak Formation, dating to the Paleocene-Eocene boundary (*21*). *Gomphos* has enlarged, gliriform

[1]Museum für Naturkunde, Humboldt Universität, Invalidenstraße 43, 10115 Berlin, Germany. [2]Division of Paleontology, American Museum of Natural History, New York, NY 10024, USA. [3]Section of Mammals, Carnegie Museum of Natural History, 5800 Baum Boulevard, Pittsburgh, PA 15206, USA. [4]Department of Geology and Geophysics, University of Wyoming, Laramie, WY 82071, USA. [5]Department of Anatomical Sciences and Neurobiology, School of Medicine, University of Louisville, Louisville, KY 40292, USA. [6]Mongolian Academy of Sciences, Geological Center, Ulan Bator, Mongolia.

*To whom correspondence should be addressed. E-mail: robert.asher@museum.hu-berlin.de

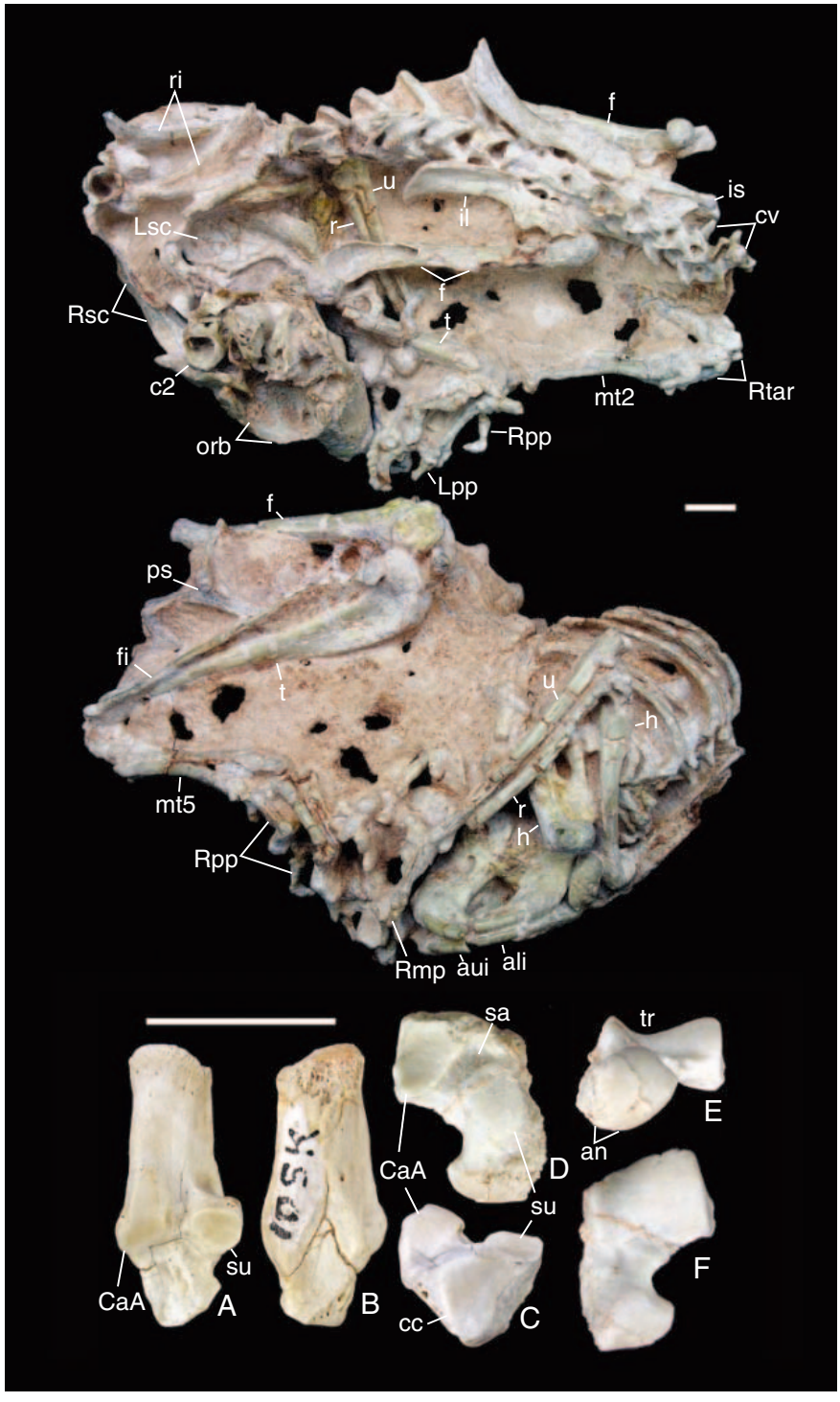

Fig. 1. (**Top**) Dorsal and (**middle**) ventral views of specimen MAE-BU 14422, an articulated skeleton of *G. elkema* from the basal Bumban Member, Tsagan Khushu, Mongolia. The inset at bottom shows a right calcaneus (MAE-BU 14423) in (**A**) dorsal, (**B**) ventral, and (**C**) anterior views and a left astragalus (MAE-BU 14424) in (**D**) ventral, (**E**) anterior, and (**F**) dorsal views. The skull is incomplete dorsally and posteriorly; breakage to the calcaneus is restricted to its proximal (posterior) surface; and the astragalus shows abrasion along the medial surface of its neck. Scale bars, 10 mm. ali, anterior lower incisor; an, astragalo-navicular facet; aui, anterior upper incisor; c2, second cervical vertebra; CaA, calcaneo-astragalar facet; cc, calcaneo-cuboid facet; cv, caudal vertebrae; f, femur; fi, fibula; h, humerus; il, ilium; is, ischium; Lpp, left pedal phalanges; Lsc, left scapula; mt2, second metatarsal; mt5, fifth metatarsal; orb, orbit; ps, pubic symphysis; r, radius; ri, ribs; Rmp, right manual phalanges; Rpp, right pedal phalanges; Rsc, right scapula; Rtar, proximal right tarsus; sa, sulcus astragali; su, sustentacular facet; t, tibia; tr, astragalar trochlea; u, ulna.

incisors in the upper and lower jaws (Figs. 1 and 2), with the lower incisor extending posteriorly within the jaw to the last molar. It differs from extant rodents and lagomorphs in having two pairs of mandibular incisors but is similar to extant lagomorphs in having two pairs of upper incisors, a narrow anterior process of the frontal bone inserting between the premaxilla and maxilla, and an auditory bulla completely ossified by the ectotympanic. It is similar to extant leporids in having a posteriorly broad, V-shaped suture between the nasal and frontal bone (Fig. 2). *Gomphos* differs from extant lagomorphs in having low-crowned, unilaterally hypsodont cheek teeth with a distinctive mesoconid on the lowers. The lower jaw has a broad, posteroventrally directed angular process and a prominent coronoid process extending superiorly above the mandibular condyle (Fig. 2). As in modern leporids, the hindlimb and foot of *Gomphos* are elongate relative to its forelimb (Fig. 1). It has an elongate ventral process of the navicular, a relatively narrow calcaneus, separate sustentacular and navicular facets on the astragalus (Fig. 1), and a posterolaterally extensive articular surface of the femoral head. Unlike those of modern lagomorphs, the proximal caudal vertebrae are robust; the fibula is unfused with the tibia; the tibial malleolus is prominent; the navicular facet on the astragalar head is wider transversely than dorsoventrally; and the calcaneus is not perforated with a canal (Fig. 1).

In order to place *Gomphos* in a phylogenetic context, we expanded on the morphological character matrix of Meng *et al*. (*1*). Specifically, we added 3 fossils and 15 living taxa to their sample of 36 fossils and 14 living taxa, for a total of 68 terminals. We also added to and modified their anatomical data set, using a total of 228 characters in our matrix (*22*). For living taxa, we also sampled five genetic markers (*4*, *23*, *24*): mitochondrial cytochrome b (cytB), nuclear α-2B adrenergic receptor (A2AB), interphotoreceptor retinoid binding protein (IRBP), von Willebrand factor (vWF), and growth hormone receptor (GHR). We combined the morphological and sequence data in a single matrix, leaving sequence data entries missing for fossil taxa, and performed phylogenetic analyses using NONA (*25*) with the WinClada (*26*) interface and PAUP (*27*, *28*).

The most parsimonious trees (MPTs) we recovered from the combined data set (Fig. 3) show *Gomphos* on the stem leading toward Lagomorpha and zalambdalestids outside the crown radiation of Placentalia. This signal was stable despite changes in character ordering (fig. S1), assumptions regarding anterior incisor homology (fig. S2), exclusion of characters (fig. S3) and taxa (fig. S4) with less than 75% representation in our anatomical data set, and treatment of third positions in our DNA data set (fig. S5). In addition, analysis of the

morphological data set constrained to agree with a recent molecular topology of Glires (*4*) also supported *Gomphos* on the stem to Lagomorpha, as well as Cretaceous eutherians outside of Placentalia (fig. S6).

Branch and bootstrap support values are not easily comparable across different phylogenetic studies (*29*, *30*); hence, we rely on them as indicators of relative support within our data set. The node subtending *Gomphos* within Duplicidentata (Fig. 3, node A) (*13*) is among the best supported in this analysis. The node defining crown Placentalia plus *Leptictis* (Fig. 3, node B) to the exclusion of zalambdalestids and other Cretaceous taxa is slightly weaker, but it is still comparable to or stronger than nodes defining leporids, ochotonids, a *Plesiadapis*-primate clade, and the stem clade encompassing rodents (Simplicidentata). Placing zalambdalestids as the sister taxon to Glires requires an additional 27 steps in the equally weighted NONA analysis; a zalambdalestid-duplicidentate clade requires 54 additional steps. As measured by Wilcoxon rank sum tests (Table 1), both alternatives can be rejected with a high level of significance.

In contrast, certain alternatives regarding the stems of Lagomorpha and Placentalia could not be rejected. The morphological data set analyzed alone reconstructs eurymylids (*1*) as stem relatives of Rodentia (fig. S7). The addition of sequences to our anatomical data set greatly influences the optimization of anatomical characters, which in turn influences the placement of fossil groups and changes the position of eurymylids, placing them instead on the stem leading to Lagomorpha (Fig. 3). However, this arrangement is only slightly more parsimonious than a eurymylid-simplicidentate clade (Table 1). Indeed, when anatomical characters with less than 75% representation in our matrix are excluded, the combined analysis places eurymylids on the stem leading to Rodentia (fig. S4). Similarly, placing *Palaeolagus* within crown Lagomorpha as sister taxon to leporids requires just two additional steps in the combined analysis. On the basis of the test provided in Table 1, these alternatives cannot be as decisively rejected as, for example, a zalambdalestid-Glires clade.

Numerous dental, cranial, and postcranial characters define Placentalia, Glires, and Duplicidentata (Fig. 3 and fig. S10). Dental characters comprise most of the changes at the base of Glires, reflecting both the highly derived nature of the rodent-lagomorph anterior dentition and to a lesser extent the proportion of dental characters in our matrix (39% dental, 35% cranial, 24% postcranial, and 2% soft tissue). Changes in dental characters also predominate in the node leading to *Palaeolagus* and crown lagomorphs (Fig. 3). Otherwise, the stems leading to both Placentalia and Lagomorpha show more cranial and postcranial than dental changes. For example, the branch on our consensus tree (Fig. 3 and fig. S10) separating Cretaceous eutherians from *Leptictis* plus Placentalia shows unambiguous dental changes for just 1 out of 18 characters. Similarly, the branch within Duplicidentata defining *Gomphos* on the stem to Lagomorpha shows two dental changes out of 15. The proportion of dental changes on these nodes remains low when ambiguous optimizations (favoring either reversals or parallelisms) are considered and when characters are optimized on each of the fully dichotomous MPTs. This result emphasizes the importance of character sampling, including the skull and postcranium as well as the dentition, in inferring phylogeny on the stems leading to both Lagomorpha and Placentalia.

Our results placing early Paleocene *Heomys* and *Mimotona* within Glires (Fig. 3, node C) and excluding Cretaceous taxa from crown Placentalia (Fig. 3, node B) reinforce the interpretation that rodents and lagomorphs diverged from other placental mammal groups within a few million years of the Cretaceous-Tertiary boundary. Although molecular estimates of Glires divergence published in recent years have varied considerably (*5*–*7*), we regard the paleontological estimate of this event to be relatively stable, supporting a date near the close of the Cretaceous.

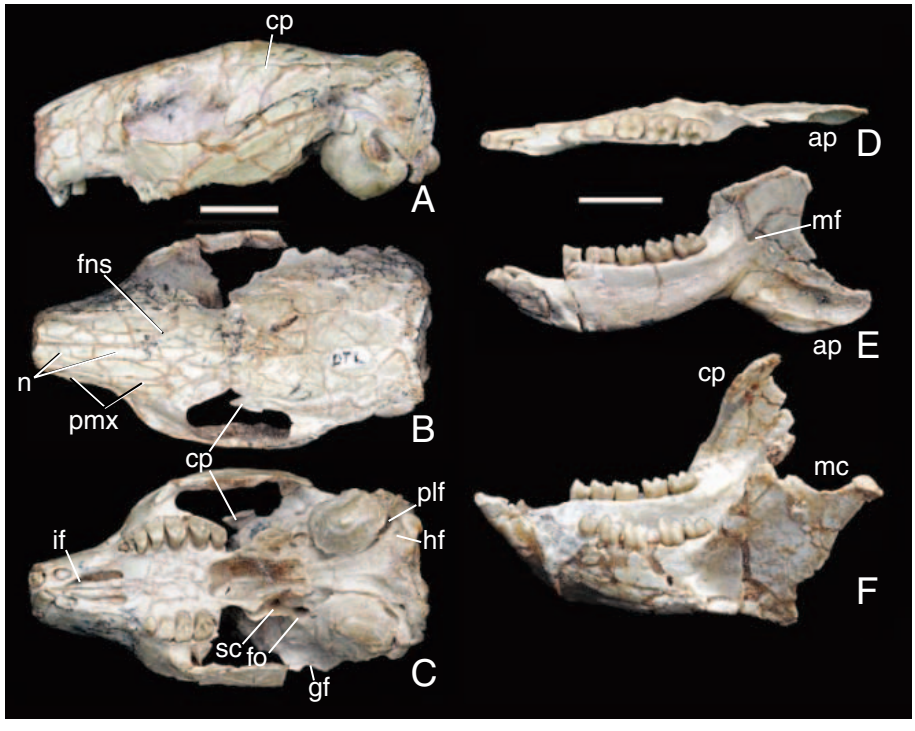

Fig. 2. (**A**) Lateral, (**B**) dorsal, and (**C**) ventral views of a *G. elkema* skull (MAE-BU 14425) and (**D**) occlusal and (**E**) internal views of the associated right mandible (MAE-BU 14425). (**F**) A lateral view of an additional *G. elkema* pair of jaws (MAE-BU 14426), preserving the coronoid process and mandibular condyle. Scale bars, 10 mm. ap, angular process; cp, coronoid process [a disarticulated fragment in temporal fossa in (A) to (C)]; fns, frontonasal suture; fo, foramen ovale; gf, glenoid fossa; hf, hypoglossal foramen; if, incisive foramen; mc, mandibular condyle; mf, mandibular foramen; n, nasal; plf, posterior lacerate foramen; pmx, premaxilla; sc, sphenopterygoid canal.

Table 1. Results of Wilcoxon rank sum tests comparing topologies, carried out with PAUP (*27*) on the combined data set with all character changes weighted equally and indels treated as missing data. As depicted in fig. S11, CP indicates monophyly of crown placentals to the exclusion of Cretaceous eutherians; ES indicates a eurymylid-simplicidentate clade; LE indicates a *Leptictis*-elephant shrew clade; PL indicates a *Palaeolagus*-leporid clade; ZD indicates a zalambdalestid-duplicidentate clade; and ZG indicates a zalambdalestid-glires clade.

Topology	Tree length	Number of character differences (*N*)	Rank sums*	*P* (one-tailed)
CP	13,732 (best)	–	–	–
ES	13,733	13	49/–42	>0.05
LE	13,739	25	208/–117	>0.05
PL	13,734	10	33/–22	>0.05
ZD	13,786	70	2201/–284	<0.005
ZG	13,759	43	770/–176	<0.005

*The significance level for the smaller of the two rank sums, in absolute value, is available from table V of (*31*).

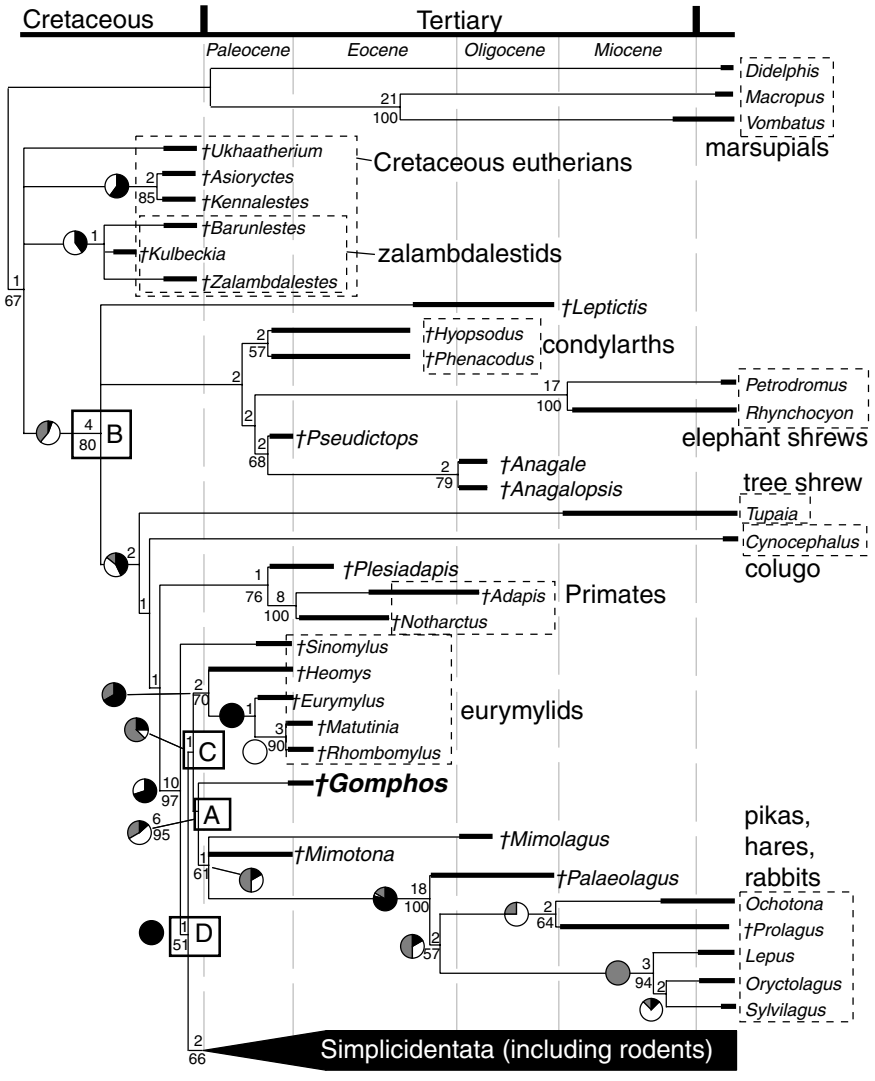

Fig. 3. Strict consensus of 30 MPTs recovered by NONA (*25*), 13,732 steps in length and resulting from combined-data analysis (all changes equal, unordered morphology plus cytB, A2AB, IRBP, vWF, and GHR), mapped on a time scale representing the Late Cretaceous to the present. Thick horizontal bars represent approximate fossil history (*32*). Estimated divergence times of marsupials (*33*), crown lagomorphs (*5*), and leporids (*34*) are also represented. Dotted vertical lines represent epoch boundaries from the Cretaceous-Tertiary through the Oligocene-Miocene. Node A represents duplicidentates excluding eurymylids; node B represents Placentalia, within which *Leptictis* was variably resolved across the 30 MPTs; node C represents duplicidentates including eurymylids; and node D represents Glires (*13*). Numbers above nodes indicate branch support, and those below nodes indicate bootstrap support indices ≥50. Pie graphs adjacent to nodes represent the proportion of unambiguous dental (black), cranial (white), and postcranial (gray) character changes, mapped onto nonterminal branches leading to Cretaceous eutherians, crown placentals, and crown lagomorphs. Full character optimizations (including reference to specific characters) and taxon samples (including Simplicidentata) are shown in fig. S10 (*22*). Daggers represent extinct taxa.

References and Notes

1. J. Meng, Y. Hu, C. K. Li, *Bull. Am. Mus. Nat. Hist.* **275**, 1 (2003).
2. W. P. Luckett, J. L. Hartenberger, Eds., *Evolutionary Relationships Among Rodents: A Multidisciplinary Analysis* (Plenum, New York, 1985).
3. J.-L. Hartenberger, *C. R. Acad. Sci. Paris, Sci., Ter., Plan.* **326**, 439 (1998).
4. D. Huchon *et al.*, *Mol. Biol. Evol.* **19**, 1053 (2002).
5. E. J. P. Douzery, F. Delsuc, M. J. Stanhope, D. Huchon, *J. Mol. Evol.* **57**, S201 (2003).
6. M. S. Springer, W. J. Murphy, E. Eizirik, S. J. O'Brien, *Proc. Natl. Acad. Sci. U.S.A.* **100**, 1056 (2003).
7. S. Kumar, S. B. Hedges, *Nature* **392**, 917 (1998).
8. L. Van Valen, *Evolution* **18**, 484 (1964).
9. M. C. McKenna, *Nat. Hist.* **103**, 56 (1994).
10. J. D. Archibald, A. O. Averianov, E. G. Ekdale, *Nature* **414**, 62 (2001).
11. J. R. Wible, M. J. Novacek, G. W. Rougier, *Bull. Am. Mus. Nat. Hist.* **281**, 1 (2004).
12. Z. Kielan-Jaworowska, *Palaeontol. Pol.* **37**, 32 (1978).
13. A. R. Wyss, J. Meng, *Syst. Biol.* **45**, 559 (1996).
14. Following Wyss and Meng (*13*), we define crown Lagomorpha as all descendants of the common ancestor of *Ochotona* and *Lepus*, the stem clade Duplicidentata as all mammals more closely related to *Lepus* than *Mus*, the stem clade Simplicidentata as all mammals more closely related to *Mus* than *Lepus*, and Glires as all descendants of the common ancestor of *Lepus* and *Mus*. Similarly, Placentalia encompasses all descendants of the common ancestor of *Loxodonta*, *Tamandua*, *Erinaceus*, and *Mus*. "Stem lagomorph" is an informal term meaning duplicidentates outside of crown Lagomorpha.
15. C. K. Li, S. Y. Ting, in (*2*), pp. 35–58.
16. J. Meng *et al.*, *Am. Mus. Novit.* **3425**, 1 (2004).
17. N. S. Shevyreva, V. M. Chkhikvadze, V. I. Zhegallo, *Bull. GA Acad. Sci.* **77**, 225 (1975).
18. V. I. Zhegallo, N. S. Shevyreva, *Jt. Sov.-Mong. Paleontol. Exp. Trans.* **3**, 269 (1976).
19. D. Dashzeveg, D. E. Russell, L. J. Flynn, *Proc. K. Ned. Akad. Wet. Ser. B* **90**, 133 (1987).
20. M. C. McKenna, J. Meng, *J. Vertebr. Paleontol.* **21**, 565 (2001).
21. G. J. Bowen *et al.*, *Science* **295**, 2062 (2002).
22. Materials and methods are available as supporting material on *Science* Online.
23. R. M. Adkins, A. H. Walton, R. M. Honeycutt, *Mol. Phylogenet. Evol.* **26**, 409 (2003).
24. C. Montgelard, S. Bentz, S. Tirard, O. Verneau, F. M. Catzeflis, *Mol. Phylogenet. Evol.* **22**, 222 (2002).
25. P. Goloboff, NONA, vers. 1.9, available at www.cladistics.org.
26. K. C. Nixon, WinClada (Beta), ver. 0.9.9, available at www.cladistics.org.
27. D. L. Swofford, *Phylogenetic Analysis Using Parsimony (*and Other Methods)*, ver. 4.0b10 (Sinauer, Sunderland, MA, 2002).
28. Our 68 terminals were sampled at the level of the genus with three exceptions: Sequence data were combined for *Monodelphis-Didelphis* and for *Elephantulus-Petrodromus*, and postcranial data from *Ctenodactylus* were combined with craniodental data from *Massoutiera* (table S1). For A2AB, IRBP, and vWF, we used the same alignment as Huchon *et al.* (*4*); alignments of cytB and GHR preserved reading frames and required few indels (*22*). We undertook analyses with NONA (*25*) using the commands hold 9999, hold/20, mult*500, and max*; polymorphisms were treated as missing data. Branch support values were calculated in NONA by searching for successively greater sets of suboptimal trees (bs; sub 2, 4, 8, 10; hold 5000, 15000, 25000, 32000), searching with mult*15 max*. Bootstraps were calculated in WinClada-NONA with 100 replicates, three searches holding one tree per replicate, and TBR branch swapping without max*. Indels were treated as missing data. We also compared results of our simultaneous analyses with a morphological analysis constrained using PAUP (*27*) to fit a molecular topology for living Glires (*4*). We used a heuristic search with 50 random addition replicates, treated polymorphisms as missing data, and ran the resulting set of trees for a further round of TBR branch swapping.
29. D. M. Hillis, J. J. Bull, *Syst. Biol.* **42**, 182 (1993).
30. M. S. Y. Lee, *Syst. Biol.* **49**, 829 (2000).
31. F. J. Rohlf, R. R. Sokal, *Statistical Tables* (Freeman, New York, 1995).
32. M. C. McKenna, S. K. Bell, *Classification of Mammals Above the Species Level* (Columbia Univ. Press, New York, 1997).
33. M. Nilsson, A. Gullberg, A. E. Spotorno, U. Arnason, A. Janke, *J. Mol. Evol.* **57**, S3 (2003).
34. C. Matthee, B. Jansen van Vuuren, D. Bell, T. J. Robinson, *Syst. Biol.* **53**, 433 (2004).

35. We thank G. Cui, L. Meeker, C. Tarka, R. Edwards, and E. Peterson for help with photography and specimen preparation; E. Douzery for alignments of A2AB, IRBP, and vWF; and J.-L. Hartenberger, K. Rose, J. Wahlert, and two anonymous reviewers for discussion and critiques of the manuscript. Supported by NSF grant nos. EAR-0120727 (J.M.), DEB-0129127 (J.R.W), DEB-0129061 (G.W.R), and DEB-0129031 (M.J.N.); by the Berlin Museum für Naturkunde; and by the American Museum of Natural History.

Supporting Online Material

www.sciencemag.org/cgi/content/full/307/5712/1091/DC1
Materials and Methods
SOM Text
Figs. S1 to S11
Table S1
References and Notes
Data Nexus Files

22 November 2004; accepted 14 January 2005
10.1126/science.1107808

Golgin Tethers Define Subpopulations of COPI Vesicles

Jörg Malsam,*† Ayano Satoh,* Laurence Pelletier,† Graham Warren‡

Coiled-coil proteins of the golgin family have been implicated in intra-Golgi transport through tethering coat protein complex I (COPI) vesicles. The p115-golgin tether is the best studied, and here we characterize the golgin-84–CASP tether. The vesicles bound by this tether were strikingly different from those bound by the p115-golgin tether in that they lacked members of the p24 family of putative cargo receptors and contained enzymes instead of anterograde cargo. Microinjected golgin-84 or CASP also inhibited Golgi-enzyme transport to the endoplasmic reticulum, further implicating this tether in retrograde transport. These and other golgins may modulate the flow patterns within the Golgi stack.

The flow pattern of materials within the Golgi stack is governed by COPI vesicles. In one view, anterograde vesicles deliver newly synthesized protein and lipid cargo to successive cisternae, where they can undergo posttranslational modifications. Retrograde vesicles would then salvage components of the fusion machinery as well as those Golgi enzymes that have strayed beyond the cisterna(e) in which they function. In another view, the protein and lipid cargo do not move forward in vesicles; rather, the retrograde COPI vesicles carry Golgi enzymes and fusion machinery back to the preceding cisterna, which matures into the next one (*1*). A recent modification to this view suggests that tubular continuities mediate the retrograde transport of Golgi enzymes, leaving COPI vesicles to carry the fusion machinery (*2*). These views are not mutually exclusive, but they do require considerable coordination of the COPI vesicle flow pattern (*3*). The key question, then, is the mechanism that underlies the targeting of COPI vesicles to particular cisterna(e).

Targeting is a multilayered process, involving tethers and SNAREs (soluble *N*-ethylmaleimide–sensitive factor attachment protein receptors) (*4*). Tethers include multiprotein complexes and coiled-coil proteins of the golgin family, the latter regulated by small guanosine triphosphatases (GTPases) of the Rab and Arl families (*5–7*). The p115-golgin tether uses giantin, GM130, and Rab1 to tether COPI vesicles to the cis-Golgi network (CGN), preparing p115 for its role in SNARE pairing that leads to vesicle fusion (*7–10*).

Department of Cell Biology, Ludwig Institute for Cancer Research, Yale University School of Medicine, 333 Cedar Street, New Haven, CT 06520–8002, USA.

*These authors contributed equally to this work.
†Present address: Max Planck Institute for Molecular Cell Biology and Genetics, Pfotenhauerstraße 108, 01307 Dresden, Germany.
‡To whom correspondence should be addressed. E-mail: graham.warren@yale.edu

Golgin-84 and CASP are recently characterized golgins that interact with each other (*11–14*). Immunoprecipitation of golgin-84 brought down CASP (20 ± 3%, $n = 4$) from detergent extracts of Golgi membranes, and immunoprecipitation of CASP brought down golgin-84 (12 ± 2%, $n = 4$). Neither antibody brought down components of the p115-golgin tether (Fig. 1A) (*12*).

The topology of the golgin-84–CASP tether was investigated with a cell-free budding assay and density-gradient centrifugation to isolate highly purified COPI vesicles (*15*). These peaked at ~40% (w/v) sucrose (Fig. 1B), and electron microscopy (EM) revealed a homogeneous population of coated vesicles, ~75 nm in diameter (Fig. 1C). Golgin-84, but not CASP, cofractionated with the COPI-coated vesicles (Fig. 1B), and immunolabeling localized golgin-84 to some of them (Fig. 1D).

Samples from the budding assay were also processed for immunolabeling, and golgin-84 was found on 77 ± 15% of those buds that labeled for β′-COP (Fig. 1E). The opposite result was obtained for CASP, which was found on only 7 ± 3% of those buds that labeled for β′-COP, most being present on cisternal membranes (Fig. 1F). Thus, the tether is asymmetric, with CASP in Golgi membranes and golgin-84 on the vesicles.

This asymmetry was confirmed by using soluble, recombinant CASP to coat glass slides that were incubated with partially purified COPI vesicles and then processed for EM

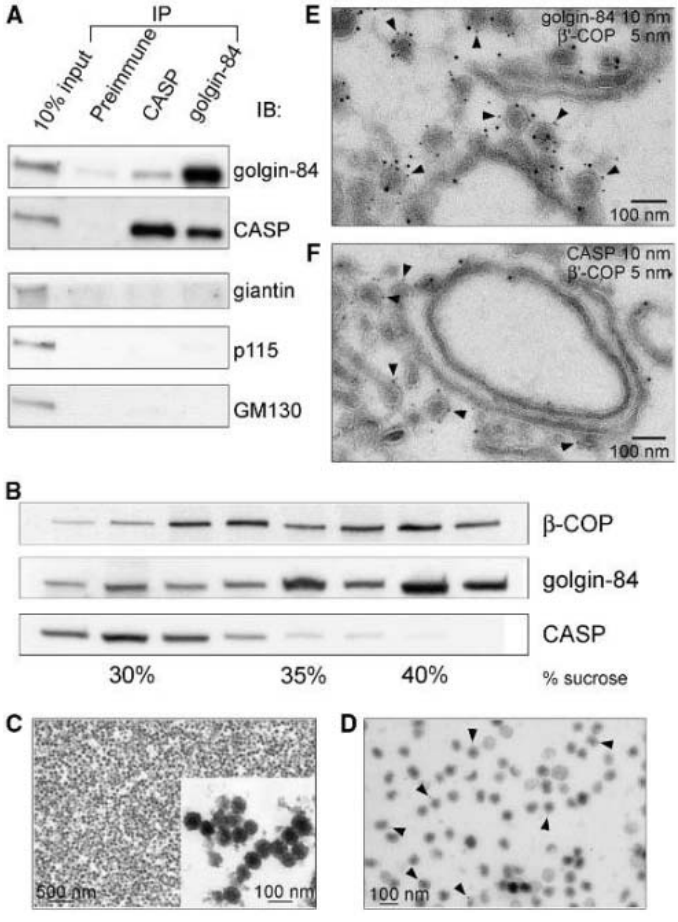

Fig. 1. The golgin-84–CASP tether. (**A**) Triton extracts of Golgi membranes (10% input at left) were immunoprecipitated (IP) with the indicated antibodies or preimmune serum, and bound proteins were analyzed by SDS–polyacrylamide gel electrophoresis, followed by immunoblotting (IB) for the indicated proteins. (**B**) Salt-washed Golgi membranes were incubated with purified coatomer, ARF1, and guanosine triphosphate (GTP) for 10 min at 37°C, followed by salt treatment to release the COPI vesicles and centrifugation to remove large membrane fragments. The remaining membranes were centrifuged to equilibrium, and fractions were analyzed for the indicated proteins. (**C** and **D**) The gradient-purified vesicles (40% sucrose) were processed for (C) negative staining, (inset) conventional EM, or (D) pre-embedding labeling by using antibodies to golgin-84 and 5 nm protein A-gold (arrowheads). (**E** and **F**) Incubation as in (B), but stopped after 3 min to enrich for COPI-coated buds. Cryosections were double-labeled for β′-COP (5 nm gold) and either (E) golgin-84 or (F) CASP (both 10 nm gold).

(Fig. 2A). Uncoating was necessary for binding (fig. S1), and although these uncoated vesicles, ~60 nm in diameter, were only a small fraction of the starting material (arrows in Fig. 2F), they alone were selectively bound (Fig. 2A). Binding was not observed to slides coated with bovine serum albumin (BSA)/soybean trypsin inhibitor (STI) (Fig. 2B) or to those coated with another coiled-coil protein, the endosomal antigen EEA1 (Fig. 2C) (*16*). Binding was also inhibited by soluble CASP (Fig. 2D) and soluble golgin-84 (Fig. 2E). Quantitation confirmed these results (Fig. 2G).

The composition of the bound vesicles was then analyzed using CASP-coated glass beads instead of slides and gradient-purified and uncoated COPI vesicles as the starting material. Bound proteins could be competed with soluble CASP, showing that they were a specific component of these vesicles. About 10% of the input golgin-84 was retrieved by the CASP beads, and this was used as the standard to compare the retrieval of other proteins (Fig. 3A).

The most notable difference between the starting and bound population of vesicles was the absence of any member of the p24 family of proteins. A representative of each of the four subfamilies was absent from the bound vesicles, a striking result because they have been implicated in the biogenesis of COPI vesicles, the cytoplasmic tails acting to bind coatomer and, thus, nucleate budding (*17*). Other proteins must clearly nucleate the budding of COPI vesicles that use the golgin-84–CASP tether; examples include the tails of Golgi enzymes (*18*). Mannosidase I and II were enriched ~5-fold and ~2-fold respectively, consistent with their movement from medial and/or trans cisternae (*7*, *19*) back to the CGN, where the p24 proteins are localized (*20*). A representative cargo protein, the polymeric immunoglobulin A receptor (pIgR), was not enriched in the CASP-binding vesicles, further supporting a role in retrograde transport (Fig. 3A).

The lowered levels of adenosine diphosphate ribosylation factor–GTPase activating protein (ARF-GAP) in the salt-washed Golgi membranes used to prepare gradient-purified COPI vesicles helped to prevent uncoating and thus increased the yield. ARF-GAP has, however, been implicated in sorting (*21*, *22*), so similar experiments were carried out with partially purified and uncoated COPI vesicles, and the compositional analysis was repeated for key proteins. CASP beads still retrieved vesicles containing Golgi enzymes but not the pIgR cargo or the p24 family member, p26 (Fig. 3B).

Another subpopulation of COPI vesicles was isolated by using the p115-golgin tether. A functional, truncated form of p115, TA (*7*), was used to coat glass beads that bound vesicles containing giantin (Fig. 3C). Binding was inhibited both by TA and by a soluble fragment of giantin but not by CASP, distinguishing this tether from that mediated by golgin-84–CASP.

The composition of the bound vesicles was then compared with the starting population and with those bound to CASP beads (Fig. 3A). In each case, the bound proteins were competed by TA and, although the efficacy was lower than when soluble CASP was used to compete binding to CASP beads,

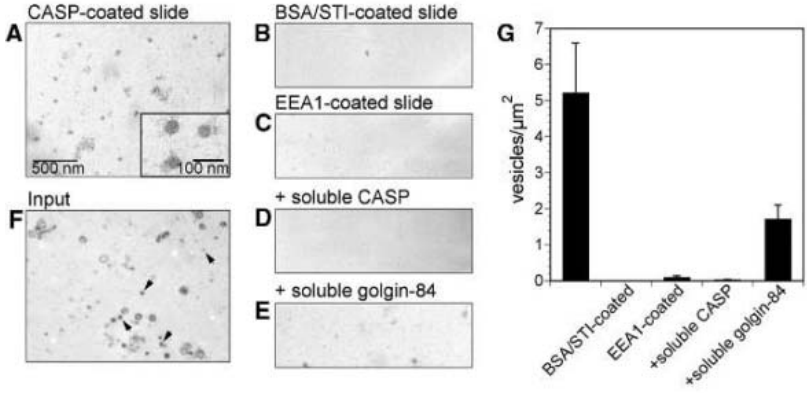

Fig. 2. Tethering of COPI vesicles to CASP-coated slides. (**A** to **E**) Golgi membranes and cytosol were used to prepare partially purified and uncoated COPI vesicles that were incubated on glass slides precoated with [(A), (D), and (E)] recombinant CASP, (B) BSA and STI, or (C) recombinant EEA1 in the absence [(A), (B), and (C)] or presence of (D) soluble CASP or (E) soluble golgin-84. Slides were then washed and processed for EM. (**F**) Input membranes. (**G**) Quantitation of the results in [(A) to (E)], presented as the mean of the number of the bound vesicles per $\mu m^2 \pm$ SD ($n = 5$).

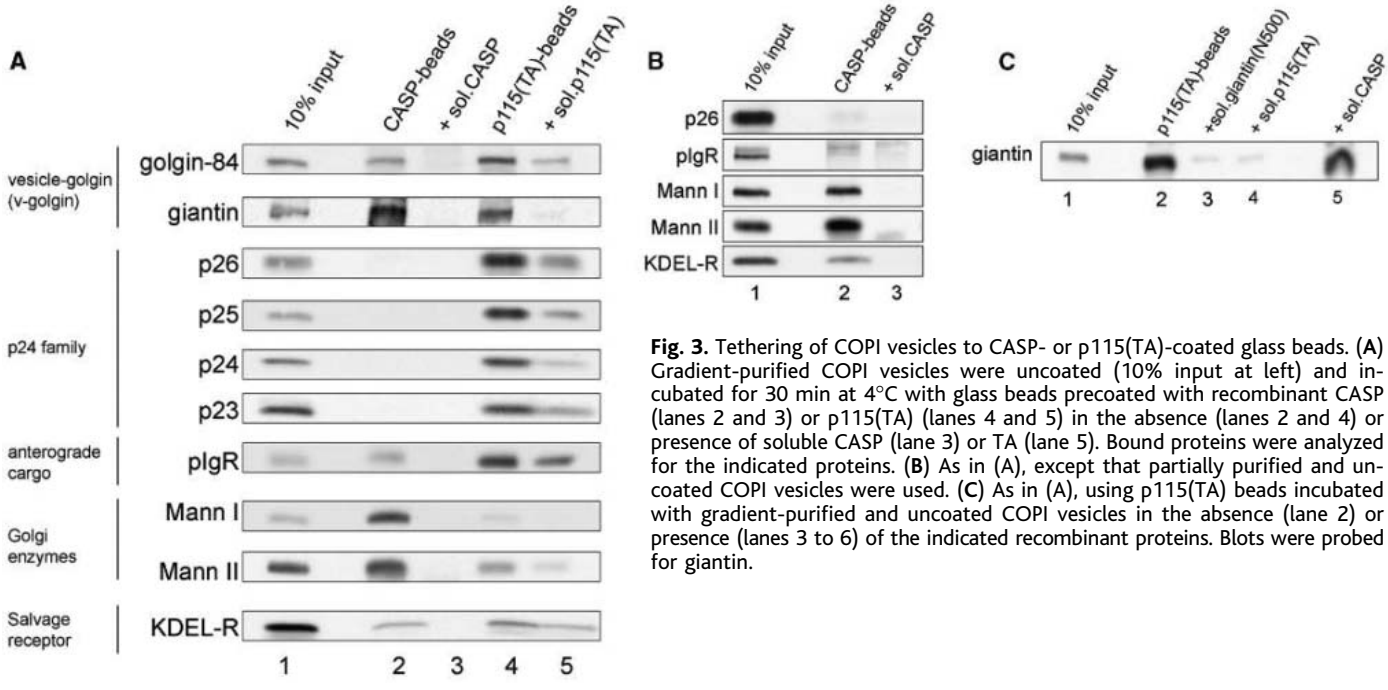

Fig. 3. Tethering of COPI vesicles to CASP- or p115(TA)-coated glass beads. (**A**) Gradient-purified COPI vesicles were uncoated (10% input at left) and incubated for 30 min at 4°C with glass beads precoated with recombinant CASP (lanes 2 and 3) or p115(TA) (lanes 4 and 5) in the absence (lanes 2 and 4) or presence of soluble CASP (lane 3) or TA (lane 5). Bound proteins were analyzed for the indicated proteins. (**B**) As in (A), except that partially purified and uncoated COPI vesicles were used. (**C**) As in (A), using p115(TA) beads incubated with gradient-purified and uncoated COPI vesicles in the absence (lane 2) or presence (lanes 3 to 6) of the indicated recombinant proteins. Blots were probed for giantin.

at worst binding was diminished by a factor of 3 and at best by at least a factor of 10. About 20% of the giantin in the input COPI vesicles was retrieved by p115(TA) beads, and this was used as the standard to compare the retrieval of other proteins.

All of the p24 family members were enriched, although to differing extents; the least was p23, and the most was p26, which was three times as high as that in the input vesicles. The cargo protein, pIgR, was also enriched by at least a factor of 3, but both Mannosidase I and II were depleted. This is consistent with the vesicles budding from the CGN, although a role in anterograde transport would have to be limited to the early part of the Golgi stack (from the CGN to cis cisternae, for example), because p115 is restricted to these membranes (*23*). COPI vesicles have been isolated by using antibodies to the tail of the p24 protein, and these are depleted for both enzymes and cargo (*22*). Thus, more than one population of p24-containing COPI vesicles likely exists, with only some carrying cargo molecules.

Each subpopulation of COPI vesicle incorporated the vesicle tether that operated in the other vesicle. The p115(TA)-binding vesicles (using giantin) contained golgin-84, and the CASP-binding vesicles (using golgin-84) contained giantin (Fig. 3A). This cannot be the consequence of cross-contamination, given the complete absence of the p24 family of proteins in the CASP-binding vesicles. A possible explanation is that both golgin-84 and giantin are membrane proteins, so if they are incorporated into vesicles that move to another part of the stack, then there must be a means of recycling them back to their original membrane. Golgin-84, for example, after fusion of the vesicles with cis membranes, would need to be recycled back to trans membranes. The obvious mechanism would be to use vesicles moving in the opposite direction and to inactivate the passenger golgin by using a reversible modification such as phosphorylation (*7*).

The cycling of Golgi enzymes through the endoplasmic reticulum (ER) (*24*, *25*) provided a means of testing the role of the golgin-84–CASP tether in retrograde transport. BSC-1 cells, stably expressing GalNAc-T2-YFP (*26*), were microinjected with Sar1^{dn} to inhibit ER export, which relocated this Golgi enzyme to the ER over a 5-hour period, the Golgi fluorescence dropping from 80% to 5% (Fig. 4B) (*25*, *27*). Neither CASP nor golgin-84 changed their locations appreciably during this time period (fig. S2). Coinjection of either soluble golgin-84 or soluble CASP substantially inhibited this retrograde movement (Fig. 4A), such that 40 to 55% of the fluorescence remained in the Golgi region (Fig. 4B). Kinetic analysis showed an increase in the halftime for relocation from ~75 min (Sar1^{dn} alone) to ~235 min (+ golgin-84 or CASP) (Fig. 4C). Coinjection of EEA1 had no effect (Fig. 4, A and B).

Agents that disrupted the p115-golgin tether had only a modest effect on the retrograde transport of GalNAc-T2-YFP. Coinjection of an N-terminal fragment of giantin or GM130 or expression of Δ63-GM130, which lacks the N-terminal domain, left 10 to 15% of fluorescence in the Golgi region, compared with 5% for Sar1^{dn} alone (Fig. 4B).

Expression of Δ63-GM130 inhibits anterograde transport of VSV-G protein by up to 60% (*28*). In contrast, microinjection of soluble golgin-84 had no significant effect on the halftime for VSV-G protein to reach the cell surface (41 min versus 38 min), and soluble CASP had only a modest effect (41 min versus 54 min) (Fig. 4D). RNA interference (RNAi) depletion of golgin-84 also has a partial effect on VSV-G protein transport (*12*).

Finally, soluble golgin-84 and CASP did not affect the retrograde movement of ERGIC53 from the CGN to the ER (fig. S3) (*29*), which suggests that the CASP-binding vesicles are moving within the Golgi, not from the Golgi to the ER. This was also supported by the relative absence of the p24 proteins and the KDEL-R in the vesicles isolated on CASP beads (Fig. 3, A and B). Earlier work did not uncover a role for COPI vesicles in the retrograde transport of Golgi enzymes to the ER (*24*), despite the presence of enzymes in isolated COPI vesicles (*9*, *22*). The present work provides a possible resolution, suggesting a two-step retrograde pathway, the first step mediated by intra-Golgi COPI transport to the CGN, the second by a COPI-independent pathway to the ER.

The ability to isolate and analyze subpopulations of COPI vesicles brings a much-needed biochemical approach to the study

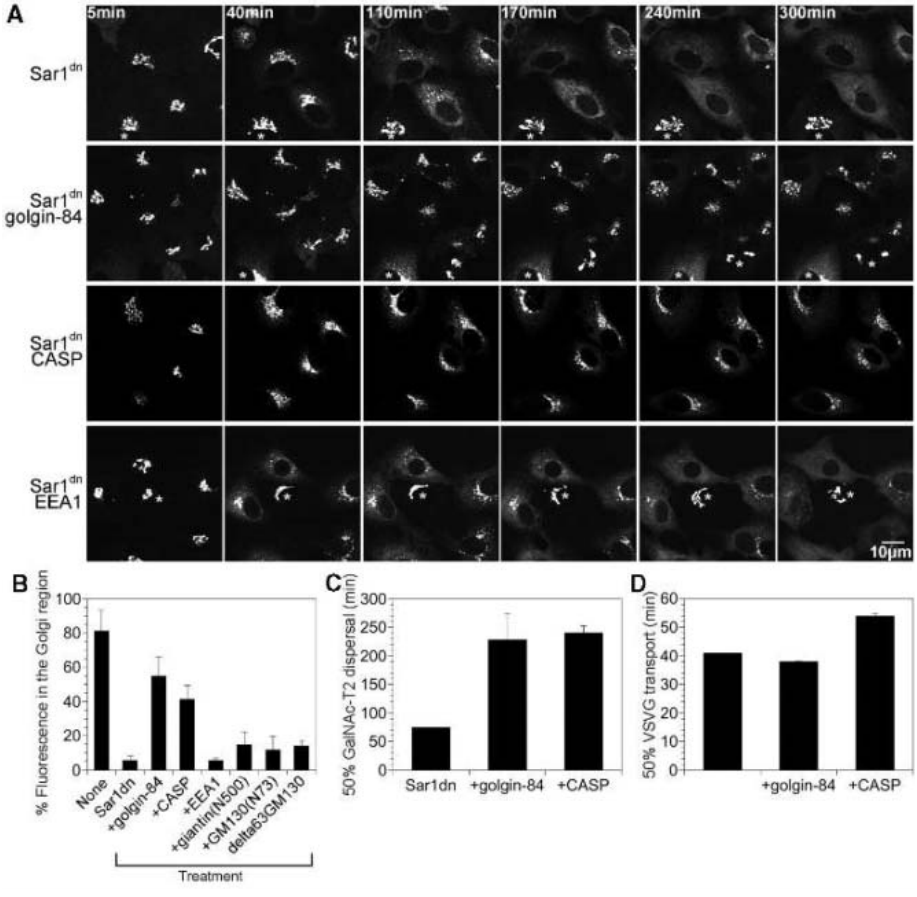

Fig. 4. Soluble golgin-84 and CASP inhibit retrograde transport of Golgi enzymes. (**A**) BSC-1 cells, stably expressing GalNAc-T2-YFP, were injected with Sar1^{dn} (top row) or coinjected with soluble golgin-84 (second row), soluble CASP (third row), or EEA-1 (bottom row). After the injection, cells were imaged at the indicated time points. Asterisks mark the uninjected cells. Bar, 10 μm. (**B**) Quantitation of results in (A), as well as additional experiments in which components of the p115-golgin tether were either coinjected with Sar1^{dn} or, in the case of Δ63GM130, expressed before injection. Results presented as the mean of fluorescence in the Golgi region ± SD (*n* ranges from 4 to 12 cells sampled). (**C**) Quantitation of the results in (A), expressed as the time taken to relocate half the GalNAc-T2 to the ER. Results presented as mean ± SD (*n* ranges from 4 to 7 cells sampled). (**D**) BSC-1 cells were microinjected with cDNA encoding tsO45 VSV-G protein and incubated at 2 hours at 40°C. Soluble golgin-84 or CASP were microinjected before shift to the permissive temperature of 32°C. The time taken for half the G protein to reach the cell surface is presented as the mean ± SD (*n* = 3 cells per condition).

of intra-Golgi transport. Other tethers should identify other subpopulations, allowing us to map the flow patterns of resident, cargo, and recycling molecules. The intersections will dictate the nature and extent of the modifications to the transiting cargo, which should help us understand the functioning of the Golgi in different cells, tissues, and organisms.

References and Notes

1. B. S. Glick, V. Malhotra, *Cell* **95**, 883 (1998).
2. A. Trucco *et al.*, *Nature Cell Biol.* **6**, 1071 (2004).
3. H. R. Pelham, J. E. Rothman, *Cell* **102**, 713 (2000).
4. S. R. Pfeffer, *Nature Cell Biol.* **1**, E17 (1999).
5. J. R. Whyte, S. Munro, *J. Cell Sci.* **115**, 2627 (2002).
6. A. K. Gillingham, S. Munro, *Biochim. Biophys. Acta* **1641**, 71 (2003).
7. J. Shorter, G. Warren, *Annu. Rev. Cell Dev. Biol.* **18**, 379 (2002).
8. B. B. Allan, B. D. Moyer, W. E. Balch, *Science* **289**, 444 (2000).
9. B. Sönnichsen *et al.*, *J. Cell Biol.* **140**, 1013 (1998).
10. M. A. Puthenveedu, A. D. Linstedt, *Proc. Natl. Acad. Sci. U.S.A.* **101**, 1253 (2004).
11. A. K. Gillingham, A. C. Pfeifer, S. Munro, *Mol. Biol. Cell* **13**, 3761 (2002).
12. A. Diao, D. Rahman, D. J. Pappin, J. Lucocq, M. Lowe, *J. Cell Biol.* **160**, 201 (2003).
13. A. Satoh, Y. Wang, J. Malsam, M. B. Beard, G. Warren, *Traffic* **4**, 153 (2003).
14. Both CASP and golgin-84 are well conserved in vertebrates, but only the former is found in yeast and only the latter in *Drosophila*. This suggests additional roles, including interactions with other golgins.
15. J. Ostermann *et al.*, *Cell* **75**, 1015 (1993).
16. F. T. Mu *et al.*, *J. Biol. Chem.* **270**, 13503 (1995).
17. W. Nickel, B. Brügger, F. T. Wieland, *J. Cell Sci.* **115**, 3235 (2002).
18. M. Dominguez *et al.*, *J. Cell Biol.* **140**, 751 (1998).
19. A. Velasco *et al.*, *J. Cell Biol.* **122**, 39 (1993).
20. M. Rojo *et al.*, *J. Cell Biol.* **139**, 1119 (1997).
21. J. Malsam, D. Gommel, F. T. Wieland, W. Nickel, *FEBS Lett.* **462**, 267 (1999).
22. J. Lanoix *et al.*, *J. Cell Biol.* **155**, 1199 (2001).
23. D. S. Nelson *et al.*, *J. Cell Biol.* **143**, 319 (1998).
24. A. Girod *et al.*, *Nature Cell Biol.* **1**, 423 (1999).
25. B. Storrie *et al.*, *J. Cell Biol.* **143**, 1505 (1998).
26. M. A. Axelsson, G. Warren, *Mol. Biol. Cell* **15**, 1843 (2004).
27. J. Seemann, E. Jokitalo, M. Pypaert, G. Warren, *Nature* **407**, 1022 (2000).
28. J. Seemann, E. J. Jokitalo, G. Warren, *Mol. Biol. Cell* **11**, 635 (2000).
29. C. Itin, R. Schindler, H. P. Hauri, *J. Cell Biol.* **131**, 57 (1995).

30. We thank all members of the Warren, Mellman, and Toomre laboratories and M. Zerial for helpful comments and discussions. This work was supported by the NIH and the Ludwig Institute for Cancer Research. A.S. is supported by the American Heart Association. Molecular interaction data have been deposited in the Biomolecular Interaction Network Database with accession codes 196357 and 196358.

Supporting Online Material

www.sciencemag.org/cgi/content/full/307/5712/1095/DC1
Materials and Methods
Figs. S1 to S3
References

30 November 2004; accepted 23 December 2004
10.1126/science.1108061

Phosphorylation and Regulation of Akt/PKB by the Rictor-mTOR Complex

Dos D. Sarbassov, David A. Guertin,* Siraj M. Ali,* David M. Sabatini†

Deregulation of Akt/protein kinase B (PKB) is implicated in the pathogenesis of cancer and diabetes. Akt/PKB activation requires the phosphorylation of Thr^{308} in the activation loop by the phosphoinositide-dependent kinase 1 (PDK1) and Ser^{473} within the carboxyl-terminal hydrophobic motif by an unknown kinase. We show that in *Drosophila* and human cells the target of rapamycin (TOR) kinase and its associated protein rictor are necessary for Ser^{473} phosphorylation and that a reduction in rictor or mammalian TOR (mTOR) expression inhibited an Akt/PKB effector. The rictor-mTOR complex directly phosphorylated Akt/PKB on Ser^{473} in vitro and facilitated Thr^{308} phosphorylation by PDK1. Rictor-mTOR may serve as a drug target in tumors that have lost the expression of PTEN, a tumor suppressor that opposes Akt/PKB activation.

The Akt/PKB kinase is a well-characterized effector of phosphoinositide 3-kinase (PI3K), and its deregulation plays important roles in the pathogenesis of human cancers. PI3K is necessary for the activation of Akt/PKB, and current models suggest that phosphatidylinositol-3,4,5-triphosphates produced upon growth factor stimulation recruit Akt/PKB to the plasma membrane by binding to its N-terminal pleckstrin homology (PH) domain. At the membrane, Akt/PKB is phosphorylated on two key residues: Thr^{308} (T308) of the activation loop by PDK1 (*1*, *2*) and Ser^{473} (S473) in the hydrophobic motif of the C-terminal tail by a kinase whose identity has been elusive. The role of S473 phosphorylation is controversial, but there is an emerging view that it precedes the phosphorylation of T308 and is important for the recognition and activation of Akt/PKB by PDK1 (*3*–*5*).

The molecular identity of the S473 kinase (S473K), at times referred to as "PDK2" or the "hydrophobic motif (HM) kinase," has been hotly debated for many years. Several candidate S473Ks have been proposed, including PDK1 (*6*), integrin-linked kinase (ILK) (*7*), Akt/PKB itself (*8*), and, most recently, DNA-PK_{cs} (*9*). Many lines of evidence argue that neither PDK1, ILK, nor Akt/PKB is the physiological S473K (*10*–*12*), and for several reasons, DNA-PK_{cs} is also unlikely to have this function. There is no *Drosophila* ortholog of DNA-PK_{cs} (*13*), and, thus, if DNA-PK_{cs} is a physiological S473K in mammals, a distinct kinase must play that role in flies even though all other core components of the pathway (e.g., PI3K, Akt/PKB, PDK1, and PTEN) are well conserved. Moreover, it has not been shown that DNA-PK_{cs} phosphorylates full-length Akt/PKB, and DNA-PK_{cs} null mice (*14*) do not suffer the growth retardation or insulin signaling defects associated with Akt1/PKB1 (*15*, *16*) or Akt2/PKB2 (*17*) null mice, respectively.

Mammalian TOR (mTOR) is a large protein kinase that exists in two distinct complexes within cells: one that contains mTOR, GβL, and raptor (*18*–*21*) and another containing mTOR, GβL, and rictor (*21*, *22*). The raptor-containing complex is sensitive to the drug rapamycin and regulates cell growth, in part by phosphorylating the hydrophobic motif of S6K1 (*23*), a member of the same family of kinases to which Akt/PKB belongs. The rictor-containing complex does not appear to be rapamycin-sensitive, and its cellular function is just beginning to be understood (*22*). Despite its structural similarity to S6K1, Akt/PKB phosphorylation is not sensitive to acute rapamycin treatment, and thus mTOR has not previously been considered as the S473K.

We used RNA interference (RNAi) in cultured *Drosophila* cells to determine the role of TOR pathway components in the phosphorylation of the hydrophobic motif sites of *Drosophila* Akt/PKB (dAKT/dPKB) and S6K (dS6K). In mammals and *Drosophila*, S6K suppresses signaling through the PI3K/Akt pathway so that inhibition of S6K boosts Akt/PKB phosphorylation (*24*–*26*). Knockdown of dS6K or dRaptor expression with double-stranded RNAs (dsRNAs) inhibited the phosphorylation and activity of dS6K and increased the phosphorylation of dAkt/dPKB (Fig. 1A). Despite reducing dS6K phosphorylation to the same extent as did dRaptor dsRNA, the dTOR dsRNA failed to increase dAkt/dPKB phosphorylation and,

Whitehead Institute for Biomedical Research and Department of Biology, Massachusetts Institute of Technology, Nine Cambridge Center, Cambridge, MA 02142, USA. Broad Institute, 320 Charles Street, Cambridge, MA 02141, USA.

*These authors contributed equally to this work.
†To whom correspondence should be addressed. E-mail: sabatini@wi.mit.edu

surprisingly, decreased it by a small amount (Fig. 1A). The contrasting effects on dAkt/dPKB phosphorylation by the dTOR and dRaptor dsRNAs suggest that dTOR has an unexpected positive role in dAkt/dPKB signaling that is not shared with dRaptor and that dTOR is required for the increase in dAkt/dPKB phosphorylation caused by dS6K inhibition. Consistent with the dRaptor-independent role for dTOR in dAkt/dPKB phosphorylation, a knockdown of dRictor reduced dAkt/dPKB phosphorylation (Fig. 1A).

Because basal dAkt/dPKB phosphorylation is low in *Drosophila* Kc_{167} cells (Fig. 1A), we verified the roles of dRictor and dTOR in cells in which dAkt/dPKB phosphorylation was enhanced by decreasing the expression of dPTEN, the negative regulator of the PI3K/Akt pathway (Fig. 1B). Knockdown of dS6K or dRaptor expression in dPTEN-depleted cells further boosted dAkt/dPKB phosphorylation. In contrast, knockdown of dRictor expression almost completely prevented the dramatic increase in dAkt/dPKB phosphorylation caused by a dPTEN knockdown, whereas the knockdown of dTOR expression caused a slightly smaller suppression (Fig. 1B). Also, dRictor and dTOR were required for the increase in phosphorylation of dAkt/dPKB caused by a knockdown in the expression of dRaptor (fig. S1).

Our results in *Drosophila* cells suggest that dTOR and dRictor have a shared positive role in the phosphorylation of the hydrophobic motif site of dAkt/dPKB. This finding was unexpected, because previously (*18*) we observed no decrease in the phosphorylation of the hydrophobic motif site of Akt/PKB after reducing mTOR expression in human cells with small interfering RNAs (siRNAs). In retrospect, however, these experiments were undertaken when RNAi-mediated knockdowns of expression in mammalian cells were relatively inefficient. Here, with the use of a lentiviral short hairpin RNA (shRNA) expression system that robustly suppresses gene expression (*22*), we obtained results in human cell lines analogous to those in *Drosophila* cells (Fig. 2A). In human HT-29 colon and A549 lung cancer cells, knockdown of rictor or mTOR expression using two different sets of shRNAs decreased phosphorylation of both S473 and T308 of Akt/PKB. Mammalian cells may try to compensate for the effects of the rictor and mTOR knockdowns by boosting Akt/PKB expression (Fig. 2A). The decrease in T308 phosphorylation is consistent with the importance of S473 phosphorylation for T308 phosphorylation (*3*) and with the fact that the $Ser^{473} \rightarrow Asp^{473}$ mutant of Akt/PKB is a better substrate than the wild-type protein for T308 phosphorylation by PDK1 (*27*). Knockdown of raptor expression increased the phosphorylation of both S473 and T308 despite reducing Akt/PKB expression. Knockdown of rictor or mTOR expression also decreased S473 phosphorylation in HeLa and HEK-293T cells, two human cell lines that, like A549 and HT-29 cells, contain wild-type PTEN (Fig. 2B). In addition, the knockdowns also decreased S473 phosphorylation in the PTEN-null PC-3 prostate cancer cell line (Fig. 2B), a result reminiscent of that in *Drosophila* cells with reduced dPTEN expression (Fig. 1B). Furthermore, the knockdowns decreased S473 phosphorylation in M059J glioblastoma cells that are null for DNA-PK_{cs}, a proposed S473K

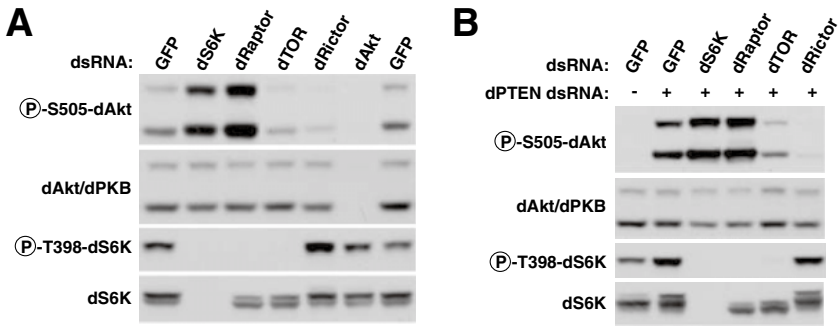

Fig. 1. *Drosophila* rictor and TOR positively regulate the phosphorylation of the hydrophobic motif site of dAkt/dPKB. (**A**) dsRNAs corresponding to the genes for the indicated proteins were transfected into Kc_{167} *Drosophila* cells (*30*). A dsRNA corresponding to green fluorescent protein (GFP) served as a negative control. After 4 days, lysates were prepared and analyzed by immunoblotting (*30*) for amounts of phospho- (P) and total dAkt/dPKB and dS6K. (**B**) dsRNAs corresponding to the genes for the indicated proteins were transfected into Kc_{167} *Drosophila* cells with (+) or without (–) a dsRNA for dPTEN, and samples were analyzed as in (A).

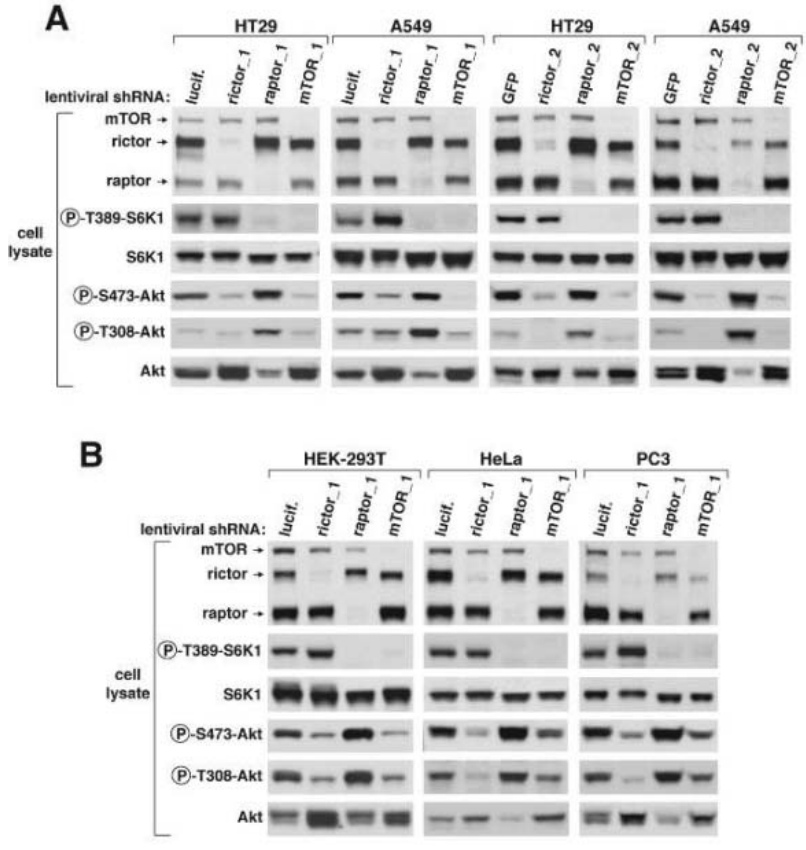

Fig. 2. Rictor and mTOR but not raptor positively regulate the phosphorylation of S473 and T308 of Akt/PKB in a variety of human cancer cell lines. (**A**) Immunoblotting was used to analyze the total amounts and phosphorylation states of the indicated proteins in two different sets of HT29 and A549 cell lines with stable decreases in rictor, raptor, or mTOR expression (*30*). Lentiviruses were used to express control shRNAs targeting luciferase or GFP or shRNAs targeting rictor, raptor, or mTOR (two distinct shRNAs per gene). (**B**) HEK-293T, HeLa, and PC3 cell lines with stable decreases in rictor, raptor, or mTOR expression were analyzed as in (A).

candidate (*9*) (fig. S2). Thus, in six distinct human cell lines, rictor and mTOR but not raptor are necessary for the phosphorylation of the hydrophobic motif of Akt/PKB.

Because the rictor and mTOR knockdowns inhibit phosphorylation events critical for Akt/PKB activity, they should affect Akt/PKB-regulated effectors. In HeLa cells, a reduction in the expression of rictor or mTOR but not raptor decreased phosphorylation of AFX (Foxo4a) (fig. S3), a forkhead family transcription factor that is a direct substrate of Akt/PKB (*28*). Because the raptor-mTOR complex directly phosphorylates the hydrophobic motif site of S6K1 (*23*), we determined whether rictor-mTOR has an analogous function for Akt/PKB. Rictor-mTOR complexes isolated from HEK-293T or HeLa phosphorylated S473 but not T308 of full-length, wild-type Akt/PKB in vitro (Fig. 3A). Immunoprecipitates of raptor, the ataxia telagiectasia mutated (ATM) protein, or protein kinase C α (PKCα) did not phosphorylate either site, and Akt/PKB did not autophosphorylate S473 (Fig. 3A). Importantly, the raptor immunoprecipitates also contain mTOR but did not phosphorylate Akt/PKB (Fig. 3A), suggesting that for mTOR to phosphorylate Akt/PKB, it must be bound to rictor and that raptor cannot substitute. This lack of phosphorylation holds even in the raptor immunoprecipitates isolated from HEK-293T cells that contain as much mTOR as the rictor immunoprecipitates (Fig. 3A). Consistent with a key role for rictor, mTOR immunoprecipitates prepared from the rictor knockdown cells did not phosphorylate Akt/PKB despite containing a similar amount of mTOR as the controls (Fig. 3B). To verify that mTOR is the S473K in the rictor immunoprecipitates, we prepared immunoprecipitates from control cells and from two different lines of mTOR knockdown cells. Although rictor levels were equivalent in all the immunoprecipitates, only those prepared from cells expressing mTOR phosphorylated Akt/PKB in vitro (Fig. 3B). Both the LY294002 and wortmannin mTOR kinase inhibitors blocked the in vitro phosphorylation of Akt/PKB by rictor-mTOR (Fig. 3C), and LY294002 acted at concentrations that inhibit S473 phosphorylation in cells (*3*). Staurosporine, an inhibitor of Akt/PKB kinase activity (*12*), did not decrease the phosphorylation of Akt/PKB by rictor-mTOR. Thus, in vitro the rictor-mTOR complex phosphorylates S473 of Akt/PKB in a rictor- and mTOR-dependent fashion and

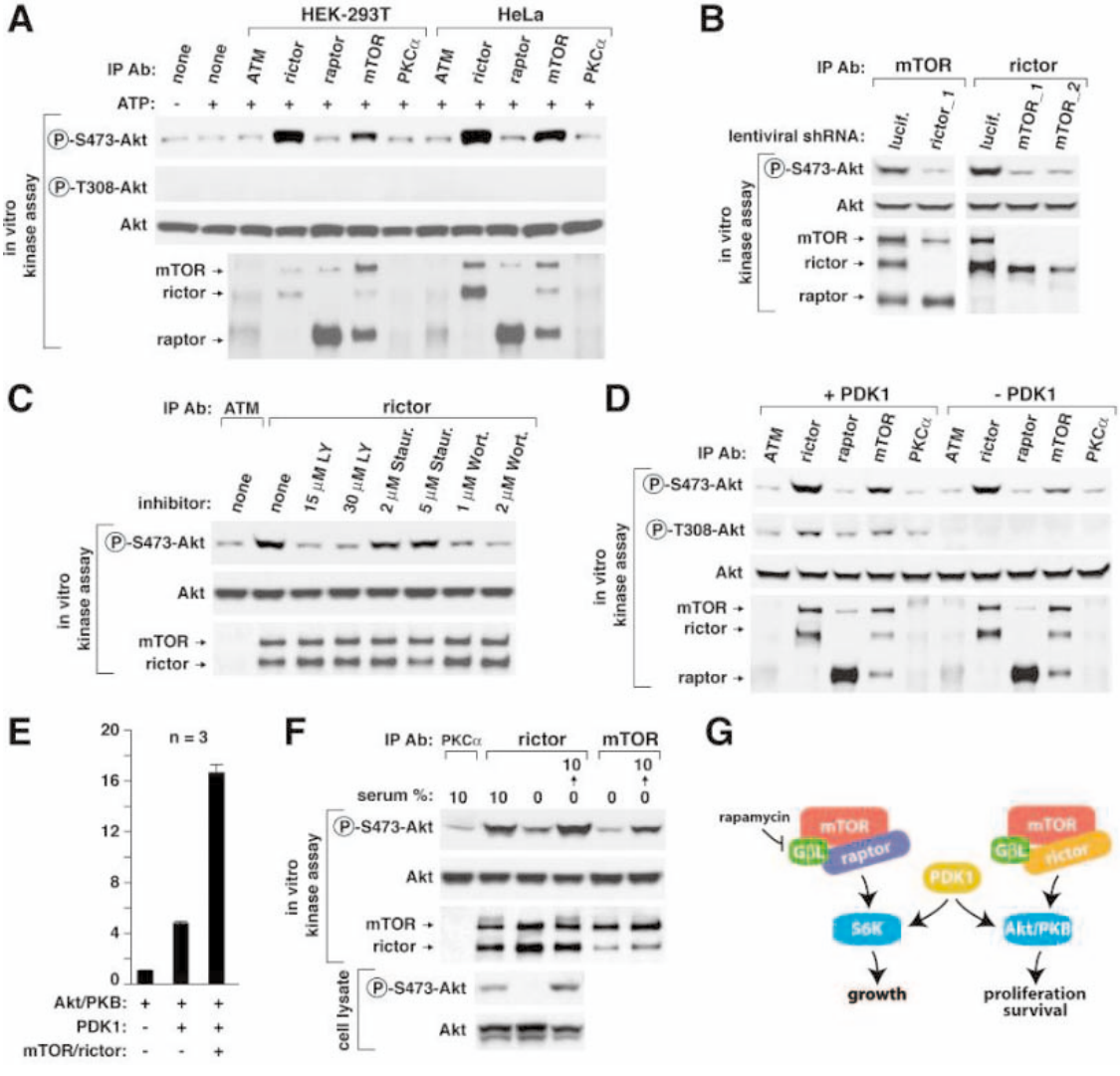

Fig. 3. The rictor-mTOR complex phosphorylates Akt/PKB on S473 in a rictor- and mTOR-dependent fashion and facilitates phosphorylation of T308 by PDK1. (**A**) Immunoprecipitates prepared from lysates of HEK-293T or HeLa cells with the indicated antibodies were used in kinase assays with full-length, wild-type Akt1/PKB1 as the substrate (*30*). Immunoblotting was used to detect the phosphorylation of Akt/PKB at S473 or T308 and the amounts of Akt/PKB, rictor, mTOR, or raptor in the kinase assays (*30*). Adenosine triphosphate was omitted from one sample to determine whether Akt/PKB authophosphorylation contributes to S473 phosphorylation. (**B**) Kinase assays were performed as in (A) with the use of cell lines with stable reductions in the expression of rictor (right) or mTOR (left), respectively. (**C**) Kinase assays containing the indicated concentrations of LY294002 (LY), staurosporine (Staur.), or wortmannin (Wort.) were performed as in (A). (**D**) The prior phosphorylation of S473 of Akt/PKB by rictor-mTOR increases the subsequent phosphorylation of T308 by PDK1. Assays were performed as in (A) with the use of immunoprecipitates from HeLa cells except that after incubation with the indicated immunoprecipitates, 100 ng of PDK1 (+PDK1) was added to half the samples for an additional 20-min incubation (*30*). Samples were analyzed with immunoblotting for the indicated phosphorylation states and protein levels. (**E**) The kinase activity of Akt/PKB after its phosphorylation with PDK1 or with rictor-mTOR followed by PDK1. (**F**) Kinase assays were performed as in (A) with the use of immunoprecipitates isolated from HeLa cells cultured for 24 hours in media containing 10% or 0% serum or from serum-deprived cells stimulated with 10% serum for 30 min. (**G**) Schematic diagram of the role of rictor-mTOR in Akt/PKB activation.

with a drug sensitivity profile consistent with mTOR being the phosphorylating kinase.

To determine whether the phosphorylation of Akt/PKB on S473 by rictor-mTOR activates Akt/PKB activity, we first used rictor-mTOR to phosphorylate Akt/PKB on S473 and then added PDK1 to the assay to phosphorylate T308. Prior phosphorylation of Akt/PKB on S473 boosted subsequent phosphorylation by PDK1 of T308 (Fig. 3D), consistent with the importance of S473 phosphorylation for T308 phosphorylation (*3*, *4*) and with the inhibitory effects of the rictor and mTOR knockdowns on T308 phosphorylation (Fig. 2AB). After phosphorylation with rictor-mTOR and PDK1, Akt1/PKB1 had about four- to fivefold more activity than after phosphorylation with PDK1 alone (Fig. 3E), confirming the important role of S473 in fully activating Akt/PKB. Because growth factors control the phosphorylation of Akt/PKB on S473, we determined whether the concentration of serum in the cell media regulated the in vitro kinase activity of rictor-mTOR toward Akt/PKB. Rictor-mTOR had decreased activity in HeLa cells deprived of serum and was reactivated by serum stimulation for 30 min (Fig. 3F), indicating that modulation of the intrinsic kinase activity of rictor-mTOR may be a mechanism for regulating S473 phosphorylation.

Our results indicate that the rictor-mTOR complex is a hydrophobic motif kinase for Akt/PKB (Fig. 3G). Rictor-TOR has essential roles in Akt/PKB hydrophobic motif site phosphorylation in *Drosophila* and human cells and in vitro phosphorylates full-length, wild-type Akt/PKB in a serum-sensitive fashion. No other proposed hydrophobic motif kinase has been shown to fulfill all these criteria. With hindsight, we do see clues in the literature to the important role of mTOR in Akt/PKB activation. Prolonged but not acute treatment of certain human cells with rapamycin partially inhibits Akt/PKB phosphorylation (*29*), and our findings provide a possible rationale to explain these results. Although rapamycin does not bind to a preformed rictor-mTOR complex (*22*), during long-term rapamycin treatment the drug should eventually sequester many of the newly synthesized mTOR molecules within cells. Thus, as the rictor-mTOR complex turns over, rapamycin may interfere with its reassembly or over time become part of the new complexes. It is reasonable to expect then that prolonged rapamycin treatment may partially inhibit rictor-mTOR activity, which would explain why rapamycin is particularly effective at suppressing the proliferation of tumor cells with hyperactive Akt/PKB. The PI3K/Akt pathway is frequently deregulated in human cancers that have lost the expression of the PTEN tumor suppressor gene, and our findings suggest that direct inhibitors of mTOR-rictor should strongly suppress Akt/PKB activity. Thus, the rictor-mTOR complex, like its raptor-mTOR sibling, may be a valuable drug target.

References and Notes

1. D. R. Alessi *et al.*, *Curr. Biol.* **7**, 261 (1997).
2. L. Stephens *et al.*, *Science* **279**, 710 (1998).
3. M. P. Scheid, P. A. Marignani, J. R. Woodgett, *Mol. Cell. Biol.* **22**, 6247 (2002).
4. J. Yang *et al.*, *Mol. Cell* **9**, 1227 (2002).
5. D. R. Alessi *et al.*, *EMBO J.* **15**, 6541 (1996).
6. A. Balendran *et al.*, *Curr. Biol.* **9**, 393 (1999).
7. S. Persad *et al.*, *J. Biol. Chem.* **276**, 27462 (2001).
8. A. Toker, A. C. Newton, *J. Biol. Chem.* **275**, 8271 (2000).
9. J. Feng, J. Park, P. Cron, D. Hess, B. A. Hemmings, *J. Biol. Chem.* **279**, 41189 (2004).
10. M. R. Williams *et al.*, *Curr. Biol.* **10**, 439 (2000).
11. D. K. Lynch, C. A. Ellis, P. A. Edwards, I. D. Hiles, *Oncogene* **18**, 8024 (1999).
12. M. M. Hill *et al.*, *J. Biol. Chem.* **276**, 25643 (2001).
13. A. S. Dore, A. C. Drake, S. C. Brewerton, T. L. Blundell, *DNA Repair (Amsterdam)* **3**, 33 (2004).
14. G. E. Taccioli *et al.*, *Immunity* **9**, 355 (1998).
15. H. Cho, J. L. Thorvaldsen, Q. Chu, F. Feng, M. J. Birnbaum, *J. Biol. Chem.* **276**, 38349 (2001).
16. W. S. Chen *et al.*, *Genes Dev.* **15**, 2203 (2001).
17. H. Cho *et al.*, *Science* **292**, 1728 (2001).
18. D.-H. Kim *et al.*, *Cell* **110**, 163 (2002).
19. D.-H. Kim *et al.*, *Mol. Cell* **11**, 895 (2003).
20. K. Hara *et al.*, *Cell* **110**, 177 (2002).
21. R. Loewith *et al.*, *Mol. Cell* **10**, 457 (2002).
22. D. D. Sarbassov *et al.*, *Curr. Biol.* **14**, 1296 (2004).
23. P. E. Burnett, R. K. Barrow, N. A. Cohen, S. H. Snyder, D. M. Sabatini, *Proc. Natl. Acad. Sci. U.S.A.* **95**, 1432 (1998).
24. F. Tremblay, A. Marette, *J. Biol. Chem.* **276**, 38052 (2001).
25. T. Radimerski, J. Montagne, M. Hemmings-Mieszczak, G. Thomas, *Genes Dev.* **16**, 2627 (2002).
26. L. S. Harrington *et al.*, *J. Cell Biol.* **166**, 213 (2004).
27. R. M. Biondi, A. Kieloch, R. A. Currie, M. Deak, D. R. Alessi, *EMBO J.* **20**, 4380 (2001).
28. G. J. Kops *et al.*, *Nature* **398**, 630 (1999).
29. A. L. Edinger, C. M. Linardic, G. G. Chiang, C. B. Thompson, R. T. Abraham, *Cancer Res.* **63**, 8451 (2003).

30. Materials and methods are presented as supporting material on *Science* Online.

31. This work was supported by a grant from the NIH (R01 AI47389) and awards from the Pew Charitable Trust and the Rita Allen Foundation to D.M.S., as well as fellowships from the Anna Fuller Fund to D.D.S., Damon Runyon Cancer Research Foundation to D.A.G., and the Howard Hughes Medical Institute to S.M.A. We thank members of the Sabatini lab for suggestions on the manuscript and M. B. Yaffe for helpful discussions. Molecular interaction data have been deposited in the Biomolecular Interaction Network Database with accession codes 195918 to 195923.

Supporting Online Material
www.sciencemag.org/cgi/content/full/307/5712/1098/DC1
Materials and Methods
Figs. S1 to S3

7 October 2004; accepted 23 December 2004
10.1126/science.1106148

Obligate Role of Anti-Apoptotic MCL-1 in the Survival of Hematopoietic Stem Cells

Joseph T. Opferman,[1,2]* Hiromi Iwasaki,[2] Christy C. Ong,[1,2] Heikyung Suh,[1,2] Shin-ichi Mizuno,[2] Koichi Akashi,[2]† Stanley J. Korsmeyer[1,2]†

Apoptosis is important in controlling hematopoietic stem cell (HSC) numbers. However, the specific BCL-2 family member(s) that regulate HSC homeostasis are not precisely defined. We tested myeloid leukemia–1 (MCL-1) as an attractive candidate that is highly expressed in HSCs and regulated by growth factor signals. Inducible deletion of *Mcl-1* in mice resulted in ablation of bone marrow. This resulted in the loss of early bone marrow progenitor populations, including HSCs. Moreover, growth factors including stem cell factor increased transcription of the *Mcl-1* gene and required MCL-1 to augment survival of purified bone marrow progenitors. Deletion of *Mcl-1* in other tissues, including liver, did not impair survival. Thus, MCL-1 is a critical and specific regulator essential for ensuring the homeostasis of early hematopoietic progenitors.

Hematopoietic stem cells (HSCs), which give rise to all cells of hematopoietic lineages, can undergo several developmental fates. These include self-renewal or differentiation into multipotent progenitors that give rise to mature hematopoietic cells (*1*). This process is tightly controlled and regulated by apoptosis (*2*). Constitutive expression of human *BCL-2* in vivo under the control of the mouse major histocompatibility class I promoter causes accumulation of HSCs and enhances their ability to form colonies in vitro and to reconstitute the hematopoietic system of lethally irradiated recipients (*3*). Thus, apoptosis appears to be an important mechanism for regulating HSC numbers, but whether one or

[1]Howard Hughes Medical Institute, [2]Dana Farber Cancer Institute, Department of Cancer Immunology and AIDS, Pathology and Medicine, Harvard Medical School, Boston, MA 02115, USA.

*Present address: Department of Biochemistry, St. Jude Children's Research Hospital, 332 North Lauderdale, Memphis, TN 38105, USA.
†To whom correspondence should be addressed. E-mail: Koichi_Akashi@dfci.harvard.edu (K.A.); Stanley_Korsmeyer@dfci.harvard.edu (S.K.)

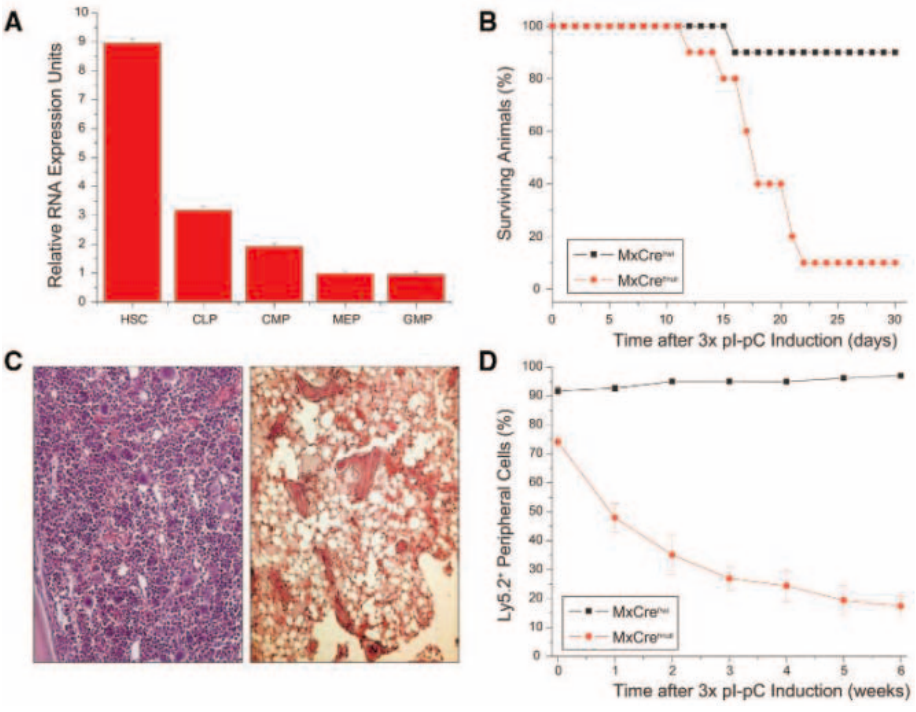

Fig. 1. Fatal failure of BM after deletion of *Mcl-1*. (**A**) Amount of *Mcl-1* mRNA in wild-type BM progenitor populations purified by flow cytometry. The mean ± the standard error of the mean (SEM) is presented of triplicate assays in which *Mcl-1* mRNA expression units were normalized to those of *HPRT*. (**B**) Kaplan-Meier survival graph for cohorts of 10 mice injected with three intraperitoneal doses of pI-pC (400 μg per dose). Log-rank test statistical analyses indicate that $P = 0.0003$. (**C**) Histological analysis of femurs from (left) MxCre$^{f/wt}$ and (right) MxCre$^{f/null}$ mice 11 days after three doses of pI-pC. Sections were stained with hematoxylin and eosin. (**D**) A total of 10^6 cell surface–marked (Ly5.2$^+$) BM cells from MxCre$^{f/wt}$ or MxCre$^{f/null}$ mice were adoptively transferred along with 10^5 wild-type (Ly5.1$^+$) BM cells into lethally irradiated (950 Rad) Ly5.1$^+$ congenic recipients. After 5 weeks of engraftment, chimeric mice were treated with three doses of pI-pC, and the percentage of peripheral blood cells expressing Ly5.2 or Ly5.1 was determined by flow cytometry. The mean percentage of Ly5.2$^+$ blood cells from three chimeric mice ± SEM is presented for each time point.

more anti-apoptotic BCL-2 family members is required for this homeostatic control has not been established (*4*).

Members of the BCL-2 family of proteins are critical regulators of cell death. Pro-apoptotic BH3 domain–only members of the BCL-2 family respond to death signals and activate the multidomain death effector proteins BAX and BAK, which constitute an obligate gateway to the intrinsic death signaling pathway that operates through the mitochondria and the endoplasmic reticulum (*5*, *6*). Conversely, anti-apoptotic BCL-2 family members bind and sequester BH3-only molecules, thus preventing activation of BAX and BAK (*7*). Individual BCL-2 family members have specific roles during hematopoiesis. *Bcl-2*-deficient mice do not have overt problems during early hematopoiesis, but over time peripheral lymphocytes are vulnerable to apoptosis, especially after activating stimuli (*8*). *Bcl-X$_L$*-deficient chimeras created by complementation of *Rag2*-deficient blastocysts generate lymphocyte progenitors; however, the survival of CD4$^+$CD8$^+$ thymocytes is compromised (*9*, *10*). BCL-X$_L$ is also indispensable for the late maturation of both primitive and definitive erythroid progenitors (*11*). *Mcl-1* deficiency results in peri-implantation lethality of mouse embryos (*12*). Conditional deletion of *Mcl-1* during early lymphocyte differentiation increases apoptosis and arrests development at the cytokine-dependent pro-B cell and double-negative T cell stages (*13*). Furthermore, induced deletion of *Mcl-1* results in loss of mature B and T lymphocytes, demonstrating a role for MCL-1 in the maintenance of the mature immune system (*13*).

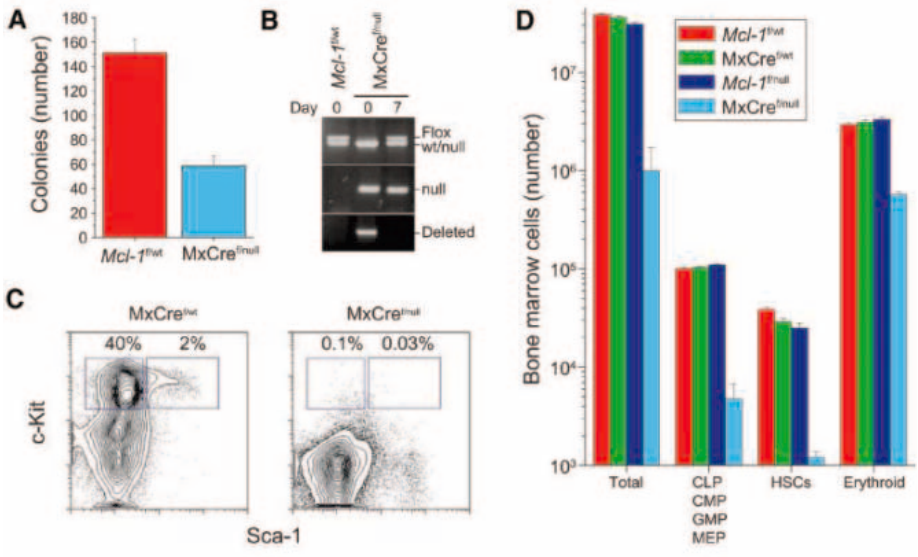

Fig. 2. Loss of BM progenitor populations including hematopoietic stem cells after *Mcl-1* deletion. (**A**) Recovered colony number from cultured BM from mice (*Mcl-1*$^{f/wt}$ or MxCre$^{f/null}$) harvested 3 days after one intraperitoneal dose of pI-pC. Data are presented as mean number of colonies from triplicate performed assays ± SEM counted 7 days after plating of 10,000 BM cells. (**B**) Genomic DNA from cultured BM [as in (A)] was analyzed by PCR to determine the representation of *Mcl-1*^{wt}, *Mcl-1*^{flox}, *Mcl-1*^{deleted}, and *Mcl-1*^{null} alleles. The day 0 BM samples are from mice injected with pI-pC (3 days before sampling), and the day 7 DNA are from cells harvested from the colony-forming assay. (**C**) The Sca-1 and c-Kit profile of mature hematopoietic lineage-negative BM (negative for B220, Ter119, CD19, CD3, CD4, CD8, Gr1, Mac-1, and CD127). Numbers indicate the percentage of lineage-negative BM for HSCs (c-Kit$^+$Sca-1$^+$, right box) and early hematopoietic progenitors (c-Kit$^+$Sca-1$^-$, left box) subsets as determined by flow cytometry from MxCre$^{f/wt}$ (left plot) and MxCre$^{f/null}$ (right plot) mice 7 days after one dose of pI-pC. Data are representative of more than five mice analyzed per genotype. (**D**) Number of BM cells from subsets (mean ± SEM) for 5 mice from each *Mcl-1*$^{f/wt}$, MxCre$^{f/wt}$, *Mcl-1*$^{f/null}$, or MxCre $^{f/null}$ genotype at 8 weeks of age.

MCL-1 is highly expressed in HSC, and its expression levels decreased in further differentiated progenitor populations such as the common myeloid progenitor (CMP) (*14*) and the common lymphoid progenitor (CLP) (*15*) as assessed by microarray analysis (*16*). To confirm this expression profile, we used real-time quantitative polymerase chain reaction (PCR) to detect the relative amounts of *Mcl-1* mRNA in purified progenitor cells

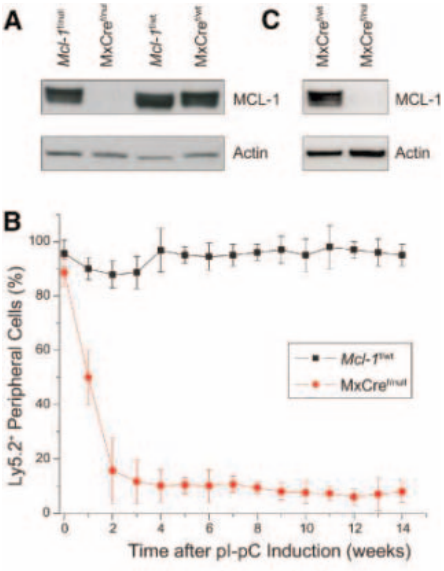

Fig. 3. Lethality of *Mcl-1*-deletion is BM-specific. (**A**) MCL-1 protein expression as determined by immunoblot of liver lysates from *Mcl-1*$^{f/null}$, or MxCre $^{f/null}$, *Mcl-1*$^{f/wt}$, MxCre$^{f/wt}$ mice 11 days after three doses of pI-pC. (**B**) Ly5.2$^+$ *Mcl-1*$^{f/wt}$ or MxCre$^{f/null}$ mice were sublethally irradiated (400 Rad) and adoptively transferred with 10^6 Ly5.1$^+$ congenic wild-type BM cells. After 5 weeks of engraftment, three doses of pI-pC were administered to the chimeric mice, and weekly blood analysis was performed by flow cytometry for Ly5.2 or Ly5.1 expression. The average percentage of peripheral blood cells that were host-derived (expressed Ly5.2$^+$) ± SEM was determined by flow cytometry for each recipient genotype. (**C**) Immunoblot analysis of liver MCL-1 protein expression from BM chimeric animals [Ly5.1$^+$ wild-type BM into Ly5.2$^+$ *Mcl-1*$^{f/wt}$ or MxCre$^{f/null}$ mice, as in (B) 14 weeks after 3 doses of pI-pC].

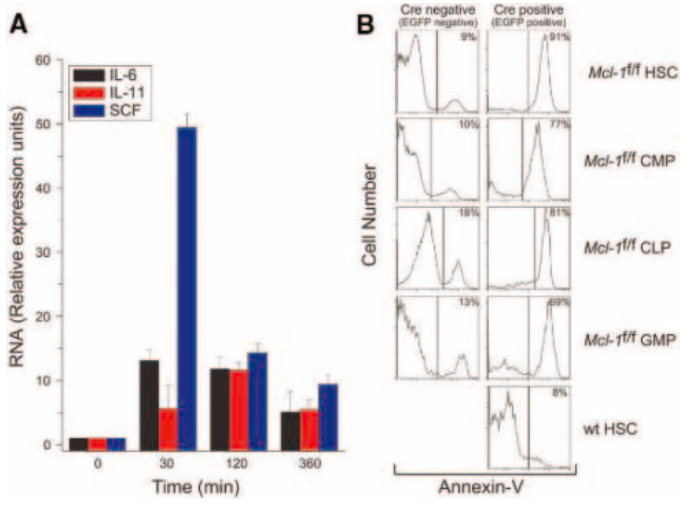

Fig. 4. Hematopoietic growth factors induce *Mcl-1* expression and require *Mcl-1* to mediate progenitor survival. (**A**) Mean ± SEM of triplicate assays for *Mcl-1* mRNA normalized to amount of *HPRT* mRNA for purified, wild-type HSCs after 30, 120, or 360 min of exposure to cytokine growth factors (20 ng/ml). (**B**) Percentage of cells undergoing apoptosis in cultured FACS-purified BM progenitor populations (HSC, CMP, CLP, and GMP) from *Mcl-1*$^{f/f}$ or wild-type mice 48 hours after transduction with MSCV-Cre-IRES-EGFP to induce deletion of *Mcl-1*. Each progenitor population was cultured in growth factors (Materials and Methods), and the percentage of cells undergoing apoptosis is presented for Cre$^+$ (EGFP-expressing) or Cre$^-$ (EGFP-negative) populations stained with annexin-V to detect phosphatidylserine exposed on the surface of dying cells. Data are representative of two independently performed experiments.

(*13*, *17*). Amounts of *Mcl-1* mRNA were higher in HSCs than in CLPs or CMPs. Megakaryocyte erythroid progenitors (MEPs) and granulocyte monocyte progenitors (GMPs) had still lower amounts (Fig. 1A).

To address whether MCL-1 is required for the maintenance of hematopoietic cells we bred conditional *Mcl-1*$^{flox(f)/f}$ mice with mice expressing the Cre recombinase under the control of the endogenous *Mx1* locus, which can be transiently activated in response to type-I interferon (IFN) (*13*, *18*). We induced in vivo deletion by intraperitoneal administration of polyinocinic-polycytidylic acid (pI-pC) to MxCre*Mcl-1*$^{f/null}$ mice (*13*, *18*). Within 12 to 21 days after treatment, the majority of MxCre*Mcl-1*$^{f/null}$ mice, but not MxCre*Mcl-1*$^{f/wt}$ control mice, began to appear moribund and were killed (Fig. 1B). At sacrifice, MxCre*Mcl-1*$^{f/null}$ mice were extremely anemic and had severely reduced numbers of bone marrow (BM) cells (Fig. 1C).

MxCre mice can induce gene deletion in various IFN-responsive tissues in response to pI-pC (*18*). To examine whether the effect of deletion was from effects on BM cells or from deletion in nonhematopoietic cells, we generated BM chimeric animals. Experimental BM expressing the Ly5.2 cell surface marker from MxCre*Mcl-1*$^{f/wt}$ or MxCre*Mcl-1*$^{f/null}$ BM was adoptively transferred with congenic wild-type carrier BM expressing Ly5.1 cell surface marker into lethally irradiated Ly5.1 congenic animals and allowed to engraft for 5 weeks. Animals were treated with pI-pC, and blood was monitored for Ly5.2$^+$ cells in the periphery. Whereas the mice reconstituted with MxCre*Mcl-1*$^{f/wt}$ BM maintained greater than 85% Ly5.2$^+$ peripheral blood cells, the peripheral blood from MxCre*Mcl-1*$^{f/null}$ reconstituted mice lost Ly5.2$^+$ cells from the periphery and the number of Ly5.1$^+$ carrier BM cells increased over 4 weeks (Fig. 1D). These data demonstrate that deletion of *Mcl-1* from chimeric animals results in the loss of BM in a cell-autonomous manner.

To determine whether *Mcl-1*-deleted cells give rise to colonies when cultured in vitro, we harvested BM from MxCre*Mcl-1*$^{f/wt}$ or MxCre*Mcl-1*$^{f/null}$ mice 3 days after pI-pC treatment. After 7 days, colony numbers and morphology were scored, revealing that BM isolated from the treated MxCre*Mcl-1*$^{f/null}$ mice generated fewer colonies than did BM from littermate controls (Fig. 2A) (*19*). Genomic DNA was isolated from the resulting colonies, and PCR assays were used to distinguish between the *Mcl-1*^{f}, *Mcl-1*^{deleted}, and *Mcl-1*^{null} alleles (*13*). The deleted allele, *Mcl-1*^{deleted}, was readily detected by PCR in the isolated BM 3 days after pI-pC treatment (day 0) (Fig. 2B). However, after 7 days of in vitro culture, only *Mcl-1*^{f} and *Mcl-1*^{null} alleles were detectable in the hematopoietic colonies (Fig. 2B). This indicates that BM progenitors lacking both copies of *Mcl-1* are not viable and that the reduced numbers of resultant colonies are the result of BM progenitors that escaped the Cre-mediated deletion.

To examine the hematopoietic populations from MxCre*Mcl-1*$^{f/wt}$ and MxCre*Mcl-1*$^{f/null}$ animals, we analyzed BM 7 days after a single intraperitoneal dose of pI-pC. The total number of BM cells present in the MxCre*Mcl-1*$^{f/null}$ mice was lower compared with that in pI-pC-treated littermate controls. When the HSC (mature hematopoietic lineage$^-$c-Kit$^+$Sca-1$^+$) and progenitor populations (lineage$^-$c-Kit$^+$Sca-1$^-$) (*14*) were analyzed by flow cytometry, both populations were depleted in BM from treated MxCre*Mcl-1*$^{f/null}$ animals (Fig. 2C) (*20*). Furthermore, the number of BM cells in mice lacking *Mcl-1* was 10% of that in control animals 7 days after pI-pC-induced deletion (Fig. 2D). This included large decreases in the HSC and other progenitor populations; however, other more differentiated progenitor populations such as erythroid progenitors (Ter119$^+$) were more subtly reduced (Fig. 2D).

The liver is sensitive to MCL-1 deletion by the MxCre system; therefore we examined *Mcl-1* deletion in this tissue (*18*). In liver, MCL-1 was undetectable by protein immunoblotting after pI-pC-mediated deletion (Fig. 3A) (*21*). However, histological analysis of liver sections from MxCre*Mcl-1*$^{f/wt}$ and MxCre*Mcl-1*$^{f/null}$ mice 14 days after pI-pC treatment did not reveal any abnormalities, suggesting that loss of MCL-1 expression does not lead to apoptosis of this tissue (*22*). To test this possibility, we adoptively transferred Ly5.1$^+$ wild-type BM into sublethally irradiated Ly5.2$^+$ MxCre*Mcl-1*$^{f/wt}$ or MxCre*Mcl-1*$^{f/null}$ mice. After 4 weeks of engraftment, the mice

were treated with pI-pC, and cells were analyzed by flow cytometry. The Ly5.2$^+$ peripheral lymphocytes from MxCre*Mcl-1*$^{f/null}$ mice were lost within 2 weeks (Fig. 3B); however, the Ly5.1$^+$ wild-type BM promoted the survival of the chimeric mice for more than 14 weeks after MxCre-mediated deletion. Liver lysates from pI-pC-treated MxCre*Mcl-1*$^{f/null}$ chimeric mice contained no detectable MCL-1 expression (Fig. 3C). Thus, deletion of *Mcl-1* in the liver is efficient, but nonhematopoietic effects of deletion do not appear to be responsible for the failure of the animals to survive.

Expression of MCL-1 is controlled by growth factor signaling pathways. Both mature lymphocytes and lymphoid progenitors increase expression of MCL-1 in response to interleukin (IL)-7 signaling (*13*). Stem cell factor (SCF) induces expression of MCL-1 in a human BM-derived cell line (*23*). To determine whether *Mcl-1* is expressed in response to growth factors in HSCs, we used real-time PCR. The amount of *Mcl-1* mRNA was greater 30 min after exposure of purified HSCs to SCF. IL-6 had a smaller effect, whereas culture with IL-11 did not induce expression (Fig. 4A) (*24*).

To assess whether *Mcl-1* is required for the survival of cultured BM progenitor populations exposed to growth factors, we used retroviral transduction of Cre into purified BM progenitor populations from *Mcl-1*$^{f/f}$ or wild-type mice (*25*). The purified BM progenitor populations (HSC, CMP, CLP, and GMP) were cultured in appropriate growth factors (*26*). By 48 hours after retroviral transduction, more than 90% of *Mcl-1*$^{f/f}$ Cre-expressing [enhanced green fluorescent protein positive (EGFP$^+$)] progenitor cells (HSCs, CMP, and CLPs) were apoptotic (Fig. 4B). Expression of Cre in wild-type BM progenitor populations did not induce apoptosis (Fig. 4B). Therefore, survival of BM progenitors in vitro requires the expression of *Mcl-1* induced by early-acting cytokine signals.

Although previous studies had implicated anti-apoptotic BCL-2 family members in regulating the homeostasis of hematopoietic progenitors (*3*), our studies indicate that a single anti-apoptotic BCL-2 family member, MCL-1, is essential for promoting the survival of HSC and other hematopoietic progenitors.

References and Notes

1. A. J. Wagers, J. L. Christensen, I. L. Weissman, *Gene Ther.* **9**, 606 (2002).
2. M. Kondo *et al.*, *Annu. Rev. Immunol.* **21**, 759 (2003).
3. J. Domen, S. H. Cheshier, I. L. Weissman, *J. Exp. Med.* **191**, 253 (2000).
4. J. Domen, *Apoptosis* **6**, 239 (2001).
5. M. C. Wei *et al.*, *Science* **292**, 727 (2001).
6. L. Scorrano *et al.*, *Science* **300**, 135 (2003); published online 6 March 2003 (10.1126/science.1081208).
7. E. H. Cheng *et al.*, *Mol. Cell* **8**, 705 (2001).
8. D. J. Veis, C. M. Sorenson, J. R. Shutter, S. J. Korsmeyer, *Cell* **75**, 229 (1993).
9. N. Motoyama *et al.*, *Science* **267**, 1506 (1995).
10. A. Ma *et al.*, *Proc. Natl. Acad. Sci. U.S.A.* **92**, 4763 (1995).
11. N. Motoyama, T. Kimura, T. Takahashi, T. Watanabe, T. Nakano, *J. Exp. Med.* **189**, 1691 (1999).
12. J. L. Rinkenberger, S. Horning, B. Klocke, K. Roth, S. J. Korsmeyer, *Genes Dev.* **14**, 23 (2000).
13. J. T. Opferman *et al.*, *Nature* **426**, 671 (2003).
14. K. Akashi, D. Traver, T. Miyamoto, I. L. Weissman, *Nature* **404**, 193 (2002).
15. M. Kondo, I. L. Weissman, K. Akashi, *Cell* **91**, 661 (1997).
16. K. Akashi *et al.*, *Blood* **101**, 383 (2003).
17. RNA was extracted (Trizol, Invitrogen, Carlsbad, CA) and cDNA synthesized (Promega, Madison, WI) for Sybr-green TaqMan real-time PCR analysis (Applied Biosystems Incorporated, Forest City, CA). Primers were Mcl-1 (forward, AGAGCGCTGGAGACCCTG; reverse, CTATCTTATTAGATATGCCAGACC) and hypoxanthine-guanine phosphoribosyl transferase (HPRT) (forward, GTTGGATACAGGCCAGACTTTGTTG; reverse, GAGGGTAGGCTGGCCTATAGGCT).
18. R. Kuhn, F. Schwenk, M. Aguet, K. Rajewsky, *Science* **269**, 1427 (1995).
19. BM was cultured in M3434 Methocult (Stem Cell Technologies, Vancouver, Canada) containing insulin, transferrin, SCF, IL-3, IL-6, and erythropoietin for 7 days.
20. Stained BM was analyzed on a FACSCalibur (Becton-Dickinson), and antibodies were purchased from BD-Pharmingen (San Diego, CA), except for anti-CD127 (eBioscience, San Diego, CA).
21. Cells were lysed in radioimmunoprecipitation assay buffer immunoblotted by using anti-MCL-1 (Rockland Immunochemical, Gilbertsville, PA) and anti-β-Actin (Chemicon, Temecula, CA).
22. J. T. Opferman, S. J. Korsmeyer, unpublished data.
23. H. M. Huang, C. J. Huang, J. J. Yen, *Blood* **96**, 1764 (2000).
24. Lineage-negative BM was positive-selected with the use of magnetic beads (Dynal, Oslo, Norway). HSCs (lineage$^-$c-Kit$^+$Sca-1$^+$) purified with the use of a MoFlow (Cytomation, Ft. Collins, CO) cell sorter were starved in cRPMI-10% fetal calf serum for 4 hours. SCF, IL-6, or IL-11 were administered to the cultures, and cells were harvested at 30, 120, and 160 min. *Mcl-1* expression levels were determined by real-time PCR.
25. H. Iwasaki *et al.*, *Immunity* **19**, 451 (2003).
26. Fluorescence-activated cell sorter (FACS)–purified progenitors were enriched from wild-type or *Mcl-1*$^{f/f}$ mice, transduced with retroviral MSCV-Cre-IRES-EGFP, and cultured in growth factors (10 ng/ml). HSC growth factors were SCF, IL-11, IL-6, and leukemia inhibitor factor. CMP growth factors were SCF, IL-11, IL-6, and IL-3. CLP factors were SCF, IL-7, and Flt3-ligand; for GMP, they were SCF, IL-11, IL-6, and IL-3. After 48 hours, the cells were stained with annexin-V and analyzed by FACS.

27. We acknowledge C. Beard and E. Williams for technical expertise, J. Fisher for animal husbandry, and E. Smith for editorial assistance. J.T.O. is supported by a postdoctoral fellowship (DRG 1664) from the Damon Runyon Cancer Research Foundation and a Special Fellowship (3421-05) from the Leukemia and Lymphoma Society. This work is supported in part by NIH grant R37CA50239 to S.J.K. and grants DK061320 and CA072009 to K.A.

6 October 2004; accepted 22 December 2004
10.1126/science.1106114

Identification of the Sex Pheromone of the German Cockroach, *Blattella germanica*

Satoshi Nojima,[1]* Coby Schal,[2] Francis X. Webster,[3] Richard G. Santangelo,[2] Wendell L. Roelofs[1]†

The sex pheromone of the German cockroach, *Blattella germanica*, has been characterized as gentisyl quinone isovalerate. This cockroach is a major cause of allergic disease and serves as a mechanical vector of pathogens, making it one of the most important residential and food-associated pests worldwide. The sex pheromone–producing gland in adult females was identified in 1993, but thermal instability of the pheromone made characterization difficult. Now, using a new preparative gas chromatography approach coupled with electroantennographic detection, we have isolated and characterized the pheromone, which we term blattellaquinone, and confirmed the identification by chemical synthesis. The synthetic pheromone was active in behavioral assays and highly effective in field trapping tests, which suggest that it may provide a new tool in cockroach population detection, monitoring, and control.

A sex pheromone that eluded natural product chemists for several decades has been characterized for the German cockroach, *Blattella germanica*, one of the most important residential and food-associated pests worldwide. Movement of these cockroaches between human and animal waste and food materials allows them to acquire, carry, and mechanically transfer pathogens (*1*, *2*). Moreover, exposure to cockroach-derived allergenic proteins in homes is associated with allergic disease and asthma, particularly in inner-city children (*3*). Cockroach control, coupled with extensive cleaning, can result in large reductions in cockroach allergens in settled household dust (*4*–*6*), but a fundamental constraint in abatement programs has been a lack of effective attractants to lure cock-

[1]Department of Entomology, New York Agricultural Experiment Station, Cornell University, Geneva, NY 14456, USA. [2]Department of Entomology and W. M. Keck Center for Behavioral Biology, Box 7613, North Carolina State University, Raleigh, NC 27695–7613, USA. [3]Department of Chemistry, State University of New York, College of Environmental Science and Forestry, Syracuse, NY 13210, USA.

*Present address: Fine Chemical Department, Shin-Etsu Chemical Co., Ltd., Chiyoda-ku, Tokyo 100-0004, Japan.

†To whom correspondence should be addressed. E-mail: wlr1@cornell.edu

roaches into traps and insecticide baits (*7*). This deficiency is probably the most important single factor contributing to a continued reliance on scheduled applications of broad-spectrum insecticides to control cockroaches.

A nonvolatile, courtship-eliciting sex pheromone on the female's cuticular surface was previously identified (*8*), but this pheromone does not have any obvious value in pest control. Based on behavioral and electrophysiological assays, a female sex pheromone that attracts males over some distance, and hence of potential utility in pest control, was discovered in 1993 (*9*). The pheromone-producing gland was anatomically localized to the pygidium, the last abdominal segment (*10*), and we observed that virgin females, but not mated females, engage in a characteristic behavior ("calling behavior"), during which they become exceptionally attractive to males (*11*, *12*). Females at this physiological stage are also highly receptive to courting males, and organic solvent extracts of these females specifically attract males, but not adult females or nymphs (*9*). However, the minute quantity of attractant produced by each female and the thermal instability of the pheromone have hampered efforts to isolate it. Here we report the purification and identification of the pheromone compound, which we accomplished by using a highly sensitive gas-chromatographic-electroantennogram detector (GC-EAD), in which the male cockroach antenna served as a biological detector, and development of a technique for GC purification of a small, thermally unstable sample for nuclear magnetic resonance (NMR) analysis (*13*).

The pygidia of ~15,000 virgin females were carefully dissected, extracted in dichloromethane, and assayed for attractiveness to males, females, and nymphs in a two-choice olfactometer device (*14*). We then followed a behaviorally guided chromatographic fractionation of the extract to purify the active fraction. First, the total lipid extract of the pygidia was separated on a silica gel column by eluting successively with mixtures of pentane-ether. The 40% ether fraction, which elicited the highest behavioral responses in males, was subjected to preparative high-performance liquid chromatography (HPLC) purification, and the active fraction was subjected to coupled GC-EAD analysis and GC-mass spectrometry (GC-MS) analysis and further purification using preparative GC (*14*). GC-EAD analyses of the behaviorally active fractions from preparative HPLC consistently revealed a single EAD-active compound (fig. S1).

The behaviorally active and EAD-active compound was subjected to GC-MS analysis in electron impact (EI) mode (*14*). It showed a base peak at a mass/charge ratio (*m/z*) of 57 (100%) and characteristic ions at $m/z = 60$ (68%), 122 (24%), 138 (16%), 150 (1.7%), 152 (1.3%), 162 (2.7%), 176 (2.0%), 180 (7.1%), 222 (0.9%), and 224 (1.1%). In chemical ionization (CI) GC-MS, the EAD-active compound showed a set of characteristic ions at $m/z = 223$ (51%), 251 (27%), and 263 (8.9%). Both the EI and CI mass spectra of the natural pheromone indicated a molecular mass of 222 g/mol (EI $m/z = 222$ and CI $m/z = 223$), suggesting a number of likely molecular formulas, including $C_{12}H_{14}O_4$, $C_{13}H_{18}O_3$, $C_{14}H_{22}O_2$, $C_{15}H_{26}O$, $C_{15}H_{10}O_2$, $C_{16}H_{14}O$, $C_{16}H_{30}$, and $C_{17}H_{18}$. Fragmentation in the EI mass spectrum gave little useful information to pare down the number of formulas.

The 600-MHz ^{1}H-NMR spectral data (Fig. 1) supported a $C_{12}H_{14}O_4$ molecular formula. Analysis of chemical shift and coupling data suggested a structure consistent with an isovalerate ester and a *para*-benzoquinone (*14*). The primary alcohol of *p*-benzoquinone is gentisyl alcohol, and the corresponding quinone is gentisyl quinone (fig. S2). Thus, gentisyl quinone isovalerate was proposed as the structure for the pheromone compound (Fig. 1, inset). Because this is a

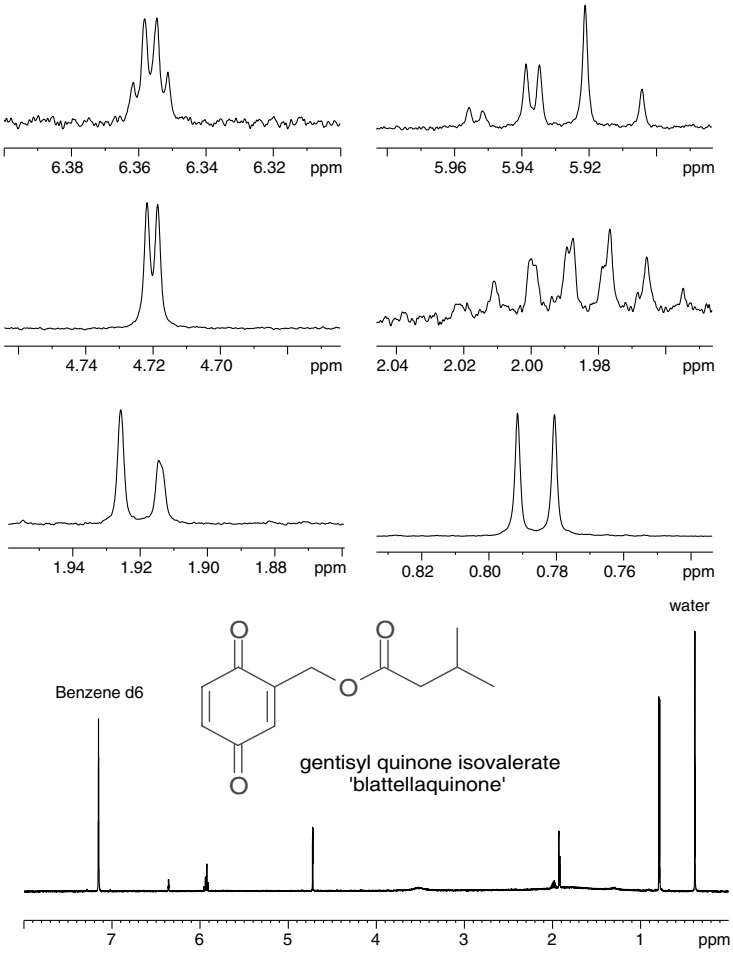

Fig. 1. The 600-MHz ^{1}H-NMR spectrum of the natural pheromone purified by preparative GC. The inset shows the chemical structure of blattellaquinone.

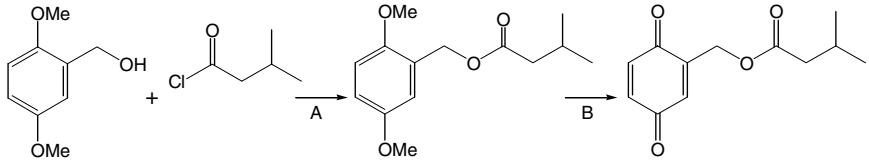

Fig. 2. Scheme for the synthesis of blattellaquinone. Acylation (A) involved addition of isovaleryl chloride to a solution of 2,5-dimethoxybenzyl alcohol, pyridine, and DMAP in CH_2Cl_2. Excess acid chloride was removed with saturated sodium bicarbonate, and the mixture was extracted with ether, washed with brine, and dried over anhydrous sodium sulfate. The crude ester in acetonitrile was oxidized (B) by adding a solution of $Ce(NH_4)_2(NO_3)_6$ in water. The mixture was extracted with CH_2Cl_2 and redissolved in ether; aqueous sodium bicarbonate was then added, and the ether extract was washed with brine and dried over anhydrous sodium sulfate. See (*14*) for more details.

previously unknown compound, and there are no recorded chemical shifts of gentisyl quinone esters in deuterobenzene, proof of structure was dependent on chemical synthesis (Fig. 2). The NMR spectrum of the synthetic compound (fig. S3) was found to be identical to that of the natural pheromone (fig. S2). We propose the common name "blattellaquinone" for this pheromone.

The biological activity of synthetic blattellaquinone was compared to that of a crude extract of virgin females in behavioral assays using two-choice olfactometers (*14*). Males exhibited a clear dose-response to the synthetic pheromone (Fig. 3). More than 60% of the males responded within 1 min by running toward 10 to 100 ng of the pheromone loaded on a filter paper disk. Responding males ran up the olfactometer within 16.4 ± 2.7 s (10 ng) and 8.9 ± 2.2 s (100 ng) of the introduction of the pheromone. When making a choice between 100 pg of synthetic blattellaquinone and a solvent control, 93.8 ± 6.2% of 53 responding males chose the pheromone. This is similar to the percentage of males (92.5 ± 2.1% of 244 males) that chose the crude dichloromethane extract of one virgin female over a solvent control. However, at high doses (10 and 100 μg), we observed that many males became disoriented as they approached the pheromone, and only 52.3 ± 7.2% (of 55 responsive males) and 68.6 ± 9.6% (of 53 responsive males), respectively, chose the pheromone. These observations suggest that precise doses and careful formulations will be required to optimize the efficiency of this pheromone in pest control.

Field tests of blattellaquinone were performed in a cockroach-infested pig farm. Whereas nymphs and adult females did not respond at any dose of the pheromone between 0 and 1 mg, adult males exhibited a clear dose-response in their behavioral attraction to pheromone-baited traps (Fig. 4). These results confirm that blattellaquinone is a female sex pheromone of *B. germanica* that specifically attracts conspecific males.

Substituted benzoquinone compounds are ubiquitous animal and plant excretions and are most commonly used as defensive secretions and feeding deterrents (*15*). Quinone-containing defensive compounds have been identified in some cockroaches (*16*). It is possible, therefore, that blattellaquinone also served a defensive function in *B. germanica* and was co-opted to play a role in sexual communication, as have some other multifunctional semiochemicals (e.g., cuticular hydrocarbons serve in waterproofing as well as in sexual and nestmate recognition in some insects). Our preliminary observation that only nanogram amounts of this compound are stored by females suggests, however, that blattellaquinone probably no longer functions in defense. It will be important to determine whether this compound occurs in immature cockroaches and in adult males, although organic solvent extracts of these stages fail to attract males (*9*).

The identification of blattellaquinone as the sex pheromone of *B. germanica* culminates a long and arduous search for a volatile attractant in this important pest species. It now offers new options in cockroach population control and allergen mitigation.

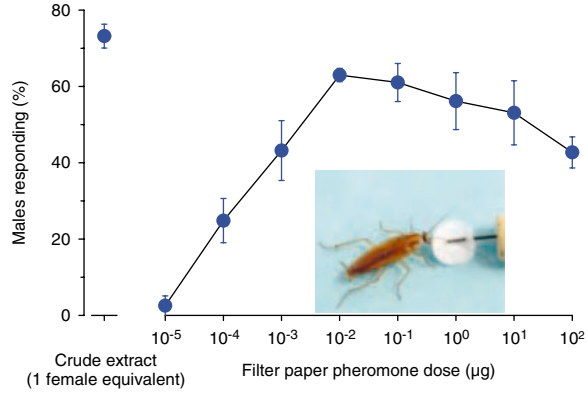

Fig. 3. Behavioral responses of male *B. germanica* to one female equivalent of a crude dichloromethane extract and to various doses of blattellaquinone. The pheromone was applied in 5 μl of dichloromethane to a filter paper disk and presented to single males acclimated in the two-choice olfactometer versus a dichloromethane-treated control filter paper disk. Behavioral response is defined as quiescent males that were stimulated to run out of their cages within 60 s. Each assay block consisted of testing 10 to 16 males in individual olfactometers and means ± SEM were calculated from 3 to 18 blocks of assays. The inset shows a male German cockroach responding to blattellaquinone emanating from a filter paper disk.

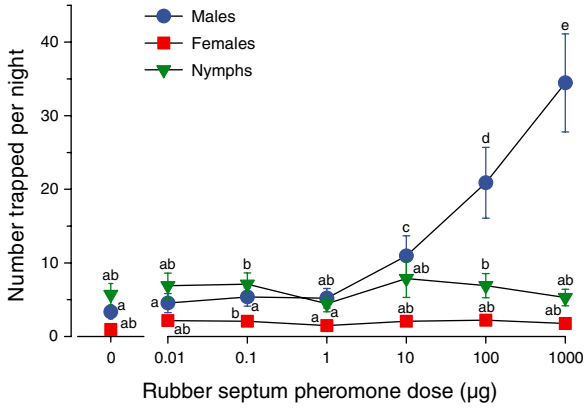

Fig. 4. Trap catches of *B. germanica* using various doses of the synthetic pheromone, blattellaquinone. The pheromone was applied in 50 μl of dichloromethane to a 5-mm sleeve-type rubber septum, which was hung inside a 1-pint (~470 ml) wide-mouth mason jar whose inside wall was treated with a thin layer of petroleum jelly (to prevent trapped cockroaches from escaping). Seven treatments were placed in a completely randomized Latin square design along five walls of a cockroach-infested pig farm, and treatments were rotated daily so that all positions along the wall received all seven treatments over seven consecutive nights (i.e., 35 replicates per dose). Data were log-transformed and analyzed by multiway analysis of variance, followed by Fisher's least significant difference mean separation (*17*). An independent trial (not shown) extended the dose-response using three treatments (0, 1, and 10 mg) along seven walls (21 replicates per dose); there were no significant differences between 1- and 10-mg doses.

References and Notes

1. R. J. Brenner, in *Understanding and Controlling the German Cockroach*, M. K. Rust, J. M. Owens, D. A. Reierson, Eds. (Oxford Univ. Press, New York, 1995), pp. 77–92.
2. L. Zurek, C. Schal, *Vet. Microbiol.* **101**, 263 (2004).
3. D. L. Rosenstreich *et al.*, *N. Engl. J. Med.* **336**, 1356 (1997).
4. S. J. Arbes Jr. *et al.*, *J. Allergy Clin. Immunol.* **112**, 339 (2003).
5. S. J. Arbes Jr. *et al.*, *J. Allergy Clin. Immunol.* **113**, 109 (2004).
6. R. McConnell *et al.*, *Ann. Allergy Asthma Immunol.* **91**, 546 (2003).
7. C. Schal, R. H. Hamilton, *Annu. Rev. Entomol.* **35**, 521 (1990).
8. R. Nishida, H. Fukami, *Mem. Coll. Agric. Kyoto Univ.* **122**, 1 (1983).
9. D. Liang, C. Schal, *Experientia* **49**, 324 (1993).
10. D. Liang, C. Schal, *Tissue Cell* **25**, 763 (1993).
11. D. Liang, C. Schal, *J. Insect Behav.* **6**, 603 (1993).
12. D. Liang, C. Schal, *J. Insect Physiol.* **40**, 251 (1994).
13. S. Nojima, D. J. Kiemle, F. X. Webster, W. L. Roelofs, *J. Chem. Ecol.* **30**, 2153 (2004).
14. Materials and methods are available as supporting material on *Science* Online.
15. T. Eisner, C. Rossini, A. Gonzalez, M. Eisner, *J. Exp. Biol.* **207**, 1313 (2004).
16. R. Brossut, *J. Chem. Ecol.* **9**, 143 (1983).
17. SAS Institute Inc., Cary, North Carolina (2000).

18. This research was supported in part by the Blanton J. Whitmire Endowment, the W. M. Keck Center for Behavioral Biology at North Carolina State University, and grants from NSF (IBN-9817075), U.S. Department of Agriculture–National Research Initiative Competitive Grants Program (2002-02633 and 2004-01118), and S. C. Johnson Wax. We thank previous workers who tackled this difficult problem in our labs, especially D. Liang, A. Zhang, and C. Gemeno, and J. Sun who expertly reared, sorted, dissected, and extracted thousands of cockroaches. We also thank D. Kiemle for help with MS and NMR and R. Tang for assistance with the chemical synthesis.

Supporting Online Material

www.sciencemag.org/cgi/content/full/307/5712/1104/DC1
Materials and Methods
Figs. S1 to S3
References and Notes

5 November 2004; accepted 27 December 2004
10.1126/science.1107163

Chronic Lymphocytic Inflammation Specifies the Organ Tropism of Prions

Mathias Heikenwalder,[1]* Nicolas Zeller,[1]* Harald Seeger,[1]* Marco Prinz,[1]*† Peter-Christian Klöhn,[2] Petra Schwarz,[1] Nancy H. Ruddle,[3] Charles Weissmann,[2] Adriano Aguzzi[1]‡

Prions typically accumulate in nervous and lymphoid tissues. Because pro-inflammatory cytokines and immune cells are required for lymphoid prion replication, we tested whether inflammatory conditions affect prion pathogenesis. We administered prions to mice with five inflammatory diseases of the kidney, pancreas, or liver. In all cases, chronic lymphocytic inflammation enabled prion accumulation in otherwise prion-free organs. Inflammatory foci consistently correlated with lymphotoxin up-regulation and ectopic induction of FDC-M1$^+$ cells expressing the normal cellular prion protein PrP^C. By contrast, inflamed organs of mice lacking lymphotoxin-α or its receptor did not accumulate the abnormal isoform PrP^{Sc}, nor did they display infectivity upon prion inoculation. By expanding the tissue distribution of prions, chronic inflammatory conditions may act as modifiers of natural and iatrogenic prion transmission.

Prions, the infectious agent in transmissible spongiform encephalopathies that selectively damage the central nervous system (CNS), are detectable in lymphoid organs long before clinical symptoms appear (*1*). PrP^{Sc}, a protease-resistant isoform of the host protein PrP^C, accumulates mostly in the CNS and lymphoid organs of infected organisms and may represent the infectious principle (*2*, *3*). In addition to PrP^C (*4*), splenic prion replication requires follicular dendritic cells (FDCs) (*5*), whose maintenance depends on B cells expressing tumor necrosis factor (TNF) and lymphotoxins (LTs) α and β (*6*–*8*). Accordingly, inhibition of LT and TNF antagonizes peripheral prion replication (*9*–*11*). However, most cellular requirements for peripheral prion replication remain unknown (*12*).

Chronic inflammatory conditions are accompanied by organized collections of B and T lymphocytes, FDCs, dendritic cells (DCs), and marginal zone and tingible body macrophages (*13*–*15*). Extranodal follicles are also prevalent in naturally occurring infections of free-ranging ruminants (*16*). Besides participating in chronic inflammatory conditions, FDCs, B lymphocytes, and other components of the immune system are involved in prion replication (*6*–*10*, *17*). We therefore reasoned that inflammation may affect prion pathogenesis. We studied this question in various transgenic and spontaneous mouse models of chronic inflammation, including nephritis, pancreatitis, and hepatitis.

[1]Institute of Neuropathology, University Hospital of Zürich, CH-8091 Zürich, Switzerland. [2]Medical Research Council Prion Unit, Department of Neurodegenerative Diseases, Institute of Neurology, Queen Square, London WC1N 3BG, UK. [3]Department of Epidemiology and Public Health and Section of Immunobiology, Yale University School of Medicine, New Haven, CT 06520, USA.

*These authors contributed equally to this work.
†Present address: Institute of Neuropathology, Georg-August-Universität, D-37073 Göttingen, Germany.
‡To whom correspondence should be addressed. E-mail: adriano@pathol.unizh.ch

First, we generated bitransgenic mice expressing LTα and LTβ in liver under the control of the albumin promoter (fig. S1A) (*18*, *19*). C57BL/6-Tg(LTab)1222 and C57BL/6-Tg(LTab)1223 mouse lines contained one copy per haploid genome of both AlbLTα and AlbLTβ transgenes (fig. S1B), with expression restricted to liver and absent from spleen, thymus, mesenteric lymph nodes, pancreas, and kidney (Fig. 1A). C57BL/6-Tg(LTab)1223 mice (henceforth termed AlbLTαβ mice) were identified as the highest expressors (Fig. 1B) and were selected for further experiments.

Livers from 4- to 6-month-old AlbLTαβ mice displayed highly organized aggregates of B220$^+$ B lymphocytes; CD3$^+$, CD4$^+$, and CD8$^+$ T cells; FDC-M1$^+$ and CD35$^+$ networks; MOMA-1$^+$ marginal zone–like festoons; CD68$^+$ tingible body macrophages; IgD$^+$ and IgG1$^+$ lymphocytes; ERTR9$^+$ cells; and NLDC-145$^+$ DCs (Fig. 2) (fig. S1C). AlbLTαβ sinusoids exhibited F4/80$^+$ Kupffer cell hyperproliferation and up-regulation of the adhesion molecules I-CAM and V-CAM (fig. S1C). Occasionally, PNA$^+$ clusters indicative of germinal center B cells were found (fig. S1C, arrowheads). None of the above features were found in livers of wild-type littermates (fig. S1C), nor could we detect abnormal histopathological features in AlbLTαβ kidneys, spleens, and thymuses.

Transgenic mice expressing LTα under the control of the rat insulin promoter (RIP) in pancreatic β islet cells and renal proxi-

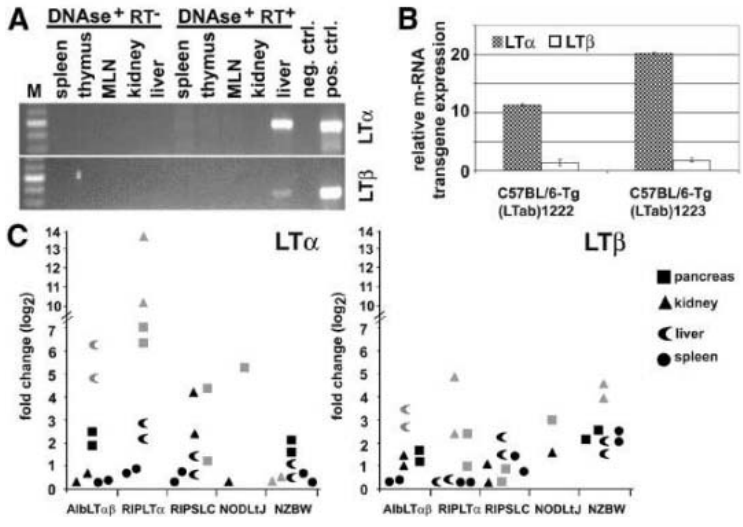

Fig. 1. Molecular and phenotypic characterization of AlbLTαβ mice. (**A**) RT-PCR analysis, using primers 1 and 2 (450 bp) for transgenic LTα and primers 4 and 5 for transgenic LTβ (390 bp) (see fig. S1A), confirmed liver-specific transgene expression in AlbLTαβ mice [negative control, master mix and H_2O; positive control, transgenic plasmid DNA (10 ng)]. (**B**) Transgene-specific real-time RT-PCR analysis identifying C57BL/6-Tg(LTab)1222 as low LTα expressor and C57BL/6-Tg(LTab)1223 as high expressor. (**C**) Real-time RT-PCR identifying total LTα and LTβ expression in organs of mice with naturally occurring or transgenetically induced inflammatory and autoimmune diseases. Each value represents the fold change (log_2) in individual organs relative to the average expression in two respective organs of control mice of the appropriate genotype. Each measurement was normalized against β-actin and expressed as fold change (log_2) relative to the wild type. Gray and black symbols denote inflamed and noninflamed organs, respectively. LTα and/or LTβ were overexpressed not only in LT transgenic organs but also in inflamed organs of RIPSLC, NZBW, and NODLtJ mice.

mal convoluted tubules (*20–22*) developed interstitial and capsular follicles in kidney and pancreatic islets with discrete $B220^+$ areas and $CD35^+$/FDC-$M1^+$ networks (*20*, *21*) (Fig. 2A). Renal and pancreatic inflammatory foci in RIPLTα and hepatic foci in AlbLTαβ mice were essentially identical in their cellular composition and expressed various complement components (Fig. 2) (fig. S1D). The splenic and lymph nodal microarchitectures of RIPLTα (n = 5), AlbLTαβ (n = 3), and wild-type mice (n = 3) were indistinguishable upon immunostaining with an exhaustive panel of immunological markers (*23*).

We then studied mice expressing the secondary lymphoid organ chemokine (SLC), also known as TCA4/CCL21, under the control of the rat insulin promoter (*22*). These mice (henceforth termed RIPSLC) contain follicles in the pancreas with organized T and B cell zones, DCs, ER-$TR7^+$ and $CD35^+$ cells, and small FDC-$M1^+$ networks (Fig. 2) (*23*).

NZBxNZW-F_1 (henceforth termed NZBW) and NODLtJ mice are considered models for systemic lupus erythematosus and autoimmune diabetes, respectively. NZBW mice develop interstitial nephritis and glomerulonephritis with distinct B and T cell areas, small FDC-$M1^+$ clusters, DCs, small PNA^+ clusters, and $IgG1^+$ cells (Fig. 2) (fig. S1E). Infiltrates lacked MAdCAM-1^+ expression but contained MOMA-1^+ cells (fig. S1E). Deposits of complement components C1q, C3, and C4 were identified within glomeruli of kidneys of NZBW mice, but not in parental NZW mice, which did not develop nephritis and were used as controls (Fig. 2) (fig. S1E) (*23*). NODLtJ mice develop spontaneous autoimmune insulitis with lymphoid follicles similar to those developing in NZBW kidneys (*24–26*); NODB10.H2b mice, which do not develop insulitis despite the presence of the NOD locus (*27*), were used as controls.

Real-time reverse transcription polymerase chain reaction (RT-PCR) analysis of LTα and LTβ expression in inflamed and appropriate control tissues revealed that 6- to 8-week-old AlbLTαβ livers overexpressed LTα by a factor of ~45 and LTβ by a factor of 8 to 10 (Fig. 1C). LT expression declined in 8- to 12-month-old transgenic mice, in parallel with hepatocyte destruction. No other organs of AlbLTαβ mice showed LT overexpression. RIPLTα mice overexpressed LTα and, to a lower extent, LTβ in kidney and pancreas, whereas RIPSLC mice had slightly up-regulated LTα expression in pancreas and kidney. LTα and LTβ were strongly up-regulated in NODLtJ pancreases, and LTβ was overexpressed in NZBW kidneys and pancreases. In summary, we detected LT up-regulation in every instance of chronic inflammation.

RIPLTα, RIPSLC, NZBW, NODLtJ, and isogenic or congenic control mice were inoculated with prions intraperitoneally [10^3 times the median lethal dose (3 $logLD_{50}$)] or intracerebrally (2.5 $logLD_{50}$). RIPLTα, RIPSLC, and control mice showed similar incubation times and attack rates of disease (Fig. 3A), and the extent of terminal PrP^{Sc} deposition was similar (fig. S2, A and B). The topography and intensity of spongiosis, gliosis, and PrP deposits were found by immunohistochemistry to be similar in the brains of all terminally sick mice (*23*). Thus, chronic pancreatitis or nephritis did not influence susceptibility to intracerebrally or peripherally administered prions, nor did these conditions affect prion titers or neuroinvasion speed. Scrapie incubation times of NZBW and NODLtJ mice could not be determined because they exceeded their natural life span. The extent and morphology of inflammation in RIPLTα and RIPSLC kidneys and pancreases, as well as in AlbLTαβ livers, were compared with age-matched mock-infected controls at several time points from 60 days post inoculation (dpi) to terminal disease. We did not detect any modulation of the inflammatory pathologies by prion infection, and intraperitoneal glucose tolerance was unaltered in prion-inoculated RIPLTα mice (fig. S2C).

We then sought to determine whether inflammation influences the distribution of prion infectivity during the preclinical phase of infection. AlbLTαβ, RIPLTα, RIPSLC, NZBW, NZW (8 to 12 weeks old), NODLtJ, NODB10 (6 months old), and C57BL/6 mice were inoculated intraperitoneally with scrapie prions (5 $logLD_{50}$) and killed at 60, 75, 90, or 100 dpi. Spleen homogenates were assayed for prion infectivity by mouse bioassay (MBA), consisting of intracerebral inoculation of *tga20* indicator mice (*28*) and comparison of scrapie incubation times to a calibration curve (*29*). All spleens displayed comparably high titers of prion infectivity per gram of tissue: 4.5 to 6 $logLD_{50}$/g (wild type), 3.5 to 5 $logLD_{50}$/g (RIPLTα), 4.2 to 6.1 $logLD_{50}$/g (AlbLTαβ), and 3.9 to 5.7 $logLD_{50}$/g (RIPSLC). Attack rates of indicator mice were 100% at all time

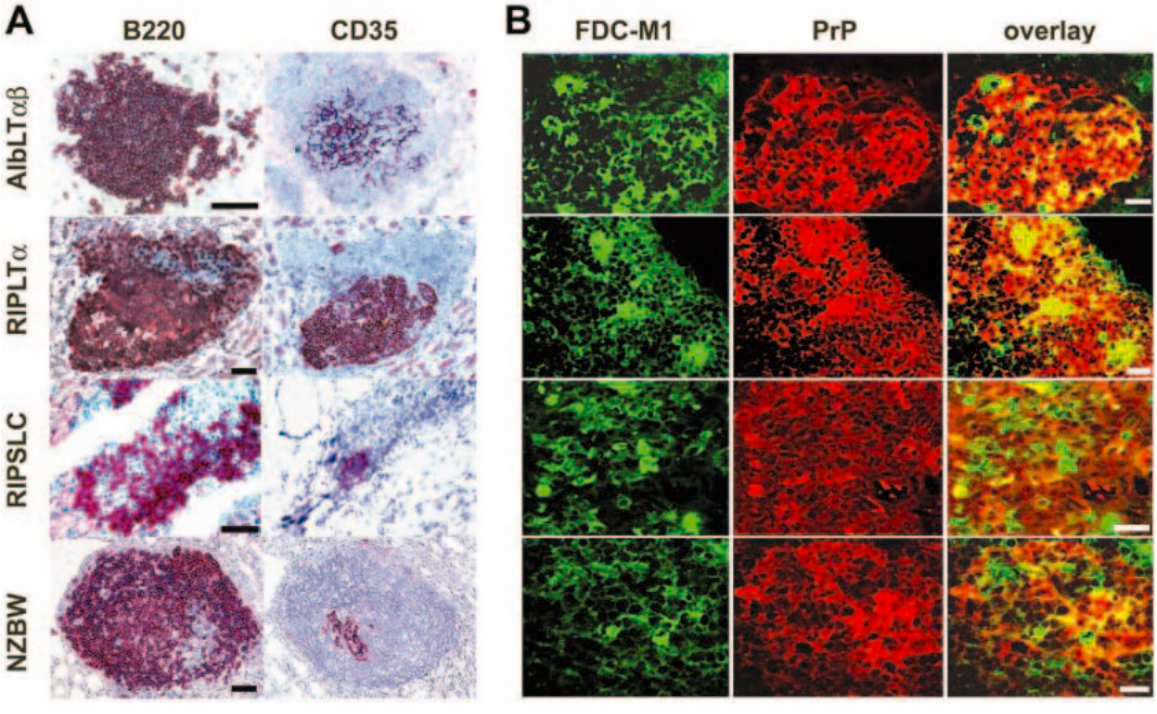

Fig. 2. Inflammatory foci in AlbLTαβ livers, RIPLTα kidneys, and NZBW and RIPSLC pancreases. Consecutive frozen sections of AlbLTαβ liver, RIPSLC pancreas, and RIPLTα and NZBW kidneys are shown. (**A**) Follicular inflammatory foci displaying organized collections of B cells (B220) and complement receptor 1–expressing cells (CD35). Scale bar, 200 μm. (**B**) Two-color immunofluorescence analysis. PrP (antiserum XN, red) mainly colocalizes with FDC networks (antibody FDC-M1, green) within follicular infiltrates in all models of follicular inflammation. Scale bar, 20 μm.

points (Fig. 3B). Nephritis and pancreatitis did not affect splenic prion replication.

Prion loads of kidneys, pancreases, and livers from prion-infected presymptomatic mice were also determined by MBA (Fig. 3B). Titers were regarded as "borderline" if attack rates were <100%. At 60 dpi, wild-type pancreas and kidney homogenates lacked measurable infectivity, whereas RIPLTα kidney and pancreas titers ranged between borderline and 1.4 $\log LD_{50}$/g. At 75 dpi, RIPLTα pancreas and kidney titers were 3.3 and 4 $\log LD_{50}$/g, respectively, whereas wild-type pancreases and kidneys were noninfectious.

At 90 dpi, all RIPSLC and RIPLTα pancreases and one RIPLTα kidney had prion titers approaching those of spleens (≤3.7 $\log LD_{50}$/g in pancreas and ≤2.4 $\log LD_{50}$/g in kidney), whereas wild-type organs displayed undetectable or borderline infectivity (Fig. 3B). Infectivity of wild-type livers, kidneys, and AlbLTαβ kidneys was borderline or below detectability, whereas AlbLTαβ livers had titers of 3.1 to 3.4 $\log LD_{50}$/g (Fig. 3B). NZBW kidneys were found to contain prion titers of 2.5 to 3.5 $\log LD_{50}$/g (n = 2), whereas NZW kidneys were noninfectious (Fig. 3C).

We subjected organ extracts to scrapie cell assays in end point format (SCEPA) or to conventional scrapie cell assays (SCA), which allow for quantification of prion infectivity with sensitivity similar to MBAs (*30*). SCEPA and MBA results with RIPLTα kidney and pancreas homogenates (60 and 90 dpi) were almost completely congruent (fig. S2D and table S1). Wild-type kidneys and pancreases contained no detectable infectivity (<2.54 $\log LD_{50}$/g), whereas prion titers in the corresponding RIPLTα extracts were high (table S1). AlbLTαβ liver prion titers (75 dpi) were >3.4 $\log LD_{50}$/g in all three liver homogenates, whereas no infectivity was detected in wild-type livers (<2.4 $\log LD_{50}$/g) (fig. S2E).

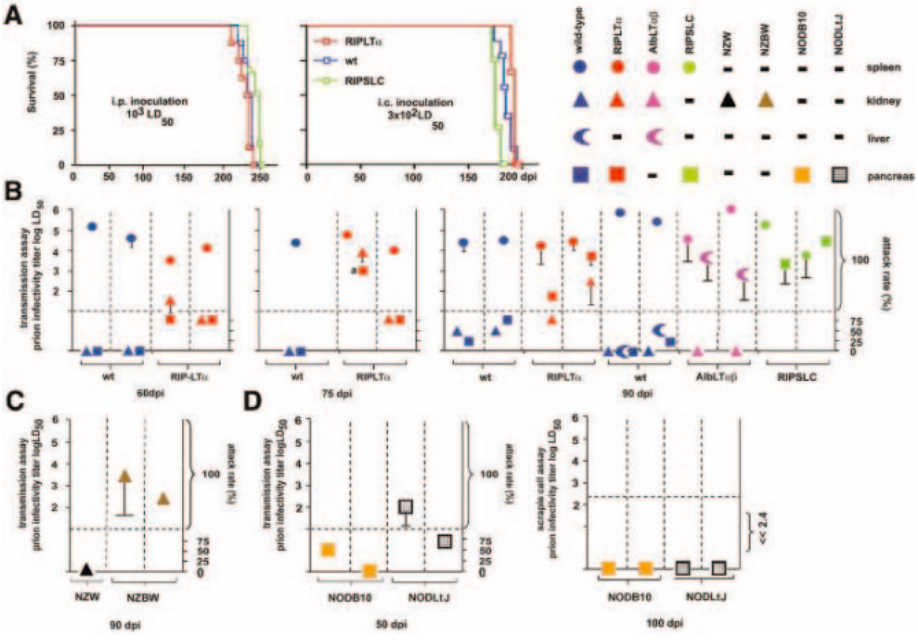

Fig. 3. The distribution of PrP^{Sc} and prion infectivity is influenced by inflammatory conditions. (**A**) Survival plots of prion-infected RIPLTα, RIPSLC, and wild-type (wt) mice, showing similar incubation times after intraperitoneal (i.p.; RIPLTα, 229 ± 10 days; wt, 234 ± 6 days; RIPSLC, 243 ± 8 days) or intracerebral inoculation (i.c.; RIPLTα, 192 ± 2 days; wt, 185 ± 6 days; RIPSLC, 174 ± 2 days). (**B**) Prion infectivity titers in spleens (circles), pancreases (squares), kidneys (triangles), and livers (crescents) of wild-type (wt) (blue), RIPLTα (red), AlbLTαβ (pink), and RIPSLC (green) mice were determined by transmission to indicator mice at 60, 75, and 90 dpi. Each column defined by vertical dashed lines represents one mouse. Data points below the dashed horizontal line indicate attack rates of <100% and were regarded as "borderline" infectivity. Error bars were drawn when standard deviation exceeded 0.75 log units. Except for one RIPLTα kidney that elicited an attack rate of 75%, RIPLTα kidneys and pancreases, RIPSLC pancreases, and AlbLTαβ livers led to an attack rate of 100% with high prion titers at 90 dpi. In contrast, wild-type kidneys, pancreases, and livers contained undetectable or at best borderline prion infectivity. ([a]) One of four *tga20* mice died shortly after inoculation from prion-unrelated causes. (**C** and **D**) Prion infectivity titers in kidneys (triangles) of NZW (black) and NZBW (brown) mice and in pancreases (squares) of NODB10 (orange) and NODLtJ (striped) mice were determined by transmission assay or SCEPA. At 90 dpi, NZBW kidneys harbored reasonably high infectivity titers, whereas NZW mice lacked prion infectivity (**C**). At 50 dpi, NODLtJ mice displayed borderline or moderate prion infectivity, whereas NODB10 mice showed no or borderline infectivity. At 100 dpi, NODLtJ mice were devoid of detectable prion infectivity, consistent with progressive islet elimination and consecutive regression of pancreatitis (D) (*23*).

We then administered scrapie prions (5 $\log LD_{50}$) intraperitoneally to 6-month-old NODLtJ mice and NODB10 mice. Pancreases of hyperglycemic NODLtJ mice contained prion titers of ≤2 $\log LD_{50}$/g at 50 dpi, whereas control NODB10 mice harbored no or borderline infectivity (Fig. 3D). All *tga20* mice (n = 7) that had developed clinical scrapie upon exposure to pancreas homogenates (50 dpi) displayed spongiosis, gliosis, and PrP^{Sc} in immunoblots (figs. S3 and S4), confirming transmission of scrapie infectivity. Similarly, all *tga20* mice that had developed clinical scrapie upon exposure to kidney, pancreas, and liver homogenates (AlbLTαβ, RIPLTα, RIPSLC, and NZBW) showed spongiosis, gliosis, and PrP^{Sc} in immunoblots (figs. S3 and S4), confirming transmission of infectivity. However, at 100 dpi (~10 months of age), pancreatic infectivity was no longer detectable in either genotype, consistent with progressive islet elimination and consecutive regression of pancreatitis in NODLtJ mice (Fig. 3D) (*23*).

We then determined PrP^{Sc} loads in organ extracts. Samples negative by conventional immunoblotting were reanalyzed after phosphotungstate (PTA) precipitation of PrP^{Sc} (*31*), enhancing sensitivity (*32*). At 60, 75, and 90 dpi, PrP^{Sc} was detectable in similar amounts in all spleens of each genotype, but not in livers, kidneys, or pancreases of wild-type mice (Fig. 4, A and B). At 60 dpi, PrP^{Sc} was undetectable in livers, kidneys, or pancreases of any genotype. At 75 dpi, we found robust PrP^{Sc} immunoreactivity in two of three AlbLTαβ livers, but not in RIPLTα kidneys and pancreases (Fig. 4A). At 90 dpi, PrP^{Sc} was readily detectable in all AlbLTαβ livers (Fig. 4A), RIPLTα kidneys, and RIPLTα pancreases (n = 6, Fig. 4B). Possible PrP^{Sc} traces were found in one wild-type kidney at 90 dpi (fig. S2F).

PTA-enhanced immunoblot analysis identified PrP^{Sc} in NZBW (n = 2) but not in NZW (n = 2) kidneys (90 dpi) (Fig. 4C) (*23*). In contrast, PTA-enhanced immunoblotting failed to reveal PrP^{Sc} in NODLtJ and NODB10 pancreases at all time points (50 and 100 dpi), consistent with the low infectivity titers of NODLtJ pancreases at 50 dpi (Fig. 3D).

By what mechanism does inflammation create novel prion reservoirs? PrP^{C} is necessary for prion replication (*4*), hence its expression might be rate-limiting. We thus investigated PrP^{C} expression in wild-type and RIPLTα kidneys and pancreases. Quantitative immunoblot analysis revealed ≤20% increase in total PrP^{C} of RIPLTα kidneys, and no changes were seen in transgenic pancreases (fig. S1F). In contrast, immunohistochemical analysis revealed foci of high PrP expression in all analyzed AlbLTαβ livers, RIPLTα kidneys and pancreases, RIPSLC pancreases, NZBW kidneys, and NODLtJ pancreases (Fig. 2B), but not in

organs of the appropriate control mice. These foci mostly colocalized with FDC-M1$^+$ networks (Fig. 2B).

To characterize the topography of PrP^{Sc} in inflamed prion-infected organs, we assayed (*33*) wild-type, RIPLTα, NZBW, and NZW kidneys as well as RIPSLC pancreases by histoblotting. RIPLTα kidneys and pancreases (90 dpi) displayed PrP^{Sc} deposits colocalizing with inflammatory infiltrates, whereas neither feature was found in scrapie-infected wild-type kidneys or pancreases (Fig. 4D). RIPSLC pancreases and NZBW kidneys (90 dpi) also showed small PrP^{Sc}-positive areas colocalizing with inflammatory infiltrates, whereas controls were devoid of PrP^{Sc}-positive areas (*23*).

Inflammatory conditions cause immune cells to migrate into parenchymal sites of pathology. Some of these immune cells—including activated B lymphocytes—express LTs, which in turn trigger differentiation of FDCs. LT-triggered events, most likely including PrP^C up-regulation in stromal FDC precursors, appear to confer prion replication competence to sites of inflammation. LT might thus represent a crucial link between inflammation and prion distribution. We tested this prediction by administering prions intraperitoneally to 6- to 8-month-old LTα$^{-/-}$ and LTβR$^{-/-}$ mice, which suffer from spontaneous inflammatory pathologies (*34*), and to age-matched controls. Despite severe multifocal chronic lymphocytic hepatitis with disseminated PNA$^+$ clusters (fig. S5, A and B), livers of prion-inoculated LTα$^{-/-}$ and LTβR$^{-/-}$ mice were found to be consistently devoid of prion infectivity (fig. S5C) and PrP^{Sc} (fig. S5D).

Our results indicate that chronic follicular inflammation, induced by a variety of causes, specifies prion tropism for otherwise prion-free organs. In most instances infectivity tended to rise with time, suggesting local prion replication. Organ-specific expression of one single proinflammatory cytokine (LTα) or chemokine (SLC) sufficed to establish unexpected prion reservoirs, suggesting differentiation of ubiquitous stromal constituents into prion replication–competent cells. In several instances, prion concentration in individual inflamed organs approached that of spleen long before any clinical manifestation of scrapie. Inflamed nonlymphoid organs not only accumulated PrP^{Sc} but also transmitted bona fide prion disease when inoculated into healthy recipient mice.

Knowledge of the distribution of prions within infected hosts is fundamental to consumer protection and prevention of iatrogenic accidents. On the basis of the failure to transmit bovine spongiform encephalopathy (BSE) infectivity from any tissue but central nervous system, intestinal, and lymphoid tissue (*35*), the risk to humans of contracting prion infection from other organs has been deemed small even in countries with endemic BSE. It may be important now to test whether superimposed viral, microbial, or autoimmune pathologies of farm animals trigger unexpected shifts in the organ tropism of prions. Conversely, the lack of infectivity in "burned-out" postinflammatory pancreases suggests that anti-inflammatory regimens may abolish ectopic prion reservoirs.

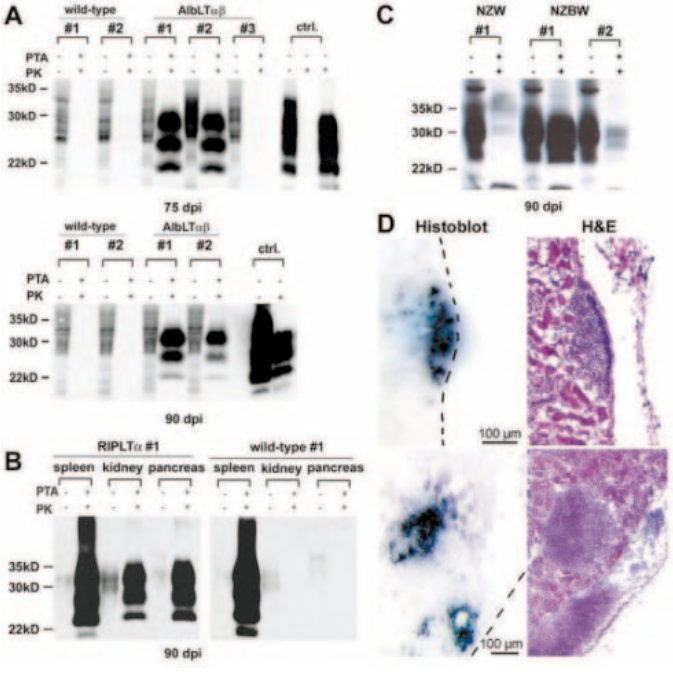

Fig. 4. PrP^{Sc} accumulates in inflamed organs of prion-infected mice. (**A**) Immunoblot analysis of liver homogenates after PTA precipitation at 75 dpi (upper blot) and 90 dpi (lower blot). PrP^{Sc} was absent in all four individual wild-type livers, but clear PrP^{Sc} signal was seen in four of five AlbLTαβ livers. Control samples (ctrl.) included undigested healthy brain, proteinase K (PK)–digested healthy brain, and PK-digested terminally scrapie-sick brain. PTA, sodium phosphotungstate precipitation. (**B**) Immunoblot analysis showed strong PrP^{Sc} signal in spleen, kidney, and pancreas of prion-infected RIPLTα mice (90 dpi), whereas PrP^{Sc} was confined to spleens of wild-type mice. (**C**) Immunoblot of NZBW and NZW mice. PrP^{Sc} was detected in kidneys of NZBW but not NZW mice. (**D**) Histoblot analysis of prion-infected kidneys. Capsular and subcapsular deposits of PrP^{Sc} colocalize with follicular infiltrates in RIPLTα kidneys. Consecutive sections display colocalization of PrP^{Sc} deposits with follicular infiltrates [hematoxylin and eosin (H&E) stain].

References and Notes

1. H. Fraser, A. G. Dickinson, *Nature* **226**, 462 (1970).
2. S. B. Prusiner, *Science* **216**, 136 (1982).
3. G. Legname *et al.*, *Science* **305**, 673 (2004).
4. H. R. Büeler *et al.*, *Cell* **73**, 1339 (1993).
5. M. Gonzalez, F. Mackay, J. L. Browning, M. H. Kosco-Vilbois, R. J. Noelle, *J. Exp. Med.* **187**, 997 (1998).
6. T. Kitamoto, T. Muramoto, S. Mohri, K. Dohura, J. Tateishi, *J. Virol.* **65**, 6292 (1991).
7. K. L. Brown *et al.*, *Nature Med.* **5**, 1308 (1999).
8. M. Prinz *et al.*, *Nature* **425**, 957 (2003).
9. F. Montrasio *et al.*, *Science* **288**, 1257 (2000).
10. N. A. Mabbott, G. McGovern, M. Jeffrey, M. E. Bruce, *J. Virol.* **76**, 5131 (2002).
11. M. Prinz *et al.*, *Proc. Natl. Acad. Sci. U.S.A.* **99**, 919 (2002).
12. A. Aguzzi, *Nature Cell Biol.* **6**, 290 (2004).
13. S. Takemura *et al.*, *J. Immunol.* **167**, 1072 (2001).
14. E. Kaiserling, *Lymphology* **34**, 22 (2001).
15. J. C. Hogg *et al.*, *N. Engl. J. Med.* **350**, 2645 (2004).
16. W. Vernau, R. M. Jacobs, V. E. Valli, J. L. Heeney, *Vet. Pathol.* **34**, 222 (1997).
17. M. A. Klein *et al.*, *Nature Med.* **7**, 488 (2001).
18. R. Magliozzi, S. Columba-Cabezas, B. Serafini, F. Aloisi, *J. Neuroimmunol.* **148**, 11 (2004).
19. See supporting data on *Science* Online.
20. D. E. Picarella, A. Kratz, C. B. Li, N. H. Ruddle, R. A. Flavell, *Proc. Natl. Acad. Sci. U.S.A.* **89**, 10036 (1992).
21. A. Kratz, A. Campos-Neto, M. S. Hanson, N. H. Ruddle, *J. Exp. Med.* **183**, 1461 (1996).
22. L. Fan, C. R. Reilly, Y. Luo, M. E. Dorf, D. Lo, *J. Immunol.* **164**, 3955 (2000).
23. M. Heikenwalder *et al.*, data not shown.
24. A. Hanninen *et al.*, *J. Clin. Invest.* **92**, 2509 (1993).
25. T. L. Delovitch, B. Singh, *Immunity* **7**, 727 (1997).
26. C. Faveeuw, M. C. Gagnerault, F. Lepault, *J. Immunol.* **152**, 5969 (1994).
27. C. P. Robinson *et al.*, *Arthritis Rheum.* **41**, 150 (1998).
28. M. Fischer *et al.*, *EMBO J.* **15**, 1255 (1996).
29. S. B. Prusiner *et al.*, *Ann. Neurol.* **11**, 353 (1982).
30. P. C. Klohn, L. Stoltze, E. Flechsig, M. Enari, C. Weissmann, *Proc. Natl. Acad. Sci. U.S.A.* **100**, 11666 (2003).
31. J. Safar *et al.*, *Nature Med.* **4**, 1157 (1998).
32. J. D. F. Wadsworth *et al.*, *Lancet* **358**, 171 (2001).
33. A. Taraboulos *et al.*, *Proc. Natl. Acad. Sci. U.S.A.* **89**, 7620 (1992).
34. A. Futterer, K. Mink, A. Luz, M. H. Kosco-Vilbois, K. Pfeffer, *Immunity* **9**, 59 (1998).
35. G. A. Wells *et al.*, *Vet. Rec.* **142**, 103 (1998).

36. We thank S. Nedospasov and D. Kuprash for LTα/β cDNA; D. Lo for Ins-TCA4/SLC mice; C. Sigurdson, G. Miele, M. Zabel, F. Montrasio, and M. Le Hir for discussions; A. Gaspert and W. Jochum for histopathological advice; and B. Odermatt, R. Moos, and G. Bosshard for support with immunohistochemistry and SCA. Supported by grants from the Bundesamt für Bildung und Wissenschaft, the Swiss National Science Foundation, and the National Center of Competence in Research (NCCR) on Neural Plasticity and Repair (A.A.); by the foundation for research at the Medical Faculty, University of Zürich, a generous educational grant of the Catello family, and a grant of the Verein zur Förderung des Akademischen Nachwuchses (M.H.); by the Medical Research Council, UK (P.-C.K. and C.W.); and by NIH grant NCI R01 CA 16885 (N.H.R.).

Supporting Online Material

www.sciencemag.org/cgi/content/full/1106460/DC1
Materials and Methods
Figs. S1 to S5
Table S1
References

18 October 2004; accepted 6 December 2004
Published online 20 January 2005;
10.1126/science.1106460
Include this information when citing this paper.

Positional Signaling Mediated by a Receptor-like Kinase in *Arabidopsis*

Su-Hwan Kwak, Ronglai Shen, John Schiefelbein*

The position-dependent specification of root epidermal cells in *Arabidopsis* provides an elegant paradigm for cell patterning during development. Here, we describe a new gene, *SCRAMBLED* (*SCM*), required for cells to appropriately interpret their location within the developing root epidermis. *SCM* encodes a receptor-like kinase protein with a predicted extracellular domain of six leucine-rich repeats and an intracellular serine-threonine kinase domain. SCM regulates the expression of the *GLABRA2*, *CAPRICE*, *WEREWOLF*, and *ENHANCER OF GLABRA3* transcription factor genes that define the cell fates. Further, the *SCM* gene is expressed throughout the developing root. Therefore, SCM likely enables developing epidermal cells to detect positional cues and establish an appropriate cell-type pattern.

A fundamental feature of development in multicellular organisms is the specification of distinct cell types in appropriate patterns. In *Arabidopsis*, the patterning of the root-hair cells and non–hair cells in the root epidermis is determined by a position-dependent mechanism (*1*, *2*). Developing epidermal cells overlying two cortical cells (the "H" cell position) preferentially differentiate as root-hair cells, whereas cells located outside a single cortical cell (the "N" position) adopt the non–hair cell fate. Both symplastic (e.g., direct cell-cell movement) and apoplastic (e.g., receptor-mediated cell-cell interaction) explanations have been proposed for the putative signaling mechanism (*3*, *4*).

A regulatory network including at least eight putative transcription factors is required to specify the root epidermal cell types through the general mechanism of lateral inhibition with feedback [reviewed in (*3*–*5*)]. WEREWOLF (WER, a MYB transcription factor), TRANSPARENT TESTA GLABRA (TTG, a WD40-repeat protein), and GLABRA3 and ENHANCER OF GLABRA3 (GL3 and EGL3, related bHLH transcription factors) appear to act in a central transcriptional complex in the N cells to promote the non–hair cell fate and mediate lateral inhibition. One of the likely targets of this complex is *GLABRA2* (*GL2*), which encodes a homeodomain transcription factor required for non–hair cell differentiation (*6*). TTG/GL3/EGL3/WER also positively regulate the *CAPRICE* (*CPC*) gene, which encodes a small one-repeat MYB protein that may mediate lateral inhibition by moving to the adjacent H cells and inhibiting the action of the WER MYB (*7*, *8*).

Department of Molecular, Cellular, and Developmental Biology, University of Michigan, Ann Arbor, MI 48109–1048, USA.

*To whom correspondence should be addressed. E-mail: schiefel@umich.edu

Although much of the transcriptional machinery used to define the two cell types is known, no information is currently available concerning the molecular basis of the positional signaling mechanism that regulates this transcriptional network. To identify mutants defective in position-dependent patterning of the root epidermal cell types, we conducted a new genetic screen based on visual examination of cell-type–specific reporter expression in mutagenized seedling roots. We reasoned that a defect in the production or perception of positional cues would not necessarily lead to a change in hair density, and therefore might require direct examination of cell pattern to detect. The *GL2*-promoter β-glucuronidase (GUS) fusion (*GL2::GUS*) was chosen as the reporter because it is expressed in the developing non–hair cells, which generates roots with easily visible "stripes" (or files) of GUS activity (*6*) (Fig. 1, A and B). An ethylmethane sulfonate–mutagenized population of the *GL2::GUS* line was generated (in the WS ecotype), and seedlings were screened for changes in GUS activity pattern within M2 families, as a result of the destructive nature of the GUS assay. One family segregated a recessive mutation that caused a patchy or "scrambled" distribution of *GL2::GUS*-expressing cells in the root epidermis (Fig. 1, A and B). Because the mutation causes a disorganized *GL2::GUS* pattern, the novel gene affected in this line was named *SCRAMBLED* (*SCM*).

Despite the strong effect of *scm-1* on the pattern of *GL2::GUS* expression, *scm-1* did not show a detectable effect on root-hair density (Fig. 1C). To determine whether the position-dependent patterning of root epidermal cell types is altered, we analyzed the arrangement of mature root-hair and non–hair cell types in *scm-1*. In wild-type roots, most cells (92%) in the H position are root-hair cells, and nearly all cells (99%) in the N position are non–hair cells (table S1). In the *scm-1* roots, only 66% of cells in the H position are root-hair cells, and 79% of cells in the N position are non–hair cells (table S1). This shows that a functional *SCM* gene is required for proper position-dependent cell-type patterning.

Because epidermal cell fate is correlated with the cortical cell arrangement, we tested the possibility that the defective cell patterning in the *scm* mutant is due to an abnormality in root structure. However, examination of wild-type and *scm* mutant roots revealed no significant differences in the cortical cell number [all roots examined ($N > 8$ for each line) possessed eight cortical cell files] or the organization of the root tissues (Fig. 1B), which indicates that the *scm* mutations do not significantly affect root structure.

We cloned the *SCM* gene by a genetic map–based strategy. Several genes within a 55-kb interval near the top of *Arabidopsis* chromosome 1 were sequenced, and we identified a single base substitution in *scm-1* that generates a premature stop codon at amino acid 324 in the putative coding region of the *At1g11130* gene (Fig. 1D). This gene encodes a predicted leucine-rich repeat receptor-like protein kinase (LRR-RLK). No biological function has been reported or assigned to this gene/protein. DNA fragments from this gene region were introduced into *scm-1 GL2::GUS* mutant plants, and an 8.4-kb fragment containing only *At1g11130* sequences was found to restore the normal *GL2::GUS* expression pattern (Fig. 1, D and E).

The deduced SCM protein is 768 amino acids and possesses all the structural features of a typical LRR-RLK (Fig. 1G), of which there are more than 200 predicted in *Arabidopsis* (*9*). The N terminus contains a hydrophobic sequence predicted to act as a signal sequence for secretion, followed by the putative extracellular domain, which includes six tandem copies of a 24-residue leucine-rich repeat (LRR; residues 85 to 231). LRRs are found in diverse eukaryotic proteins and typically participate in protein-protein interactions (e.g., ligand binding and/or receptor dimerization) (*10*). A single predicted transmembrane domain is near the center of SCM (amino acids 342 to 362), and the C terminus contains a putative intracellular kinase domain that possesses most of the signature sequences for a serine-threonine protein kinase (amino acids 496 to 764) (*11*) (fig. S1).

A second *scm* mutant (*scm-2*) was obtained from the Salk Institute Genomic Analysis Laboratory collection (*12*). We verified that *scm-2* has a transferred DNA (T-DNA) insertion within the third intron of the *SCM* gene (Fig. 1D). This *scm-2* mutant has an altered pattern of epidermal cell types similar to *scm-1* (table S1), which provides additional support for the important role of the *SCM*/*At1g11130* gene in epidermal patterning.

Northern blot analysis showed that *SCM* RNA is present in the roots and shoots of wild-type seedlings, although no obvious shoot phenotype was observed in the *scm* seedlings (Fig. 1F). The *SCM* RNA is substantially reduced in *scm-1* and undetectable in *scm-2* (Fig. 1F). Because *scm-2* affects the *SCM* transcript at an earlier point than *scm-1* (Fig. 1D) and lacks detectable *SCM* mRNA (Fig. 1F), it was used as the *scm* reference mutant for our subsequent analyses.

To further define the role of the SCM receptor-like kinase, we analyzed the effect of *scm-2* on the expression of several transcription-factor genes in the specification pathway. In independent experiments, the non–hair-cell–expressing *GL2::GUS*, *CPC::GUS*, and *WER::GFP* promoter-reporter transgenes were introduced into the *scm-2* by crossing. In each line, we found a disorganized pattern of reporter gene expression (Fig. 1E and Fig. 2, A to C). We quantified these effects and discovered that, in each line, *scm-2* significantly reduces the frequency of H cells that lack reporter expression and the frequency of N cells that express each reporter (table S2). To determine whether SCM affects the expression pattern of *GL2*, *CPC*, and *WER* independently or coordinately, we generated a *scm-2* line that possessed both the *GL2::GUS* and *WER::GFP*, and we assayed both reporters in the same roots. We discovered a clear correlation between GUS-expressing cells and GFP-expressing cells in this line (Fig. 2C), implying that the SCM receptor affects the expression of both genes in a similar way in the same cells. We also examined the role of SCM on a hair-cell–expressing transcription-factor reporter, *EGL3::GUS*, and we observed a similar disorganized pattern of GUS expression in the *scm-2 EGL3::GUS* root epidermis (Fig. 2D). Together, these results show that the SCM receptor is required for position-dependent transcription of both non–hair-cell and hair-cell regulators, which indicates that it acts in an upstream signaling pathway to influence the entire cell-fate transcriptional network.

To further examine the importance of the SCM receptor during root epidermis development, we evaluated the relative cell-division rate in the H and N positions of the *scm-2* mutant. In wild-type roots, cells in the H position have ~30% greater cell-division rate than the developing N cells (*13*). We discovered that the *scm-2* mutant has a significant reduction in the relative division rate in the H and N positions (relative H/N cell-division rate: Col wild-type, 1.35 ± 0.01; *scm-2*, 1.18 ± 0.02). Together with our other findings, this indicates that SCM acts at an early stage of root epidermal development and affects all known cell characteristics.

The SCM receptor may mediate patterning by enabling epidermal cells to detect an asymmetrically distributed positional cue or by being differentially expressed in the H or N cell positions. To address this issue, we analyzed *SCM* gene expression during root epidermis development, using in situ RNA hybridization and promoter-reporter gene fusion experiments. In the wild-type roots, we observed a strong antisense *SCM* hybridization signal throughout the developing root, especially within and near the meristem initials, but not in the root cap (Fig. 3A). Transverse sections showed that, in the epidermis, the *SCM* antisense probe hybridized to cells in

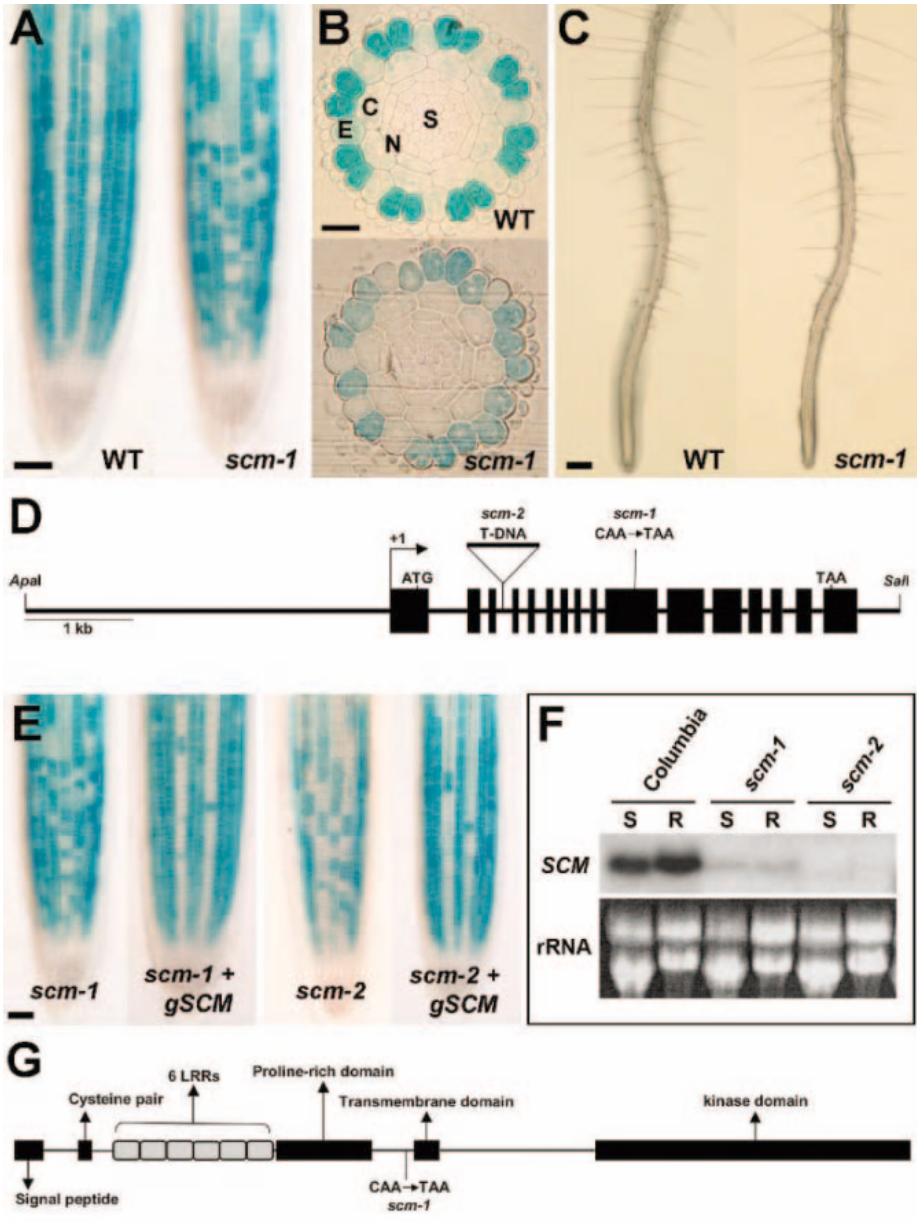

Fig. 1. Identification and cloning of the *SCM* gene. (**A**) Expression of the *GL2::GUS* reporter gene during root development. Four-day-old seedlings were histochemically assayed for GUS activity. The *scm-1* mutation disturbs the normal file-specific *GL2* expression pattern. Root hairs are not visible in this developmental region; they form on cells above the field of view in these photos. Scale bar, 50 μm. (**B**) Spatial expression of the *GL2::GUS* reporter gene in transverse root sections. Plastic sections were taken from the meristematic region of wild-type and *scm-1* seedling roots harboring the *GL2::GUS* transgene. E, epidermis; C, cortex; N, endodermis; S, stele. Scale bar, 25 μm. (**C**) Seedling-root phenotype of wild-type and *scm-1* mutant plants. Scale bar, 200 μm. (**D**) The intron and exon organization of the *SCM* locus. The positions of the *scm-1* and *scm-2* mutations and the 8.4-kb complementing ApaI-SalI fragment are shown. (**E**) Complementation of the *scm* mutant phenotype. Expression of the *GL2::GUS* reporter gene during root development in the *scm-1* and *scm-2* mutants and in transgenic lines harboring the 8.4-kb *SCM* genomic fragment (*gSCM*). Scale bar, 50 μm. (**F**) Northern blot with total RNA from shoots (S) and roots (R) of 4-day-old wild type, *scm-1*, and *scm-2* mutants hybridized with a *SCM* probe. The rRNA levels were used as loading controls. (**G**) Domain organization of the predicted SCM LRR-RLK protein.

both the H and the N cell position (Fig. 3B). For the reporter-gene experiments, we fused the 5′ and 3′ *SCM* genomic sequences from the complementing *SCM* fragment to the coding region of the *GUS* or *GFP* reporters. Similar to the in situ hybridization results, the *SCM::GUS* and *SCM::GFP* reporters were expressed throughout the developing root tissues, including epidermal cells, in the meristematic region (Fig. 3, C and D). Together, these results show that *SCM* gene expression and mRNA accumulation occurs at the time when position signaling is acting, and it is not confined to a particular type of epidermal cell.

These results expand our understanding of the establishment of the position-dependent pattern of root epidermal cell types. It is likely that, at an early stage in epidermal development, positional cues from underlying root cells are distributed in a nonuniform manner to differentially activate the SCM receptor in the N and H cells and that, after signal transduction, this leads to a difference in the expression of the cell-fate transcription factors in these cells. Because the WER MYB controls the expression of all other known transcription factors, including *GL2* and *CPC* (*4*, *14*), the *WER* gene is an attractive candidate for the primary target of this SCM signaling pathway. The SCM-mediated difference in transcription-factor gene expression is likely to be amplified and stabilized by the known lateral-feedback loops (*4*) and to lead to the establishment of distinct gene expression patterns and cell fates.

Together with previous findings, this work shows that two different cell signaling mechanisms are employed during root epidermis development. One of these (described here) uses a putative plasma membrane–bound receptor kinase, SCM, to enable epidermal cells to perceive extracellular positional cues, and may be analogous to the kind of receptor-mediated mechanisms that help metazoan cells make their developmental decisions (*15*). The other previously identified signaling mechanism acts later and uses the mobile transcription factor, CPC, which likely moves directly from cell to cell by means of plasmodesmata to mediate lateral inhibition (*7*). Thus, a distinct combination of apoplastic and symplastic signaling appears to specify the root epidermis cell fates in *Arabidopsis*.

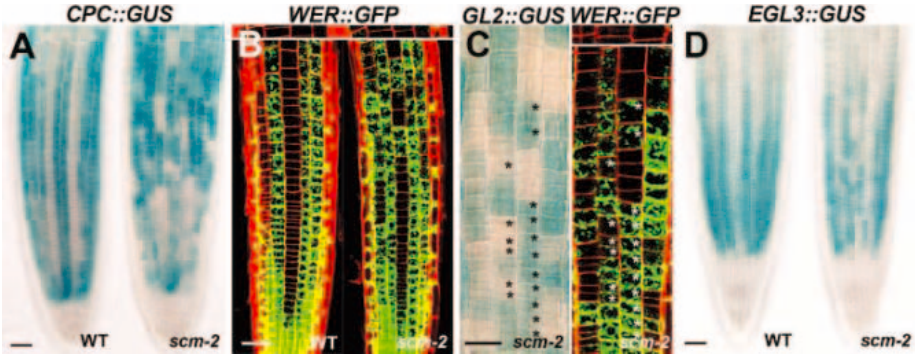

Fig. 2. SCM is required for position-dependent gene expression. (**A**) Expression of the *CPC::GUS* reporter gene in wild-type and *scm-2* seedling roots. Scale bar, 50 μm. (**B**) Expression of the *WER::GFP* reporter gene in wild-type and *scm-2* seedling roots. Propidium iodide (red) was included to visualize cell boundaries. The upper inset shows the relative positions of the underlying cortical cells. Scale bar, 50 μm. (**C**) Expression of the *GL2::GUS* and *WER::GFP* reporter genes in a single *scm-2* seedling root. The root was first examined for GFP expression and then was assayed for GUS activity. Asterisks mark ectopic reporter-expressing cells and ectopic reporter-nonexpressing cells. Scale bar, 50 μm. (**D**) Expression of the *EGL3::GUS* reporter gene in wild-type and *scm-2* seedling roots. Scale bar, 50 μm.

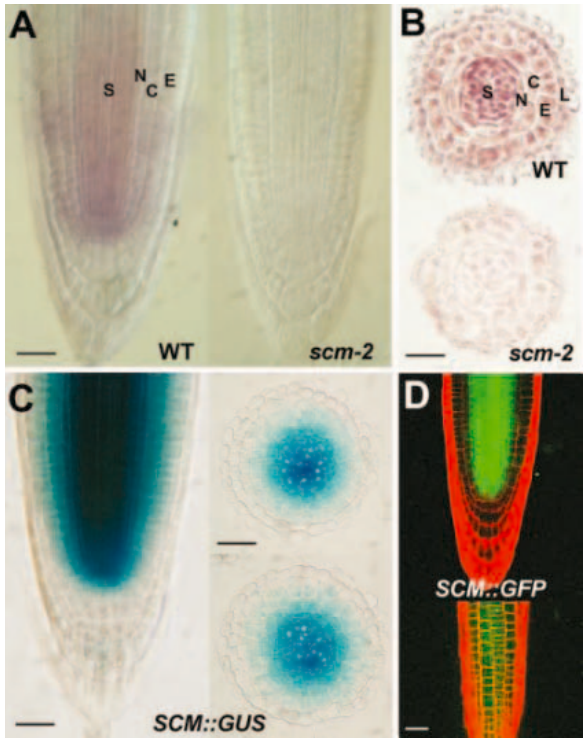

Fig. 3. Expression of *SCM* gene in the developing *Arabidopsis* root. (**A**) Whole-mount in situ RNA hybridization of *SCM* mRNA in wild-type and *scm-2* mutant (negative control) seedling root tips. Roots were exposed to a digoxigenin-labeled *SCM* antisense RNA probe. In a separate experiment, a *SCM* sense RNA probe was used and no signal was detected on wild-type roots (data not shown). S, stele; N, endodermis; C, cortex; E, epidermis. Scale bar, 25 μm. (**B**) Transverse sections of wild-type and *scm-2* mutant roots from the meristematic region of 4-day-old seedlings exposed to a digoxigenin-labeled antisense RNA probe. S, stele; N, endodermis; C, cortex; E, epidermis; L, lateral root cap. Scale bar, 25 μm. (**C**) Expression of *SCM::GUS* promoter-reporter gene fusion in the wild-type seedling root tip. Left panel contains longitudinal view; right panels contain transverse sections at two different developmental stages showing GUS activity in epidermal layer. Scale bar, 25 μm. (**D**) Expression of *SCM::GFP* promoter-reporter gene fusion in the wild-type seedling root tip. Upper panel contains optical section from median longitudinal view; lower panel contains optical section of the overlying epidermal layer alone, showing GFP accumulation in the epidermal cells. Scale bar, 25 μm.

References and Notes

1. L. Dolan *et al.*, *Development* **120**, 2465 (1994).
2. M. E. Galway *et al.*, *Dev. Biol.* **166**, 740 (1994).
3. B. Scheres, *Curr. Biol.* **12**, R804 (2002).
4. J. C. Larkin, M. L. Brown, J. Schiefelbein, *Annu. Rev. Plant Physiol. Plant Mol. Biol.* **54**, 403 (2003).
5. J. Schiefelbein, *Curr. Opin. Plant Biol.* **6**, 74 (2003).
6. J. D. Masucci *et al.*, *Development* **122**, 1253 (1996).
7. T. Wada *et al.*, *Development* **129**, 5409 (2002).
8. T. Wada, T. Tachibana, Y. Shimura, K. Okada, *Science* **277**, 1113 (1997).
9. S. H. Shiu, A. B. Bleecker, *Proc. Natl. Acad. Sci. U.S.A.* **98**, 10763 (2001).
10. B. Kobe, A. V. Kajava, *Curr. Opin. Struct. Biol.* **11**, 725 (2001).
11. S. K. Hanks, A. M. Quinn, *Methods Enzymol.* **200**, 38 (1991).
12. J. M. Alonso *et al.*, *Science* **301**, 653 (2003).
13. F. Berger, C. Y. Hung, L. Dolan, J. Schiefelbein, *Dev. Biol.* **194**, 235 (1998).
14. M. M. Lee, J. Schiefelbein, *Cell* **99**, 473 (1999).
15. M. Freeman, J. B. Gurdon, *Annu. Rev. Cell Dev. Biol.* **18**, 515 (2002).
16. We thank M. M. Lee for technical assistance and helpful discussions, J. Fuzak and C.-Y. Hung for assistance, and Y. Lin, M. Simon, C. Bernhardt, S. Clark, and J. Li for helpful discussions. We acknowledge the Salk Institute Genomic Analysis Laboratory and the Arabidopsis Biological Resource Center (Columbus, OH) for providing the *scm-2* line. This work was supported by the Post-doctoral Fellowship Program of Korea Science and Engineering Foundation (KOSEF) (S.-H.K.) and by a grant from the NSF (IBN-0316312).

Supporting Online Material
www.sciencemag.org/cgi/content/full/1105373/DC1
Materials and Methods
Fig. S1
Tables S1 and S2
References

17 September 2004; accepted 14 December 2004
Published online 23 December 2004;
10.1126/science.1105373
Include this information when citing this paper.

Proliferation of Functional Hair Cells in Vivo in the Absence of the Retinoblastoma Protein

Cyrille Sage,[1] Mingqian Huang,[1] Kambiz Karimi,[2] Gabriel Gutierrez,[3] Melissa A. Vollrath,[4] Duan-Sun Zhang,[4] Jaime García-Añoveros,[5] Philip W. Hinds,[3] Jeffrey T. Corwin,[2] David P. Corey,[4] Zheng-Yi Chen[1]*

In mammals, hair cell loss causes irreversible hearing and balance impairment because hair cells are terminally differentiated and do not regenerate spontaneously. By profiling gene expression in developing mouse vestibular organs, we identified the retinoblastoma protein (pRb) as a candidate regulator of cell cycle exit in hair cells. Differentiated and functional mouse hair cells with a targeted deletion of *Rb1* undergo mitosis, divide, and cycle, yet continue to become highly differentiated and functional. Moreover, acute loss of *Rb1* in postnatal hair cells caused cell cycle reentry. Manipulation of the pRb pathway may ultimately lead to mammalian hair cell regeneration.

In fish, amphibians, and birds, regeneration of sensory hair cells through asymmetric cell divisions of supporting cells can contribute to recovery of hearing and balance after hair cell loss caused by trauma or toxicity (*1*, *2*). Mammalian hair cells do not spontaneously regenerate, even though supporting cells in vestibular sensory epithelia retain a limited ability to divide (*3*, *4*). Consequently, hair cell death in mammals often leads to permanent impairment of hearing and balance.

As the inner ear develops, hair cell progenitor cells exit from the cell cycle and, like neurons, terminally differentiate. Negative cell cycle regulators apparently maintain the postmitotic status of hair cells and contribute to their terminal differentiation. The cyclin-dependent kinase inhibitors p27Kip1 and p19Ink4d participate in cell cycle exit of hair cell progenitors and in hair cell apoptosis, respectively (*5*, *6*). However, the key regulators of cell cycle exit and concomitant hair cell terminal differentiation remain elusive.

The retinoblastoma protein pRb, encoded by the retinoblastoma gene *Rb1*, functions in cell cycle exit, differentiation, and survival (*7*, *8*). pRb is a member of the pocket protein family, which includes p107 (encoded by *Rbl1*) and p130 (encoded by *Rbl2*). Like pRb, p107 and p130 cause cell cycle arrest when overexpressed (*9*).

Germline pRb$^{-/-}$ animals die in utero around embryonic day (E) 13.5, with severe defects in lens development, hematopoiesis, myogenesis, osteogenesis, and neurogenesis (*7*, *10*–*12*). In both the central and peripheral nervous systems, neurons undergo ectopic mitoses and subsequent apoptosis (*11*, *13*). Mice with *Rb1* conditionally deleted in the central nervous system show an increase in neuronal number due to aberrant S phase entry, without apoptosis (*14*–*16*). However, it

[1]Neurology Service, MGH-HMS Center for Nervous System Repair, Massachusetts General Hospital and Harvard Medical School, Boston, MA 02114, USA. [2]Department of Neuroscience, University of Virginia School of Medicine, Charlottesville, VA 22908, USA. [3]Radiation Oncology, Molecular Oncology Research Institute, Tufts-New England Medical Center, Boston, MA 02111, USA. [4]Howard Hughes Medical Institute and Department of Neurobiology, Harvard Medical School, Boston, MA 02115, USA. [5]Departments of Anesthesiology, Physiology, and Neurology, Northwestern University Institute for Neuroscience, Chicago, IL 60611, USA.

*To whom correspondence should be addressed. E-mail: zhengyi@helix.mgh.harvard.edu

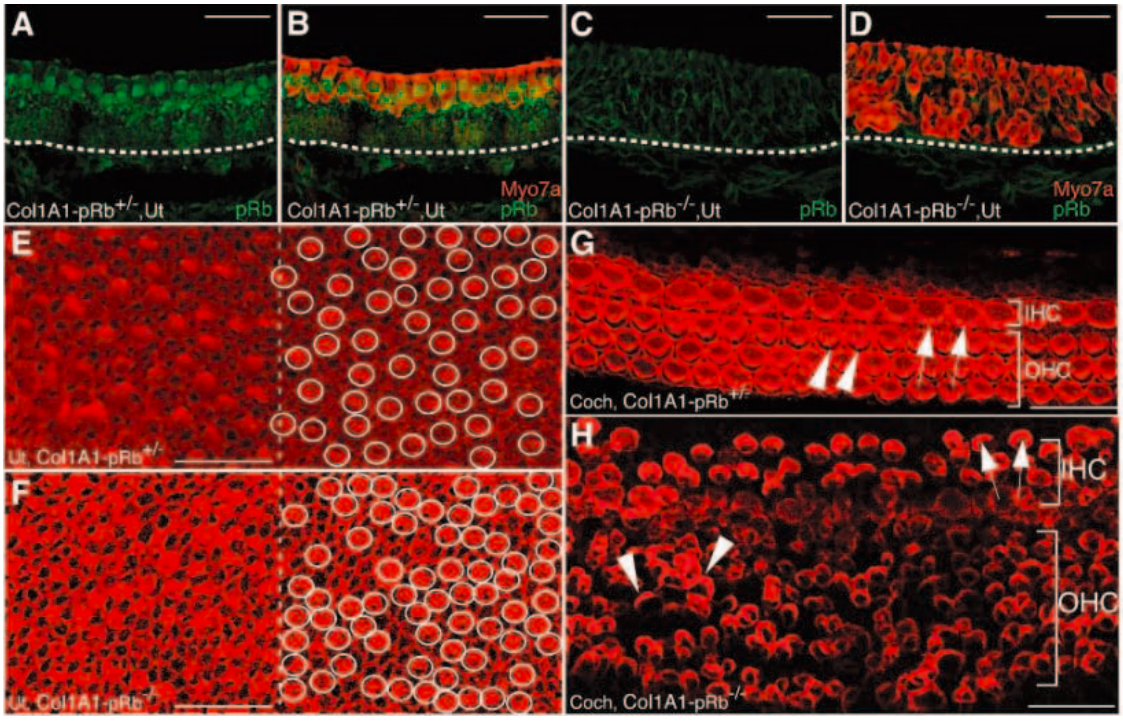

Fig. 1. Expression of *Rb1* in the inner ear and increased hair cell numbers in Col1A1-pRb$^{-/-}$ mice. (**A** and **B**) An antibody to pRb primarily stained hair cells in an E18.5 control utricle; an antibody to myosin-7a (Myo7a) marked hair cells. (**C** and **D**) pRb was absent in an E18.5 Col1A1-pRb$^{-/-}$ utricle; note multiple-layer hair cells in Col1A1-pRb$^{-/-}$ utricle. Dashed lines show basal lamina. (**E** to **H**) Confocal images of rhodamine phalloidin-labeled hair bundles in the E18.5 utricular macula [(E) and (F)] and midturn of the cochlea [(G) and (H)]. The distribution of hair cells in the Col1A1-pRb$^{-/-}$ utricle was abnormal, as indicated by clustered hair bundles [circles in (F)], in contrast to the normal mosaic pattern in the control (E). In the cochlea, inner hair cells (arrows) and outer hair cells (arrowheads) remained separated by pillar cells, which do not have hair bundles. Uniform orientation of the hair bundles was altered in Col1A1-pRb$^{-/-}$ cochlear hair cells (H). Ut, utricle; Coch, cochlea; IHC, inner hair cell; OHC, outer hair cell. Scale bars, 25 μm.

is not clear whether these supernumerary neurons are highly differentiated or functional.

To identify molecules involved in cell cycle regulation during hair cell development, we studied gene expression in the developing mouse utricle, a balance organ of the inner ear, with the use of oligonucleotide microarrays. We noticed that retinoblastoma family members show a suggestive pattern: From E14.5 to postnatal day (P) 12, *Rb1* expression was constant, *Rbl1* showed down-regulation, and *Rbl2* exhibited up-regulation (*17*). An antibody to pRb weakly labeled all cells in the E12.5 otocyst (fig. S1A), and labeling was prominent in all hair cells from embryo to adult (fig. S1, B to F). Therefore, pRb could be required to suppress cell division in hair cells.

Because germline pRb$^{-/-}$ mice die around E13.5 (*10*), when hair cells are extremely immature, we studied a conditional pRb knockout. Mice with loxP sites flanking exon 19 of the *Rb1* gene (*Rb1*^{loxp}) (*18*) were crossed with mice carrying *cre* under the control of the 3.6-kb collagen 1A1 (Col1A1) promoter, which express *cre* recombinase in a pattern similar to endogenous Col1A1 (*19*). Because these pRb conditional knockout mice (Col1A1-pRb$^{-/-}$) die perinatally, we studied embryos. By in situ hybridization, Col1A1 was detected ubiquitously in the E11.5 otocyst but later reduced in hair cells and supporting cells (fig. S2). In Col1A1-pRb$^{-/-}$ inner ears, pRb was undetectable in the sensory epithelium (Fig. 1, C and D).

If pRb regulates cell cycle exit in hair cells, its loss might permit cell cycle reentry and increase hair cell numbers. We tested this hypothesis by counting cells with hair bundles in E18.5 Col1A1-pRb$^{-/-}$ utricles. Relative to littermate controls, Col1A1-pRb$^{-/-}$ utricles had 40% more cells with bundles [Col1A1-pRb$^{-/-}$: 1406 ± 73 (mean ± SD), $N = 3$; Col1A1-pRb$^{+/-}$: 987 ± 62, $N = 5$; $P < 0.05$] (Fig. 1, E and F). A greater increase in hair bundle number was observed in cochleas. Whereas littermate controls had one row of inner hair cells and three rows of outer hair cells, Col1A1-pRb$^{-/-}$ cochleas had three or four rows of inner hair cells and seven or eight rows of outer hair cells. Most Col1A1-pRb$^{-/-}$ cochlear hair cells had bundles, but many were not properly oriented (Fig. 1, G and H).

The increase in hair cell number in Col1A1-pRb$^{-/-}$ ears suggested that new hair cells arose through an increase in differentiation-competent progenitor cells and/or through continuing hair cell division. To study progenitor cell proliferation, we injected E13.5 pregnant mice with 5-bromo-2′-deoxyuridine (BrdU) 4 hours before embryo harvest. In the primordial organ of Corti, the p27Kip1-positive "zone of nonproliferating cells" (ZPNC) harbors postmitotic sensory precursor cells (*20*). We found BrdU-positive cells in the p27Kip1-positive region of Col1A1-pRb$^{-/-}$ mice (Fig. 2N) but not in controls (Fig. 2M). Therefore, pRb is involved in cell cycle exit of sensory progenitor cells.

To test hair cell proliferation specifically, we injected E16.5 pregnant mothers with BrdU and harvested embryos at E18.5. During normal development, mouse hair cells become postmitotic as early as E12.5 (*21*). As expected, no hair cells or cochlear supporting cells were BrdU-positive in control mice (Fig. 2, I and K). In contrast, many hair cells and cochlear supporting cells were BrdU-positive in Col1A1-pRb$^{-/-}$ mice, indicating that they had entered S phase (Fig. 2, J and L). BrdU labeling in hair cells tended to be weaker than in supporting cells, which suggests that the hair cells had further divided, diluting the BrdU (84% of hair cells were weakly labeled versus 58% of supporting cells, with "weak" considered less than half the level of the brightest supporting cells). We also observed an increased ratio of outer hair cells to Deiters' cells, suggesting contin-

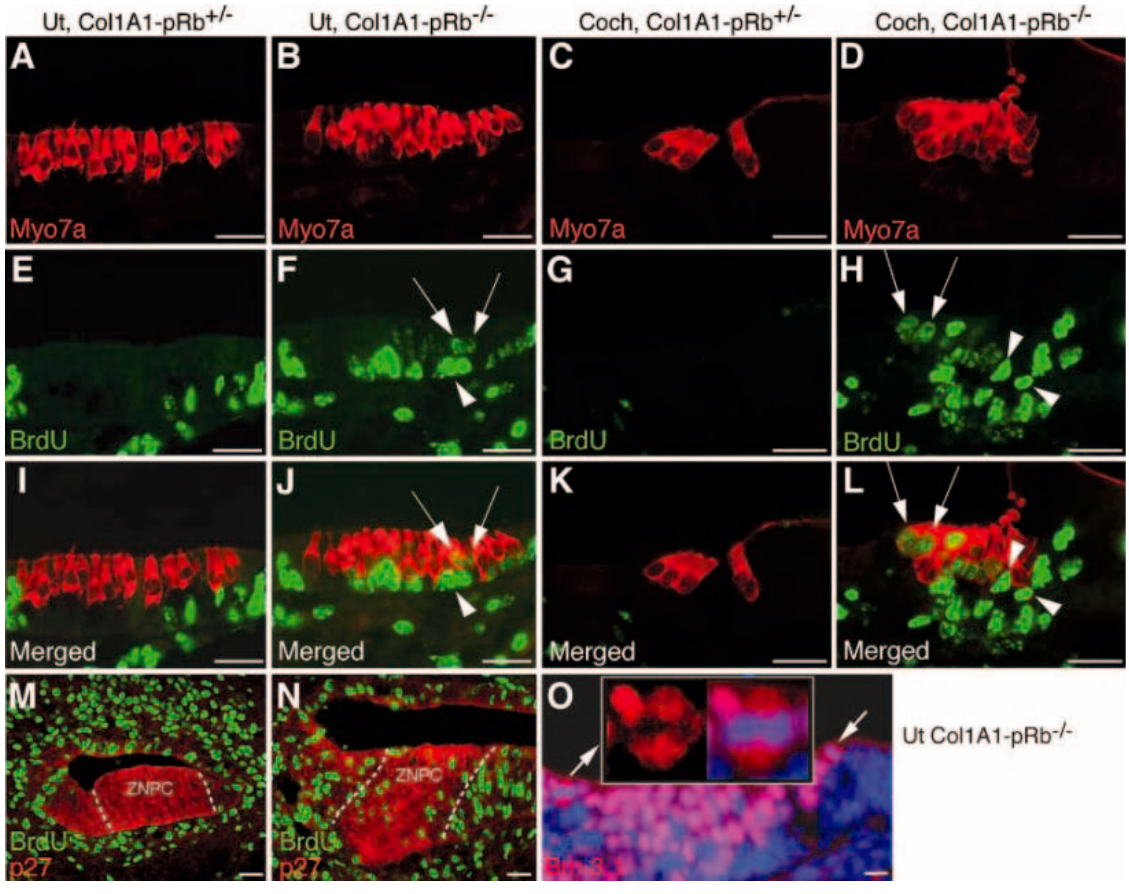

Fig. 2. Sensory progenitor cells and hair cells undergoing mitosis in Col1A1-pRb$^{-/-}$ mice. An antibody to Myo7a labels hair cells. (**A**, **E**, and **I**) In E18.5 control utricular macula, BrdU labeling was not found in hair cells but appeared in some supporting cells. (**B**, **F**, and **J**) In Col1A1-pRb$^{-/-}$ utricular macula, BrdU labeling appeared in both hair cells and supporting cells. (**C**, **G**, and **K**) No BrdU labeling in control cochlear hair cells or supporting cells. (**D**, **H**, and **L**) BrdU labeling of Col1A1-pRb$^{-/-}$ cochlear hair cells and supporting cells. Overall hair cell labeling was weaker (arrows) than supporting cells (arrowheads) [(F), (H), (J), and (L)]. (**M**) No BrdU labeling in control progenitor cells in the ZPNC (demarcated by dashed lines) of the primordial organ of Corti at E13.5. (**N**) BrdU labeling in Col1A1-pRb$^{-/-}$ progenitor cells. (**O**) Hair cells in M phase of cell cycle, as shown by cytoplasmic-like labeling by Brn-3.1 and condensed nuclear labeling by DAPI (arrows). (Inset) A hair cell in M phase with Brn-3.1 alone (left) and Brn-3.1 plus DAPI labeling (right). Scale bars, 25 μm [(A) to (N)], 10 μm (O).

uous hair cell division [Col1A1-pRb$^{-/-}$: ratio = 1.45 ± 0.057 (mean ± SD), N = 51; Col1A1-pRb$^{+/-}$: ratio = 0.79 ± 0.037, N = 22; P < 0.0001]. The proliferation of Col1A1-pRb$^{-/-}$ cochlear supporting cells appeared to be cell specific (fig. S3), as we saw more Deiters' cells than in controls (S100A1 labeling) but not more Pillar cells (p75ntr labeling).

We also identified dividing cells with an antibody to proliferating cell nuclear antigen (PCNA) (*22*). In E13.5 and E18.5 Col1A1-pRb$^{-/-}$ utricles, but not in controls, most hair cells stained strongly for PCNA (fig. S4). In cochleas as well, Col1A1-pRb$^{-/-}$ hair cells and supporting cells were strongly PCNA-positive, unlike controls (fig. S4, M to R). Finally, hair cells in metaphase were observed in E18.5 Col1A1-pRb$^{-/-}$ utricles (Fig. 2O). Staining with 4′,6′-diamidino-2-phenylindole (DAPI) and an antibody to the hair cell–specific transcription factor Brn-3.1 showed that for hair cells in M phase, Brn-3.1 labeling appeared to be cytoplasmic and separated from DAPI-labeled condensed chromosomes that were segregating into two daughter nuclei during mitosis (Fig. 2O, arrows and inset).

Most apical hair cells in E18.5 Col1A1-pRb$^{-/-}$ utricles showed highly differentiated morphology, including pear-shaped cell bodies and intact hair bundles. Hair bundles were labeled with antibodies to espin (an actin cross-linker) and Ptprq (present in highly differentiated cochlear hair bundles) (Fig. 3, A to D) (*23*, *24*). An antibody to tubulin revealed, as in controls, nerve fibers surrounding most Col1A1-pRb$^{-/-}$ hair cells (Fig. 3, E and F), and an antibody to the synaptic vesicle protein synaptophysin showed labeling around many Col1A1-pRb$^{-/-}$ hair cells (fig. S5), suggesting that Col1A1-pRb$^{-/-}$ hair cells can attract axons and form synapses. Other markers of differentiated hair cells were also detected in Col1A1-pRb$^{-/-}$ mice, including Brn-3.1 (Fig. 2O), Lhx3 (Fig. 3, B and D), Gfi1, Math1, calretinin, and parvalbumin 3. In contrast to a conditional pRb$^{-/-}$ mouse model where retinal rods failed to differentiate (*25*), cell fate determination and subsequent differentiation were largely intact in the proliferating Col1A1-pRb$^{-/-}$ hair cells. Therefore, Col1A1-pRb$^{-/-}$ hair cells become differentiated without switching off proliferation, indicating that hair cell fate determination and differentiation do not require pRb function.

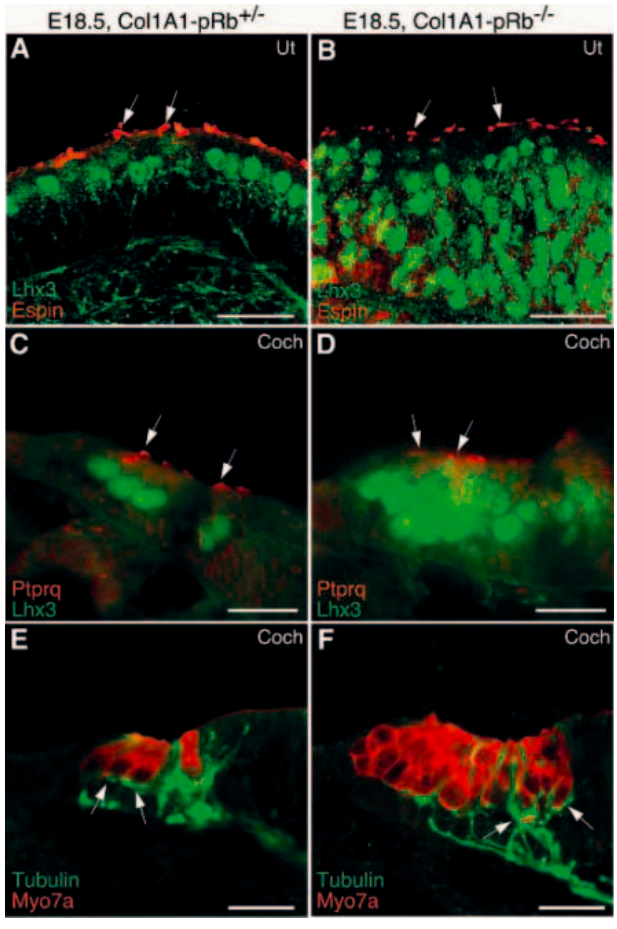

Fig. 3. Hair cells labeled with differentiating hair cell markers. (**A** to **D**) Lhx3 labels hair cell nuclei. Antibodies to espin labeled hair bundles (arrows) in control (A) and Col1A1-pRb$^{-/-}$ utricles (B). Antibodies to Ptprq labeled hair bundles (arrows) in control (C) and Col1A1-pRb$^{-/-}$ cochleas (D). (**E** and **F**) Antibodies to tubulin labeled nerve fibers surrounding hair cells marked with Myo7a (arrows) in control (E) and Col1A1-pRb$^{-/-}$ cochleas (F). Note labeling surrounding multiple inner hair cells in the Col1A1-pRb$^{-/-}$ cochlea (F). Scale bars, 25 μm.

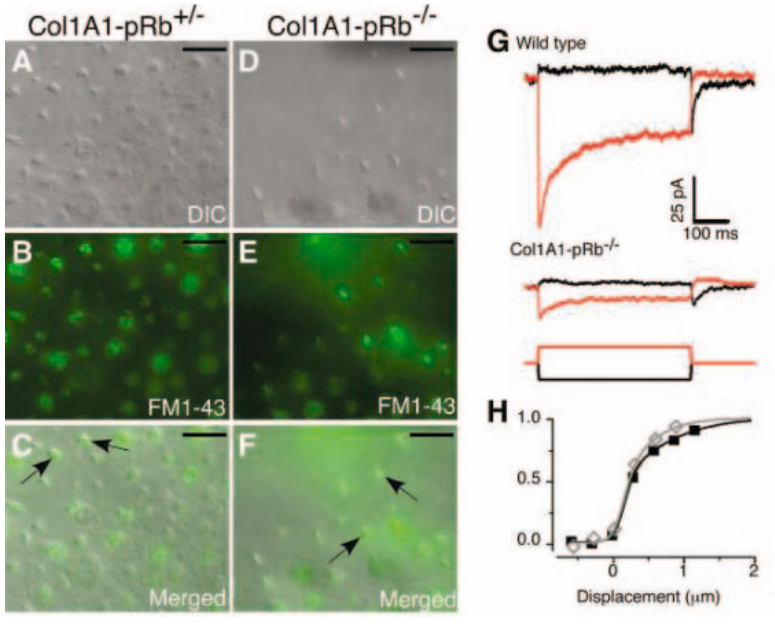

Fig. 4. Functional mechanotransduction by Col1A1-pRb$^{-/-}$ and control hair cells at E18.5. (**A** to **F**) FM1-43 accumulation by utricular hair cells. After exposure to FM1-43 for 1 min, most hair bundles [differential interference contrast images, (A) and (D)] were labeled with FM1-43 [green, (B) and (E)] in both control [(A) to (C)] and Col1A1-pRb$^{-/-}$ [(D) to (F)] mice, indicating that these cells had functional mechanotransduction channels. Arrows indicate clearly labeled bundles. (**G**) Transduction currents elicited in control (top) and Col1A1-pRb$^{-/-}$ (middle) littermates by step deflections of the hair bundle (bottom). Adaptations of the transduction currents in response to positive (red) and negative (black) hair bundle deflections were revealed. The wild-type response is typical of transduction currents in neonatal mice (*31*). However, transduction currents in Col1A1-pRb$^{-/-}$ mice were small: Peak transducer current (mean ± SEM) was 14.2 ± 2.9 pA (n = 4). (**H**) Normalized current-displacement relations for the control and Col1A1-pRb$^{-/-}$ transduction currents shown in (G). These two hair cells had similar operating ranges. Scale bars, 10 μm.

The sine qua non of hair cell function is mechanosensitivity. FM1-43, a fluorescent dye, enters hair cells through open mechanotransduction channels and so serves as a vital optical assay for mechanosensitivity (*26*, *27*). We observed FM1-43 labeling in bundles and cell bodies of most hair cells in both control (Fig. 4, A to C) and Col1A1-pRb$^{-/-}$ utricles (Fig. 4, D to F). Because most hair cells in Col1A1-pRb$^{-/-}$ utricles are PCNA-positive, FM1-43 entry can occur in cycling hair cells.

We then recorded transduction currents in control and Col1A1-pRb$^{-/-}$ hair cells. Transduction currents were evoked in four randomly selected Col1A1-pRb$^{-/-}$ hair cells (Fig. 4, G and H), although currents were smaller than in controls (10 to 20 pA versus ~200 pA in controls). Currents might be smaller if bundles had little time to develop between cell divisions, especially with the known delay between bundle formation and transduction (*28*). Transduction currents showed a normal activation range and adaptation time course. Thus, specialized hair cell function does not require pRb.

To determine whether apoptosis occurs in Col1A1-pRb$^{-/-}$ hair cells, we assayed for activated caspase-3. We did not detect any caspase-3–positive cells in Col1A1-pRb$^{-/-}$ sensory epithelium nor in controls (fig. S6). Therefore, loss of pRb itself does not appear to lead to cell death in the inner ear.

The prominent expression of *Rb1* in postnatal hair cells and the fact that acute loss of pRb causes cell cycle reentry in quiescent or senescent cells (*29*) suggests a role for pRb in maintaining hair cells' nonproliferative status. To test this hypothesis, we cultured floxP-pRb utricles and infected them with adenovirus carrying *cre* recombinase, acutely deleting the *Rb1* gene in infected hair cells (*30*). Utricular hair cells are mature at P10 and postmitotic at both stages studied (E17.5 and P10). After continuous culture in the presence of BrdU, no labeling was detected in hair cells infected with adenovirus carrying green fluorescent protein (GFP) (Fig. 5, A to D) or in uninfected floxP-pRb hair cells (Fig. 5, F and H, arrows), whereas hair cells infected with adenovirus carrying *cre* recombinase incorporated BrdU (Fig. 5, E to H). There were fewer BrdU-labeled hair cells in P10 cultures than in E17.5 cultures, likely because of the lower efficiency of infection of P10 hair cells. Additionally, more pRb was present in infected P10 hair cells after culture, which suggests that *cre*-mediated recombination or pRb degradation was less efficient in P10 cultures. All the infected hair cells lost hair bundles (*30*), so we could not test function. Nonetheless, the damaged hair cells reentered the cell cycle.

Cochleas in Col1A1-pRb$^{-/-}$ mice were studied for conversion of supporting cells to hair cells. If this were the main pathway for increased hair cell number, we would expect that p27Kip1-labeled supporting cells would label with Math1 (the earliest hair cell marker) or that Math1-positive cells would appear in supporting cell regions outside the hair cell region. However, in neither case did we find such cells. Although we cannot completely exclude cell fate conversion, it is most likely that increased hair cell precursors and subsequent hair cell division are primarily responsible for the overproduction of hair cells.

We have shown that differentiated mammalian hair cells can continue to cycle and divide in the absence of pRb, so that functional hair cells can be generated through divisions of preexisting hair cells. Furthermore, acute ablation of pRb in differentiated hair cells led to cell cycle reentry. The demonstration that pRb critically regulates hair cell division opens new opportunities for hair cell regeneration and for creating cell lines for hearing research. For hair cell regeneration, it will be important to determine whether a reversible block of pRb function in hair cells might be achieved in place of permanent deletion of the *Rb1* gene. Thus, the regulated inactivation of pRb—through the use of small interfering RNA (siRNA), a small-molecule inhibitor of pRb, or reversible manipulation of pRb-modifying kinases—may result in production of functional hair cells followed by restoration of normal cell cycle exit. These results also show that an irreversible switch from proliferation is not required for "terminal" differentiation, because cycling cells in the absence of pRb are highly differentiated and functional. Our findings may have implications for regenerating other functional cells through manipulation of negative cell growth control genes.

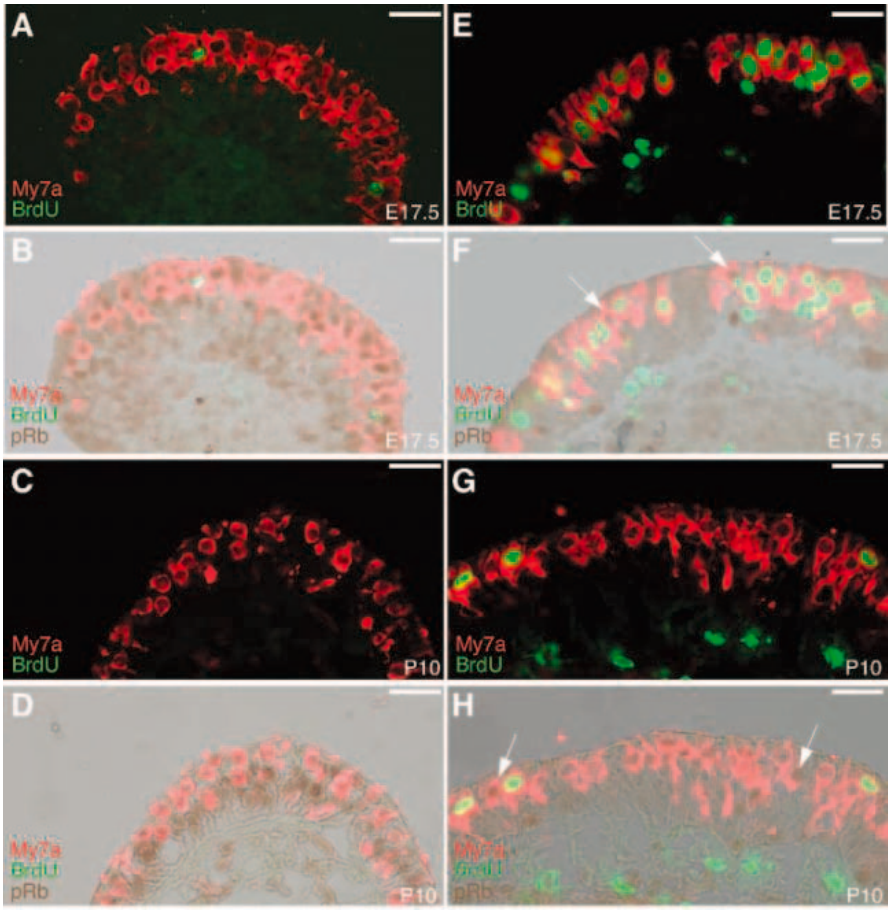

Fig. 5. Cell cycle reentry by postmitotic hair cells after acute deletion of the *Rb1* gene. (**A** to **D**) floxP-pRb utricles at E17.5 [(A) and (B)] and P10 [(C) and (D)] were infected with adenovirus carrying GFP as controls, then cultured with addition of BrdU. All hair cells are pRb-positive and BrdU-negative. The two BrdU-positive cells [(A) and (B)] are not hair cells. (**E** to **H**) floxP-pRb utricles at E17.5 [(E) and (F)] and P10 [(G) and (H)] were infected with adenovirus carrying *cre* recombinase and GFP. Cell cycle reentry by the infected hair cells (pRb-negative) was shown by BrdU labeling [(F) and (H)]. As an internal control, no BrdU labeling was in the uninfected hair cells (pRb-positive, arrows). Scale bars, 25 μm.

References and Notes

1. J. T. Corwin, D. A. Cotanche, *Science* **240**, 1772 (1988).
2. B. M. Ryals, E. W. Rubel, *Science* **240**, 1774 (1988).
3. A. Forge, L. Li, J. T. Corwin, G. Nevill, *Science* **259**, 1616 (1993).
4. M. E. Warchol, P. R. Lambert, B. J. Goldstein, A. Forge, J. T. Corwin, *Science* **259**, 1619 (1993).
5. H. Lowenheim *et al.*, *Proc. Natl. Acad. Sci. U.S.A.* **96**, 4084 (1999).

6. P. Chen *et al.*, *Nature Cell Biol.* **5**, 422 (2003).
7. M. Classon, E. Harlow, *Nature Rev. Cancer* **2**, 910 (2002).
8. M. M. Lipinski, T. Jacks, *Oncogene* **18**, 7873 (1999).
9. M. Classon, N. Dyson, *Exp. Cell Res.* **264**, 135 (2001).
10. T. Jacks *et al.*, *Nature* **359**, 295 (1992).
11. K. L. Ferguson, R. S. Slack, *Neuroreport* **12**, A55 (2001).
12. D. M. Thomas *et al.*, *Mol. Cell* **8**, 303 (2001).
13. R. S. Slack, H. El-Bizri, J. Wong, D. J. Belliveau, F. D. Miller, *J. Cell Biol.* **140**, 1497 (1998).
14. K. L. Ferguson *et al.*, *EMBO J.* **21**, 3337 (2002).
15. D. MacPherson *et al.*, *Mol. Cell. Biol.* **23**, 1044 (2003).
16. S. Marino, D. Hoogervoorst, S. Brandner, A. Berns, *Development* **130**, 3359 (2003).
17. Z.-Y. Chen, data not shown.
18. M. Vooijs, H. te Riele, M. van der Valk, A. Berns, *Oncogene* **21**, 4635 (2002).
19. F. Liu *et al.*, *Int. J. Dev. Biol.* **48**, 645 (2004).
20. P. Chen, J. E. Johnson, H. Y. Zoghbi, N. Segil, *Development* **129**, 2495 (2002).
21. M. Xiang, W. Q. Gao, T. Hasson, J. J. Shin, *Development* **125**, 3935 (1998).
22. A. L. Woods *et al.*, *Histopathology* **19**, 21 (1991).
23. L. Zheng *et al.*, *Cell* **102**, 377 (2000).
24. R. J. Goodyear *et al.*, *J. Neurosci.* **23**, 9208 (2003).
25. J. Zhang *et al.*, *Nature Genet.* **36**, 351 (2004).
26. J. E. Gale, W. Marcotti, H. J. Kennedy, C. J. Kros, G. P. Richardson, *J. Neurosci.* **21**, 7013 (2001).
27. J. R. Meyers *et al.*, *J. Neurosci.* **23**, 4054 (2003).
28. G. S. Geleoc, J. R. Holt, *Nature Neurosci.* **6**, 1019 (2003).
29. J. Sage *et al.*, *Nature* **424**, 223 (2003).
30. J. R. Holt *et al.*, *J. Neurophysiol.* **81**, 1881 (1999).
31. M. A. Vollrath, R. A. Eatock, *J. Neurophysiol.* **90**, 2676 (2003).

32. We thank L. Goodrich, D. Fekete, M. Holley, and J. Macklis for critical comments on the manuscript. D.P.C. is an Investigator of the Howard Hughes Medical Institute. Supported by NIH grants DC-04546 (Z.-Y.C.), DC-00200 (J.T.C.), and DC-AG20208 (P.W.H.) and by a Pfizer/AFAR Innovations in Aging Research grant (Z.Y.C.).

Supporting Online Material
www.sciencemag.org/cgi/content/full/1106642/DC1
Materials and Methods
Figs. S1 to S6
References

22 October 2004; accepted 3 January 2005
Published online 13 January 2005;
10.1126/science.1106642
Include this information when citing this paper.

Learned Predictions of Error Likelihood in the Anterior Cingulate Cortex

Joshua W. Brown* and Todd S. Braver

The anterior cingulate cortex (ACC) and the related medial wall play a critical role in recruiting cognitive control. Although ACC exhibits selective error and conflict responses, it has been unclear how these develop and become context-specific. With use of a modified stop-signal task, we show from integrated computational neural modeling and neuroimaging studies that ACC learns to predict error likelihood in a given context, even for trials in which there is no error or response conflict. These results support a more general error-likelihood theory of ACC function based on reinforcement learning, of which conflict and error detection are special cases.

Despite remarkable recent advances in cognitive neuroscience, it remains unclear how the brain learns to exert cognitive control over behavior. ACC and neighboring areas in the frontal medial wall play a role in monitoring and controlling goal-directed behavior (*1*–*3*). Error-related negativity (ERN/Ne) (*4*–*6*) and single-unit studies propose that ACC detects errors as discrepancies between actual and intended events (*7*). Alternatively, ACC may detect conflict between mutually incompatible response processes (*8*–*10*) such as incorrect versus correct responses. However, it has not been clear how the ACC learns what constitutes an error or that a given set of responses conflict. We develop here a computational model that demonstrates how ACC might not detect conflict or errors per se but rather more generally represent a prediction of error likelihood (*11*). In particular, the model makes a very specific prediction regarding ACC activity dynamics: The ACC response to a given task condition will be proportional to the perceived likelihood of an error in that condition.

The error-likelihood hypothesis also posits a training signal by which stimulus-specific ACC effects are acquired. This training signal may be dopaminergic. Phasic midbrain dopamine neuron activity is critically involved in reinforcement learning (*12*, *13*), and phasic suppression of dopamine apparently drives the ERN/Ne (*11*). Thus, phasic dopamine suppression occurring in response to errors might serve as a training signal (*14*, *15*) that causes ACC to respond more strongly to contexts in which errors are more frequent.

We formalized the error-likelihood hypothesis as a computational neural model to (i) examine how ACC representations might develop through experience and (ii) explicitly investigate the implications of the hypothesis (*16*). To test the model, we used a change variant (Fig. 1) of the well-known stop-signal paradigm used to examine inhibitory control (*17*). Previous work has demonstrated that stop-signal trials are associated with increased ACC activity in humans (*18*) and related medial frontal areas in other primates (*7*, *19*). The task consisted of conditions associated with high and low error rates crossed with the presence or absence of response conflict. Comparison of correct trials without response conflict across high and low error-rate conditions afforded assessment of error-likelihood effects while controlling for response conflict and errors.

In the computational model (Fig. 2A), simulated ACC neuron units received inputs repre-

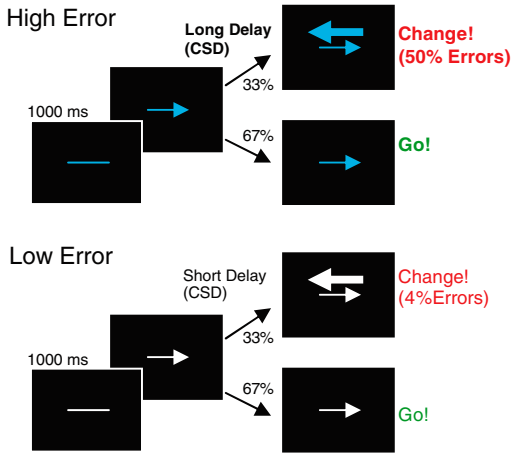

Fig. 1. Change signal task. An initial difficulty cue (plain line) appeared for 1000 ms. For a given trial, cue color (white or blue, equiprobable and randomly intermixed) predicts low versus high error likelihood, respectively. Then a go signal was presented (left- or right-pointing arrow made by extending the plain line to → or ←) that indicated the required button-press response (left index finger for left arrow and right index finger for right arrow). On 33% of the trials, a change (conflict) signal was added to the go signal after a variable CSD relative to go signal onset. This change signal (a second, larger arrow appearing above the first and pointing in the opposite direction) indicated that the response had to be left-right reversed from that indicated by the go signal. Both change and go signals remained visible until a response deadline of 1000 ms after go signal onset. A 500-ms blank interval occurred before the onset of the next trial. All stimuli for a given trial were the same color. Error rates were explicitly set and controlled by dynamically adjusting the CSDs for each error-likelihood condition independently with the use of a staircase algorithm. The low-error condition had shorter CSDs, whereas the high-error condition had longer CSDs, reflecting the well-established positive monotonic relationship between CSD and error rate in stop-signal tasks (*17*).

Department of Psychology, CB 1125, Washington University, St. Louis, MO 63130, USA.

*To whom correspondence should be addressed. E-mail: jwbrown@artsci.wustl.edu

senting stimulus features. Neuroanatomically, there is a lack of evidence for direct sensory inputs to ACC; yet such inputs may arrive either via high-level perceptual pathways or frontal areas that show stimulus specificity (*20*). When errors were committed, ACC units also received an error signal representing phasic suppression of afferent midbrain dopaminergic signals (*12*, *13*). ACC units were adaptive such that the synaptic weight from a given stimulus-specific representation to a given ACC unit increased when both were active and the error signal was also present. Learning within the ACC was competitive. As weights increased from active stimulus-specific inputs to ACC units that were active during an error trial, weights decreased from inactive stimulus units. This constraint, along with lateral excitation between spatially contiguous ACC units, global lateral inhibition among ACC units, and random activity noise, led to a greater number of spatially contiguous ACC units representing conditions reliably associated with errors.

The adaptive error-likelihood model was directly compared against an alternative competing computational model of ACC function (Fig. 2B) in which ACC measures response conflict in terms of the coactivation of incompatible response representations (*21*). In the response conflict model, input synaptic weights to the ACC were fixed rather than adaptive and originated from response rather than stimulus-specific representations.

In both models, activity from ACC excited a control signal that sent persistent, nonspecific inhibition to the response layer. This in turn slowed responses on trials after high ACC activity. Although other kinds of control signals may also be generated by ACC, this control mechanism has been examined in previous modeling work and found sufficient to account for trial-to-trial adjustments in behavioral performance driven by ACC activity fluctuations (*22*).

Simulations conducted with the change-signal task revealed that both the error-likelihood and conflict ACC models showed a similar pattern of behavioral performance, and subsequent experimental testing revealed that both provided very good fits to human behavioral data (*16*). However, despite being fit only to behavioral and not neuroimaging data, the two models showed important differences in the pattern of ACC activity exhibited across task conditions. In the error-likelihood model, ACC activity was greater for change than for go trials [change activity was 0.07 and go activity was 0.05, $F(1,17) = 757$, $P < 0.0001$], as expected (Fig. 2A), but was also greater on high-error change trials than on low-error change trials [high activity was 0.11 and low activity was 0.06, $F(1,17) = 263$, $P < 0.0001$], even when excluding all trials where errors were committed. Even more surprisingly, this error-likelihood effect was also present on correct go trials, which should have no associated conflict [high activity was 0.07 and low activity was 0.03, $F(1,17) = 519$, $P < 0.0001$]. Nevertheless, the error-likelihood model exhibited this effect, because high-error go trials contained a stimulus feature (color) that was associated with an increased likelihood of error commission. Because of the learned associations (embodied as strong synaptic connectivity) between this stimulus feature and ACC units, the presentation of this feature, even in the absence of other features that might cause conflict or errors (i.e., the change signal), was sufficient to increase activity in the ACC. In contrast, the conflict ACC model did not show this pattern of activation (Fig. 2B). Specifically, the conflict model did not exhibit a correct-trial high-error go versus low-error go effect [high activity was 0.13 and low activity was 0.13, $F(1,17) = 0.47$, $P = 0.50$].

Thus, the two models, which instantiate alternative accounts of ACC function, make different predictions regarding the pattern of ACC activity during the change-signal task. In particular, a critical test of the error-likelihood versus conflict-monitoring hypotheses is whether or not the correct, high-error condition go trials yield greater ACC activity than correct, low-error condition go trials. Both of these conditions exclude conflict, change signal delay (CSD), and error effects. Random equiprobable interleaving of high- and low-condition trials further ensures that effects of this comparison could only be driven by current cue color, which predicts error likelihood. We investigated these predictions experimentally in an event-related functional magnetic resonance imaging (fMRI) study of 16 human participants performing the same change-signal task simulated with the models (*16*).

Two regions of interest (ROIs) within the ACC and the neighboring functionally related

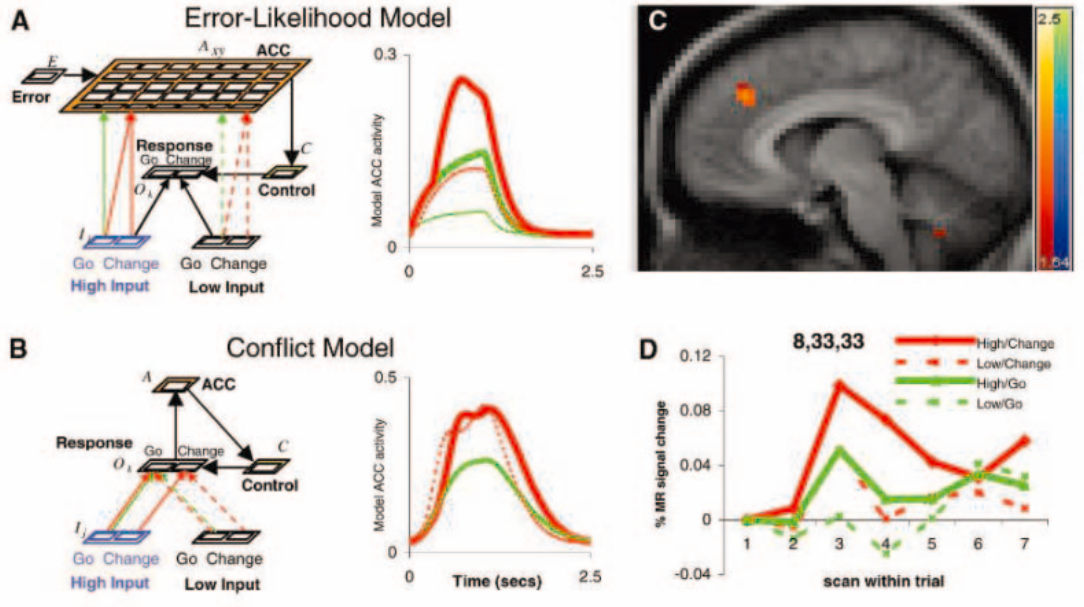

Fig. 2. Error-likelihood effects. Computational models of (**A**) error likelihood and (**B**) conflict detection generate competing predictions regarding effects of high versus low error rate conditions on ACC activity (*16*). Only the error-likelihood model predicts effects of high-error–versus low-error–likelihood conditions in the low-conflict go (thick green versus thin green lines) as well as high-conflict change conditions (thick red versus thin red lines). Model activity is proportional to neural firing rate. (**C**) Region 1 at (8,33,33) in right ACC was identified by a conjunction of several independent statistical tests for significant effects during correct trials. Shown is the z score of high/go minus low/go (restricted to voxels for which $P < 0.05$, one-tailed, uncorrected t test), masked by voxels that also showed a significant effect of both change > go and high/change > low/change (each $P < 0.05$, one-tailed, uncorrected t test). The conjunction analysis mask reduces the sample size considerably to only a few regions, effectively correcting for multiple comparisons while maintaining sensitivity to complex effects. (**D**) Time course of event-related fMRI activation in region 1 (averaged across all voxels) in each task condition. Analysis of the activation-magnitudes (again, averaged across whole region) confirms that all predicted effects are statistically significant [for change > go, $t(15) = 2.52$ and $P < 0.03$; for high/change > low/change, $t(14) = 2.25$ and $P < 0.05$; and for high/go > low/go, $t(14) = 2.17$ and $P < 0.05$]. Time courses shown are those without reaction time effects partially correlated out.

medial wall performance-monitoring areas (*23*) were identified that showed significant effects ($P < 0.05$) for all three of the following contrasts (analyzed by using only correct trials): change greater than go (change > go), high error-likelihood/change greater than low error-likelihood/change (high/change > low/change), and high error-likelihood/go greater than low error-likelihood/go (high/go > low/go). Region 1 (22 voxels; right dorsal ACC; Talairach 8,33,33) (Fig. 2C) overlapped anatomically with an ACC region previously identified to show conflict effects in several go/no go and stop tasks (*18*). Region 2 was found more superiorly (18 voxels; left anterior pre-supplementary motor area (pre-SMA); –2,27,54) with change > go [$t(15) = 2.87$, $P < 0.02$] and high > low effects in both change [$t(14) = 3.52$, $P < 0.004$] and go [$t(14) = 2.56$, $P < 0.03$] conditions (*24*). Critically, ROI analyses (Fig. 2D) confirmed that the effects observed within these regions were highly similar to those observed in the error-likelihood model simulation (Fig. 2A) (*25*). Other ROIs in the right dorsolateral prefrontal cortex and bilateral inferior parietal lobule and cerebellum also showed these same effects (table S1) (*16*) but were not analyzed in detail. Nevertheless, it is possible that these regions implement ACC-driven control signals (*1*), consistent with our computational model.

The error-likelihood hypothesis further postulates that error predictions in the ACC are acquired through task experience via a dopaminergic-training signal that is elicited after error commission. Simulations of the error-likelihood and conflict models again made competing predictions in this regard (Fig. 3, A and B). Specifically, the error-likelihood but not the conflict-detection simulation showed gradually emerging effects of high versus low conditions over the course of a session. fMRI results (Fig. 3C) are consistent with the error-likelihood model (Fig. 3A) but not the conflict model (Fig. 3B). With regard to the origin of training signals driving these learning effects, analysis of fMRI blood oxygen level–dependent (BOLD) responses also revealed increased ACC activity on error trials that differentiated between errors committed in the high and low conditions in a manner consistent with a dopaminergically based training signal (Fig. 4).

The current results support an error-likelihood account of ACC function in which ACC learns to signal, via the magnitude of its activity, the predicted likelihood of an error occurring in response to a given task condition. This proposed function may be highly adaptive, serving as an early-warning system that recruits cognitive control to match its predicted demand. This matching behavior of ACC responses (and subsequent cognitive control) may be seen as a complement to Herrnstein's matching law (*26*). Whereas the matching law predicts increases in neural activity associated with motor responses in proportion to the likelihood of positive reinforcement (*27*), the error-likelihood model predicts that ACC activity will occur in proportion to the likelihood of negative reinforcement. Furthermore, our results are consistent with the idea that a dopaminergic training signal in ACC plays a common role in reinforcement learning and recruitment of cognitive control (*11*).

Conflict and error detection ACC effects are accounted for as special cases of the error-likelihood model. Errors generally occur more frequently with cues that map to conflicting responses compared with cues that map to the same response. Thus, response conflict effects in ACC may reflect a higher error likelihood rather than an explicit computation of response conflict per se. Similarly, previous studies show frontal medial activity in response to errors, even before external feedback (*4*, *28*). Adding a connection in the error-likelihood model from the response to ACC layers might allow ACC to respond selectively to particular combinations of stimuli and internal representations of incorrect response execution, which are highly predictive of undesired consequences. Under these conditions, the model would be expected to show error effects in ACC, even before external feedback (*11*, *28*). Thus, the model (and the associated theoretical framework) provides a tool for understanding how error, conflict, and error-likelihood prediction effects may all be acquired by ACC after continued exposure to task environments. More generally, the results presented here illustrate the benefits of tightly integrating neuroimaging studies with computational modeling, because the two methods together provide a strong basis for hypothesis generation and theory testing regarding the neural mechanisms of cognition.

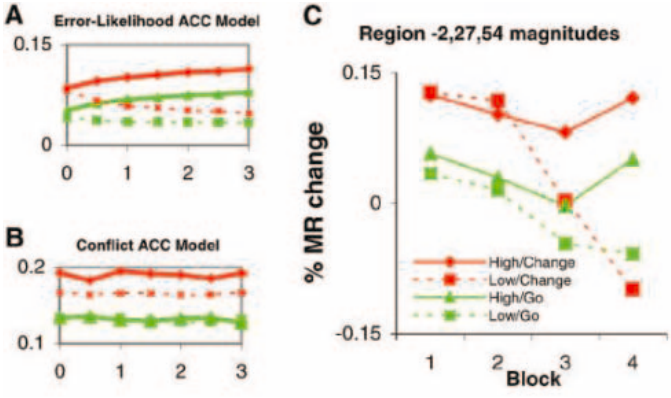

Fig. 3. Learning effects across time. (**A**) The error-likelihood computational model with adaptive ACC inputs predicts an initial effect of change > go and a subsequently growing effect of high > low in each of the change and go conditions. (**B**) The conflict computational model with fixed ACC inputs predicts an effect of high/change > low/change and change > go but no effect of high/go > low/go. None of these effects varied with time. MR, magnetic resonance. (**C**) fMRI results are consistent with the error-likelihood but not the conflict ACC model. During the first two blocks, activity in the anterior pre-SMA region shows effects of change > go but not of high > low, despite the fact that CSDs have equilibrated by the beginning of the second block (fig. S1). By the third and fourth blocks, both the change and go conditions show evidence of discrimination between high- and low-error conditions, and this discrimination eventually dominates the discrimination between change and go trials by the end of the session.

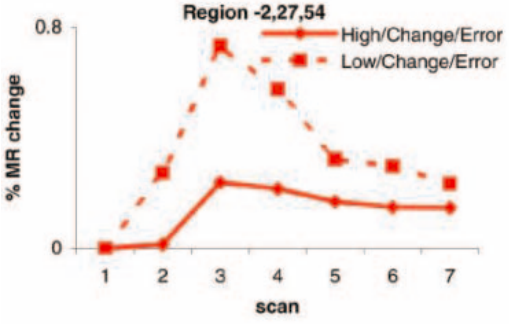

Fig. 4. Error effects consistent with dopaminergic training signals. Error-related activity on change trials is greater for the low-error condition than for the high-error condition [region 2 shown: $t(14) = 3.13$, $P < 0.01$]. When error likelihood is lower, actual errors more highly suppress phasic dopamine cell activity (*29*). According to the error-likelihood hypothesis, dopamine suppression serves as a training signal and increases ACC activity (*11*). Therefore, errors of commission in the low-error condition should be associated with a stronger transient depression of dopamine activity and consequently greater ACC activation than in the high condition. Notably, this pattern is the opposite of that predicted and found for correct trials, where the high condition leads to greater activity than the low condition. We did not model this effect of dopamine signaling in the simulation error signal inputs, but we tested this prediction for the entire ACC region in which voxels showed an effect of change > go ($P < 0.05$). The predicted effect was found in this whole-ACC region [$t(14) = 2.29$, $P < 0.04$], although one subject was excluded for lack of errors in the low/change condition. In general, dopaminergic error signals might also drive plasticity without necessarily exciting target cells, because conflict effects have been found in cells without error responses (*19*).

References and Notes

1. J. G. Kerns *et al.*, *Science* **303**, 1023 (2004).
2. J. D. Schall, V. Stuphorn, J. W. Brown, *Neuron* **36**, 309 (2002).
3. G. Bush, P. Luu, M. I. Posner, *Trends Cogn. Sci.* **4**, 215 (2000).

4. W. J. Gehring, M. G. H. Coles, D. E. Meyer, E. Donchin, *Psychophysiology* **27**, S34 (1990).
5. J. Hohnsbein, M. Falkenstein, J. Hoorman, *J. Psychophysiol.* **3**, 32 (1989).
6. P. S. Bernstein, M. K. Scheffers, M. G. H. Coles, *J. Exp. Psychol. Hum. Percept. Perform.* **21**, 1312 (1995).
7. S. Ito, V. Stuphorn, J. W. Brown, J. D. Schall, *Science* **302**, 120 (2003).
8. C. S. Carter *et al.*, *Science* **280**, 747 (1998).
9. M. M. Botvinick, L. Nystrom, K. Fissel, C. S. Carter, J. D. Cohen, *Nature* **402**, 179 (1999).
10. A. W. MacDonald, J. D. Cohen, V. A. Stenger, C. S. Carter, *Science* **288**, 1835 (2000).
11. C. B. Holroyd, M. G. Coles, *Psychol. Rev.* **109**, 679 (2002).
12. W. Schultz, P. Dayan, P. R. Montague, *Science* **275**, 1593 (1997).
13. J. O'Doherty, P. Dayan, K. Friston, H. Critchley, R. Dolan, *Neuron* **38**, 329 (2003).
14. J. W. Brown, D. Bullock, S. Grossberg, *Neural Networks* **17**, 471 (2004).
15. S. Bao, V. T. Chan, M. M. Merzenich, *Nature* **412**, 79 (2001).
16. Materials and methods are available as supporting material on *Science* Online.
17. G. D. Logan, W. B. Cowan, *Psychol. Rev.* **91**, 295 (1984).
18. K. Rubia *et al.*, *Neuroimage* **13**, 250 (2001).
19. V. Stuphorn, T. L. Taylor, J. D. Schall, *Nature* **408**, 857 (2000).
20. D. Boussaoud, S. P. Wise, *Exp. Brain Res.* **95**, 28 (1993).
21. M. M. Botvinick, T. S. Braver, D. M. Barch, C. S. Carter, J. C. Cohen, *Psychol. Rev.* **108**, 624 (2001).
22. A. D. Jones, R. Cho, L. E. Nystrom, J. D. Cohen, T. S. Braver, *Cogn. Affect. Behav. Neurosci.* **2**, 300 (2002).
23. K. R. Ridderinkhof, M. Ullsperger, E. A. Crone, S. Nieuwenhuis, *Science* **306**, 443 (2004).
24. In addition to the ACC effects, there was also a small but reliable difference in behavioral performance across the two go conditions, with reaction times slightly slower for high/go versus low/go [736 ms versus 710 ms, $F(1,15) = 5.80$, $P < 0.05$]. Because of this pattern, a potential alternative is that the reaction time differences are the causal mechanism underlying differences in ACC activity (if this ACC region was purely sensitive to response-related activity) rather than error-likelihood effects. To rule out this potential confound, ACC activity was reestimated after partially correlating out reaction time as a nuisance covariate. The effects of high/go and low/go remained significant in regions 1 [$t(14) = 2.67$, $P < 0.02$] and 2 [$t(14) = 2.29$, $P < 0.04$].
25. A whole-ACC ROI consisting of all Brodmann areas 24 and 32 voxels that showed significant change > go effects also showed effects of high/change > low/change ($P < 0.04$). The high/go > low/go effect did not reach significance in this ROI ($P = 0.21$), but high/go activity was numerically greater than low/go in 288 of 291 voxels (binomial test, $P < 0.00001$). High and low activities also apparently diverged with training as expected, but this did not reach significance.
26. R. Herrnstein, *J. Exp. Anal. Behav.* **4**, 267 (1961).
27. L. P. Sugrue, G. S. Corrado, W. T. Newsome, *Science* **304**, 1782 (2004).
28. C. B. Holroyd *et al.*, *Nat. Neurosci.* **7**, 497 (2004).
29. C. D. Fiorillo, P. N. Tobler, W. Schultz, *Science* **299**, 1898 (2003).
30. The authors thank C. Hoyer for help with data collection and C. Holroyd, J. Reynolds, A. Schaeffer, J. Schall, and V. Stuphorn for helpful comments. Supported by Office of Naval Research N00014-00-1-0715. Partial funding support was also received by the Director of Central Intelligence's Intelligence Technology Innovation Center. The authors declare that they have no competing financial interests.

Supporting Online Material

www.sciencemag.org/cgi/content/full/307/5712/1118/DC1
Materials and Methods
Fig. S1
Table S1

28 September 2004; accepted 27 December 2004
10.1126/science.1105783

Flexible Control of Mutual Inhibition: A Neural Model of Two-Interval Discrimination

Christian K. Machens,[1] Ranulfo Romo,[2] Carlos D. Brody[1]*

Networks adapt to environmental demands by switching between distinct dynamical behaviors. The activity of frontal-lobe neurons during two-interval discrimination tasks is an example of these adaptable dynamics. Subjects first perceive a stimulus, then hold it in working memory, and finally make a decision by comparing it with a second stimulus. We present a simple mutual-inhibition network model that captures all three task phases within a single framework. The model integrates both working memory and decision making because its dynamical properties are easily controlled without changing its connectivity. Mutual inhibition between nonlinear units is a useful design motif for networks that must display multiple behaviors.

In our daily lives, our minds can flit from thought to thought with remarkable speed and flexibility (*1*). A simplified task that requires rapid shifts between different mental actions is known as two-interval discrimination (two stimuli separated by a time interval; Fig. 1A). Subjects must first perceive a brief stimulus, called f1, maintain it in working memory for several seconds, and then compare it with a brief second stimulus, called f2, to immediately decide which of the two stimuli was larger. The task requires both working memory and decision making, interfacing between the two in a rapid switch from one to the other.

The biophysical mechanisms underlying the performance of this task remain unknown. Spiking neural-network models, built to serve as mechanistic accounts of cognitive neural activity, have focused so far on only single cognitive processes (*2*–*8*). Few models (*9*, *10*), and no spiking network models, have addressed the question of how more than one computation and dynamic can be implemented in a single network. Yet cognitive acts typically require more than one type of computation. Many cognitive psychology models do integrate multiple processes, but do not address biophysical mechanisms (*11*). On the basis of recent neurophysiological data (Fig. 1) (*12*–*17*), we use a nonlinear dynamical systems approach (*18*–*21*) to design a simple and testable spiking-neuron model of two-interval discrimination. The model integrates three key processes into a single framework that proposes mechanistic links between the different processes, as well as between biophysical properties and neural and behavioral phenomena. These processes are fast initial loading of stimulus f1 into working memory, slow maintenance of working memory, and fast decision making.

Figure 1, C and D show the firing rates of two prefrontal cortical (PFC) neurons recorded from previously trained macaque monkeys while they performed a two-interval discrimination task in which f1 and f2 were the frequencies of mechanical vibrations applied to the tip of a finger (*12*, *16*, *22*). The dynamics of the activity of these neurons depends strongly on the phase of the task. During the loading of f1 into working memory, there is a rapid flow to an f1-dependent firing rate. During the maintenance of f1 in working memory, there is a long-lasting persistence of f1-dependent firing rates, despite the absence of the stimulus. During the comparison/decision phase, upon presentation of the second stimulus f2, the firing rates quickly segregate into one of two categories, depending on the monkey's subsequent choice of a "yes" or "no" push-button answer to the question, "Is f1 greater than f2?" Responses similar to these PFC responses are also found in ventral (*17*) and medial (*14*) premotor cortices. For brevity, here we will refer collectively to these three areas as "frontal lobe areas." We highlight two aspects of the frontal lobe data. First, signals are encoded in complementary sets of roughly equal numbers of neurons (*12*, *14*, *17*). One set is composed of "plus" neurons, defined as neurons with a delay-period firing rate that is a monotonically increasing function of f1 (Fig. 1C). Plus neurons typically fire the most for "yes" decisions after presentation of f2. The complementary set are "minus" neurons, defined as those which have delay period firing rates that are monotonically decreasing functions of f1, and fire the most for "no" decisions (Fig. 1D). Because higher f2 stimuli are more likely to lead to "no" decisions; plus neurons are excited by high f1 stimuli but inhibited by high f2 stimuli. The converse occurs for minus neurons

[1]Cold Spring Harbor Laboratory, 1 Bungtown Road, Cold Spring Harbor, NY 11724, USA. [2]Instituto de Fisiología Celular, Universidad Nacional Autónoma de México, 04510 México, D.F., México.

*To whom correspondence should be addressed. E-mail: brody@cshl.edu

(fig. S9) (*23*). Each of the two sets of neurons carries all the information necessary for the task; the existence of two apparently redundant sets is so far unexplained.

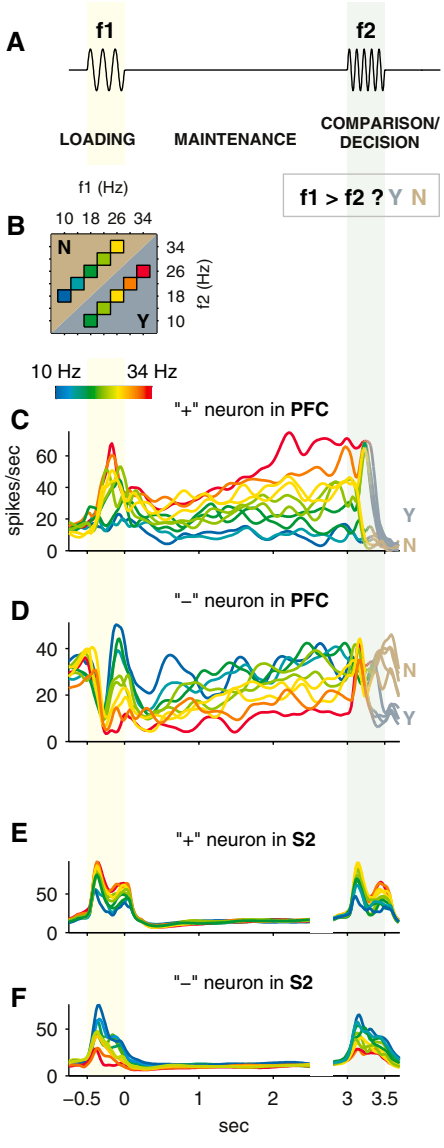

Fig. 1. The two-interval discrimination task and neuronal responses to it in the PFC and the S2 cortices. (**A**) Schematic diagram of each trial of the task. (**B**) Typical stimulus set used in the neurophysiological studies we focus on here (*14, 17, 44, 45*). Stimuli are frequencies of mechanical vibrations applied to the tip of a monkey's finger, and each colored box indicates a (f1, f2) stimulus pair. For each pair, monkeys made the correct response more than 91% of the time (*16, 22*). (**C** to **F**) Neuronal responses. The rainbow color code at the upper left indicates the f1 value applied during each type of trial. Y/N color code indicates the push button pressed by the monkey at the end of each trial. (C) and (D) show smoothed firing rates of two different PFC neurons recorded over many trials. (C) shows a plus neuron and (D) shows a minus neuron. (E) and (F) show neuronal responses in area S2 (*13, 15*). For (E) and (F) only, rainbow colors for $t > 2.8$ s indicate value of f2.

Second, the same neurons that show graded delay-period activity, which represents working memory of f1, also show categorical activity after stimulus f2, which represents the monkey's decision (*14*, *17*, *24*). This finding contrasts with current mathematical psychology models of two-interval discrimination, which have implicitly assumed that working memory and decision making are processes represented by separate variables (*25*–*28*). Instead, we propose an algorithm (Fig. 2) in which both memory and decision outcome are represented by the value of a single state variable (horizontal axis). The dynamical modes of the system are described by a hypothetical energy function L (vertical axis), the shape of which does not depend on the value of the state variable. The state variable always evolves so as to reduce L. During the loading phase, the external stimulus creates a single minimum in L (a single stable point) at a position determined by the value of f1. This forces the state into an f1-dependent position. During the memory maintenance phase, there is no longer an external stimulus that determines the shape of L. The memory of f1 is represented by the state's position, and for this to remain steady, the L function must be approximately flat [a line attractor configuration (*2*, *29*, *30*)]. During the comparison/decision phase, we map stimulus f2 onto the same horizontal axis as f1. All state positions to the left of f2 now represent memories of f1 values that are less than f2. States to the right of f2 represent memories of f1 that are greater than f2. If a peak in L (an unstable point) is created at the position given by f2, the state will evolve in one of two opposite directions, depending on the yes or no answer to f1 > f2? If the horizontal axis stands for a firing rate that grows from left to right, the plots mimic the activity of plus neurons through all phases of the task. If the firing rate grows from right to left, the plots mimic minus neurons.

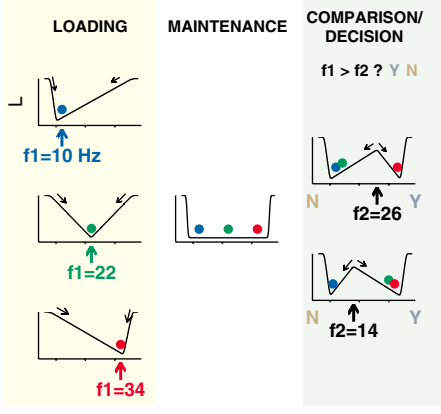

Fig. 2. One-dimensional dynamical algorithm for two-stimulus–interval discrimination. The value of the state variable (horizontal axis) is used to represent both memory of f1 (maintenance) and decision-making outcome (comparison/decision).

We propose that the frontal-lobe areas instantiate this dynamical algorithm. The task-relevant sensory inputs to these frontal areas arise from the secondary somatosensory cortex (S2) (Fig. 1, E and F) (*31*). During the first stimulus, responses in the S2 are similar to those in the PFC: there are both plus (Fig. 1E) and minus (Fig. 1F) neurons (*13*, *15*). Unlike the PFC, however, during most of the delay period, S2 neuron firing rates are low and not f1-dependent. Also in contrast with the PFC, immediately after presentation of f2, neurons in the S2 respond to f2 with the same plus- or minus-type firing-rate dependence with which they responded to f1 (*32*).

Clues about the underlying frontal-lobe neural architecture come from the analysis of firing rate covariations between pairs of PFC neurons. These tend to be positive if both neurons are plus, or if both are minus, but negative when one is plus and one is minus (*33*), leading us to consider the architecture sketched in Fig. 3A. In a simplified version of this circuit (Fig. 3B), each node represents a population of neurons, and each node's output variable is the average activity of the population. Figure 3C shows a node's i/o function, which is defined as its output, expressed as a resulting postsynaptic conductance, as a function of excitatory input (*34*). The overall shape obtained, with a threshold below which output is negligible and with saturation at high outputs, is characteristic of many neuron models.

To study graphically the dynamics of the circuit in Fig. 3B, we show in black in Fig. 3D the output of the plus node as a function of the inhibitory input from the minus node. An additional excitatory input, E, is held constant here. The minus node's i/o function can be plotted by exchanging the horizontal and vertical axes to form the brown axes and curve in Fig. 3D. This phase-plane plot now describes the complete dynamics of the system, because we can follow the input to output activity of each node as it reverberates around the circuit loop. Points where the two i/o curves intersect are known as fixed points, or steady states. These may be stable (like the minimum in L during loading as seen in Fig. 2) or unstable (like the maximum in L during comparison/decision).

During the first stimulus [loading phase (Fig. 3E)], inputs from the S2 area are active. Together with the external input E, they can shift the i/o functions along their input axes. If both nodes receive the same S2 input, then by symmetry, the crossing point of the two i/o curves must lie along the 45° diagonal of the phase-plane plots. However, we propose that S2 plus neurons project to frontal plus neurons, and S2 minus neurons project to frontal minus neurons. As a result, the position of the single stable point is determined by the value of f1, thus instantiating the loading mode of Fig. 2. Horizontal position in Fig. 2 corre-

sponds here to the angle of θ (defined in top phase plane, Fig. 3E).

During the delay period [maintenance phase (Fig. 3F)], the inputs from S2 are silent. The value of *E* and the neuronal-model parameters can be chosen such that the two i/o curves largely overlap. This creates a quasi-continuous line of stable points (a line attractor) and thus instantiates the maintenance mode of Fig. 2 (*35*).

During the comparison/decision phase (Fig. 3G), we propose that an external control signal, which indicates that the current stimulus should be treated as f2, not f1, reduces the otherwise constant excitatory input *E*. For low enough *E*, the system has two stable fixed points on either side of a single unstable fixed point, as required for this phase in Fig. 2. In the data, frontal neurons switch the sign of their stimulus dependence between f1 and f2 (*23*), but S2 sensory neurons do not. The net functional connection between S2 and frontal neurons must therefore change sign. To match this in the model, we used the circuit shown in Fig. 3H to switch the net S2-to–frontal plus neuron connections between loading (Fig. 3E, top) and comparison/decision (Fig. 3G, top). A similar circuit was used for frontal minus neuron connections (*36*). As a result of this input sign switch, increasing f2 moves the unstable fixed point from lower to higher θ (Fig. 3G), which matches the f1-dependence of the stable fixed point during loading (Fig. 3E). This completes instantiation of the comparison/decision mode of Fig. 2.

The continuous-variable nodes of the model of Fig. 3 were each replaced by 250 noisy, leaky, integrate-and-fire neurons in order to produce a spiking neuron model with almost identical behavior (fig. S4). Figure 4A shows firing rates for one spiking neuron from the plus node and one neuron from the minus node, qualitatively capturing key aspects of the data. The sign of correlations between pairs of neurons in the model also matches the pattern found in the experimental data (Fig. 4B).

The one-dimensional algorithm of Fig. 2 produces testable predictions separate from the neural instantiation proposed here. If the decision is reported when the state reaches one of the two final stable points in Fig. 2, and if the distance to the final stable point is a dominant factor in the time required to reach it, then it follows that on trials where f1 equals f2 (50% "yes" responses, 50% "no") and f1 and f2 are near the high end of the range of stimuli, "yes" decisions will be reached faster than "no" decisions. The converse is true at the low end of the range (Fig. 4D). At the neural instantiation level, both the fine-tuned (Fig. 3) and robust (*34*, *35*) instantiations rest on populations of mutually inhibitory neurons. If the strength of inhibitory connections were increased [e.g., by use of benzodiazepines (*37*)], then the memory maintenance mode would be perturbed in the direction of the comparison/decision mode, with a single unstable point. Because of the circuit's symmetry, the effect would be similar to an f2 stimulus in the middle of the range (≈ 22 Hz), even though no stimulus would be present (Fig. 4C). The psychophysical correlate would be a tendency to categorize f1 into high or low rather than remembering it accurately.

Unlike previous line attractor models (*3*, *5*, *6*), which relied mostly on mutual exci-

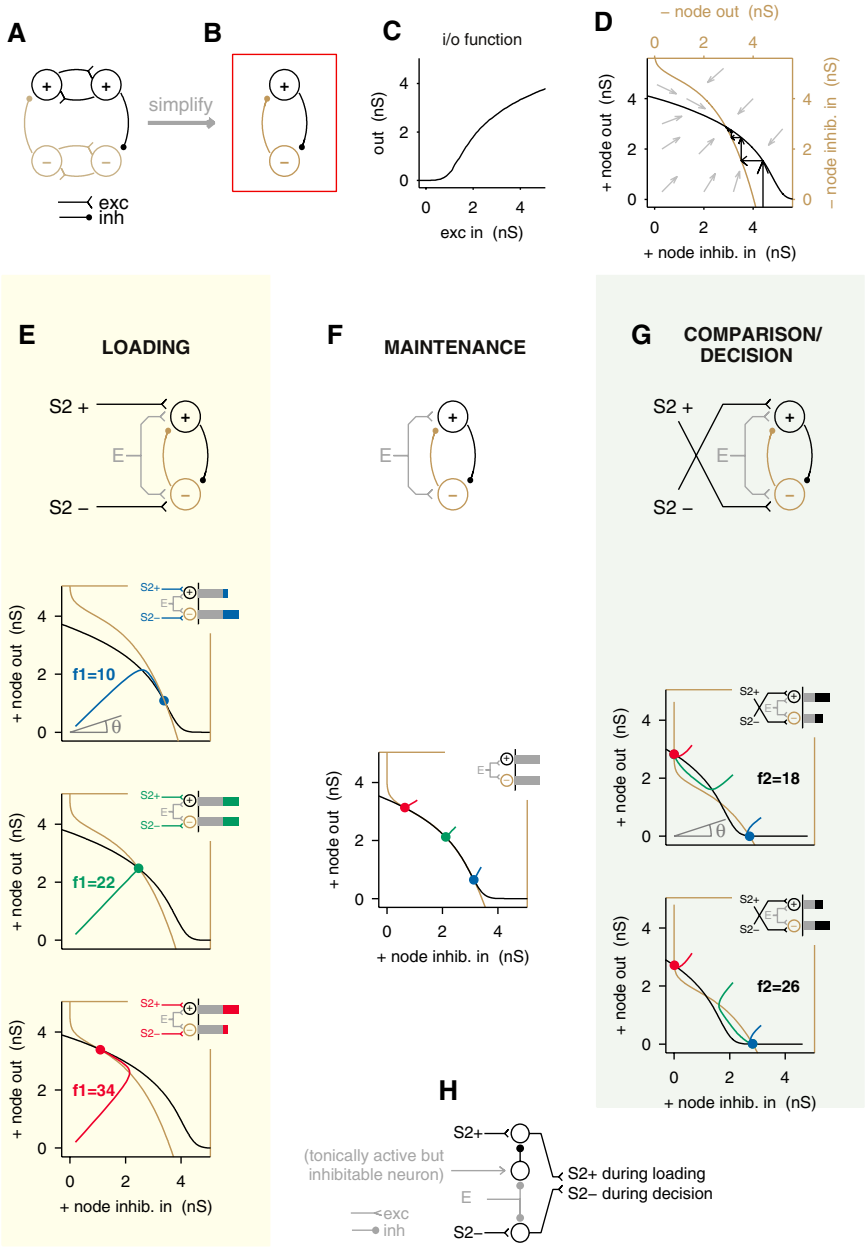

Fig. 3. Mutual inhibition model implements the dynamical modes of Fig. 2. (**A** and **B**) Circuit diagrams. Each node represents a population of neurons. (**C**) Input/output of a node as a function of excitatory input (nS, nanoSiemens). (**D**) Phase-plane plot of both i/o functions allows tracing out the dynamics of the mutual inhibition circuit. (Black arrows indicate stepping discretely between nodes, for illustration, and gray arrows indicate continuous time dynamics, as used in actual simulations.) (**E**) Loading. The top panel shows inputs to the circuit. The lower three panels show the effect of three different values (10, 22, and 34 Hz) of the first stimulus (f1). Colored lines show dynamical trajectories, starting from (0,0) and ending at filled circles. (**F**) Maintenance. Removing inputs from S2 results in a quasi-continuum of stable points. Dynamical trajectories start from correspondingly colored endpoints of trajectories in (E). (**G**) Comparison/decision. The lower panels show i/o functions and dynamics for f2 = 18 (top) and f2 = 26 (bottom). The final state depends on the answer to f1 > f2? Trajectories start from the endpoints of (F). For all plots in (E), (F), and (G), angle θ corresponds to horizontal position in Fig. 2. (**H**) Input switching circuitry. At high *E*, S2 plus signals pass through, but at low *E*, S2 minus signals pass through.

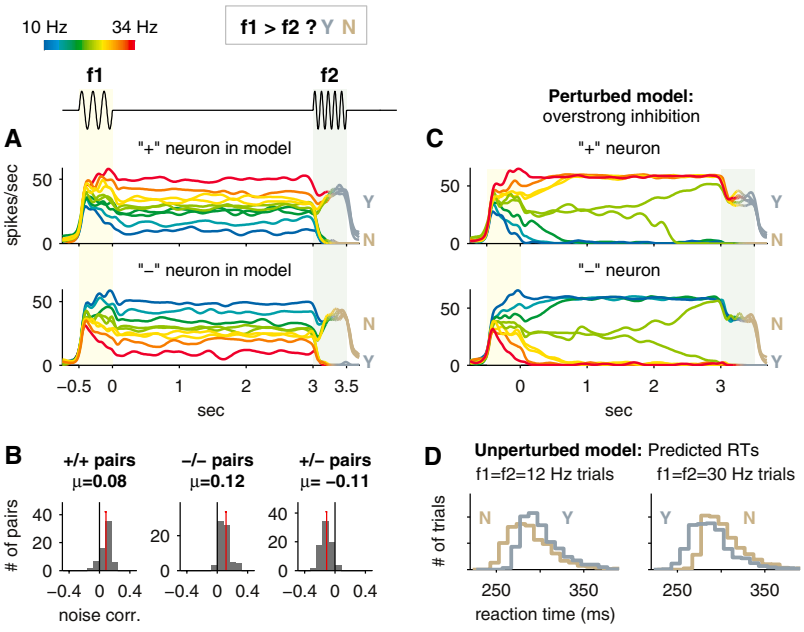

Fig. 4. Model responses and predictions. (**A**) Same format and stimulus values as Fig. 1, C and D. Simulated activity for one neuron from the plus node population (top) and one neuron from the minus node population (bottom), averaged over trials. (**B**) Histograms of noise correlations (*41*) during the maintenance phase, compiled over pairs of neurons in the model. (**C**) Predicted firing rates in model where inhibition is overstrong. (**D**) One-dimensional algorithm (Fig. 2) predicts asymmetry in "yes" and "no" reaction times (RTs). See text for sufficient conditions under which this prediction follows. Particular RT values shown here were obtained by using the model of Fig. 3 with small amounts of Gaussian noise added at each time step.

tation, we implemented both working-memory and decision-making dynamics through mutual inhibition. This facilitated the use of a single simple circuit for both. The use of neuron models with i/o functions that are nonlinear above threshold, instead of linear or threshold-linear models (*38–40*), further allowed straightforward control of the circuit's dynamical mode through an external excitation signal.

Our daily mental lives have an enormous variety of highly flexible dynamics. What is the neural basis of this flexibility? Do frontal lobes contain many separate modules of neurons, each capable of a particular type of computation and its attendant dynamics? Or, as the data of Fig. 1, C and D have inspired us to propose here, can single modules of frontal lobe neurons rapidly reconfigure their dynamical properties, switching between different behaviors as the cognitive flow requires? If single modules are indeed flexible, what is the range of dynamics and computations that they can display? We have only begun to address these questions here. But we believe they are fundamental, and lie at the heart of the nature of the neural architecture underlying cognition.

References and Notes

1. E. K. Miller, J. D. Cohen, *Annu. Rev. Neurosci.* **24**, 167 (2001).
2. H. S. Seung, *Proc. Natl. Acad. Sci. U.S.A.* **93**, 13339 (1996).
3. H. S. Seung, D. D. Lee, B. Y. Reis, D. W. Tank, *Neuron* **26**, 259 (2000).
4. X. J. Wang, *Neuron* **36**, 955 (2002).
5. P. Miller, C. D. Brody, R. Romo, X. J. Wang, *Cereb. Cortex* **13**, 1208 (2003).
6. A. A. Koulakov, S. Raghavachari, A. Kepecs, J. E. Lisman, *Nature Neurosci.* **5**, 775 (2002).
7. Y. Loewenstein, H. Sompolinsky, *Nature Neurosci.* **6**, 961 (2003).
8. E. Brown *et al.*, *Int. J. Bifurcat. Chaos,* in press.
9. S. L. Moody, S. P. Wise, G. di Pellegrino, D. Zipser, *J. Neurosci.* **18**, 399 (1998).
10. E. Salinas, *Neural Comput.* **15**, 1439 (2003).
11. A. Miyake, P. Shah, Eds., *Models of Working Memory: Mechanisms of Active Maintenance and Executive Control* (Cambridge Univ. Press, Cambridge, ed. 1, 1999).
12. R. Romo, C. D. Brody, A. Hernandez, L. Lemus, *Nature* **399**, 470 (1999).
13. E. Salinas, A. Hernandez, A. Zainos, R. Romo, *J. Neurosci.* **20**, 5503 (2000).
14. A. Hernandez, A. Zainos, R. Romo, *Neuron* **33**, 959 (2002).
15. R. Romo, A. Hernandez, A. Zainos, L. Lemus, C. D. Brody, *Nature Neurosci.* **5**, 1217 (2002).
16. C. D. Brody, A. Hernandez, A. Zainos, R. Romo, *Cereb. Cortex* **13**, 1196 (2003).
17. R. Romo, A. Hernandez, A. Zainos, *Neuron* **41**, 165 (2004).
18. H. R. Wilson, *Spikes, Decisions, Actions: Dynamic Foundations of Neuroscience* (Oxford Univ. Press, Oxford, ed. 1, 1999).
19. H. D. Abarbanel, M. I. Rabinovich, *Curr. Opin. Neurobiol.* **11**, 423 (2001).
20. P. Dayan, L. F. Abbott, *Theoretical Neuroscience* (MIT Press, Cambridge, MA, ed. 1, 2001).
21. F. C. Hoppensteadt, *An Introduction to the Mathematics of Neurons* (Cambridge Univ. Press, Cambridge, ed. 2, 1997), pp. 155–158.
22. A. Hernandez, E. Salinas, R. Garcia, R. Romo, *J. Neurosci.* **17**, 6391 (1997).
23. PFC neurons change the net sign of their stimulus dependence between stimuli f1 and f2. That is, the higher the stimulus value applied during the loading phase, the higher a PFC plus neuron's firing rate and the lower the minus neuron's firing rate. Yet the higher the stimulus value applied during comparison/decision, the lower the PFC plus neuron's firing rate and the higher the PFC minus neuron's firing rate because higher f2s are more likely to lead to "no" decisions (fig. S9).
24. C. Brody, *et al.*, in preparation.
25. D. Green, J. Swets, *Signal Detection Theory and Psychophysics* (J. Wiley, New York, 1966).
26. R. Ratcliff, *Psychol. Rev.* **88**, 552 (1981).
27. S. Link, *The Wave Theory of Difference and Similarity* (L. Erlbaum, Hillsdale, NJ, 1992).
28. R. Luce, *Response Times: Their Role in Inferring Elementary Mental Organization* (Oxford Univ. Press, Oxford, 1991).
29. X. J. Wang, *Trends Neurosci.* **24**, 455 (2001).
30. C. D. Brody, R. Romo, A. Kepecs, *Curr. Opin. Neurobiol.* **13**, 204 (2003).
31. S. T. Carmichael, J. L. Price, *J. Comp. Neurol.* **363**, 642 (1995).
32. During the late part of the second stimulus, the firing of many S2 neurons becomes correlated with the monkey's decision (*15*), but this occurs after decision-correlated activity arises in the PFC, and thus cannot be causal to it. For simplicity, in the model we treat only the initial creation of decision-correlated activity in the PFC, before it has propagated back to area S2.
33. During the delay period and across trials using identical f1 stimuli, we calculated the noise correlation r between pairs of neurons (*41*). We found covariation between pairs of plus neurons [$r = 0.13 \pm 0.04$ (SE), $n = 32$ pairs, and pairs of minus neurons ($r = 0.08 \pm 0.03$, $n = 17$). But pairs where one neuron is plus and the other is minus were anticovaried ($r = -0.08 \pm 0.02$, $n = 58$) (*24*).
34. Materials, methods, and documented computer code are available as supporting material on *Science* Online.
35. Good overlap in Fig. 3F requires high precision in the design of the i/o function shapes. This is a generic difficulty that all line attractors face (*30, 42*). We address this issue in the supporting online text by adapting the solution proposed by Koulakov *et al.* (*6*) to create a more robust model. Despite its greatly increased dimensionality, the more robust model can still be approximately described in terms of two variables (fig. S6), similar to the diagrams of Fig. 3.
36. The circuit of Fig. 3H is only one possible way to switch input signs. See (*43*) for another possibility.
37. U. Rudolph, H. Mohler, *Annu. Rev. Pharmacol. Toxicol.* **44**, 475 (2004).
38. A. Morishita, A. Yajima, *Kybernetik* **11**, 154 (1972).
39. H. Seung, in *The Handbook of Brain Theory and Neural Networks*, M. Arbib, Ed. (MIT Press, Cambridge, MA, ed. 2, 2003), pp. 94–97.
40. M. Usher, J. L. McClelland, *Psychol. Rev.* **108**, 550 (2001).
41. E. Zohary, M. N. Shadlen, W. T. Newsome, *Nature* **370**, 140 (1994).
42. H. S. Seung, D. D. Lee, B. Y. Reis, D. W. Tank, *J. Comput. Neurosci.* **9**, 171 (2000).
43. E. Salinas, *J. Neurosci.* **24**, 1113 (2004).
44. R. Romo, E. Salinas, *Annu. Rev. Neurosci.* **24**, 107 (2001).
45. R. Romo, E. Salinas, *Nature Rev. Neurosci.* **4**, 203 (2003).

46. C.K.M. and C.D.B. jointly developed and implemented the model and wrote the paper. R.R. conceived and carried out the experiments.

This work was supported in part by a Swartz Foundation Fellowship to C.K.M.; an International Research Scholars Award from the Howard Hughes Medical Institute and awards from Direccion General de Asuntos del Personal Academico–Universidad Autonoma Nacional de Mexico and the Millennium Science Initiative–Consejo Nacional de Ciencia y Tecnologia to R.R.; and by a Sloan Foundation Research Fellowship, an award from the Redwood Neuroscience Institute, and NIH grant 1R01MH067991-01 to C.D.B. We thank J. D. Cohen, Z. F. Mainen, S. S. -H. Wang, and A. M. Zador for comments on the manuscript, and J. J. Hopfield for discussion.

Supporting Online Material

www.sciencemag.org/cgi/content/full/307/5712/1121/DC1
Materials and Methods
Figs. S1 to S9
References
Model S1

17 August 2004; accepted 6 January 2005
10.1126/science.1104171

Toploader Balances

The Excellence XS Toploader balance features leading-edge weighing technology, solid design, simple operation, and unmatched connectivity. It brings together speed, accuracy, and communications without compromise. The weighing cell is one example of the balance's state-of-the-art weighing technology; two microprocessors accelerate measurement and reduce stabilization time by up to 20 percent. The instrument's fully automatic internal adjustment means that it provides precise measurement every time. Full-metal housing provides protection against corrosive chemicals and prevents penetration by dust and liquids.

Mettler Toledo For information 800-METTLER www.mt.com/us

Larger Volume Pipette Tips

The P1000 Tips for the Biomek NX and FX Span-8 systems are large-volume tips certified to be ribonuclease-free and deoxyribonuclease-free. They pipette a full 1 ml with a barrier. They are suitable for biological sample applications such as DNA (genomic and plasmid) purification, RNA isolation, protein purification, and broadcast dispensing of reagents for assay development and dilution studies.

Beckman Coulter For information 800-742-2345 www.beckmancoulter.com

Non-Spill Couplings

NS4 ABS Series Non-Spill Couplings are made of acrylonitrile butadiene styrene to enable medical device manufacturers to extend the benefits of non-spill functionality to applications requiring both medical-grade quality and gamma sterilization. The use of medical-grade material with the ability to be gamma sterilized makes the product suitable for a wide range of applications, including medical lasers, surgical equipment, cooling systems, advanced patient temperature therapy, cold therapy, and fluid collections systems. NS4 ABS features a non-spill shutoff valve that enhances operator safety and speeds connection time.

Colder Products For information 800-444-2474 www.colder.com

Flash Luminescence Reader

The CyBi-Lumax flash HT is a new flash luminescence reader that enables high throughput and data quality in functional screening of G-protein coupled receptors and calcium channels useful in drug discovery. A new 16-channel dispenser enables flash luminescence reading times of less than 60 seconds for 384-well plates and less than 3 min in the 1536-well format. The instrument offers a solution for dispensing of cells to start the receptor activation signal within the reader. A unique cell recirculation function ensures homogeneous cell dispensing for unsurpassed data quality. Cell stress has been eliminated by optimization of pumps and nozzles.

CyBio For information +49 36 41 351 0 www.cybio-ag.com

Primer Sets

More than 40 canine, feline, and chicken Primer Sets for RT-PCR (reverse-transcription polymerase chain reaction) evaluation of cytokine-related messenger RNA expression are now available. Each Primer Set comes with gene-specific PCR primers and a positive control sufficient for 30 reactions, as well as a data sheet with protocol recommendations. The sets have been carefully designed and tested.

Pierce Biotechnology For information 800-487-4885 www.endogen.com

Improved Spectroscopy

Difficult measurements in the ultraviolet and visible regions can be achieved using fiber optic diode array spectrometry. The versatility of fiber optic sample access allows measurements to be taken in locations that would normally be impossible. Examples of some novel applications include: absorbance measurements inside a calorimeter cell, incident light measurements 30 m below the surface of the sea, in situ measurements in boiling liquids, and in-line reaction monitoring at concentrations a thousand times too high for conventional instrumentation.

AstraNet Systems For information 01223 872197 www.astranetsystems.com

Stereotaxic Surgery Videomicroscope

Using this Videomicroscope, researchers can view surgical sites hands-free on a clear and color-accurate 6.4-in flat panel monitor. The Videomicroscope has a continuous magnification range of more than 50×, so even the smallest surgical procedure is visible and clear. Magnification, along with brightness, focus, and other functions, is controlled with an easy-to-use mouse. The Videomicroscope can be connected to a VGA monitor or television, and images can be saved to a computer.

Stoelting For information 630-860-9700 www.stoeltingco.com

New Protein Immunoblotting Method

A new protein immunblotting technique using Immobilon transfer membranes is designed to overcome high nonspecific binding of secondary antibodies. The procedure involves blotting proteins onto a sheet of Immobilon membrane. The membrane is probed with the primary antibody and then assembled with a second membrane sheet. Both membrane sheets undergo a second blotting under acidic conditions. This second blot allows the primary antibody molecules to desorb from their corresponding antigen and transfer onto the second membrane, while the antigen and the interfering proteins remain bound to the first membrane. The second membrane can then be probed by secondary antibodies without the risk of nonspecific binding. The method is suitable for a wide range of research applications.

Millipore For information 800-MILLIPORE www.millipore.com/immobilon

Newly offered instrumentation, apparatus, and laboratory materials of interest to researchers in all disciplines in academic, industrial, and government organizations are featured in this space. Emphasis is given to purpose, chief characteristics, and availability of products and materials. Endorsement by *Science* or AAAS of any products or materials mentioned is not implied. Additional information may be obtained from the manufacturer or supplier by visiting www.science.labvelocity.com on the Web, where you can request that the information be sent to you by e-mail, fax, mail, or telephone.

International Careers Report: **Singapore**

PUTTING IT ALL TOGETHER

Singapore has successfully set up the infrastructure for a thriving life science industry. Now, its government is taking the next step: encouraging overseas pharmas and biotechnology firms to set up research centers and other institutions in the city state. BY PETER GWYNNE

About 20 years ago, the government of Singapore decided to create the foundations of a life science enterprise. Advised by such luminaries as Nobel laureates Sydney Brenner and David Baltimore, the city state began to set up research institutions devoted to individual facets of life science and to boost existing biology departments in local universities.

In June 2000, the next stage began. "Philip Yeo [chairman of the government's Agency for Science, Technology and Research (A*STAR)] and some cabinet ministers decided that we ought to build life sciences as a pillar of the economy," recalls Kong Hwai Loong, executive director of A*STAR's Biomedical Research Council. Since then, the research institutions have matured, global pharmaceutical and biotechnology companies have set up regional research centers in the country, and Singaporean startups have become more prominent. During the last year, many of those organizations have moved into Biopolis, a complex close to the National University of Singapore and the National University Hospital that is intended to stimulate the advance of life science by offering shared facilities and services and encouraging life scientists to mingle across organizations and disciplines. CONTINUED »

Agency for Science, Technology and Research
http://www.a-star.edu.sg

Exploit Technologies
http://www.exploit-tech.com

GlaxoSmithKline Singapore
http://www.gsk.com

Johns Hopkins Singapore
http://www.jhs.jhmi.edu

Nanyang Technological University
http://www.ntu.edu.sg

National University of Singapore
http://www.nus.edu.sg

Novartis Institute for Tropical Diseases
http://www.novartis.com

Swiss House Singapore
http://www.swisshouse.org.sg

International Careers Report: **Singapore**


PAUL HERRLING

Only a Start

Promising as they are, those efforts represent only a start. "We are humble enough to realize that the initial phase of building up the infrastructure and the legal and technical structures are not difficult for Singapore," Kong explains. "The challenge of the future is to go into areas for which no country has a good role model to emulate – such as issues of getting enough people to take up science and bridging the gap between basic science and translational research."

Yeo has started to attack those issues by setting up a scholarship scheme. Run by the A*STAR Graduate Academy, and intended to train 1,000 life science Ph.D.s in 10 years, it has awarded 400 scholarships and fellowships since it started in 2001. "The objective of the scholarships is to attract more Singaporeans to take up life science," Kong says. "After a few years, they will see industry as an attractive career, and so help to stimulate the economy."

Representatives of the life science industry recognize the benefits of working in the city state. "We have a longstanding history of working with Singapore; we have two manufacturing sites and our Asia-Pacific head office here," says Mark Duxon, head of the Center for Research in Cognitive and Neurodegenerative Diseases and Disorders, a research organization that pharmaceutical company GlaxoSmithKline set up last year. "There's a tangible sense that things are happening in Singapore with respect to the biological sciences. The government has matched that vision with the Biopolis facility."

Paul Herrling, head of corporate research for Novartis, had an equally positive experience when he helped to set up the Novartis Institute for Tropical Diseases, a Singapore-based facility intended to carry out research on diseases endemic to the third world that are unlikely to attract the attention of drug companies based in Europe and North America. "One of the key tests for us to go there was the ability to recruit young talent," says Herrling, who is chairman of the new institute. "We never had any problems recruiting; the only limitations were space. We have roughly 70 people on board from 16 different nations."

International Ambience

Singapore's government works hard to maintain that type of international appeal. In recent months, prominent British scientists Sir David Lane and Sir George Radda have joined the country's life science community or its advisory boards. What attracts them? "They see in us a bunch of people who know what they are doing and have a vision and dream that they share," Kong declares. "Also, they are increasingly convinced that the sciences in Biopolis are leading edge, so that people can advance their careers in Singapore."

Recruitment of such individuals does more for Singapore than increase the quality of its research. It helps to attract other potential recruits who might otherwise have doubts about the quality of the science carried out in Singapore. "It's very impressive in terms of the people they've been able to attract," says Ian McNiece, director of Johns Hopkins Singapore. "The proximity of top people opens the doors to collaborations."

The creation of Johns Hopkins Singapore last year as a branch of the Baltimore university represents another facet of Singapore's attraction to the global life science community. "We are focused on developing more into an academic institute – a division of the Johns Hopkins University School of Medicine," says McNiece, who is also a member of Johns Hopkins Oncology Center in Baltimore. "We're recruiting internationally for six to eight faculty who will be based in Singapore but will also have primary appointments in Baltimore."

Local universities, as well as overseas institutions, recruit heavily from abroad, emphasizing the buzz that surrounds the field. "My general feeling is that it is an extremely dynamic environment that's developing quite rapidly," says Markus Wenk, who joined the National University of Singapore (NUS) as an assistant professor of biochemistry in January of last year. "There's an awareness that this is a place that might have an impact in the future."


SUZANNE HRABA-RENEVEY

Tax Incentives and Political Commitment

Singapore's government has a long history of bringing in overseas corporations in addition to individual scientists. "The Economic Development Board (EDB) is very effective at attracting companies to Singapore, using tax incentives and a political commitment to research, education, and entrepreneurship," says Suzanne Hraba-Renevey, executive director of Swiss House Singapore, an organization that acts as a kind of two-way clearinghouse between Singapore and Swiss companies. "The government has created a suitable environment in terms of manpower, infrastructure, and legislative policies," Hraba-Renevey continues. "They have also made Singapore an effective hub for surrounding countries."

One secret of the country's appeal to pharmas and other international life science companies is its effort to make transitions to Singapore as user-friendly as possible. "Our institute is a public-private partnership with EDB," explains Herrling of the Novartis Institute for Tropical Diseases. "The board has been absolutely crucial. Rather than our having to run around to various ministries, we had one contact group – a liaison group of brilliant young people at EDB who opened all the doors for us."

Ultimately, however, the ability to carry out top-notch science has emerged as a crucial factor in decisions to locate in the city state. "Financial incentives exist," GlaxoSmithKline's Duxon concedes. "But it comes down to being able to do research of a quality similar to what we do in the United States and Europe."

In some cases, Singapore offers the chance to carry out more than Western researchers can. "We have contributed to the ethical discussions on issues like ethical cloning," Kong says. "This has allowed us to

move ahead on issues such as therapeutic cloning and embryonic stem cells [research on which is restricted in several Western countries]. The success factor is the smallness of the country and the ability to do things well."

Biopolis plays a major role in Singapore's press for success. "It is an epicenter," Kong says. "It has given visibility to life science in Singapore." Duxon of GlaxoSmithKline, who moved to Singapore five months ago, agrees. "I was increasingly impressed with what has been done at Biopolis in a very short time with the whole idea of bringing academic institutions, pharmas, and research institutions into one campus," he says.


ALEX LAW

Benefits of Biopolis

The S$500 million (US$305 million) biomedical hub consists of seven buildings linked by sky bridges and clustered in an area of 2 million square feet. Two of the buildings house private biomedical companies. The other five accommodate A*STAR's biomedical research institutes, devoted to bioinformatics, bioprocessing technology, genomics, molecular and cell biology, and bioengineering and nanotechnology. Another tenant is Exploit Technologies Pte Ltd.; that A*STAR institution has the task of identifying, protecting, and exploiting intellectual property created by the research institutes.

The campus offers several benefits to research groups and individual scientists. Shared scientific services include facilities for electron microscopy, nuclear magnetic resonance, X-ray crystallography, histology, DNA sequencing, and the identification, sequencing, and weight determination of proteins. And a biological resource center offers small animal facilities and quarantined rooms to academic and commercial research groups. The shared facilities have particular value for startup companies and small research groups because they allow the organizations to reduce their overhead. "We get the same stuff for less money, and so we can hire more people," notes Novartis's Herrling.

Even more important to Singapore's life science community, Biopolis encourages interactions among scientists from different organizations, including nearby universities. "We're very close – a five-minute cab ride away," explains Wenk of NUS. "Biopolis is great because seminars take place there. It's the center of gravity of biomedical research." Like NUS, Nanyang Technological University (NTU) contributes regular speakers to seminars in Biopolis. "We are also constantly engaging in cultural and scientific exchanges, ranging from conferences and meetings to social events," says James Tam, dean of NTU's School of Biological Sciences, agrees.

The set-up of the campus also encourages informal meetings among researchers. "You meet them as you go to lunch in the little cafes with outdoor seating that were designed to facilitate mixing and collaboration among busy people," Johns Hopkins's McNiece says. Overall, Kong summarizes, "Biopolis brings together a complete spectrum of research capabilities. That allows the researchers to interact easily with each other."

The Swiss Connection

Swiss companies have had their own links with Singapore for several years, setting up regional offices and research groups. During the past five years, however, corporate Switzerland has expressed a broader interest in the city state. Last July, as a result of that interest, the Swiss government launched Swiss House Singapore as an intermediary between the two nations' science and technology communities. "We call ourselves a door opener," says Suzanne Hraba-Renevey, executive director of the new organization.

The new Swiss House – the third to be set up, following those in Boston and San Francisco – has a wide range of duties. "We cover tertiary education, research, and entrepreneurship. We are a low-risk, as well as a proximity- and cost-effective tool for our partners in Switzerland and Singapore," Hraba-Renevey explains.

The organization got up to speed quickly. "We have some very specific inquiries from Swiss companies asking about opportunities for startups and requesting information on what's going on in Singapore. We set up meetings with the Economic Development Board (EDB) and venture capitalists. And we provide a working space at nominal price, as well as contacts with working groups here that allow our partners to look at local opportunities," Hraba-Renevey reports. "At the educational and research levels, we are supporting the common Master's degree in tropical diseases organized by the Novartis Institute for Tropical Diseases, the National University of Singapore, the University of Basel, and the Swiss Tropical Institute. We also hope to provide financial support for Singaporean students to travel to Switzerland to take classes in language immersion programs. Another type of activity of ours is organizing and/or participating in large events such as the educational fair Career 05, in which nine of the Swiss universities will have the opportunity to present their programs."

The organization originally set up shop in the Swiss embassy, but it quickly moved into Biopolis. "Being there allows us to relate very easily to the Singaporean science agencies and EDB," Hraba-Renevey says. "We have a direct research link, as five of the national research institutes sit here as well as private research institutes such as Novartis and Johns Hopkins University. We also have a connection to business. That is exactly the mix we are covering: government, research, education, and innovation."

Collaborative Enterprises

Singapore's life science authorities in general and the Biopolis campus in particular also encourage interaction among disciplines and institutions. "People seem very excited about collaborations," says McNiece, who started to organize joint research efforts as soon as he arrived in Singapore. "My interest is in cord blood for transplant therapy," he says. "Several companies have an interest in growing blood cells from cord blood."

Government research institutions provide a ready source of scientists and subjects for joint projects. "We started an impor- CONTINUED »

International Careers Report: **Singapore**

tant collaboration with the Genome Institute early last year," says Herrling. "We suspected that an epidemic of dengue fever in Indonesia might have been a new serotype of the disease. We did serotyping, intending the results to be published. The collaboration worked extremely well and is still going on. It is clear that we can work well with the scientists around us."

Universities stand to gain particular benefit from collaborations fostered by the Singaporean authorities. "These collaborations are necessary in sharpening our competitiveness maintaining our edge, as the School of Biological Sciences was established to play a leading role in Singapore's life sciences initiative," says Alex Law, vice dean of NTU's School of Biological Sciences. The school has several shared programs with research institutes in Biopolis, including disease oriented projects that focus on such topics as cancer and the use of stem cells in regenerative medicine. "We have a research collaboration with Novartis that we initiated last May," NUS's Wenk adds. "We specialize in lipids and Novartis was interested. The company is funding our group, with staff and work shuttling between them and us." The expected result: "It makes us more visible," Wenk continues. "It also makes it easier for me to recruit; 95 percent of the people who apply to my lab want to do this collaborative work."

Companies obviously receive a quid pro quo from collaborations in which they take part. "We're discussing collaborations with EDB; we're keen on putting some Ph.D. scholarships in place or having full-time Ph.D. students in the research institutes," GlaxoSmithKline's Duxon says. "Having academic research partners helps to ensure that there are people trained with some appreciation of drug discovery and the ability to bring along new ideas."

JAMES TAM

Joint Degrees and Scholarships

Collaboration also extends to training. "We're setting up a joint degree program with Swiss institutions – the University of Basel, the Swiss Tropical Institute, and the Novartis Institute for Tropical Diseases," Wenk says. "This is probably one of the first Master's programs involving the fine line between academic and corporate research. We're doing the final tuning of the financing and administrative issues. We expect a first intake of students in summer this year."

A reservoir of well-trained life scientists is the target of the A*STAR scholarship scheme that started in 2001. The scholarships take two forms. One sends 19-year-old Singaporean students to overseas universities to gain their degrees and bring back their skills to their native land. The other permits scientists with Bachelor's degrees to obtain their Ph.D.s at the National University of Singapore, Nanyang Technological University, or a renowned overseas university. "This scheme provides substantial manpower to the universities," Kong says. "Students have two supervisors, one at each university, so that faculty members of the universities get to know each other. We find that young people form the best bridges."

The quality of the local scientific manpower has certainly played a major part in persuading global biomedical companies to set up in Singapore. When Duxon and a representative from GlaxoSmithKline's business development and finance group visited Singapore to see if the context was right to do neuroscience preclinical research, he recalls, "It was clear that there was a very good skill base in biological sciences."

The result was the company's first satellite site in Southeast Asia, and its first center of excellence outside the United States and Europe. "The surroundings of biotechs, research institutes, and academic institutions meant a lot to us when we invested S$63 million [US$38.5 million] to help establish offices and laboratories to support 30 to 35 people focused on lead optimization as part of our drug discovery," Duxon says. The new center concentrates on diseases that involve the degeneration of memory, such as schizophrenia and Alzheimer's disease. The company has also helped the British High Commission set up a science and technology office in Biopolis.

MARKUS WENK

Depth of Commitment

The Novartis Institute for Tropical Diseases will initially work on potential treatments for dengue fever and tuberculosis, which continue to afflict the populations of Southeast Asian nations. Novartis will make the treatments available to poor patients in endemic countries on a not-for-profit basis. "The institute will have roughly 100 people," says Herrling. The company shows the depth of its commitment through its leadership. "We brought in Alex Matter, probably our best drug discovery person and the man who led the team that developed Gleevec, as director of the institute," Herrling says.

As an established global pharma, Novartis will have no trouble developing any drugs that emerge from the institute. Singaporean research institutes must take a different route to translating their findings into marketable products. Their vehicle: Exploit Technologies. The organization works closely with researchers to find commercial partners who will develop their inventions into new products, processes, and therapies. "We research the market for specific technologies, tapping into researchers' contacts and our own commercial contacts, and using web and in-house commercial intelligence databases," states the institution's website. "We are continually expanding our knowledge of companies' technology needs and performing consumer and market research to better understand industrial needs."

Beyond its inclusive coverage of everything from basic research to marketing, Singapore has one more item to offer life scientists: a satisfying lifestyle. "It is a very tolerant and multicultural environment – an incredible melting pot," Duxon says. "It's a smorgasbord of cultures." That boosts Singaporean science as well as scientists. "From a research perspective," Duxon concludes, "you want as many sources of ideas as possible."

A former science editor of Newsweek, *Peter Gwynne (pgwynne767@aol.com) covers science and technology from his base on Cape Cod, Massachusetts, U.S.A.*

This is the first of three features on postdoctoral opportunities this year. The next will appear in the 29 April issue of Science.

70th CSHL Symposium: Molecular Approaches to Controlling Cancer

June 1 - 6, 2005 **abstracts due: March 9, 2005**

Organized by **Bruce Stillman & David Stewart, Cold Spring Harbor Laboratory**

Topics include

Molecular pathways in cancer
Cancer oncogenes and tumor suppressor genes
Development and validation of therapeutic targets
Diagnostic and early detection markers
Animal models for human cancer
Cancer progression and metastasis
Cancer stem cells
Anti-angiogenic strategies

Speakers include

Jerry Adams, Walter & Eliza Hall Institute of Medical Research, Australia
James Allison, HHMI/Memorial Sloan Kettering Cancer Center
Mariano Barbacid, Centro Nacional de Investigaciones Oncologica, Spain
Stephen Baylin, Johns Hopkins University School of Medicine
Philip Beachy, Johns Hopkins University School of Medicine
Robert Benezra, Memorial Sloan Kettering Cancer Center
Rene Bernards, Netherlands Cancer Institute
Anton Berns, Netherlands Cancer Institute
J. Michael Bishop, University of California, San Francisco
Mina Bissell, Lawrence Berkeley National Laboratory
Joan Brugge, Harvard Medical School
Judith Campisi, Lawrence Berkeley National Laboratory
Sara Courtneidge, Van Andel Research Institute
Titia de Lange, The Rockefeller University
Ronald DePinho, Dana Farber Cancer Institute
Robert Eisenman, Fred Hutchinson Cancer Research Center
Stephen Elledge, Harvard Medical School
Gerard Evan, University of California, San Francisco
Andrew Feinberg, Johns Hopkins University School of Medicine
Judah Folkman, Children's Hospital /Harvard Medical School
Stephen Friend, Merck Research Laboratories
Todd Golub, The Broad Institute
Joseph Gray, Lawrence Berkeley National Laboratory
Carol Greider, Johns Hopkins University School of Medicine
Daniel Haber, Massachusetts General Hospital
Douglas Hanahan, University of California, San Francisco
Ed Harlow, Harvard Medical School
James Herman, Johns Hopkins University
Tyler Jacks, HHMI/Massachusetts Institute of Technology
William Kaelin, Dana-Farber Cancer Institute/HMS
Raghu Kalluri, Beth Israel Deaconess Medical Center
Michael Kastan, St. Jude Children's Research Hospital
Mary-Claire King, University of Washington
Stanley Korsmeyer, Dana Farber Cancer Institute/HMS
David Lane, University of Dundee, UK
Jacqueline Lees, Massachusetts Institute of Technology
Arnold Levine, Institute for Advanced Studies, Princeton
David Livingston, Dana-Farber Cancer Institute/HMS
Scott Lowe, Cold Spring Harbor Laboratory
Joan Massague, Memorial Sloan Kettering Cancer Center
Frank McCormick, University of California, San Francisco
Matthew Meyerson, Dana-Farber Cancer Institute/HMS
Sean Morrison, University of Michigan
Pier-Paolo Pandolfi, Memorial Sloan-Kettering Cancer Center
Luis Parada, UT Southwestern Medical Center
Nikola Pavletich, Memorial Sloan Kettering Cancer Center
Carol Prives, Columbia University
Charles Sawyers, University of California, Los Angeles
Charles Sherr, HHMI/St. Jude Children's Research Hospital
Craig Thompson, University of Pennsylvania
Thea Tlsty, University of California, San Francisco
Terry Van Dyke, University of North Carolina at Chapel Hill
Maarten Van Lohuizen, Netherlands Cancer Institute
Harold Varmus, Memorial-Sloan Kettering Cancer Center
Robert Weinberg, Whitehead Institute for Biomedical Research
Zena Werb, University of California, San Francisco
Michael Wigler, Cold Spring Harbor Laboratory
Paul Workman, Cancer Research UK
George Yancopoulos, Regeneron Pharmaceuticals, Inc.

Cold Spring Harbor Laboratory
Meetings & Courses Program
1 Bungtown Road, Cold Spring Harbor, NY 11724
Phone 516 367 8346 Fax 516 367 8845
Email meetings@cshl.edu **http://meetings.cshl.edu**